Topology and disorder effects in interacting and open quantum spin systems and analogues

Ephraim Bernhardt

INSTITUT POLYTECHNIQUE DE PARIS

NNT : 2023IPPAX077

Thèse de doctorat

Topology and disorder effects in interacting and open quantum spin systems and analogues

Thèse de doctorat de l'Institut Polytechnique de Paris
préparée à l'École polytechnique

École doctorale n°626 École doctorale de l'Institut Polytechnique de Paris (EDIPP)
Spécialité de doctorat : Physique

Thèse présentée et soutenue à Palaiseau, le 18 Septembre 2023, par

M. EPHRAIM BERNHARDT

Composition du Jury :

M. Peter P. Orth Professeur, Universität des Saarlandes	Président
M. Alberto Rosso Directeur de recherche au CNRS, LPTMS, Université Paris-Saclay	Rapporteur
M. Thomas Schmidt Professeur, Université du Luxembourg	Rapporteur
M. Cristiano Ciuti Professeur, MPQ, Université Paris-Cité	Examinateur
M. Michel Ferrero Chargé de recherche au CNRS, CPhT, École Polytechnique	Examinateur
M. Loïc Henriet Chief Technology Officer, PASQAL	Examinateur
M. Matteo Rizzi Professeur, THP, Universität zu Köln	Examinateur
Mme Karyn Le Hur Directrice de recherche au CNRS, CPhT, École polytechnique	Directrice de thèse
M. Cyril Elouard Junior Professor, LPCT, Université de Lorraine	Invité

Abstract

This PhD thesis is concerned with the interplay of effects of disorder, localization, interaction with the environment and topology in quantum many-body systems. It aims at studying said interface both from a fundamental interest, as well as to develop perspectives with regards to applications in quantum technology. A special focus of this thesis is on spin systems, as they form a suitable platform for probing above mentioned effects and are also interesting from the perspective of experimental realizations and applications. Starting from a single spin-1/2 in a radial magnetic field, topology can be defined from the poles of the ground state manifold. This model is analogous to several other condensed matter models, such as the Haldane model or the Kitaev wire. The definition of topology in the spin model can be extended to interacting systems comprising multiple spins, as well as to open systems coupled to an environment.

Experimentally, this topology can be probed from a dynamic protocol driving the magnetic field acting on the spin in time. In this setup, the thesis investigates a 'quantum dynamo effect' occurring as a consequence of the driven dissipative dynamics when coupling to an environment. This effect bears an intriguing connection with the 'dynamically accessed topology' of the spin. This thesis defines and investigates thermodynamic properties of this effect corresponding to a work-to-work conversion coherently displacing certain modes of the environment. It opens perspectives for energy transfers on the quantum scale through an environment. The definitions and probes are compared using different analytical and numerical techniques for evaluating the driven dissipative dynamics.

In interacting systems composed of several spins, the topology of each spin can be studied and has previously been shown to yield fractional values depending on the symmetry of the model. This thesis emphasizes the behavior of this fractional topological phase when disorder is introduced and shows that the latter can lead to its extension. An interpretation of these effects in terms of Majorana fermions is discussed, enabling considerations for applications in quantum information.

The effects of disorder and localization physics are discussed in depth for a model which can be realized using cold atoms and can in a certain limit be mapped to a spin model as well. A particular form of quenched disorder can be realized in this system through coupling to a second particle species. In this case, there is an interesting connection to $\mathbb{Z}_2$ lattice gauge theories when the impurities introducing disorder to the system acquire quantum dynamics themselves. This thesis investigates the interplay between an applied $\mathcal{U}(1)$ gauge field allowing to define a local current and this special form of disorder and in particular proposes to use this current as an indicator of the localization properties. A numerical study using exact diagonalisation demonstrates the presence of a many-body localized phase in this model. This phase is identified from the scaling of the entanglement entropy and witnessed by the bipartite fluctuations and the local current. The thesis

offers perspectives for a fundamental understanding of the interplay of topology, open system dynamics and disorder effects in quantum systems and bridges with experimental realizations and applications.

Publications

The following articles have been published during the course of this PhD:

1. Ephraim Bernhardt, Fan Yang and Karyn Le Hur. **Localization dynamics from static and mobile impurities**. *Physical Review B*, 104(11):115113, 2021. doi:10.1103/PhysRevB.104.115113.

2. Ephraim Bernhardt, Cyril Elouard and Karyn Le Hur. **Topologically protected quantum dynamo effect in a driven spin-boson model**. *Physical Review A*, 107(2):022219, 2023. doi:10.1103/PhysRevA.107.022219.

Another article, concerning the contents described in Chap. 3, about fractional topology, disorder, the relation to Majorana fermions and applications to quantum information, has been submitted to the preprint server arXiv and is in preparation for submission to a journal at the time of writing of this manuscript:

3. Ephraim Bernhardt, Brian Chung Hang Cheung and Karyn Le Hur. **Majorana fermions and quantum information with fractional topology and disorder**. *arXiv:2309.03127*, 2023. doi:10.48550/arXiv.2309.03127.

Acknowledgements

I first and foremost would like to thank Karyn Le Hur for her supervision of my PhD thesis and all the guidance and help she gave me during these years. Working with her and in her group has taught me a lot and I feel extremely grateful for all the time, patience and effort she dedicated to me and my project. When I started my PhD in 2020 in a period of large uncertainty, it was a great relief to have a supervisor who was available, understanding and interested. Thank you!

During my PhD, I had the great privilege to collaborate with Cyril Elouard and Fan Yang. I learned a lot from them, both about physics and about the ways of doing good research. Cyril's visit at CPhT is a nice memory of two intense and fruitful days, and in general I profited a lot from his creativity and availability. Similarly, when working with Fan at the start of my project and even prior, during my Master's, it was immensely helpful to discuss with her the small and big questions that arose.

I would like to thank the reviewers of my PhD manuscript - Alberto Rosso and Thomas Schmidt - for their willingness to fulfill this task and for being part of the jury as well. Furthermore, I would like to thank all the examiners - Peter P. Orth, Cristiano Ciuti, Matteo Rizzi, Michel Ferrero and Loïc Henriet for accepting to participate in the jury. Albert Rosso and Michel Ferrero already constituted the jury of my midterm-defense, and I am grateful for their evaluations and their advice, both on scientific and personal subjects. I would also like to thank Loïc Henriet and Peter P. Orth for the helpful discussion we had.

My time at CPhT was - although mainly virtually in the beginning of my PhD - an opportunity to meet bright colleagues and I am grateful for all the engaging encounters. I especially want to thank Fan, Philipp, Joel, Julian, Frederick and Sariah for having shared an office, many conversations and their support.

During my time at CPhT, I benefitted a lot from the uncomplicated adminsitrative support provided by Florence Auger, Malika Lang and Fadila Debbou. Similarly, the impeccable IT support of Yannick Fitamant, Danh Pham-Kim, Ilandirayane Settoumaran, Vazoumana Fofana and Jean-Luc Bellon was an important backup. Thank you a lot!

My PhD work was funded by the DFG as part of the research unit 'FOR2414,' which I sincerely acknowledge. I would like to thank the entire steering comitee for having set up this project. It was a pleasure to participate at the conferences, taskforce meetings, the summer school and the PhD retreat, which all provided me with valuable insights and I am happy to have met many colleagues there.

For having facilitated my stay in Paris, I would like to express my gratitude to the alumni association of École polytechnique and in particular to Yves Stierlé for his assistance.

I am fortunate to have good friends with whom I went through the Master's and who afterwards chose a somewhat similar path as me. The exchanges we had during the time of

our PhDs were valuable and dear to me, and I would like to thank in particular Francesco, Pulkit, Gabriele and Eugenio, along with many other friends whose open ear was a great help during these challenging times.

My family has always played a special role for me, and I cannot be anything but grateful to Doris and Michael Liebers, as well as Annerose, Holm, Ulrike, Sarah, Aaron, Joseph and Leah-Ruth Bernhardt. Having the certainty of their support has always been invaluable to me.

Lastly, I would like to thank Olya for everything, and in particular for being by my side during all these years and just being who she is.

Contents

Chapter 1

Introduction

The study of topological properties of condensed matter systems has attracted a lot of attention in recent years. At the core of this interest is the fact that topological phases cannot be explained by the traditional theory of spontaneous symmetry breaking due to Landau [1, 2]. Topological phases constitute thus new phases of matter, which makes their investigation relevant from a fundamental physical interest. As the name 'topological' suggests, these properties do not depend on local changes, but are rather evaluated as a global property of the system [2]. Interest in them is in addition fueled by exotic properties that are promising for technological applications: A common feature of topological phases is a bulk-edge correspondence, in which topological properties of the bulk manifest themselves in the occurence of topologically protected states on the boundary of the system [3]. An example are topological insulators, which are insulating in the bulk, but show conducting edge modes, which are in fact related to the topological properties of the bulk [2].

A concrete and foundational example for this is the integer quantum Hall effect discovered experimentally in 1980 [4]. In a two-dimensional electron gas subject to a strong magnetic field, it was found that the transverse Hall resistance (and thereby also the Hall conductance σ_{xy}) develops quantized plateaus as a function of the applied gate voltage. The remarkable stability of these plateaus hints at their topological origin. The relation found experimentally reads

$$\sigma_{xy} = \nu \frac{e^2}{h}, \tag{1.1}$$

where e is the elementary charge, h is the Planck constant and ν is an integer. Theoretical considerations of this peculiar effect followed suit [5–7]. The band structure of a two-dimensional electron gas in a strong magnetic field is described by Landau levels, with finite gaps inbetween. It can be shown that the transverse conductivity due to a band is related to its topology: In particular, the integer ν observed experimentally is given by a sum of a topological invariant - the so-called Chern number - for each occupied band,

i.e., [2, 7]

$$\nu = \sum_{\alpha} C_{\alpha}, \tag{1.2}$$

with

$$C_{\alpha} = \frac{1}{2\pi} \int d\vec{k} \mathcal{F}^{\alpha}_{\vec{k}}. \tag{1.3}$$

Here, $\mathcal{F}^{\alpha}_{\vec{k}} = \vec{\nabla} \times \mathcal{A}^{\alpha}_{\vec{k}}$ is the Berry curvature of band α defined from the Berry connection $\mathcal{A}^{\alpha}_{\vec{k}} = i \left\langle \psi^{\alpha}(\vec{k}) \right| \vec{\nabla}_{\vec{k}} \left| \psi^{\alpha}(\vec{k}) \right\rangle$ with $\left| \psi^{\alpha}(\vec{k}) \right\rangle$ the Bloch wave function [8] and the integration ranges over the first Brillouin zone. Similarly to the integral of the Gaussian curvature over a surface defining its genus, the Chern number is an invariant defined from an integration of the Berry curvature over the Brillouin zone [2]. This demonstrates the topological nature of the integer quantum Hall effect.

In 1988, it has been realized by Haldane that a similar Quantum Hall effect can also occur in a lattice model, namely graphene with additional complex next-nearest neighbor hopping [9]. In this setup, which we will briefly describe in Sec. 1.1.2, chiral edge states can be obtained explicitly as a manifestation of the above mentioned bulk-edge correspondence [2]. As a lattice model, an attractive feature of the Haldane model is that it can be realized using tunable implementations [10], making it an interesting model both for experimental verifications of topological properties, but also for further theoretical developments of these (see e.g. [11–13]).

Another instance of the bulk-edge correspondence is that of a topological p-wave superconducting wire, which we will also introduce in Sec. 1.1.2. It has a topological phase, in which it exhibits exotic Majorana edge modes [14].

Phases of quantum matter with topological properties are attractive, since such properties are stable against local perturbations and disorder and therefore interesting for technological applications [2]. Especially the above mentioned p-wave superconducting wire is of high interest for potential applications in topological quantum computing [15–17]. Coming back to the example of the integer quantum Hall effect from above, one can on the one hand show that the quantization of the transverse conductance is stable upon adding small disorder [6]. On the other hand, and less intuitively, disorder is playing a crucial role for the occurence of the quantum Hall plateaus by localizing states that do not contribute to the conductivity, as we will discuss below in Sec. 1.3.1. The interplay between topological properties and disorder is thus a complex field, giving rise to subtle properties, as we will see also in Chap. 3.

The study of disorder effects in quantum systems has itself given rise to a variety of curious new phenomena and phases. Anderson localization [18], a phenomenon occuring for particles in a 'dirty' environment, inherently because of the wave character of quantum

particles, was a milestone in this field. We will be focussed on localization effects in a particular quantum system tailored for experimental realizations in Chap. 4. Ever since the work of Anderson, the study of more complex setups with interactions among particles [19–21] has paved the way for the discovery of a phenomenon termed 'many-body localization' (MBL), describing closed systems which do not thermalize after a long time evolution. Remarkably, MBL is the only known mechanism showing this feature of non-thermalization in a robust way [22]. The understanding of this phase is essential in order to design applications in quantum technologies operating in the disordered, interacting, dynamic regime [23]. We will present a study of the MBL properties of a particular spin system in Chap. 5.

However, the necessity for the understanding of thermodynamic notions in the quantum realm in order to enable functional applications is a more general one. Even though the laws of thermodynamics, formulated for classical systems, can be generalized to quantum settings under certain restrictions [24], there are quantum setups not described by these conditions [25, 26] and generalizations are desirable [27]. In Chap. 2, we will discuss the 'quantum dynamo effect', describing a situation in which a driven system coupled to a bath can under certain conditions transfer work into the bath. Curiously, this setup and the effect show parallels with a topological invariant that can be defined for a spin in a radial magnetic field, but is in fact a model with several analogues in condensed matter, such as the above mentioned Haldane model. We will therefore start by introducing these topological notions with some detail for such a spin system.

1.1 Topological properties of a spin-1/2

A remarkable feature of condesed matter physics is that seeminlgy very different models can be mapped onto each other and in this way their similar physical properties are understood. This allows on the one hand to understand effects occuring in several models on a similar footing and on the other hand it opens the perspective to simulate systems, which otherwise would not be easily accessible, in an analogous setup. This is the paradigm of quantum simulation [28], where one tries to probe models from various areas of physics (ranging from condensed matter systems to, for example, gravitational physics) in a controllable, realizable quantum system. More generally, an early instance in which two different systems were successfully understood by mapping them onto each other is the Kramers-Wannier duality, which allows to map the high and the low-temperature regime of the two-dimensional Ising model onto each other [29]. Another interesting example is the duality between lattice gauge theory and generalized gauge invariant Ising models discovered by Wegner [30, 31]. We will discuss a special instance of this in Sec. 4.3.2.

In the realm of this thesis, we will be concerned in particular with spin models and their analogues in the context of topological properties, open system dynamics and disordered

setups. A recurrent motive throughout this work is the discussion of analogies between different systems, which can be used to gain a better understanding of physical properties: We will discuss a spin in a radial magnetic field which can be used to investigate the topological transition in the Haldane model and the Kitaev wire (see below in Sec. 1.1.2). This spin system exhibits interesting dynamical properties when coupled to an environment, that we will discuss especially in the light of the 'quantum dynamo effect' [32,33] in Chap. 2.

1.1.1 The model

The simplicity of the model of a spin-1/2 in a radial field enables studies of more complex setups where several such systems interact, giving rise to exotic fractional topological phases [12]. This will be the subject of Chap. 3, where we investigate such a model in the light of its response to disorder and find a disorder-enabled fractional topological region in the phase diagram in Fig. 3.5. Starting with a simple setup, consider a system governed by the Hamiltonian [12,32,34]

$$\mathcal{H}_{\text{rad}}(\theta,\phi) = -\frac{H}{2}(\sin\theta\cos\phi\sigma^x + \sin\theta\sin\phi\sigma^y + \cos\theta\sigma^z) - \frac{M}{2}\sigma^z, \tag{1.4}$$

where σ^α are the usual Pauli matrices for a spin-1/2, that is here subject to a radial field parametrized by the two angles θ and ϕ which are the parameters of this system. Here and throughout this thesis, we set $\hbar = 1$. In order to introduce the notion of topology of such a spin-1/2, let us first introduce the most important definitions. We will then exemplify the relation of this model to other condensed matter models in Sec. 1.1.2.

Calculating the Chern number for a spin-1/2

It has been realized in [34] that the Berry curvature can be understood in generic systems as a linear response to a change in an external parameter. In fact, given a parameter (labelled by μ) of a quantum system, one can define the associated Berry connection

$$A_\mu = i\langle\psi|\partial_\mu|\psi\rangle, \tag{1.5}$$

which then has a purely geometric interpretation [34]. One can then define the Berry curvature

$$\mathcal{F}_{\mu\nu} = \partial_\mu A_\nu - \partial_\nu A_\mu. \tag{1.6}$$

Consequently, if the parameter field lives on a compact manifold, one can then define the Chern number as [34]

$$C = \frac{1}{2\pi}\int_{\mathcal{S}} dS_{\mu\nu}\mathcal{F}_{\mu\nu}, \tag{1.7}$$

where the integration ranges over the compact parameter manifold $\mathcal{S}$ with surface element $dS_{\mu\nu}$ and the state for which it is calculated should be gapped from the other states in the

energy surface to observe a quantization of the Chern number. This quantization can be understood as a dynamical quantum Hall effect in parameter space, as has been pointed out in [34]. Following [34], we can define the Berry connection and curvature in Eqs. (1.5) and (1.6) for a dynamical quantum Hall effect in the parameter space of the spherical model in Eq. (1.4). This procedure in a way disregards the fact that they are spherical coordinates, treating them as Cartesian. This corresponds to the point of view that we are simply adapting the definitions of these quantities to a general parameter manifold without considering an embedding into Euclidean space.

It is straightforward to adapt Eqs. (1.5) and (1.6) for spherical coordinates and demonstrate that this leaves Eq. (1.7) unchanged for the concrete model of a spin in a radial field[1] [35, 36]. We will see below in Eq. (1.15) that this Chern number depends only on the spin expectation values at the two poles: Choosing a bipartition of the spherical parameter manifold, there is a homeomorphism mapping each hemisphere to the two-dimensional Euclidean space. This underlines that both of the approaches are equivalent, as long as a bipartition of the sphere is implemented. This will be crucial also for a generalization of these definitions for interacting systems, that we discuss in Sec. 1.1.3.

To take the definition from Eq. (1.7) to practice, let us consider a central system of this thesis which is a spin-1/2 in a radial magnetic field given by Eq. (1.4). As we will see, this example can showcase rich physics and is relevant to understanding the topological properties of a variety of other physical systems that can be mapped to it.

Related to the discussion above, the Berry curvature and therefore the Chern number of this system are defined upon sweeping through the domain of these parameters, i.e., $\theta \in [0, \pi]$ and $\phi \in [0, 2\pi)$. The system under consideration can be diagonalized and yields the eigenenergies

$$E_\pm = \mp \frac{1}{2}\sqrt{(H\cos\theta + M)^2 + (H\sin\theta)^2},$$

with corresponding eigenstates [36]

$$|\psi_+\rangle = \mathrm{e}^{-i\frac{\phi}{2}} \cos\left(\frac{\tilde{\theta}}{2}\right) |\uparrow\rangle + \mathrm{e}^{i\frac{\phi}{2}} \sin\left(\frac{\tilde{\theta}}{2}\right) |\downarrow\rangle, \tag{1.8a}$$

$$|\psi_-\rangle = -\mathrm{e}^{-i\frac{\phi}{2}} \sin\left(\frac{\tilde{\theta}}{2}\right) |\uparrow\rangle + \mathrm{e}^{i\frac{\phi}{2}} \cos\left(\frac{\tilde{\theta}}{2}\right) |\downarrow\rangle, \tag{1.8b}$$

where $\tilde{\theta}$ is defined from

$$\cos\tilde{\theta} = \frac{H\cos\theta + M}{\sqrt{(H\cos\theta + M)^2 + (H\sin\theta)^2}}, \quad \sin\tilde{\theta} = \frac{H\sin\theta}{\sqrt{(H\cos\theta + M)^2 + (H\sin\theta)^2}}. \tag{1.9}$$

[1] A detailed discussion including the said demonstration can be found in the supplemental material of [35].

Note that in the solution given in Eqs. (1.8), there is a global gauge freedom to multiply by a ϕ-dependent global phase, but the relative phase between the states $|\uparrow\rangle$ and $|\downarrow\rangle$ is fixed to $e^{i\phi}$. On a general level, for the rotationally symmetric problem[2], one can write the ground state wave function as [12]

$$|\psi\rangle = \sum_k c_k(\theta)|\Phi_k(\phi)\rangle, \tag{1.10}$$

where $|\Phi_{k=\pm}(\phi)\rangle$ is an orthonormal basis for the spin. In this way, we see that the dependence on the angle ϕ is absorbed into the basis, while the dependence on θ is in the coefficients $c_k(\theta)$, which is justified by the symmetry argument and the fact that at the poles with $\theta = 0, \pi$, the physical properties should not depend on the angle ϕ. A common choice of basis is [36]

$$|\Phi_+(\phi)\rangle = e^{-i\frac{\phi}{2}}|\uparrow\rangle, \tag{1.11a}$$

$$|\Phi_-(\phi)\rangle = e^{i\frac{\phi}{2}}|\downarrow\rangle. \tag{1.11b}$$

From the ground state $|\psi_+\rangle$ in Eq. (1.8a), the Berry connections can be evaluated exactly using Eq. (1.5) and read

$$A_\theta = 0, \tag{1.12}$$

$$A_\phi = \frac{\cos\tilde{\theta}}{2}. \tag{1.13}$$

The Berry connections are independent of the polar angle ϕ of the spherical parameter space, which is a manifestation of the rotational symmetry of the Hamiltonian in Eq. (1.4). From here, we can calculate the Berry curvature $\mathcal{F}_{\phi\theta}$ using Eq. (1.6) and finally integrate to find the Chern number using Eq. (1.7) as

$$C = \frac{1}{2}(\mathrm{sgn}(H+M) - \mathrm{sgn}(-H+M)). \tag{1.14}$$

Note that there are thus three possible values C can take in this system, that is $C \in \{-1, 0, 1\}$. When $H > M > 0$, we find $C = 1$, whereas for $|H| < |M|$ we find $C = 0$. Note that for the spin in the first case, one would have $\langle\sigma^z(\theta = 0)\rangle = 1$ and $\langle\sigma^z(\theta = \pi)\rangle = -1$, while in the second case we find $\langle\sigma^z(\theta = 0)\rangle = 1$ and $\langle\sigma^z(\theta = \pi)\rangle = 1$. This allows for an interpretation of the Chern number in terms of the accessed ground state manifold of the spin: When the topology is non-trivial (i.e., $C \neq 0$), upon winding around the parameter manifold, the spin winds completely around its ground state manifold as well. With trivial topology (i.e., $C = 0$), the ground state manifold is not fully explored for a similar protocol. The Chern number can also be interpreted as a topological charge contained

[2]The rotational symmetry refers to rotations around the z-axis.

within the parameter manifold spanned by the magnetic field: The degeneracy point of the Hamiltonian being within this space corresponds to $C = 1$, while it being outside corresponds to $C = 0$ [12, 32, 35, 37]. Note that in the model of Eq. (1.4), one can in the ground state identify $\mathrm{sgn}(H + M) = \langle \sigma^z(\theta = 0) \rangle$ and $\mathrm{sgn}(-H + M) = \langle \sigma^z(\theta = \pi) \rangle$. For a spin in a radial magnetic field, it can be shown from the definitions that in general [32]

$$C = \frac{1}{2} \left(\langle \sigma^z(\theta = 0) \rangle - \langle \sigma^z(\theta = \pi) \rangle \right). \tag{1.15}$$

This equation explicitly allows to measure the Chern number defined in Eq. (1.7) for the system under consideration solely from the poles of the parameter space. A way to interpret this is similarly in terms of the winding around the ground state manifold. In Sec. 1.1.3, we discuss a generalization of this notion to interacting systems. Before doing so, let us explore how the model of a spin in a radial magnetic field is not only interesting in its own right, but also has applications to other models.

1.1.2 From a spin-1/2 to other condensed matter models

The Haldane model

The Haldane model already evoked above is a two-dimensional model for a honeycomb layer with complex hopping amplitudes, realizing a quantum Hall effect [9]. It is based on the tight-binding description of graphene, which is known to yield massless Dirac fermions at two points of the Brillouin zone which are called the K and K' points (or Dirac points), with a linear dispersion relation and thus semimetallic properties [38, 39]. Here we will see that the physics at the Dirac points is closely related to the topological properties of the model through a mapping of these two points to the poles of a spherical parameter manifold of a pseudo-spinor.

To see this analogy, we start from the unit cell of graphene, which contains two sites for which a priori there is a sublattice symmetry (cf. Fig. 1.1a)). However, introducing a staggered potential offset m between the two sites of the unit cell breaks this symmetry and opens a gap in the energy spectrum, thus creating insulating behaviour. Such a term is also called a *Semenoff-mass* [12, 40]. The particles can hop between neighboring sites with a hopping amplitude t_1.

The realization of Haldane was that this model exhibits a Quantum Hall effect when complex second nearest neighbor hoppings of the form $t_2 e^{i\varphi}$ are added, which correspond to the effect of a magnetic field with zero net flux around one unit cell [3, 9]. Such a term also opens a gap at the K and the K' points of the Brillouin zone, but it can be shown that the occupied band has a different geometry than in the situation with only nearest-neighbor hopping and a Semenoff mass. In fact, this is related to the Chern number defined in a general form in Eq. (1.7) above for an integration over the Brillouin zone, i.e., with $\mu = k_x$,

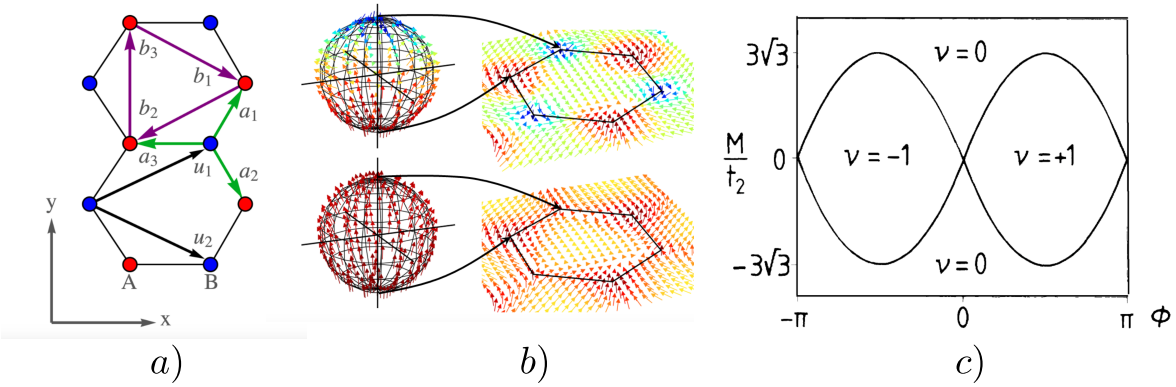

a) *b)* *c)*

Figure 1.1: Summary of the Haldane model. a) Reprinted with permission from the supplemental material of [11]. Setup and notations of the Haldane model in real space. b) Reprinted with permission from the supplemental material of [37]. Pictorial representation of the mapping between the spin in a radial field and the Haldane model in momentum space. Notably, the poles map to the K and K' points, respectively. The upper panel represents the topological phase, while the lower panel represents the trivial phase. c) Reprinted with permission from [9]. Phase diagram obtained by Haldane in 1988. In the plot, ϕ is the complex hopping phase associated with the second nearest-neighbor hopping t_2, M is the Semenoff mass and ν is the topological invariant equivalent to C with the mapping to the spin. Copyright (2023) by the American Physical Society for all figures.

$\nu = k_y$ and $dS_{\mu\nu} = dk_x dk_y$. The value of the Chern number C can be evaluated for each band and is intimately connected to the transport properties of the system. In particular, the transverse Hall conductance is proportional to the Chern number of the occupied band, i.e., [3, 36]

$$\sigma_{xy} = \frac{e^2}{h} C. \tag{1.16}$$

The analogy with the sphere model introduced above can be seen by writing the Hamiltonian of the Haldane layer in Fourier space, which reads with the nearest-neighbor and next-nearest neighbor lattice vectors $\vec{a}_i$ and $\vec{b}_i$ defined from Fig. 1.1a) [9]

$$\mathcal{H}_{\text{Haldane}} = \sum_k (c^\dagger_{\vec{k},A}, c^\dagger_{\vec{k},A}) H(\vec{k}) \begin{pmatrix} c_{\vec{k},A} \\ c_{\vec{k},A} \end{pmatrix}, \tag{1.17}$$

with

$$H(\vec{k}) = \vec{d} \cdot \vec{\sigma} + \epsilon \mathbb{1}, \tag{1.18}$$

where $\vec{\sigma}$ is the vector of Pauli matrices, $\mathbb{1}$ is the 2-by-2 identity matrix, $\vec{k} = (k_x, k_y)$ and

$$d_x = t_1 \sum_i \cos\left(\vec{k} \cdot \vec{a}_i\right), \tag{1.19}$$

$$d_y = t_1 \sum_i \sin\left(\vec{k} \cdot \vec{a}_i\right), \tag{1.20}$$

$$d_z = m - 2t_2 \sin\varphi \left(\sum_i \sin\left(\vec{k} \cdot \vec{b}_i\right)\right), \tag{1.21}$$

$$\epsilon = 2t_2 \cos\varphi \left(\sum_i \cos\left(\vec{k} \cdot \vec{b}_i\right)\right). \tag{1.22}$$

Expanding the Hamiltonian around the Dirac points K and K' given by $\frac{2\pi}{3a}\left(1, \pm\frac{1}{\sqrt{3}}\right)$ where a is the nearest-neighbor distance, one finds effectively [9, 37, 41]

$$H(k)^{\pm} = v_F(q_x^{\pm}\sigma^x \pm q_y^{\pm}\sigma^y) + v_F^2(m \mp 3\sqrt{3}at_2 \sin\varphi)\sigma^z, \tag{1.23}$$

with the Fermi velocity $v_F = \frac{3}{2}t_1 a$ and the $H(k)^{\pm}$ are the expansions around the K and K' point respectively, so that $\vec{q}^{+} = \vec{k} - \vec{K}$ and $\vec{q}^{-} = \vec{k} - \vec{K}'$. We see that the Hamiltonian at the K and K' points corresponds to the spin Hamiltonian in Eq. (1.4) at the north and the south pole respectively [35, 37]. This correspondence is shown pictorially in Fig. 1.1b). Just like the topological phase transition was determined by the comparison of M and H for the spin (cf. Eq. (1.14)), the topology of the Haldane layer is determined by the comparison of m and $3\sqrt{3}at_2$. According to this development, Haldane predicted a topological phase transition for $|m/t_2| < 3\sqrt{3}|\sin\varphi|$ (see Fig. 1.1c). This analogy has been used to test the phase topological phase transition in the Haldane model experimentally using the analogous spin system [35, 37]. The lattice model is also experimentally realizable with cold atoms [10, 42].

Therefore, the mapping onto a spin-1/2 on the one hand provides an elegant way to understand topological properties of the Haldane model and on the other hand allows to study topological phase transitions experimentally in a simple way. In the following paragraph, we will see that this analogy is useful also for understanding topological properties of another condensed matter model, namely the so-called Kitaev wire.

Kitaev wire

The model of a one-dimensional p-wave supercoductor has gained popularity due to the topical explanation of the occurence of Majorana fermions (see below) at its edges by Kitaev [14] and is hence often referred to as *'Kitaev wire'*. The fact that such systems are believed to have promising applications for storing and processing quantum information [43, 44] has motivated a lot of research on them in recent years [45–50]. As we will explore in this section, the interesting property of hosting free Majorana edge states is

inherently connected to the topological properties of the system, which can be understood from an analogy to the spin-1/2 system studied above.

Let us first introduce the model of a one-dimensional system hosting spinless fermions [14, 51]

$$\mathcal{H}_{\text{wire}} = -t\sum_j c_j^\dagger c_{j+1} + \Delta e^{i\varphi}\sum_j c_j^\dagger c_{j+1}^\dagger + \text{h.c.} - \mu\sum_j c_j^\dagger c_j. \tag{1.24}$$

Here $c_i^\dagger$ and c_i are the fermionic creation and annihilation operators at site i, t is the hopping amplitude between two neighboring sites, Δ is the superconductive pairing strength, φ in this section is the superconducting phase and μ is the chemical potential. Experimental proposals to realize such a Hamiltonian include heterostructures (such as semiconducting nanowires in proximity to a superconductor) [49, 50] or supercoducting qubits [44].

In the following paragraph, we will explain how the topological properties of this model can be understood from a mapping to the Bloch sphere from Sec. 1.1 and explain the occurence of Majorana bound states in more detail.

Topology from the sphere

Applying a Fourier transformation, the model can be written in a Bogoliubov-de-Gennes-form when defining $\Psi_k^\dagger = (c_k^\dagger, c_{-k})$ as [51–53]

$$\mathcal{H}_{\text{wire}} = \sum_k \Psi_k^\dagger \begin{pmatrix} -(\frac{\mu}{2} + t\cos(ka)) & i\Delta e^{i\varphi}\sin(ka) \\ -i\Delta e^{-i\varphi}\sin(ka) & (\frac{\mu}{2} + t\cos(ka)) \end{pmatrix} \Psi_k, \tag{1.25}$$

where a is the distance between two neighboring sites. From the 2-by-2-form of this matrix, the connection with the Hamiltonian in Eq. (1.4) is already starting to become apparent. We define pseudo-spinors and an anlogue to a magnetic field by [51]

$$\vec{S}_k = \begin{pmatrix} c_k^\dagger c_{-k}^\dagger + c_{-k}c_k \\ -i(c_k^\dagger c_{-k}^\dagger - c_{-k}c_k) \\ c_k^\dagger c_k - c_{-k}c_{-k}^\dagger \end{pmatrix}, \qquad \vec{d}_k = \begin{pmatrix} -\frac{\Delta_k + \Delta_k^*}{2} \\ \frac{\Delta_k - \Delta_k^*}{2i} \\ -\epsilon_k \end{pmatrix}, \tag{1.26}$$

with $\Delta_k = i\Delta e^{i\varphi}\sin(ka)$ and $\epsilon_k = -(\frac{\mu}{2} + t\cos(ka))$. The Hamiltonian can be rewritten as [51]

$$\mathcal{H}_{\text{wire}} = -\sum_k \vec{d}_k \cdot \vec{S}_k. \tag{1.27}$$

As such, the relation with the spin model is clear: The momentum and the superconducting phase map to a polar angle and an azimuthal angle on a sphere [51]. A sweep along θ in the spin model thus corresponds to a sweep along the momentum k in the Kitaev wire. It can be shown that $\theta = 0$ can be identified with $ka = 0$ and $\theta = \pi$ with $ka = \pi$. The superconducting phase corresponds to a free parameter winding around the xy-plane.

Taking over the definition from Eq. (1.15) [36, 51], we can write for this model

$$C = \frac{1}{2}\left(\langle S^z(ka=0)\rangle - \langle S^z(ka=\pi)\rangle\right). \tag{1.28}$$

Since at these two 'poles', the off-diagonal components of the Hamiltonian in the BdG-form vanish, the ground state in terms of the pseudo-spinor is either in the up- or in the down-state. Thus, we can interprete this number equivalently as counting the winding of the pseudo-spinor state along its effective ground state manifold (that is, a Bloch sphere) when 'winding' the momentum k along half of the Brillouin zone.

This is in fact similar to the interpretation of the $\mathbb{Z}_2$ invariant commonly defined for the Kitaev wire, which in this langauge corresponds to $\nu = \langle S^z(ka=0)\rangle \langle S^z(ka=\pi)\rangle$ [14, 36, 52, 53]. It can then be identified with [36]

$$\nu = 1 - 2C^2. \tag{1.29}$$

From this simple prescription, we can determine the topological phase transition point of the Kitaev wire. If $t = \Delta$, we see that the invariants C and ν change at $\mu = \pm 2t$. For $|\mu| > 2t$, the wire is in a topologically trivial phase with $\nu = 1$ and $C = 0$. For $|\mu| < 2t$, we find in turn $\nu = -1$ and $C = 1$, corresponding to a winding along the Bloch sphere for a sweep through the Brillouin zone. This is therefore the topological phase.

On the one hand, the Kitaev wire model is widely popular for this conceptual realization of a topological phase transition by relatively simple means. On the other hand, it has the attractive feature of forming Majorana bound states at its edges in the topological phase as a manifestation of the bulk-edge correspondence, which makes it especially interesting for applications in quantum technology. We will study this feature in the next paragraph.

Majorana fermions

Majorana fermions are fermionic particles that are their own anti-particles [54]. In the realm of condensed matter, they are hypothesized as effective excitations in various models [14, 55–57]. In the Kitaev wire, the topological phase features Majorana fermions at the edges. Another example is the spin-boson model discussed below (cf. Sec. 1.2.2), where a mapping of the spin degree of freedom to Majorana fermions can be used to study the phase transition of the spin-boson model using a renormalization group approach [58].

To introduce Majorana fermions and demonstrate the enthusiasm for them in the condensed matter community, we stay with the example of the Kitaev wire. One can

introduce two Majorana fermions at each site of the model in Eq. (1.24) by

$$\eta_i = \frac{c_i^\dagger + c_i}{\sqrt{2}}, \tag{1.30a}$$

$$\alpha_i = \frac{c_i^\dagger - c_i}{\sqrt{2}i}, \tag{1.30b}$$

and check that they fulfill fermionic anticommutation relations

$$\{\eta_i, \eta_j\} = \delta_{ij}, \qquad \{\alpha_i, \alpha_j\} = \delta_{ij} \qquad \text{and} \qquad \{\eta_i, \alpha_j\} = 0, \tag{1.31}$$

as well as the defining properties

$$\eta_i^\dagger = \eta_i \qquad \text{and} \qquad \alpha_i^\dagger = \alpha_i. \tag{1.32}$$

In terms of these new operators, the Hamiltonian from Eq. (1.24) reads

$$\mathcal{H}_{\text{wire}} = i(t+\Delta)\sum_j \eta_j \alpha_{j+1} + i(t-\Delta)\sum_j \eta_{j+1}\alpha_j - i\mu\sum_j \alpha_j\eta_j. \tag{1.33}$$

In order to identify two different physical regimes of this model, it is now instructive to consider two limiting cases, as has been put forward by Kitaev [14]. For simplicity, we set $\varphi = 0$.

1. $t = \Delta = 0$, $\mu < 0$: In this case, the Hamiltonian consists only of the chemical potential term. The two Majorana fermions on each site are thus coupled locally, defining the unique ground state.

2. $t = \Delta$, $\mu = 0$: The Hamiltonian reads simply $\mathcal{H}_{\text{wire}} = i2t\sum_j \eta_j\alpha_{j+1}$. Adjacent Majorana fermions from neighboring sites are coupled with one individual Majorana fermion at each end of the chain remaining free, giving a doubly degenerate ground state.

These are two distinct phases that cannot be smoothly connected, implying that this result holds generally even when departing from these two fine tuned limits [52]: The first case corresponds to the topologically trivial case with $\nu = 1$ and $C = 0$. The second case however correponds to the topological case with $\nu = -1$ and $C = 1$, as can easily be seen from the winding of the pseudo-spinor from Eq. (1.26).

This constitutes a simple, yet compelling example of the bulk-edge corerspondence in a topological phase. The latter can be understood by simple means using the analogy to a spin in a radial field, which therefore proves a useful tool. In the following section, we will see how the notions established above can be generalized to the case of interacting systems.

1.1.3 Generalization for interacting systems

In the previous sections, we saw how a Chern number can be defined in parameter space, how it can be interpreted and to what other models of condensed matter this is relevant. Here we want to show an elegant way in which this can be generalized even further, giving rise to a fractionalization of the *partial Chern number* [12], which we will define below. As mentioned above, the Chern number from Eq. (1.7) can, for a single spin, be interpreted as the winding around the ground state manifold or a topological charge. Here, we will extend this to interacting systems using a similar formalism. For this, consider two interacting spin-1/2 according to

$$\mathcal{H} = \sum_{i=1}^{2} \mathcal{H}_{\mathrm{rad},i} + r_z \sigma_1^z \sigma_2^z, \tag{1.34}$$

where $\mathcal{H}_{\mathrm{rad},i}$ is given by Eq. (1.4) and the model thus consists of two coupled copies of the model for one spin discussed above. Defining the Berry connection and the Berry curvature of the i-th spin from the derivative operator acting on site i (i.e., $\partial_\alpha^1 = (\partial_\alpha \mathbb{1}_1) \otimes \mathbb{1}_2$ and $\partial_\alpha^2 = \mathbb{1}_1 \otimes (\partial_\alpha \mathbb{1}_2)$) as [12]

$$A_\mu^i = i\langle\psi|\partial_\mu^i|\psi\rangle, \tag{1.35}$$

$$\mathcal{F}_{\phi\theta}^i = \partial_\phi^i A_\theta^i - \partial_\theta^i A_\phi^i, \tag{1.36}$$

extends the above notions to each of the subsystems of the interacting system. The system described by Eq. (1.34) is still rotationally invariant for rotations around the z-axis. We can therefore generalize Eq. (1.10) and write the ground state wave function as [12]

$$|\psi\rangle = \sum_{kl} c_{kl}(\theta) |\Phi_k(\phi)\rangle_1 |\Phi_k(\phi)\rangle_2, \tag{1.37}$$

where $|\Phi_{k=\pm}(\phi)\rangle_i$ is an orthonormal basis for spin i and can for example be taken to be Eq. (1.11). To write the wave function in this form, we again required rotational symmetry around the z-axis, so that the coefficients $c_{kl}(\theta)$ do not depend on the polar angle ϕ and in particular, at the poles, all values of ϕ are equivalent. The partial Chern number can then be defined by [12]

$$C_i = A_\phi^i(0) - A_\phi^i(\pi). \tag{1.38}$$

Note that $A_\phi^i(\theta)$ is a gauge-dependent quantity, while C_i is gauge-independent [12].

The partial Chern number

To prove Eq. (1.38), one starts from the definition of C_i as an integral of the Berry curvature and writes [12]

$$C_i = \frac{1}{2\pi} \int_0^{2\pi} d\phi \int_0^{\pi} d\theta \mathcal{F}_{\phi\theta}^i = -\frac{1}{2\pi} \int_{S^2} d\vec{S} \cdot (\vec{\nabla} \times \vec{A}^i), \tag{1.39}$$

where $\vec{A}^i = (A^i_\phi, A^i_\theta)^T$. Splitting the sphere into two submanifolds by choosing some boundary separating the north and the south pole, one can choose a specific gauge on each of them such that the ϕ-component of the Berry connection vanishes at the pole of each of the submanifolds [12]. One can then use Stokes' theorem to evaluate the integral above by a contour integration along the boundary. Changing the gauge, one arrives at Eq. (1.38). For the details on this derivation, we refer to [12, 36].

Using $\sigma^z_i = |\uparrow\rangle_i \langle\uparrow|_i - |\downarrow\rangle_i \langle\downarrow|_i$ to rewrite Eq. (1.38) with the wave function from Eq. (1.37), we find

$$C_i = \frac{1}{2}\left(\langle\sigma^z_i(\theta=0)\rangle - \langle\sigma^z_i(\theta=\pi)\rangle\right). \tag{1.40}$$

Similar to Eq. (1.15) for an individual spin, this formula allows to determine the partial topology of one of the spins solely from its expectation values at the poles of the parameter space. We can again interprete it as the winding around the ground state manifold of the spin i, but now superpositions of different paths are possible due to the interaction with the second spin. The difference with Eq. (1.15) thus lies in the fact that the expectation value is now influenced by the interaction with the other spin. One can tune a situation in which $\langle\sigma^z_i(\theta=0)\rangle = 1$ and $\langle\sigma^z_i(\theta=\pi)\rangle = 0$ by requiring [12]

$$\frac{H}{2} + \frac{M}{2} > r_z > \frac{H}{2} - \frac{M}{2}, \tag{1.41}$$

for which the ground state at the south pole corresponds to

$$|GS(\theta=\pi)\rangle = \frac{1}{\sqrt{2}}(|\uparrow\downarrow\rangle + |\downarrow\uparrow\rangle). \tag{1.42}$$

This is a maximally entangled state between the two sites, similar to the famous EPR-pair [59] or Bell state [60]. From Eq. (1.40), we then immediately find $C_i = 1/2$, which demonstrates how, in the interacting case, fractional values of C_i can arise. Compared to a single spin, the possibility of forming an entangled state between the two spins is opened, which makes the interpretation of the partial topology of one of the spins less intuitive. If on mean-field level, the coupling to a second spin can be thought of giving rise to an additional field acting on the first spin, the possible superposition of different states of the second spin effectively gives rise to a superposition of the ground state of the fist spin winding around and not winding around the Bloch sphere, or equivalently the topological charge being within and ouside of the sphere described by the parameters [12].

This striking, yet simple way to realize fractional topological numbers based on entanglement between to subsystems can be generalized using the considerations from Sec. 1.1.2 to two coupled Haldane layers [12] or Kitaev wires [51]. In physical terms, this partial Chern number defines a topological phase given the interaction [12] and an exchange symmetry between two subsystems. The concrete fractional values of the partial Chern number (i.e., $C_i = 1/2$ for the parameters in the range given by Eq. (1.41)) are

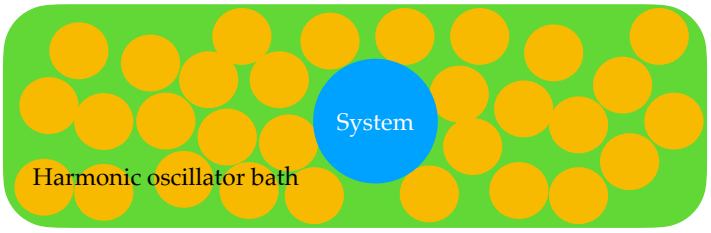

Figure 1.2: Schematic of a system coupled to an environment: The system in blue is coupled to harmonic oscillator modes (shown in yellow) constituting the environment. One is often interested in the effective dynamics of the system under consideration (in blue), for which one might observe decoherence. The entire system (shown in green) is still closed and is assumed to evolve unitarily.

dependent on the concrete model under study and the types of interaction. It is one goal of this thesis to see to which extent the notions introduced here can be generalized to systems with different interactions, disordered systems and open systems, studying interacting spin models. For this, the following section will introduce a few key notions for the study of open and driven quantum systems.

1.2 Open quantum systems

The study of open quantum systems is a long standing endeavour, steming from the fact that in laboratory and real-life applications, quantum systems inherently interact with their environment [61]. In fact, this has been realized already in the earlier years of quantum mechanics by John von Neumann [62]. The study of open systems has of course been active even before the discovery of quantum mechanics in the realm of classical mechanics and thermodynamics [63], but new concepts are needed to adopt a quantum description of open systems [64] and remain in fact an active field of study until today, notably in the form of quantum thermodynamics [65–68] and in the light of emerging applications [69–74].

1.2.1 Generalities

A common approach to study open quantum systems is to separate the Hamiltonian of the entire system into the part describing the microscopic system $\mathcal{H}_S$, the macroscopic environment or 'bath' $\mathcal{H}_B$ and their mutual interaction $\mathcal{H}_{SB}$, i.e., [61, 66]

$$\mathcal{H} = \mathcal{H}_S + \mathcal{H}_B + \mathcal{H}_{SB}. \tag{1.43}$$

Coupling to an environment leads to dissipation of energy from the system into the bath, as well as decoherence of the state of the system [64, 75].

A common way to model the bath is to consider an infinite collection of quantum

harmonic oscillators [76], schematically shown in Fig. 1.2. A well-established class of models is that of Caldeira-Leggett models [77–79] in which the bath is modelled as an infinite collection of one-dimensional quantum harmonic oscillators and the system is a single quantum particle. Then, $\mathcal{H}_B$ takes the form [64, 79, 80]

$$\mathcal{H}_B = \sum_k \left(\frac{p_k^2}{2m_k} + \frac{m_k \omega_k^2 x_k^2}{2} \right), \tag{1.44}$$

while the coupling term reads

$$\mathcal{H}_{SB} = \hat{\mathcal{O}} \sum_k c_k x_k, \tag{1.45}$$

where x_k and p_k are the position and momentum operators of the k-th bath ocillator, m_k and ω_k are its mass and its frequency, $\hat{\mathcal{O}}$ is an observable of the system and c_k is the coupling constant to the k-th environment mode. The coupling strength in relation to the frequency of each mode can be expressed through the spectral function [79, 80]:

$$J(\omega) = \frac{\pi}{2} \sum_k \frac{c_k^2}{m_k \omega_k} \delta(\omega - \omega_k). \tag{1.46}$$

The spectral function characterizes the bath and is defined from the Fourier transform of the autocorrelation of the average force induced by the bath at thermal equilibrium on the system [64]. Calling this force $R = \sum_k c_k x_k$, this definition reads

$$\mathcal{F}\left(\langle R(t)R(0)\rangle_T\right)[\omega] = J(\omega) \coth\left(\frac{\beta\omega}{2}\right), \tag{1.47}$$

where we denoted the Fourier transform by $\mathcal{F}$.

Perhaps the most famous instance of the class of Caldeira-Leggett models is the spin-boson model, in which the system is a two-level system, that can thus be interpreted as a spin-1/2. We will study how the fundamental notions of quantum open systems such as decoherence, dissipation and a related quantum phase transition can be understood from this model.

1.2.2 The spin-boson model

The spin-boson model, a special instance of the Hamiltonian in Eq. (1.43), features a spin as its system coupled to a bosonic environment, usually with the z-component of the spin. This gives rise to a Hamiltonian of the form [64, 79, 80]

$$\mathcal{H} = -\frac{\epsilon(t)}{2}\sigma^z - \frac{\Delta(t)}{2}\sigma^x + \frac{\sigma^z}{2} \sum_k g_k (b_k^\dagger + b_k) + \sum_k \omega_k b_k^\dagger b_k. \tag{1.48}$$

Here, we used the bosonic creation and annihilation operators $b_k^\dagger, b_k$ with

$$b_k = \sqrt{\frac{m_k\omega_k}{2}}\left(x_k + \frac{i}{m_k\omega_k}p_k\right),$$

to rewrite the position and momentum operators of the harmonic oscillator bath. Therefore, we defined the coupling constants $g_k = c_k(2m_k\omega_k)^{-1/2}$, so that the spectral density reads

$$J(\omega) = \pi\sum_k g_k^2\delta(\omega-\omega_k). \tag{1.49}$$

Here and throughout this thesis, let us assume that the environment is described by an Ohmic spectral function with an exponential large frequency cut-off, which is assumed to be the largest energy scale in the model, i.e., [79, 80]

$$J(\omega) = 2\pi\alpha\omega e^{-\omega/\omega_c}, \tag{1.50}$$

with $\omega_c \gg \Delta$. The parameter α determines the coupling strength between the spin and the bath and plays a crucial role in determining a quantum phase transition, as we will see below.

The amplitudes $\epsilon(t)$ and $\Delta(t)$ can be time-dependent and in fact the 'quantum dynamo effect' arising in the model of Eq. (1.48) studied in Chapter 2 relies on a driven configuration of the spin part of the Hamiltonian. In order to introduce the physics of open systems in a general way, we shall in this introductory section first consider the case of a time-independent spin part of the Hamiltonian, in particular with $\Delta(t) = \Delta$.

In order to gain an intuitive view on how the coupling to the bath can influence the spin and even induce a quantum phase transition, let us consider the unbiasesd version of the model defined in Eq. (1.48) with $\epsilon(t) = 0$. If the coupling constants $g_k \to 0$, the spin dynamics is only controlled by the spin part of the Hamiltonian $\mathcal{H}_{\rm spin} = -\frac{\Delta}{2}\sigma^x$. The ground state for $\Delta > 0$ is simply $\frac{1}{\sqrt{2}}(|+\rangle_z + |-\rangle_z)$ (where $|\pm\rangle_z$ correspond to $|\uparrow\rangle$ and $|\downarrow\rangle$ respectively in the notation from above). The situation changes when the coupling to the environment is turned on.

In order to get a good understanding of the physics in play, let us first discuss an intuitive approach to study the spin dynamics with coupling to a bath which leads to a result that is not consistent. The problems occuring in this reasoning will be closely related to the quantum dynamo effect we introduce in Chap. 2.

In the basis of σ^z, we can consider what happens to the bath if the spin is in the state $|+\rangle_z$ or $|-\rangle_z$. There are then two possibilities for the Hamiltonian involving the bath, i.e.,

$$\mathcal{H}_{\rm bath}^{\pm} = \pm\frac{1}{2}\sum_k g_k(b_k^\dagger + b_k) + \sum_k \omega_k b_k^\dagger b_k = \sum_k \omega_k b_{k,\pm}^\dagger b_{k,\pm}, \tag{1.51}$$

where $b_{k,\pm} = b_k \pm \frac{1}{2}\frac{g_k}{\omega_k}$ and we neglected a constant contribution in this transformation. This corresponds to displacing all of the oscillators so that the ground state for each of these sectors fulfills for all k [81, 82]

$$b_{k,\pm}\,|\psi_\pm\rangle = 0 \quad \Longrightarrow\; b_k\,|\psi_\pm\rangle = \mp\frac{1}{2}\frac{g_k}{\omega_k}\,|\psi_\pm\rangle\,. \tag{1.52}$$

It is thus a many-body coherent state for the bosonic modes and can be written as

$$|\psi_\pm\rangle = \prod_k |\psi_{\pm,k}\rangle\,, \tag{1.53}$$
$$\text{with} \quad |\psi_{\pm,k}\rangle = \exp\left(\mp\frac{1}{2}\frac{g_k}{\omega_k}(b_k^\dagger - b_k)\right)|0\rangle\,,$$

where $|0\rangle$ is the vacuum of the b_k operators. The ground state of the entire system will with this reasoning be an entangled state between the spin and the bath. If $\mathcal{H}_{\text{spin}} = -\frac{\Delta}{2}\sigma^x$, the lowest lying eigenstates would then be

$$|\Sigma_\pm\rangle = \frac{1}{\sqrt{2}}\left(|+\rangle_z \otimes |\psi_+\rangle \pm |-\rangle_z \otimes |\psi_-\rangle\right). \tag{1.54}$$

With $\Delta > 0$, the ground state is $|\Sigma_+\rangle$, for which $\langle\sigma^z\rangle = 0$ and

$$\begin{aligned}\langle\sigma^x\rangle = \langle\psi_+|\psi_-\rangle = \exp\left(-\frac{1}{2}\sum_k \frac{g_k^2}{2\omega_k^2}\right) &\overset{(1.49)}{=} \exp\left(-\frac{1}{2\pi}\int_0^\infty d\omega \frac{J(\omega)}{\omega^2}\right),\\ &\overset{(1.50)}{=} \exp\left(-\alpha\int_0^\infty d\omega \frac{e^{-\omega/\omega_c}}{\omega}\right).\end{aligned} \tag{1.55}$$

Here, we took the continuum limit to switch from a summation over the modes to an integration of the frequency variable. The last expression predicts that all tunneling between the spin states is suppressed already for arbitrarily small coupling $\alpha > 0$. This result cannot be correct, as a small coupling to the bath should merely have a perturbative effect [75, 83]. The problem with this calculation lies in fact in the treatment of low-frequency modes: For modes with large frequencies, one can assume that the reasoning of displaced oscillators is correct, as those modes will remain equilibrated to the spin at all times. For low-frequency modes, this does not hold and in fact one needs to treat them differently. This is done using a procedure called *adiabatic renormalization*, described in App. D.1.

There, one effectively neglects frequencies lower than a certain, self-consistent threshold and studies the convergence of the emerging renormalized tunneling element that we call Δ_r. For $\alpha < 1$ and with an Ohmic spectral density, one finds that the tunneling element gets renormalized in

$$\tilde{\mathcal{H}} = -\frac{\Delta_r}{2}\sigma^x + \sum_k \omega_k b_k^\dagger b_k, \tag{1.56}$$

as [64, 79]

$$\Delta_r = \Delta \left(\frac{\Delta}{\omega_c} \right)^{\frac{\alpha}{1-\alpha}} . \tag{1.57}$$

For $\alpha > 1$, on the other hand, one observes that the tunneling element is renormalized to zero, thus leading to a localization of the spin in one of the two states $|\pm\rangle_z$. From this consideration, one identifies a quantum phase transition at $\alpha = 1$ between a localized phase (for $\alpha > 1$) and a delocalized phase (for $\alpha < 1$) [83]. In addition, in the delocalized phase with $\alpha < 1$, we see from Eq. (1.57) that there is a crossover from coherent to incoherent behavior [80] at $\alpha = 1/2$, for which the exponent becomes larger than one and initializing the spin in an eigenstate of σ^z, coherent oscillations will be suppressed.

Note that in the discussion above, when tracing over the bath degrees of freedom, we have assumed that the environment evolves essentially freely and thus acts as a fluctuating force on the spin. We will come back to the discussion of the spin-boson model in Chap. 2, where we discuss it in the light of a driven protocol, i.e., time-dependent coefficients $\Delta(t)$ and $\epsilon(t)$ and study a possibility to coherently excite certain bath modes and thus transfer energy from the spin to the bath in a work-to-work conversion. We will in particular come back to the results from above and compare them to more advanced techniques used to study the spin-boson model in Sec. 2.3.2. In order to put this into a broader context, we have to introduce some notions of quantum thermodynamics.

1.2.3 Quantum energy and quantum thermodynamics

The study of open quantum systems naturally leads to the field of quantum thermodynamics, which is driven by the desire to understand work and heat transfers on the quantum scale [68]. Especially with the development of quantum technologies and quantum computing devices picking up speed, this understanding is essential for implementing such technologies and for their efficient operation. The distinction of work and heat in the quantum regime remains controversial, as here the delimitation between these two quantities can be ambiguous [67]. Phenomenologically, one expects the first law of thermodynamics to hold also for quantum systems, i.e., [67]

$$dE = \delta W - \delta Q, \tag{1.58}$$

where dE is the change in internal energy of a system and δW and δQ are the variations in work and heat, respectively. For a quantum system, the repartition between the latter two is problematic to justify [67]. Other questions concern the thermalization of a quantum bath, making it difficult to define a temperature [84] and new noise sources arising in the context of quantum mechanics, such as projective measurements [68]. Nevertheless, it is possible to formulate the first and the second law of thermodynamics for a quantum system, and demonstrate them from microscopic grounds [24], which requires however to

put certain restrictive assumptions [27]. In particular, for a setup as the one shown in Fig. 1.2, one would assume that work is done to the system by an external work reservoir, acting only on the system and not on the environment. This is reflected in the system Hamiltonian (i.e., $\mathcal{H}_S$ in Eq. (1.43)) becoming explicitly time-dependent [24]. One can then show that the work done to the entire system (including the environment), from the first law of thermodynamics corresponds to [24]

$$W(t) = \int_0^t dt' \,\mathrm{Tr}\left(\frac{\partial \mathcal{H}}{\partial t'}\rho(t')\right), \tag{1.59}$$

where $\rho(t)$ is the density matrix of the full system.

Heat, on the other hand, can be viewed as an energy flow from the system to the environment, thus quantified by the change of internal energy of the bath and shown to fulfill the second law of thermodynamics [24]. It is remarkable that the laws of thermodynamics, formulated for classical systems, can find applications in quantum systems as well. However, for a full quantum description, questions about the restrictions posed by the assumptions remain controversial: How can the 'work reservoir' be thought of in a microscopic description and would heat flows to the system affect these laws? Similarly, can a heat bath function as a work source as well [27]? Recent theoretical studies show the possibility that energy flows from a reservoir, usually considered as heat, can also contain contributions showing the properties of work [25, 26].

In Chap. 2 we will discuss a driven instance of the model in Eq. (1.43), where the system is a spin-1/2 similar to the one introduced in Eq. 1.4. We will demonstrate how this realizes a transfer of work into the coupled environment [33]. It is important to emphasize that the study of energy transfers on the quantum scale is not only of interest for a better understanding of the validity of the laws of thermodynamics, but also as a prerequisite for the development and efficient operation of quantum technologies [73, 74, 85]. In general, the study of open systems is of course also relevant since systems implemented in a laboratory always interact with their environment to some degree. It therefore allows to understand *realistic settings* better, which is important for all sorts of applications.

Another step towards the study of realistic settings is the consideration of disorder: Just like quantum systems interact with their environment, they are subject to some degree of disorder in their setup. Similarly to open system dynamics, this has lead to the discovery of myriad new phenomena, relevant also from a fundamental theoretical point of view, as we will see in the following section.

1.3 Disorder and localization physics

It has been realized by Anderson in 1958 that in certain lattice models the spatial extension of the wave function decays exponentially in the presence of a disordered potential [86].

This phenomenon called Anderson localization is a consequence of the interference of the wavefunction when scattering at impurities and is in contrast to the disorder-free case, in which the wave function extends through the entire lattice. It has consequently spurred a lot of theoretical [87–90], experimental [91–94] and numerical [95, 96] interest. In this section, we will give a small cross section of key notions and will describe how localization can influence the topological properties of a physical system. In Sec. 1.4, we will then see how the notions of localization are influenced by the presence of interactions between particles.

1.3.1 Anderson localization

Anderson in 1958 studied 'diffusion in a random lattice'. The model can be described by a fermionic tight-binding Hamiltonian with a random on-site potential [18, 86, 97, 98]

$$\mathcal{H}_{\text{Anderson}} = \sum_{\langle m,n \rangle} t c_m^\dagger c_n + \text{h.c.} + \sum_n \mu_n c_n^\dagger c_n, \tag{1.60}$$

where c_j is the fermionic annihilation operator of a particle at site j. The key insight of Anderson was that the transport across a medium described by such a Hamiltonian with a disordered chemical potential μ_n can vanish due to destructive interference of the particle wave functions upon scattering at impurities. In one dimension, this leads to an exponentially decaying wave-function of the form [97]

$$|\psi(x)|^2 \propto \exp\left(-\frac{|x|}{\xi_{\text{loc}}}\right), \tag{1.61}$$

where $x = ja$ with j the index of a site, a the lattice constant and ξ_{loc} is the localization length, a characteristic length scale of the system under consideration. The wave functions are thus confined to certain regions of the chain, which justifies the notion of *localization*.

This is of course very different from a homogeneous system: If the chemical potential is not disordered, i.e., $\mu_n = \mu$, the eigenstates of the system in one dimension are the usual Bloch waves extending over the entire chain [98]. The phenomenon of Anderson localization is highly dependent on the dimensionality: It is well established that one- and two-dimensional systems always localize in the presence of disorder [86, 88, 89]. In three-dimensional systems, one observes a transition from a metallic to insulating behaviour at a certain energy threshold, the so-called mobility edge [99]. Anderson localization is a general phenomenon occuring for waves in disordered media, it has therefore been found to apply for example also to light waves [100] and sound waves [101]. Its importance for understanding physical observations especially in low-dimensional systems is underlined by the vast available literature on the topic.

One particularly intriguing implication of Anderson localization concerns the stability

of plateaus of the transverse conductivity formed in the integer quantum Hall effect for a two-dimensional electron gas already mentioned above. Anderson localization here plays an important role in stabilizing these Quantum Hall plateaus [102, 103]. To get a better intuition for this, imagine a Quantum Hall sample whose energy eigenstates are described by Landau levels. Introducing disorder through a spatially randomly varying potential, one would still expect the system to exhibit an integer quantum Hall effect as long as the clean eigenenergies are much larger than the energy fluctuations coming from the disorder [104]. In presence of disorder, one would then expect a broadening of the Landau levels [5]. The quantization of the conductance shown in Eq. (1.1) can be demonstrated for disorder free systems with an integer filling factor ν. Varying the magnetic field from these integer filling factors, quasi-particle defect states are developed by the system. However, under the presence of disorder, these states get localized and do not contribute to the Hall conductivity of the sample, thus explaining the quantized conductance found in experiments [105]. This curious relation of the topological properties observed in the integer quantum Hall effect and Anderson localization demonstrate the inherent relevance of the study of disorder effects in topological systems. These relations can also be observed in other systems: A prominent example is the *Topological Anderson insulator*, in which disorder increases the size of a topological phase, which we will discuss below.

1.3.2 Topological Anderson insulator

Topological properties of materials are expected to be unaltered upon application of disorder up to a certain strength of the latter, at which it would drive a transition to a trivial phase [104]. Another way to put it is that a topological state can exist in spite of (a sufficiently weak) disorder [106]. In the numerical study of topological insulator models, the following surprising observation has been made: Under certain conditions, a model that is in a topologically trivial phase can be driven into a topological phase by the application of disorder [106, 107]. The phenomenon has been explained by a renormalization of the system parameters due to the disorder: In the trivial phase, but close to the transition point, this renormalization can yield an effective topological model - the topological Anderson insulator (TAI) [106]. This effect has been verified experimentally in a realization of the Su-Schrieffer-Heeger (SSH) model [108]. The results are shown in Fig. 1.3. The SSH model is a one-dimensional topological model with two inequivalent sites per unit cell and thus different hopping amplitudes for inter- and intracell hopping [109, 110]. Recently, several groups have implemented variants of this model experimentally [111–113]. The model implemented in [108] leading to the results shown in Fig. 1.3 was of the form

$$\mathcal{H}_{\mathrm{SSH}} = \sum_n \left(-im_n c^\dagger_{n,a} c_{n,b} + t c^\dagger_{n+1,b} c_{n,a} + \mathrm{h.c.} \right), \tag{1.62}$$

where a and b denote the two different sites in the n-th unit cell. The intracell hopping amplitudes m_n were disordered as $m_n = t(m + W\omega_n)$ with W being the disorder strength and ω_n being uniformly distributed random variables drawn from the interval $[-0.5, 0.5]$ [108]. Note that in the clean case with $W = 0$, following a strategy similar to the one used in 1.1.2 for the Haldane model and the Kitaev wire, defining pseudo-spinors in Fourier space $c_k^\dagger = (c_{k,a}^\dagger, c_{k,b}^\dagger)$, the Hamiltonian in Eq. (1.62) can be rewritten as [110]

$$\mathcal{H}_{\text{SSH}} = \sum_k c_k^\dagger \quad (\vec{h}(k) \cdot \vec{\sigma}) \quad c_k, \tag{1.63}$$

with

$$h(k) = (t\cos(ka), -t(m + \sin(ka)), 0)^T, \tag{1.64}$$

where a is the length of one unit cell. We see that a mapping to a spin in a radial field can be achieved in this model as well, but a topological invariant ν is now defined only from a winding in the xy-plane. This winding number is in fact equivalent to the Zak-phase, i.e. the integration of the Berry connection of a one-dimensional system across its Brillouin zone [110]. In the experimental results shown in Fig. 1.3, the autors rather used the 'mean chiral displacement' $\langle \mathfrak{C} \rangle$ as an indicator of the topological phase transition. This uses the fact that the SSH model possesses a chiral symmetry, which can be seen from the anticommutation of the Hamiltonian in Eq. (1.63) with σ^z [110]. The chiral displacement operator is for this model defined by $\mathfrak{C} = 2\sigma^z X$ [108, 114], where X is the operator designating the unit cell (i.e., the displacement) of a state it is acting on. It can be shown that in the thermodynamic limit, and averaging over disorder, measuring the mean chiral displacement allows to conclude upon the winding number of the system [108, 114].

Recently, a similar TAI state of matter has also been verified experimentally in the disordered Haldane model (cf. Sec. 1.1.2) [115]. This effect has interesting implications: The possibility of implementing topological systems not only insensitive to disorder, but harnessing it for the very realization of these properties has promising potential with regards to real world applications.

In Sec. 1.1 we saw how the topological invariant of the Haldane model can be understood in terms of the topology of a spin-1/2 in a radial magnetic field. As the definition of the latter can be extended to interacting systems as well (cf. Sec. 1.1.3), it is interesting to think about the interplay of interactions, disorder and the (partial) topology in spin and analogous systems. This will be the subject of Chap. 3.

Taking a step back from the TAI to localization physics, it proves already a challenging problem to study the interplay of disorder and interactions. This leads us to the fascinating and active field of *many-body localization*.

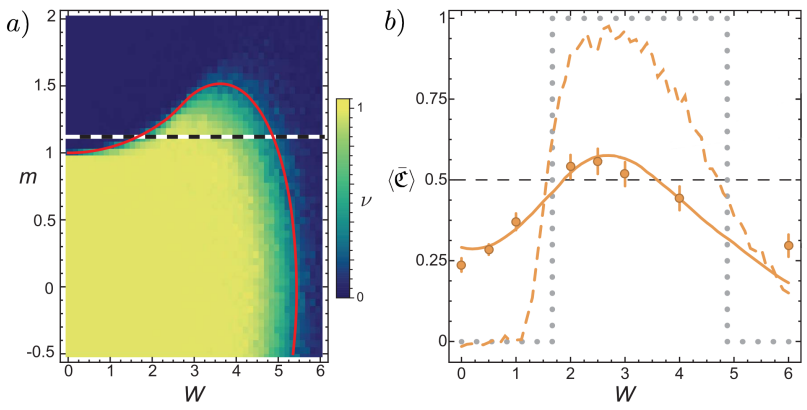

Figure 1.3: From Fig. 3 of [108]. Reprinted with permission from AAAS. a) Numerical phase diagram (disorder average) of the SSH chain from Eq. (1.62) showing a topological invariant ν as a function of the intracell tunneling amplitude m and a disordered additional contribution to this amplitude W. For strong values of disorder, the topological phase with $\nu = 1$ is extended. b) Cross section along the black and white bar from a). Experimental data (gold dots with error bars) for measurement of the expectation value of the chiral displacement operator $\mathfrak{C}$ used as an experimental indicator of the topological properties for a realization of the SSH chain with cold atoms and averaged over 50 disorder realizations. The gold solid and dashed lines show numerical results, the gray dotted line shows analytical predictions.

1.4 Many-body localization

In 1977, Philipp W. Anderson was awarded the Nobel prize in physics for his work on disordered systems[3]. In his Nobel lecture, he expressed his excitement about the fact that 'a theory of localization with interactions is beginning to appear' [18]. Following his work, it has been established that localization can in fact prevail and even be reinforced with interactions [19]. However, these considerations concerned only the ground state of the system. The analysis of disordered interacting states was later extended to systems with excitations [20–22].

When localization prevails in a quantum system with many *interacting* constituents at non-zero temperature, one speaks about *many-body localization (MBL)* [22]. The notion of a finite temperature - therefore, a finite excitation present in the system - distinguishes this phenomenon from Anderson localization with interactions studied in [19] as a ground state phenomenon, occuring at zero temperature. In order to detect MBL, a study of the spectral properties of a system is necessary[4].

[3]He was awarded jointly, together with Sir Nevill F. Mott and John H. van Vleck.

[4]As a side remark, let us mention that an interesting open question concerns the smooth connectedness of the MBL phase and the so-called Bose glass phase in interacting bosonic systems: The Bose glass denotes an insulating phase in interacting bosonic systems at zero temperature, theoretically described in [19]. The Bose glass phase shares the non-ergodicity property with the MBL phase, i.e., it does not thermalize upon perturbing certain parameters of the system [22]. The question is thus whether the Bose glass is the low energy limit of the MBL phase in an interacting bosonic system, as has been suggested by several theoretical studies [116, 117]. Recently, the non-ergodic property of the Bose glass has been

A widely studied one-dimensional model showing this phenomenon is the random-field XXZ-chain with the Hamiltonian [119, 120]

$$\mathcal{H}_{\text{disordered XXZ}} = \sum_i \left(J_{\text{xy}}(\sigma_i^x \sigma_{i+1}^x + \sigma_i^y \sigma_{i+1}^y) + J_z \sigma_i^z \sigma_{i+1}^z + h_i \sigma_i^z \right). \tag{1.65}$$

Note that this corresponds to the disordered fermionic model from Eq. (1.60) (upon application of a Jordan-Wigner transformation [121] mapping spin-1/2 to fermionic degrees of freedom[5]) with a nearest-neighbor interaction term proportional to J_z. The longitudinal field h_i is a random variable introducing disorder to the system. It can for example be drawn from a uniform distribution bounded by a critical field strenght h_c, so that $h_i \in [-h_c, h_c]$ with $h_c > 0$. In Chap. 5 we will consider a setup where h_i is drawn from a Bernoulli distribution, so that it takes one of the two values $\pm h_c$ with probability 0.5 respectively, which is interesting with regards to experimental realizations. Here we will introduce some key features of the MBL phase, mainly following [120] and [122]. Consequently, we will discuss its experimental and technological relevance.

1.4.1 Properties of the MBL phase

An important property of an MBL phase is the violation of the so-called eigenstate thermalization hypothesis (ETH). The ETH conjectures that the eigenstates of an isolated quantum system take a thermal form, meaning that the expectation values of local operators depend smoothly on the energy of the state of the system. Another way to put this is that the state of a subsystem (i.e., when tracing over the rest of the system), is thermal in a sense that its density matrix can be described by a thermal ensemble at a temperature determined by the state of the full system [120, 123]. Each subsystem can then be described as a system coupled to an environment, similar to the discussion in Sec. 1.2. This implies that a system obeying the ETH will inevitably lose the memory of its initialization: It will thermalize and thus all that matters is the energy that was initally stored in the configuration. For thermalization to occur, it is necessary to have an efficient transfer of energy throughout the system [122]. This allows to get a first intuition why non-interacting localized systems could escape the ETH: If the disorder strength is dominant, the system will simply remain in a pure state [120]. It has been shown that this can still be the case when interactions are added [21, 124]. This non-thermalization of the eigenstates has the consequence that states with similar energy can have very different properties - meaning that local observables can take different expectation values for such states [120]. The relation of the MBL phase with the violation of the ETH thus hints that in order to detect an MBL phase, one has to consider spectral properties of a system.

claimed to be verified experimentally [118]. Further experimental advances are hoped to shine more light on this intriguing question.

[5] We introduce this mapping in Eq. (3.31).

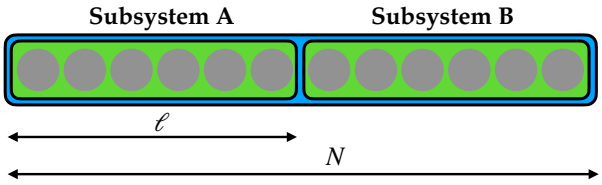

Figure 1.4: Adapted from [126]. A system with N sites is partitioned into two subsystems A (with ℓ sites) and B (with $N - \ell$ sites).

One way to detect an MBL phase is therefore to study the level statistics of a system: In a regime obeying the ETH, the distribution of level spacings are expected to be that of a Gaussian orthogonal ensemble, while in a localized situation one expects Poisson statistics [125].

Another way of detection of an MBL phase lies in the determination of the entanglement entropy of a subsystem for an isolated system at non-zero energy [120, 122, 125, 126]. For that, one bipartitions the system into two subsystems and evaluates the density matrix ρ_A of a subsystem A by tracing over the degrees of freedom of the subsystem B, i.e., $\rho_A = \mathrm{Tr}_B \left(|\psi\rangle \langle\psi| \right)$. The entanglement entropy is then defined by

$$S = -\,\mathrm{Tr}\, \rho_A \ln \rho_A. \tag{1.66}$$

This is shown pictorially in Fig. 1.4.

In a thermal state, one expects a volume-law scaling of the entanglement entropy, which should thus be verified for a state in a regime of the ETH [120, 125]. For the situation in Fig. 1.4, this means that the entanglement entropy evaluated for the subsystem A grows linearly with ℓ. On the contrary, in a localized state, the entanglement entropy is much smaller and follows an area law [120], implying for a one-dimensional system that it remains constant when changing the subsystem size. The properties of the entanglement entropy in an MBL phase can be understood from the presence of local integrals of motion in that phase, as demonstrated in [127, 128]. The emergence of these local conserved quantities intuitively explains that the entanglement entropy is bounded in the MBL phase. These local integrals of motion can be understood as effective spins and coupling between them decays exponentially with the distance [122]. Therefore, entanglement spreads logarithmically in time in a system in the MBL phase [122, 129]. This is a feature commonly used to identify the MBL phase [120, 126, 130] and we will make use of this in Chap. 5. There we will study the scaling of the entanglement entropy and another quantity, called the bipartite fluctutations [131], which serves as a witness of an MBL phase. For details, we refer to Sec. 5.1. The advantage of studying these bipartite fluctuations rather than the entanglement entropy is that they are more easily accessible experimentally. We will give an overview over the experimental relevance and challenges of MBL below.

1.4.2 Verification and application

Advances in experimental techniques and quantum simulation have made an experimental study of MBL feasible in recent years. A challenge is the identification of the MBL phase, as the entanglement entropy is not easily accessed experimentally. One therefore often resorts to signatures probing the violation of the ETH in the system as witnesses of the MBL phase.

Ultracold atoms provide a controllable platform to implement lattice models and we will refer to them in the context of experimental realizations throughout this thesis (cf. Sec. 4.4.1). In order to detect the MBL phase, one then uses 'indirect' measures[6], such as the imbalance of the particle number between even and odd sites, as a witness of the MBL transition [132]. A non-relaxation of this imbalance hints at the presence of an MBL state. Although detectable through such measurement, an active debate remains around the 'smoking-gun' character of such experiments and about the scaling and the properties of these quantities and the MBL phase in exteded systems more generally [133]. On a technical level, other experimental techniques such as superconducting circuits [134, 135] or the use of crystalline materials [136] are also available to implement the respective models[7].

In the light of applications, not only the question of how to implement an MBL phase (using, e.g., quantum simulation), but also the role of MBL for quantum computing devices is relevant. Such platforms are inherently interacting and reliant on localization to preserve the many-body state [23]. In the same time, the importance of MBL for a correct operation of these devices has been pointed out only recently [23] and motivates further study both on theoretical and experimental grounds.

[6] This is in a way similar in spirit to the use of the expectation value of the chiral displacement operator to detect the topological phase of the SSH model discussed in Sec. 1.3.2.

[7] See also [22] for a wider overview.

Chapter 2

Topological quantum dynamo

As discussed in the introductory Sec. 1.2, extending notions of classical thermodynamics such as work, heat or the efficiency of energy transfers into the quantum realm is a challenging, yet promising endeavour. Understanding of these processes enables applications in quantum technologies thought of in theoretical, idealized setups and in the same time inspires new mechanisms. In parallel, a lot of interest is dedicated to understanding topological properties of matter, both from the scientific community, but also with regards to applications. In this chapter, we will study the 'quantum dynamo effect' [32], a new effect occuring in a driven system coupled to an environment and corresponding to a work transfer into the bath for modes close to resonance with the driving velocity [33].

A dynamic realization of the topological model of a spin-1/2 in a radial magnetic field introduced in Sec. 1.1 opens pathways to study both of these effects in the same time. On the one hand, coupling such a spin to a bosonic bath realizes a driven spin-boson model. The spin-boson model itself is a standard example to understand effects in open quantum systems [64, 79, 80], as discussed in Sec. 1.2.2. In the driven case, it can serve as a case study for applications to convert energy on the quantum scale, as we will see in this chapter. On the other hand, the model of a spin-1/2 in a radial magnetic field is also an example of a topological model, which has been realized and studied experimentally [35,37]. In the spirit of studying the interplay of topology and driven dissipative dynamics, it has been realized in [32] that a dynamical realization of this topological model can exhibit new physical properties when coupling to a resonant bosonic mode, which has been called the *quantum dynamo effect*. We will study this effect in a driven spin-boson model of the form [32, 33]

$$\mathcal{H} = \mathcal{H}_{\text{spin}}(t) + \frac{\sigma^z}{2} R + \mathcal{H}_{\text{bath}}. \tag{2.1}$$

The spin part takes the form of the model of a spin-1/2 in a radial magnetic field introduced in Eq. (1.4), where the latter is explored through a dynamic driving protocol [32–34]:

$$\mathcal{H}_{\text{spin}}(t) = -\frac{H}{2} \left(\cos(vt)\sigma^z + \sin(vt)\sigma^x\right). \tag{2.2}$$

Note that this corresponds to setting $\theta = vt$ and $\phi = 0$ in Eq. (1.4). The former allows to evolve the system from the north pole of its parameter space at $t = 0$ to the south pole at $t = \pi/v$ and thus bridges naturally with the definition of a topological invariant from the poles, as we will see below. Building on the definitions and the discussion in Sec. 1.1, we will define the dynamically accessed topology in Sec. 2.1, following [32]. We will then define the *quantum dynamo effect* phenomenologically and thermodynamically and analyze it in detail for the coupling to a single mode in Sec. 2.2. This corresponds to setting

$$R = g(b + b^\dagger) \quad \text{and} \quad \mathcal{H}_{\text{bath}} = \omega b^\dagger b. \tag{2.3}$$

An analysis of the dynamically accessed topological properties of the spin in this case will lead to Eq. (2.46) relating the energy transfer due to the dynamo effect and the dynamically accessed Chern number of the spin.

We will then generalize our results for coupling to an Ohmic bath of bosonic modes in Sec. 2.3. There we will set

$$R = \sum_k g_k(b_k + b_k^\dagger) \quad \text{and} \quad \mathcal{H}_{\text{bath}} = \sum_k \omega_k b_k^\dagger b_k, \tag{2.4}$$

as in the spin-boson model defined in Eq. (1.48). We will see that due to the driven dynamics and the coupling to an environment, work done to drive the system can be transferred into coherent excitation of certain modes of the environment, thus leading to a work-to-work conversion.

The results presented here have their source in a project I worked on together with Cyril Elouard and Karyn Le Hur [33]. The quantum dynamo effect has previously been introduced by the group of Karyn Le Hur [32]. The project presented here was aimed at identifying and classifying the quantum dynamo effect from analytical and numerical calculations. Together with Karyn Le Hur and Cyril Elouard, we developed the thermodynamic definitions and their relation with the topological properties of the model. I tested them numerically by implementing exact diagonalization for coupling to a single mode and to several modes and a stochastic approach for the bath dynamics which had previously been developed in the group of Karyn Le Hur [75, 137, 138] (see App. B for an overview of the used numerical techniques). Cyril Elouard developed a GKLS Master equation approach, to which we compared analytical and numerical results[1], and deepened the thermodynamical definitions, also by contributing insights from his other recent activities [27].

[1] These comparisons will also be shown in this chapter, but for the details on the derivation we will refer to [33].

2.1 A radially driven spin and its dynamically accessed topology

In order to define the notion of the *dynamically accessed topology* we will first consider the free spin, driven using a dynamical protocol, as described by the Hamiltonian in Eq. (2.2), in a bit more depth. The dynamics of this model can be solved exactly, for example by switching to a frame rotating with the time-dependent field using the transformation [33]

$$U_{\text{rot}} = e^{-\frac{ivt}{2}\sigma^y}, \tag{2.5}$$

giving the time-independent Hamiltonian

$$\mathcal{H}^{\text{rot}}_{\text{spin}} = -\frac{H}{2}\sigma^z - \frac{v}{2}\sigma^y. \tag{2.6}$$

The spin expectation values can then be evaluated as [33]

$$\langle\sigma^x(t)\rangle = \frac{H^2}{\Omega^2}\sin(vt) - \frac{v}{\Omega}\cos(vt)\sin(\Omega t) + \frac{v^2}{\Omega^2}\sin(vt)\cos(\Omega t), \tag{2.7a}$$

$$\langle\sigma^y(t)\rangle = 2\frac{vH}{\Omega^2}\sin^2(\Omega t/2), \tag{2.7b}$$

$$\langle\sigma^z(t)\rangle = \frac{H^2}{\Omega^2}\cos(vt) + \frac{v}{\Omega}\sin(vt)\sin(\Omega t) + \frac{v^2}{\Omega^2}\cos(vt)\cos(\Omega t), \tag{2.7c}$$

with $\Omega = \sqrt{H^2 + v^2}$ the energy splitting between the eigenstates of the effective Hamiltonian in the rotating frame. Note that non-adiabaticity introduced by driving with a finite speed manifests itself by an oscillating spin component in y-direction. Adiabaticity is defined in this setup solely from the difference between v and H and one recovers the adiabatic dynamics for $v \ll H$:

$$\langle\sigma^x(t)\rangle \simeq \sin(vt), \tag{2.8a}$$

$$\langle\sigma^z(t)\rangle \simeq \cos(vt), \tag{2.8b}$$

corresponding to the undriven result when setting $vt = \theta$, i.e., the expectation values one would get in the ground state from Eq. (1.8a). The condition for an adiabatic evolution is modified when coupling to a bath, as we will discuss below.

2.1.1 Dynamically accessed topology

Closely linked to the discussion of adiabaticity is the definition of the Chern number: Adapting the definition of the Chern number for a spin in a radial field from Eq. (1.15) to the driven setup under consideration, it is useful to introduce the *dynamically measured*

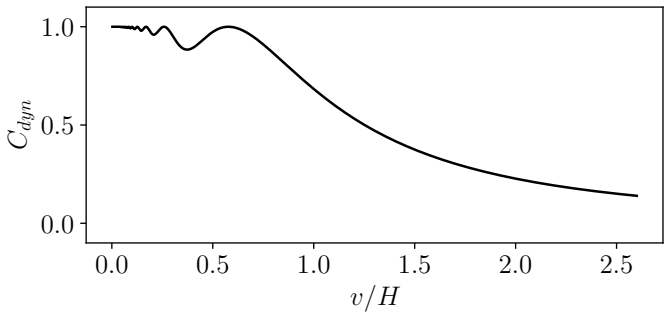

Figure 2.1: C_{dyn} calculated from Eq. (2.9) using Eq. (2.7c) as a function of v/H with $H = 1.0$ and v varying between 0.0 and 2.5.

Chern number C_{dyn} as [32]

$$C_{\mathrm{dyn}} = \frac{1}{2}\left(\langle\sigma^z(t=0)\rangle - \langle\sigma^z(t=\pi/v)\rangle\right), \tag{2.9}$$

which is obtained from a measurement of the spin expectation values when the poles have been accessed using the dynamic protocol. In this sense, it can be understood as an estimate for the actual Chern number C when using such a protocol, i.e.,

$$C_{\mathrm{dyn}} = C + \mathcal{O}\left(v/H\right). \tag{2.10}$$

It is therefore not a quantized number anymore, but one expects to gain a good understanding of the topology of the system from it when $v \ll H$. A plot of C_{dyn} calculated from Eq. (2.9) with the exact analytical result for a driven spin in Eq. (2.7c) is shown in Fig. 2.1 showing that for $v/H \ll 1$, $C_{\mathrm{dyn}} \to C$, while for larger values it starts to deviate.

In [32] it was shown that this view on adiabaticity changes when the interaction of the system with its environment is in addition taken into account. We will therefore discuss some general effects of coupling to an environment on the dynamically accessed topology in the following.

2.1.2 Influence of the environment on dynamics and topology

We model the environment by implementing it as a bath of quantum harmonic oscillators as described in Sec. 1.2.2. The coupling to a bath takes the form of Eq. (2.4). The model thus obtained corresponds to a *driven spin-boson model* [139–141] as discussed in Sec. 1.2.2. The spectral density is defined from Eq. (1.49) and we are here working with an Ohmic spectral density with an exponential cut-off given by Eq. (1.50), i.e.,

$$J(\omega) = 2\pi\alpha\omega e^{-\omega/\omega_{\mathrm{c}}}. \tag{2.11}$$

The coupling strength is determined by α. As described in Sec. 1.2.2, the coupling between the system and the environment leads to an effective reduction of the spin tunneling coefficient (i.e. the coefficient of σ^x in Eq. (2.2)) [75,79], which can be understood from the adiabatic renormalization procedure outlined in App. D.1. Another way to formalize this is the polaron transformation described in App. D.2. The renormalized tunneling element described in Eq. (1.57) now picks up a time-dependence, i.e., [32,33]

$$\Delta_r(t) = H\sin(vt)\left(\frac{H\sin(vt)}{\omega_c}\right)^{\frac{\alpha}{1-\alpha}}. \tag{2.12}$$

In [32] it was shown that a natural criterion for quasi-adiabaticity is thus

$$v \ll \Delta_r\left(t = \frac{\pi}{2v}\right). \tag{2.13}$$

The interplay of the driving and the coupling to a bath thus lead to a new condition under which the dynamically measured Chern number can be seen as an estimate of the true Chern number of the system.

The effects of the bath discussed up to now merely described the effective shift of the spin state due to the coupling to the bath. However, the coupling between the spin and the bath also induces a shift in the bath state which in combination with the driving can lead to a resonance effect termed the *quantum dynamo effect* [32,33] which we will discuss in the following.

2.2 The quantum dynamo effect for coupling to one mode

The state of a free bath at thermal equilibrium at inverse temperature β is described by

$$\rho_{\text{bath}} \propto e^{-\beta\mathcal{H}_{\text{bath}}}, \tag{2.14}$$

leading to

$$\langle R\rangle = \left\langle \sum_k g_k(b_k + b_k^\dagger)\right\rangle = 0. \tag{2.15}$$

This implies that the bath does not exert an average force onto a system coupled to it. However, for the model described by Eq. (2.1), there is a mutual interaction between the spin and the bath due to the coupling term in Eq. (2.1). A non-zero expectation value of the system observable $\langle\sigma^z\rangle$ then has the average effect of displacing the coupled bath operators, which can in turn effectively drive the system. A schematic of this effect is shown in Fig. 2.2. In the model under consideration, these effects can be pronounced, as the bath modes are non-interacting and linear. In general, non-linearities can occur in

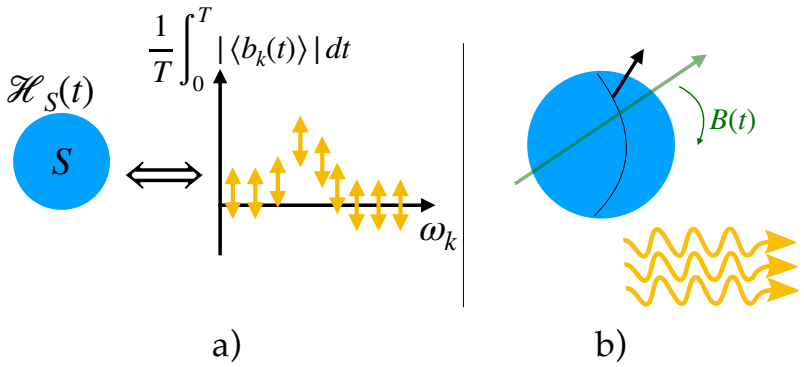

Figure 2.2: Adapted from [33]. Schematic of the quantum dynamo effect. a) Coherently driving (represented by an explicitly time-dependent Hamiltonian) a system S (in blue) coupled to a bosonic bath can induce a finite coherent displacement (averaged over one period of the driving) of some of the bath modes (represented by a shift for modes close to resonance, while high frequency modes have a purely fluctuating effect), corresponding to a work-to-work conversion. b) A spin (black arrow) subject to a rotating magnetic field of fixed amplitude (green arrow), which results in the emission of coherent light in the bosonic bath vacuum.

many-body systems [142], which can give rise to finite lifetimes of the excitations [143, 144]. As mentioned in Sec. 1.2.2, the considered model of an Ohmic bath has nevertheless a strong and long-standing experimental relevance [145–150].

In the following, we denote the average force exerted by the bath on the spin as the *induced field* $h(t)$, i.e.,

$$h(t) = \langle R(t)\rangle = \left\langle \sum_k g_k (b_k(t) + b_k(t)^\dagger) \right\rangle . \tag{2.16}$$

This quantity is helpful for understanding the quantum dynamo effect in an intuitive way. In order to analyze it at a lower level of complexity first, we will in the following consider the coupling of the spin in a rotating magnetic field to a *single bosonic mode* before generalizing the introduced notions to a coupling to a bath in Sec. 2.3.

2.2.1 Phenomenological definition of the dynamo

For the case of coupling to one mode, the Hamiltonian reads

$$\mathcal{H} = -\frac{H}{2}(\sin(vt)\sigma_x + \cos(vt)\sigma_z) + g(b + b^\dagger)\frac{\sigma_z}{2} + \omega b^\dagger b. \tag{2.17}$$

The induced field then is defined as

$$h_\omega(t) = \left\langle g(b(t) + b(t)^\dagger) \right\rangle . \tag{2.18}$$

We use the subscript ω to underline that this is the field induced onto the spin by one bosonic mode with a frequency ω. Note that the resonant driving in this setup corresponds to a velocity $v = \omega$. Using this definition of the induced field and the Heisenberg equation of motion, we find [32, 33]

$$\frac{1}{\omega^2}\ddot{h}_\omega + h_\omega = -\frac{g^2}{\omega}\langle\sigma^z\rangle. \tag{2.19}$$

This equation reflects the coupling of the dynamics of the spin and the bosonic mode evoked earlier and we will show below how the dynamo effect arises for resonant driving.

Initial conditions

In order to evaluate the dynamics precisely, we need to specify the initial conditions. Throughout this chapter, we will consider the spin to be initialized in the up-state, i.e., $|\uparrow\rangle_z$. Two different setups for the mode (or more generally a set of bath modes) are commonly considered [32, 33, 75, 151]:

1. Preparation (1): The bath mode is initially in the ground state of the combined system under the restriction that $\langle\sigma^z(t)\rangle = 1$, i.e., in the ground state of the Hamiltonian

   $$\mathcal{H}_{\text{boson}} = \frac{g}{2}(b + b^\dagger) + \omega b^\dagger b. \tag{2.20}$$

   This stated corresponds to the shifted vacuum, where the shift comes from the coupling to the upward pointing spin, so that $(b + g/(2\omega))\,|GS\rangle = 0$. This results in the following initial condition on h_ω:

   $$h_\omega(0) = g(\langle b(0)\rangle + \langle b^\dagger(0)\rangle) = -\frac{g^2}{\omega}. \tag{2.21}$$

2. Preparation (2): The bosonic mode is initialized in its free vacuum and there is no interaction between the spin and the bath, i.e. $|GS\rangle = |\uparrow\rangle_z \otimes |0\rangle$. This results in $h_\omega(0) = 0$.

The formal solution of Eq. (2.19) is then given by

$$h_\omega(t) = -g^2 \int_0^t dt' \sin(\omega(t - t'))\,\langle\sigma^z(t')\rangle - \delta_{(1)}\frac{g^2}{\omega}\cos(\omega t). \tag{2.22}$$

The symbol $\delta_{(1)}$ distinguishes the two initial condition and takes the value 1 for preparation (1) and 0 for preparation (2). We will in this chapter focus on preparation (1). In the following, we present two cases in which the analysis is analytically tractable.

Weak coupling and adiabatic driving

For weak coupling between the spin and the mode, we can assume that their mutual influence on their dynamics is small. If in addition the driving velocity is small, we

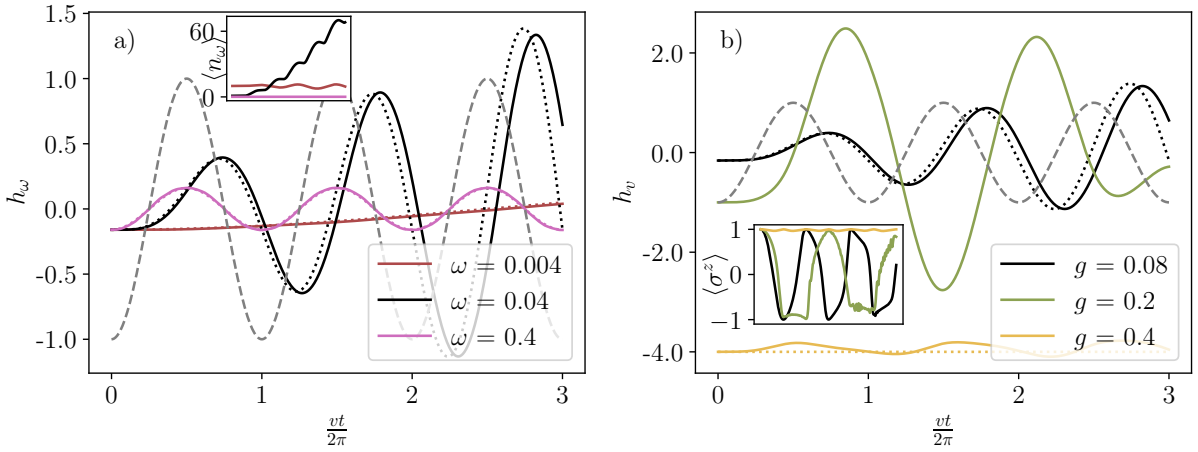

Figure 2.3: One-mode dynamo, from [33]. a) Induced field as a function of vt (with $v = 0.04$) from numerical exact diagonalization of the Hamiltonian in Eq. (2.17) for a total of three driving periods. ω is varied, while $g^2/\omega = 0.16$ is kept fixed. The dotted lines show the comparison to Eqs. (2.24)-(2.26). The inset shows the corresponding expectation values of the occupation number $\langle n_\omega \rangle$. b) Induced field of a resonant mode with $\omega = v = 0.04$ for different values of the coupling g. The corresponding expectation value of $\langle \sigma^z \rangle$ is shown in the inset. The dotted lines show theoretical predictions from the unitary spin limit in Eq. (2.26) for $g = 0.08$ and from the frozen spin limit in Eq. (2.29) for $g = 0.4$. For comparison, in both plots the external field in z-direction (i.e. $-H\cos(vt)$) is shown by a gray dashed line. In all simulations, $H = 1.0$ and the system is initialized in preparation (1). The Hilbert space of the bosonic mode was truncated at an occupation of $N_b = 200$ and we checked that the achieved occupations are well below this number.

approximately recover $\langle \sigma^z(t) \rangle \sim \cos(vt)$. Plugging this into Eq. (2.19), we find the solution

$$h_\omega = \frac{g^2\omega}{\omega^2 - v^2}\left(\frac{v^2}{\omega^2}\cos(\omega t) - \cos(vt)\right), \tag{2.23}$$

for preparation (1). From this result, we can gain a first understanding of why the case of a resonant frequency is special:

- If $\omega \ll v$, the induced field simplifies to:

$$h_\omega(t) = -\frac{g^2}{\omega}\cos(\omega t) + \mathcal{O}\left(\frac{\omega^2}{v^2}\right), \tag{2.24}$$

  that is, the initial field evolves almost freely.

- If $\omega \gg v$, the spin evolves almost statically as felt by the mode. Therefore, the latter approximately remains equilibrated to it, i.e.,

$$h_\omega(t) = -\frac{g^2}{\omega}\cos(vt) + \frac{1}{v}\mathcal{O}\left(\frac{v^3}{\omega^3}\right). \tag{2.25}$$

  This corresponds to the field from shifted oscillators and is consistent with the

considerations from Sec. 1.2.2.

- Finally, in the resonant case $\omega = v$, we find:

$$h_v(t) = -\frac{1}{2}g^2 t\sin(vt) - \frac{g^2}{v}\cos(vt). \tag{2.26}$$

We observe from the first term how the amplitude of the field in the resonant case builds up in time and thus gets more important for the dynamics of the spin. This can also be confirmed by exact diagonalization, see Fig. 2.3a). We also observe that the effect of the induced field in this case opposes the change of the spin induced by the driving field (see also Fig. 2.3). This is phenomenologically similar to Faraday's law of induction, which motivated the designation 'quantum dynamo effect' in [32, 33]. Note that this back-action can also be identified from the induced field averaged over half a period of the driving:

$$\int_0^{\pi/v} h_v(t')dt' = -\frac{1}{2}\frac{g^2}{v^2}\pi, \tag{2.27}$$

which is actually independent of the initial preparation [33].

The shift induced in the bosonic mode can be interpreted as a coherent displacement and thus energy stored in the mode which can be rendered 'useful' by coupling to a cavity and thus triggering emission of microwave photons, for example [152, 153]. This gives an additional motivation of the term 'quantum dynamo effect': A rotation of the quantum system leads to the emission of light (cf. also Fig. 2.2b)). Note furthermore that the occupation of the bosonic mode in the case considered in this section increases quadratically in time. Concretely, for weak coupling and slow driving, we can evaluate the occupation number of the bosoic mode to be

$$\Delta\langle n_{\omega=v}\rangle = \frac{g^2}{16}t^2 + \frac{g^2}{16v}t\sin(2vt) + \frac{g^2}{32v^2}\left(3(\cos(2vt)-1)\right). \tag{2.28}$$

This can also be confirmed from a numerical study of this system, as shown in the inset of Fig. 2.3a).

Frozen spin limit

The opposite limit of a very strong interaction between the spin and the environment is also analytically tractable. Considering the effective dynamics of the spin under the action of the driving Hamiltonian $\mathcal{H}_{\text{spin}}$ and the induced field (acting through a term $\mathcal{H}_{\text{induced}} = h(t)/2\sigma^z$, we readily see that for $-h(t) > H \gg v$, the state of the spin will be restricted to the northern hemisphere of the Bloch sphere. If $-h(t) \gg H > 0$, we can

approximate $\langle\sigma^z(t)\rangle \simeq 1$. Plugging this into Eq. (2.22), we obtain

$$h_\omega(t) = -\frac{g^2}{\omega}, \tag{2.29}$$

for preparation (1). This results in the field remaining fixed at its initial value and we see that the full system is static in this case. This can also be confirmed using exact diagonalization, see Fig. 2.3b). From Eq. (2.29) we see that the frozen spin limit is reached for $g^2/\omega \gg H$. As opposed to the previously discussed case of weak coupling, no energy can be transferred between the different parts of the system in this limit, therefore we understand that no quantum dynamo effect takes place in this situation.

In the following, we will make the definition of the dynamo effect more precise by considering the actual energy transferred to the bath by the dynamic response and comparing it to the work done by driving the system.

2.2.2 Thermodynamic analysis

General definitions

In order to precisely define the dynamo effect, we compare the work done by driving the system to the energy stored in coherent displacement of the bosonic mode due to its dynamic response to the system evolution. The work provided by the drive can be defined with the variation of total energy of the combined system of spin and bosonic mode, i.e.,

$$W_{\mathrm{dr}}(t) = \int_0^t dt' \left\langle \frac{\partial \mathcal{H}(t')}{\partial t} \right\rangle. \tag{2.30}$$

This corresponds to Eq. (1.59) and thus to the view that work is done to the spin by coupling it to an external work reservoir [24]. The energy associated with a coherent displacement of the bath modes is given by

$$E_{\mathrm{dis}}(t) = \omega |\langle b(t)\rangle|^2. \tag{2.31}$$

Note that this definition includes a contribution due to the adiabatic response of the mode to the spin dynamics, as well as an energy contribution coming from the shift of the mode due to the coupling to the spin in the ground state of the joint system. As the former can be expected to average to zero over one period of the driving and the latter needs to be introduced to the system in the process of coupling it, we neglect them in the consideration of the efficiency of the quantum dynamo effect [33]. This corresponds to defining the dynamically induced field without the adiabatic contributions coming from equilibration of the modes to the spin state (cf. also the discussion in Sec. 1.2.2) We therefore define the dynamo energy as the coherent energy of displacement of the bosonic mode with the

adiabatic contribution subtracted as a reference, i.e.,

$$E_{\rm dyn}(t) = \omega \left| \langle b(t) \rangle + \frac{g}{\omega} \frac{\langle \sigma^z \rangle}{2} \right|^2 . \tag{2.32}$$

The associated energy flow can be evaluated from the Heisenberg equation of motion for the mode and reads

$$\dot{E}_{\rm dyn}(t) = \left(h(t) + \frac{g^2}{\omega} \langle \sigma^z(t) \rangle \right) \frac{\langle \dot{\sigma}^z(t) \rangle}{2}. \tag{2.33}$$

We then define the average efficiency of the dynamo as

$$\eta_{\rm dyn} = \frac{\Delta E_{\rm dyn}}{W_{\rm dr}}. \tag{2.34}$$

We are using the notation ΔX to designate the change of a variable X with respect to its initial value, i.e., $\Delta X = X(t) - X(0)$.

The system is comprised of the spin and the bosonic mode, therefore the total energy balance reads

$$W_{\rm dr} = \Delta E_{\rm spin} + \Delta E_{\rm int} + \Delta E_{\rm bos}, \tag{2.35}$$

where $E_{\rm spin} = \langle \mathcal{H}_{\rm spin} \rangle$, $E_{\rm int} = \left\langle g(b + b^\dagger) \frac{\sigma^z}{2} \right\rangle$ and $E_{\rm bos} = \left\langle \omega b^\dagger b \right\rangle$. Using the definition of the dynamo energy, we can also write an energy balance for the coherent displacement energy of the bath mode with its adiabatic contribution as a reference (i.e., the dynamo energy) and the associated energy of fluctuations, i.e.,

$$W_{\rm dr} = \Delta E_{\rm spin} + \Delta E_{\rm dyn} + \Delta E_{\rm fluct}, \tag{2.36}$$

with

$$E_{\rm fluct}(t) = \omega \left(\left\langle \left(b^\dagger(t) + \frac{g}{\omega} \frac{\sigma^z(t)}{2} \right) \left(b(t) + \frac{g}{\omega} \frac{\sigma^z(t)}{2} \right) \right\rangle - \left| \langle b(t) \rangle + \frac{g}{\omega} \frac{\langle \sigma^z(t) \rangle}{2} \right|^2 \right). \tag{2.37}$$

The work done to the system by driving is thus shared between excitations of the spin, coherent displacement of the bosonic mode from its adiabatic reference due to the dynamic nature of the driving process and fluctuations of the field around this mean value. Assuming the system is initialized with $E_{\rm fluct} = 0$, it is clear that $\Delta E_{\rm fluct} > 0$ and therefore

$$\eta_{\rm dyn} = 1 - \frac{\Delta E_{\rm fluct}(t) + \Delta E_{\rm spin}(t)}{W_{\rm dr}(t)} \leq 1. \tag{2.38}$$

The efficiency of the dynamo thus defined is bounded by one and takes onto account excitations of the spin and fluctuations of the bosonic mode as sources of inefficiency.

Calculations for analytic limits

For resonant driving with $v = \omega$, coming back to the limit of weak coupling and quasi-adiabatic driving (i.e. $v \ll H$), we use the approximation $\langle \sigma^z(t) \rangle \simeq \cos(vt)$ and plug it into Eq. (2.30) to evaluate the work done by driving the system. This gives

$$W_{\mathrm{dr}}(t) = \frac{g^2}{32v}\Big(5(1-\cos(2vt)) + 2v^2t^2 - 2vt\sin(2vt)\Big), \tag{2.39}$$

and we see that besides oscillations with the frequency of the driving velocity, there is a quadratic increase in time of the work done by driving the system. On the other hand, evaluating the dynamo energy by integrating Eq. (2.33) gives

$$\Delta E_{\mathrm{dyn}}|_{\omega=v} = \frac{g^2}{32v}\Big(1-\cos(2vt) + 2v^2t^2 - 2vt\sin(2vt)\Big). \tag{2.40}$$

Note that there is a contribution similarly increasing quadratically in time, as for the work. Therefore, when the oscillatory components vanish, we see that all the work will be transferred into dynamo energy. More precisely, we observe that for $n \in \mathbb{N}$

$$\eta_{\mathrm{dyn}}\left(t = n\frac{\pi}{v}\right) = 1. \tag{2.41}$$

The times of unit efficiency correspond precisely to the poles of the Bloch sphere. This is consistent with the energy of fluctuations taking the form

$$\Delta E_{\mathrm{fluct}} = \frac{g^2}{4v}\sin^2(vt), \tag{2.42}$$

thus constituting a source of inefficiency of the dynamo when deviating from the poles. When driving the system for several periods, the fraction of work going into coherent displacement of the bosonic mode will increase, as the weight of the quadratic contribution in the work and the dynamo energy increases. We can therefore assume the efficiency to approach unity in the long time limit if the approximation of weak coupling remained true (which given Eq. (2.26) is not fulfilled for arbitrary long times, as the field induced back on the system also increases in time and can lead to a breakdown of the dynamo, as we will discuss below).

Coming back to the frozen spin limit in which the induced field is exerting a strong influence on the spin and 'freezing' it to $\langle \sigma^z(t) \rangle \simeq 1$, we found above that the induced field with preparation (1) will also be constant (cf. Eq. (2.29)), from which we can immediately conclude with Eq. (2.33) that $\Delta E_{\mathrm{dyn}} = 0$. From above considerations in the weakly coupled case, we see that the frozen spin limit can not only be reached by initializing the system with $g^2/\omega \gg H$, but also by driving the resonant system for a sufficiently long time and an induced field thus building up (coresponding to the contribution with linearly increasing

amplitude in Eq. (2.26)). We therefore expect the induced field to have an increasing influence on the spin in the resonant case and at a time around $t \gtrsim H/2g^2$ to lead to a breakdown of the dynamo effect. This is accompanied by a 'freezing' or restriction to the northern hemisphere of the Bloch sphere of the spin. This can also be observed in Fig. 2.3b): When the induced field grows, the dynamics of $\langle\sigma^z(t)\rangle$ increasingly deviates from its free solution and therefore also the induced field deviates from this analytical prescription (cf. the curve with $g = 0.08$ in Fig. 2.3b)). This is even more pronounced for the curve with $g = 0.2$, where the induced field strongly opposes the effect of the external driving field such that it is not justified anymore to compare this to the solution derived under the assumption that the spin almost follows its free evolution. The dynamo effect then breaks down and the induced field does not increase further. This breakdown occurs when the induced field is of the same order of magnitude as the external field and opposing it. Increasing g even further (cf. the curve with $g = 0.4$), initially the induced field is larger than the external field and the spin dynamics are thus from the beginning almost frozen, hindering the dynamo effect.

To observe this breakdown in more detail, we present numerical results regarding the performance of the resonant dynamo in the following section. The simultaneous breakdown of the dynamo and freezing of the spin makes a curious connection with the dynamically accessed topology of the spin: Restricting the spin to the northern hemisphere of the Bloch sphere corresponds to $C_{\mathrm{dyn}} \to 0$. We will make this connection more precise in Sec. 2.2.3

Numerical performance study

To interpolate between the two analytically accessible limits, we study the dynamo effect numerically for the intermediate parameter regime. From now on, we focus on the resonant case with $\omega = v$. For this, we evolve the system in time for a driving from north to south pole, as we identified the poles as the regions of best performance in the previous section. Reading out the change in dynamo energy ΔE_{dyn} and the associated efficiency η_{dyn} allows to make conclusions about optimal parameter regimes of operation. In the previous section, we found close to unit efficiency at quasi-adiabatic driving speed, suggesting slow driving as optimal. However, this necessarily increases the time needed to reach the south pole. To account for situations in which the operating time matters, we analyze the output power averaged over the driving time as an additional performance indicator, i.e., $\Delta E_{\mathrm{dyn}}/t_f$ where t_f is the final time of the driving.

The numerical results are shown in Fig. 2.4. From Fig. 2.4a) we see the range of validity of the results obtained above in the limit of weak coupling and adiabatic driving, which is for a certain driving speed limited by a threshold value of g/v at which the dynamo energy rapidly starts to decrease when further increasing the coupling. Smaller driving velocities allow for larger dynamo energies, which is related to better stability of the effect in these cases. The corresponding efficiencies shown in Fig. 2.4b) similarly

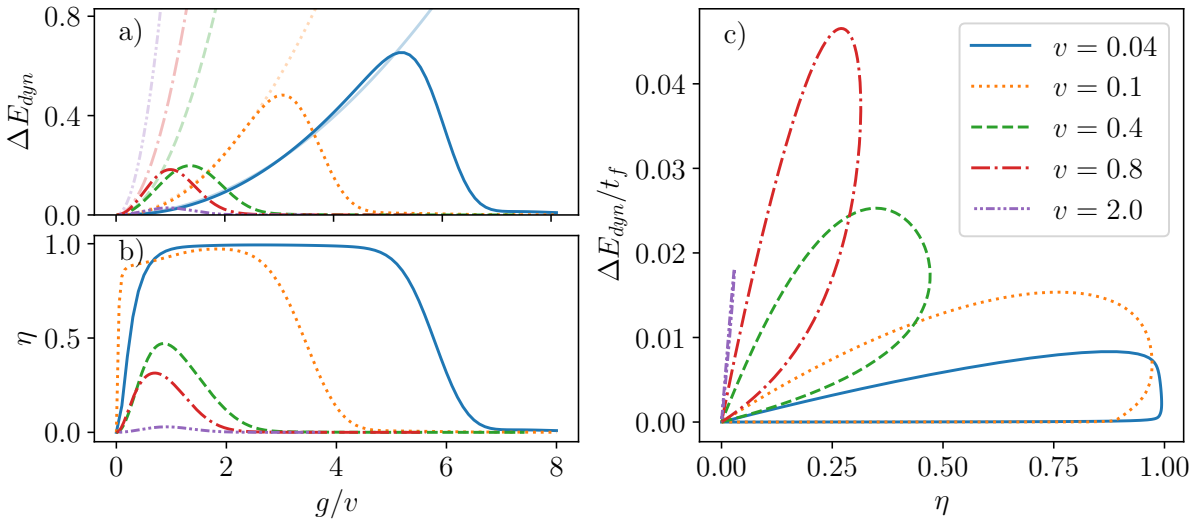

Figure 2.4: Performances of the one mode dynamo, from [33]. a) Plot of ΔE_{dyn} for different velocities as a function of g/v at $t_f = \pi/v$. Each line style represents a different driving velocity where the color intensive lines show results from ED, while the light lines show a comparison to Eq. (2.32) at $t = \pi/v$. b) The corresponding efficiencies η as a function of g/v. c) Parametric plot of η vs $\Delta E_{\text{dyn}}/t_f$ (averaged output power) for different velocities and with a parameter g/v at $t_f = \pi/v$. The ED results are based on a simulation of the time evolution under Hamiltonian Eq. (2.17) with $H = 1.0$ and starting from preparation (1). The Hilbert space of the bosonic mode is truncated for each data point at a value well beyond the expectation value of the maximally reached occupation.

show that small velocities are beneficial for an efficient dynamo. In Fig. 2.4c), we show a parametric plot of the averaged output power (i.e. $\Delta E_{\text{dyn}}/t_f$) and the efficiency η_{dyn} with g/v as a parameter. This demonstrates that in terms of the output power averaged over the time of the process, there is a well defined maximum at non-optimal efficiency, which is largest for intermediate driving speeds. On the one hand, for large values of the paramter g/v, the dynamo energy, the averaged output power and the efficiency all go to zero, as a large shift in the bosonic mode leads to a strong induced field 'freezing' the spin. On the other hand, a breakdown of the effect is also occurring when v is decreased too much, as this firstly leads to a stronger initially induced field (in preparation (1): $h(0) = -g^2/v$) and secondly increases the time of the experiment, thus decreasing the averaged output power.

The plots in Fig. 2.4 show a large range of the parameter g/v, thus interpolating between the weak coupling and the frozen spin limit discussed before. The analytical understanding provided above is therfore restricted to these limits. More general statements can be made if we include the topological properties of the spin in our analysis, which will be discussed in the next section.

2.2.3 Topological properties

As shown in Sec. 1.1, the topology of a spin-$\frac{1}{2}$ is determined by the ratio between the radial field and the constant offset field. In this chapter, we are studying a dynamic protocol to access the radial field. An additional coupling to a resonant bosonic mode gives rise to an induced field acting on the spin and an energy transfer to the bosonic mode through the dynamo effect. As analyzed above, this effect breaks down simultaneously with the spin getting 'frozen' on the northern hemisphere of the Bloch sphere. This suggests that the dynamo effect is related to the dynamically accessed topology of the spin, defined in Sec. 2.1.

Relation of the dynamo energy to the dynamic Chern number

In Fig. 2.4a), the transparent lines show the analytical results derived under the approximation $\langle\sigma^z(t)\rangle \simeq \cos(vt)$ (quasiadiabatic driving, weak coupling). This corresponds to a situation where $C_{\mathrm{dyn}} \to C = 1$ according to Eq. (1.15). Comparing to the numerical results shown by the color intensive lines in Fig. 2.4a), we observe that this approximation is valid while both lines remain close to each other. On the other hand, when $\Delta E_{\mathrm{dyn}} \to 0$ for larger values of g/v, we reach (if v still is quasi-adiabatic) $C_{\mathrm{dyn}} \to C = 0$ and $\langle\sigma^z(t)\rangle \simeq 1$.

Let us thus for adiabatic driving approximate $\langle\sigma^z(t)\rangle \simeq C(\cos(vt) - 1) + 1$, which is certainly a rough estimate, but correctly captures the topology of the spin, i.e., it is correct at the poles. Using Eq. (2.22) to evaluate the induced field and plugging it into Eq. (2.33), we find

$$h(t) + \frac{g^2}{v}\langle\sigma^z(t)\rangle = -\frac{1}{2}Cg^2 t\sin(vt), \tag{2.43}$$

and hence

$$\dot{E}_{\mathrm{dyn}} = \frac{g^2 vt}{4}\sin^2(vt)C^2. \tag{2.44}$$

Integration over half a period (i.e., adiabatic driving from north to south pole as required for the evaluation of the topology) then gives [33]

$$\Delta E_{\mathrm{dyn}}\left(t = \frac{\pi}{v}\right) = \frac{g^2\pi^2}{16v}C^2. \tag{2.45}$$

Departing from the adiabatic limit, we replace $C \to C_{\mathrm{dyn}}$ and find [33]

$$\Delta E_{\mathrm{dyn}}\left(t = \frac{\pi}{v}\right) = \frac{g^2\pi^2}{16v}C_{\mathrm{dyn}}^2. \tag{2.46}$$

The breakdown of the dynamo effect is thus related to a change in the dynamically accessed topology of the spin. The energy transferred into coherent displacement of the bath mode decreases with the square of the dynamically measured Chern number. Numerical results obtained using exact diagonalization can be seen in Fig. 2.5a) and show good agreement

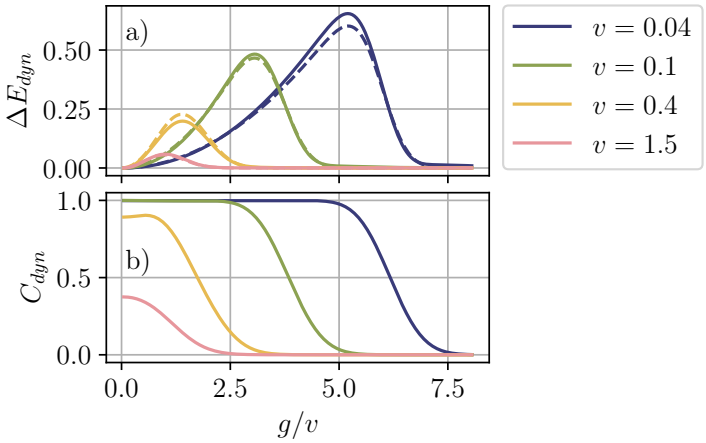

Figure 2.5: From [33]. The dynamo energy for coupling to a resonant mode from ED simulations (solid lines) and the prediction from Eq. (2.46) with C_{dyn} measured numerically (dashed lines) as a function of g/v. b) The dynamically measured Chern number from the same simulation as a function of g/v. For both figures, $H = 1.0$, the system was initialized in preparation (1) and the Hilbert space of the bosonic mode is truncated at a value well beyond the expectation value of the filling.

with Eq. (2.46).

The quantity C_{dyn} thus becomes interesting in its own right (rather than just being an estimate of C), as it signals the breakdown of the dynamo effect. Physically, the dynamically accessed topology may change when increasing the driving speed (thus introducing oscillations of higher order in the dynamics of the spin, which for the free spin is reflected in Eq. (2.7c)), when increasing entanglement between the spin and the mode (thus departing from a unitary evolution of the spin) or when adding an offset field (realized by the term in M in Eq. (1.4) or by an induced field). Stabilizing the dynamically accessed topology of the spin thus can help to delay the breakdown of the dynamo effect. We will exploit this observation in the following section.

Effect of a constant bias field

As argued above, one of the factors influencing C_{dyn} and thereby the dynamo effect through Eq. (2.46) is an offset field acting on the spin. This can be the induced field discussed in this chapter (in this case, it is in general time-dependent) or an external bias field as the term in M in Eq. (1.4). This implies that such a constant bias field can also attenuate or accelerate the breakdown of the dynamo effect and as such be used to tune it to the relevant output power. To be clear, consider the initially induced field $h(0) = -g^2/v$. Including a term

$$\mathcal{H}_{\mathrm{bias}} = -\frac{M}{2}\sigma^z, \tag{2.47}$$

in the Hamiltonian, with $0 > M > -H$ this field opposes the initially induced field while the prepared spin state $|\uparrow\rangle$ is still the ground state. This allows to stabilize the dynamo

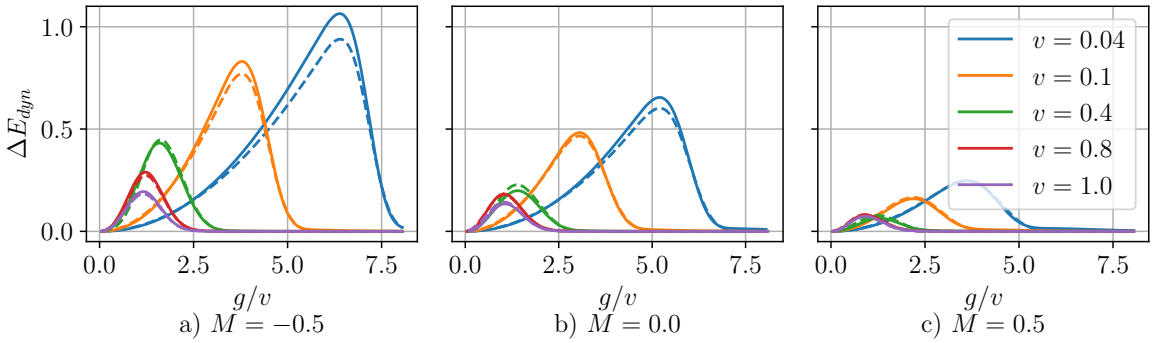

Figure 2.6: Comparison of the change in dynamo energy (for coupling to one resonant mode) after driving for half a period between numerical results and Eq. (2.46) with C_{dyn} measured numerically (dashed lines), as a function of g/v. The parameters are a) $M = -0.5$, b) $M = 0.0$ and c) $M = 0.5$. The system is initialized in preparation (1) and with $H = 1.0$. The Hilbert space of the bosonic mode is truncated for each data point at a value well beyond the expectation value of the filling and the parameter g/v ranges from 0.0 to 8.0.

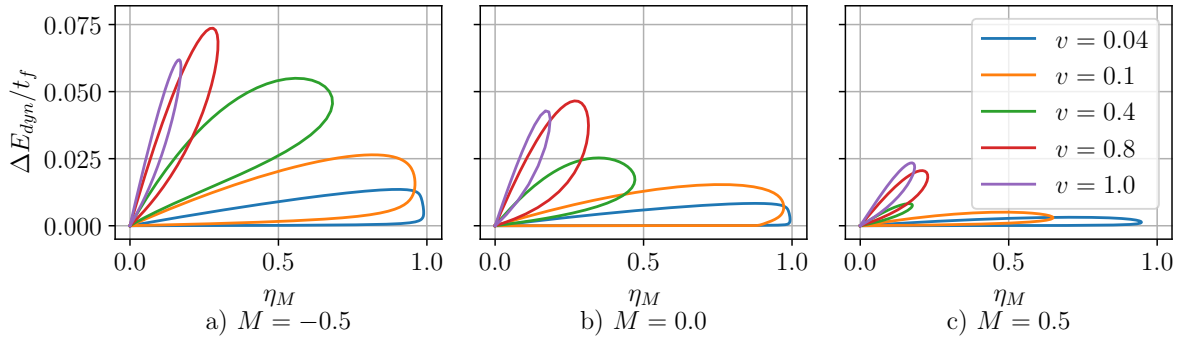

Figure 2.7: Adapted from [33]. The averaged output power as a function of the efficiency η_M defined in Eq. (2.48) with a parameter g/v from ED simulation with a) $M = -0.5$, b) $M = 0.0$ and c) $M = 0.5$. The parameters are the same as in Fig. 2.6.

effect for larger induced fields without leading to a breakdown. To calculate the efficiency in this setup, we subtract the introduced energy imbalance M between the spin ground states at the north and the south pole from the work, i.e.

$$\eta_M = \frac{\Delta E_{\text{dyn}}}{W_{\text{dr}} - M}. \tag{2.48}$$

This definition reflects the fact that M is an additional one-shot resource that can be consumed after initialization. Note that the definition of η in Eq. (2.34) is still sensible over full periods of the driving. We study the effect of such a term numerically in Fig. 2.7 in analogy to the results shown in Fig. 2.4c). From these results, we confirm that $M > 0$ decreases the averaged output power, while $M < 0$ increases the maximally

attainable averaged output power and preserves high efficiency. In this way, adding a constant negative offset field M constitutes a way to adapt the dynamo to desired output parameters. The dynamo energy is still related to the dynamically measured Chern number C_{dyn} through Eq. (2.46), so this way to modify the dynamo is inherently possible because of the topological properties of the considered system. We show a comparison of numerical results and Eq. (2.46) relating the change in dynamo energy to the dynamically measured Chern number for different values of M in Fig. 2.6

After having shown how the quantum dynamo effect is defined for coupling to one bosonic mode and and how it is in this case related to the topological properties of the system, we want to generalize these results for the case of coupling to an environment with a broad spectrum. This will be the subject of the following section.

2.3 The quantum dynamo effect for coupling to a bath

We now want to generalize the considerations for coupling to a bath instead of just one single mode. In this case, the induced field can be defined by Eq. (2.16). We first derive a few general formulae which are useful in order to study the quantum dynamo effect from the observed spin dynamics. We then present different techniques that can be employed in order to study the dynamo effect analytically and numerically. Finally, we present results for the performance of the dynamo effect and discuss its topological properties.

2.3.1 Generalities on the dynamo effect with a bath

Adiabatically and dynamically induced field

Getting back to the model introduced in Eq. (2.1), we first note that the induced field is now made up of a collection of bosonic modes. The full dynamics of the system is thus described by a set of coupled differential equations. Here, we are focussing on preparation (1). For the modes, we can write from the Heisenberg equation of motion

$$\left\langle \dot{b}_k(t) \right\rangle + i\omega_k \left\langle b_k(t) \right\rangle = -ig_k \frac{\langle \sigma^z(t) \rangle}{2}, \tag{2.49}$$

which formally yields

$$\langle b_k(t) \rangle = e^{-i\omega_k t} \left\langle b_k(0) \right\rangle - ig_k \int_0^t dt' e^{-i\omega_k (t-t')} \frac{\langle \sigma^z(t') \rangle}{2}. \tag{2.50}$$

Integrating by parts yields

$$\langle b_k(t)\rangle = -\frac{g_k}{\omega_k}\frac{\langle\sigma^z(t)\rangle}{2} + \frac{g_k}{\omega_k}\int_0^t dt' e^{-i\omega_k(t-t')}\frac{\langle\dot{\sigma}^z(t')\rangle}{2}, \tag{2.51}$$

where we have used that in preparation (1), $\langle\sigma^z(0)\rangle = 1$ and $\langle b_k(0)\rangle = -\frac{g_k}{2\omega_k}$. Eq. (2.51) allows to analyze the contribution to the dynamics of the mode (and therefore the induced field) separately: The first term is similar to the induced field one would obtain for a fixed configuration of the spin, exerting an average force and thereby shifting the equilibrium value of the spins. When evaluating the induced field by this term, this gives rise to what we call the *adiabatically induced field* by one mode k, i.e.,

$$h^k_{\mathrm{ad}} = -\frac{g_k^2}{\omega_k}\langle\sigma^z\rangle, \tag{2.52}$$

which would be the only contribution if all the modes had a high frequency (cf. the discussion in Sec. 1.2.2). Here, we are analyzing the contributions to the induced field corresponding to an adiabatic setup for all the modes, separating them from the non-adiabatic contributions (where the latter correspond to the second term in Eq. (2.51)). The total field induced in an adiabatic setting is thus

$$h_{\mathrm{ad}} = \sum_k h^k_{\mathrm{ad}} = -\sum_k \frac{g_k^2}{\omega_k}\langle\sigma^z\rangle = -\langle\sigma^z\rangle\int_0^\infty \frac{J(\omega)}{\pi\omega}d\omega. \tag{2.53}$$

In the last step, we assumed that the number of bath modes is going to infinity and justifies taking the continuum limit, in which the coupling strength is described by the spectral density defined in Eq. (1.49). Using an Ohmic spectral density of the form of Eq. (2.11), we find

$$h_{\mathrm{ad}} = -2\alpha\omega_c\langle\sigma^z\rangle. \tag{2.54}$$

The second contribution to the right hand side of Eq. (2.51) then gives rise to a dynamically induced field, inherently connected to a variation of $\langle\sigma^z\rangle$ in time:

$$h^k_{\mathrm{dyn}}(t) = \frac{g_k^2}{\omega_k}\int_0^t dt' \cos(\omega_k(t-t'))\langle\dot{\sigma}^z(t')\rangle, \tag{2.55}$$

and therefore (in the continuum limit)

$$h_{\mathrm{dyn}}(t) = \int_0^t dt'\int_0^\infty d\omega\frac{J(\omega)}{\pi\omega}\cos(\omega(t-t'))\langle\dot{\sigma}^z(t')\rangle. \tag{2.56}$$

With an Ohmic spectral density we obtain [33]

$$h_{\mathrm{dyn}}(t) = \int_0^t dt'\frac{2\alpha\omega_{\mathrm{c}}}{1+\omega_{\mathrm{c}}^2(t-t')^2}\langle\dot{\sigma}^z(t')\rangle. \tag{2.57}$$

Note that $(1+\omega_c^2 t^2)^{-1}$ vanishes for $|t|$ greater than a few ω_c^{-1}. Since we assume ω_c to be a large frequency cut-off and therefore the largest energy scale of the model, the typical spin evolution occurs on much longer time-scales so that we can approximate $\langle\sigma^z(t')\rangle \simeq \langle\sigma^z(t)\rangle + (t'-t)\langle\dot{\sigma}^z(t)\rangle$ and perform the integration over t'. We then obtain [33]

$$h_{\mathrm{dyn}}(t) = 2\alpha \arctan(\omega_c t)\langle\dot{\sigma}^z(t)\rangle - \frac{\alpha}{\omega_c}\log\left(1+\omega_c^2 t^2\right)\langle\ddot{\sigma}^z(t)\rangle \approx \alpha\pi\langle\dot{\sigma}^z(t)\rangle\,. \tag{2.58}$$

In the last step, we used that $\arctan(\omega_c t) \sim \pi/2$ for $t \gg \omega_c^{-1}$ and we neglected the second term since we assume that ω_c is the largest energy scale of the problem. Eq. (2.58) thus gives a simple, approximate way to evaluate the dynamically induced field from the spin dynamics. Note that the thus induced field opposes the change of the spin (i.e. it acts to maintain it in its position), which is again in analogy to Faraday's law of induction and hints the occurrence of a dynamo effect in this setup as well. We can use Eqs. (2.54) and (2.57) to evaluate the two contributions to the induced field directly from the spin dynamics[2], i.e.,

$$h(t) = h_{\mathrm{ad}} + h_{\mathrm{dyn}} \approx -2\alpha\omega_c\langle\sigma^z(t)\rangle + \alpha\pi\langle\dot{\sigma}^z(t)\rangle\,. \tag{2.59}$$

For experimental purposes, this allows to evaluate the induced field from a measurement of the spin evolution. Furthermore, we can use established analytic and numerical methods to evaluate the spin dynamics and hence conclude on the induced field. Before describing several such methods, let us make the definition of the quantum dynamo effect more precise, in the sense of energetic definition as in Sec. 2.2.2.

Thermodynamic definition

In order to identify the quantum dynamo effect from the energy transferred to the bath into coherent displacement of the modes, we again compare it to the work done by driving the system. The latter is defined by Eq. (2.30). The energy flows between the different constituents of the total system $\mathcal{H}_{\mathrm{spin}}$, $\mathcal{H}_{\mathrm{int}} = \frac{\sigma^z}{2}R$ and $\mathcal{H}_{\mathrm{bath}}$ (cf. Eq. (2.1)) can be evaluated as

$$\dot{E}_{\mathrm{spin}} = -\frac{H}{2}\left(-v\sin(vt)\langle\sigma^z\rangle + v\cos(vt)\langle\sigma^x\rangle\right) - \left\langle\frac{\dot{\sigma}^z}{2}R\right\rangle, \tag{2.60a}$$

$$\dot{E}_{\mathrm{int}} = -\left\langle\frac{\sigma^z}{2}\dot{R}\right\rangle, \tag{2.60b}$$

$$\dot{E}_{\mathrm{bath}} = \left\langle\frac{\dot{\sigma}^z}{2}R\right\rangle + \left\langle\frac{\sigma^z}{2}\dot{R}\right\rangle. \tag{2.60c}$$

[2]For preparation (2), there will be an additional contribution to the total induced field, which stems from the fact that the system is not initialized in an eigenstate of the full Hamiltonian. This therefore corresponds to a contribution free contribution, which will however quickly be dissipated away for coupling to a bath, as described in [33].

Therefore (and in general), adapting Eq. (1.59),

$$W_{\mathrm{dr}} = -\frac{H}{2}\int_0^t \left(-v\sin(vt)\langle\sigma^z\rangle + v\cos(vt)\langle\sigma^x\rangle\right), \tag{2.61}$$

so that the work done by driving to the entire system can be determined from the spin dynamics.

For the dynamo energy, as in Sec. 2.2.2, we consider the energy stored in coherent displacement of the bath modes with their adiabatic displacement as a reference. This amounts to [33]

$$E_{\mathrm{dyn}}(t) = \sum_k \omega_k \left|\langle b_k(t)\rangle + \frac{g_k}{\omega_k}\frac{\langle\sigma^z(t)\rangle}{2}\right|^2. \tag{2.62}$$

From Eq. (2.51), we see that only the dynamic part of the induced field contributes to this quantity, as required. We can therefore write with Eq. (2.55):

$$\dot{E}_{\mathrm{dyn}}(t) = h_{\mathrm{dyn}}(t)\frac{\langle\dot{\sigma}^z(t)\rangle}{2}. \tag{2.63}$$

Using Eq. (2.58), we find

$$\Delta E_{\mathrm{dyn}} \approx \frac{\alpha\pi}{2}\int_0^t dt' \left\langle\dot{\sigma}^z(t')\right\rangle^2. \tag{2.64}$$

Furthermore, we can again identify from the energy balance (2.36),

$$E_{\mathrm{fluct}}(t) = \sum_k \omega_k\left(\left\langle\left(b_k(t)^\dagger + \frac{g_k}{\omega_k}\langle\sigma^z(t)\rangle\right)\left(b_k(t) + \frac{g_k}{\omega_k}\langle\sigma^z(t)\rangle\right)\right\rangle - \left|\langle b_k(t)\rangle + \frac{g_k}{\omega_k}\frac{\langle\sigma^z(t)\rangle}{2}\right|^2\right), \tag{2.65}$$

and if initially $E_{\mathrm{fluct}}(0) = 0$, the efficiency of the dynamo $\eta_{\mathrm{dyn}} = \frac{\Delta E_{\mathrm{dyn}}}{W_{\mathrm{dr}}} \leq 1$ for full periods of driving [33]. The energy stored in coherent displacement of the bath modes with the adiabatic displacement as a reference can be understood as work exchanged with the bath, which can be justified from considering the remainder of the energy variation of the bath as heat and showing that it fulfills the second law of thermodynamics [27, 33]. This justifies to speak of a work-to-work conversion through the dynamo effect. Note that from Eq. (2.63), the dynamo energy can be evaluated only from the spin evolution, as h_{dyn} can be evaluated from it equivalently. Therefore, we will in the following present techniques to solve for the spin dynamics of the driven spin-boson model we are considering.

2.3.2 Techniques to solve the spin dynamics

As described in Sec. 1.2.2, the study of a quantum system coupled to an environment has been a field of extensive interest for decades [76, 77, 79, 83, 154] and remains an active area of research (closely related also to the driven setup under study in this chapter, cf.

e.g. [32, 75, 150, 155, 156]). In this section we will discuss several approaches used to tackle this problem and show how (and under which conditions) they can be applied to the driven model under consideration. The employed techniques can roughly be clustered into four categories:

- Expressing the spin dynamics using a real-time path integral: This method, developed by Feynman and Vernon [76] allows to express the spin evolution as a sum over different spin paths, whose weight is determined by the influence functional arising when integrating over the bosonic degrees of freedom. This path integral can then be simplified:
  - Using what is called the non-interacting blip approximation (NIBA), an approximate analytic solution can be derived [64, 139, 141].
  - Treating the influence functional stochastically, a stochastic Schrödinger equation can be derived which then gives rise to a numerically exact method to solve for the spin dynamics [75, 137, 151].
- Exact solution by mapping to the Kondo model: The time-independent spin-boson model can be mapped to the anisotropic Kondo model [157] which has been solved by the Bethe ansatz [158]. This can give useful insights for certain limiting cases of the driven model as well.
- Master equations: The influence of an environment on a system at weak coupling can be treated using a Gorini-Kossakowski-Sudarshan-Lindblad (GKLS) master equation [61, 159]. In the studied case of a periodically driven system, this gives rise to a so-called Floquet-Markov master equation [33, 141]. This approach was developed by Cyril Elouard for the work published in [33] and we will in this thesis use it for a comparison. Below we will briefly discuss the assumptions made when using this technique.
- Exact diagonalization: Solving the Schrödinger equation governing the evolution of the full system can be attempted numerically, but is of course limited by the dimensionality of the Hilbert space quickly increasing when adding more degrees of freedom (i.e., more bosonic modes). This technique is thus limited to modelling a spin coupled to a small finite number of bosonic modes, but can nevertheless serve as a useful benchmark for other results [33].

We will describe these approaches in more detail and apply them to the radially driven spin-boson model in the following.

Expressing the spin dynamics using a path integral

The idea to express the evolution of a system (as the spin described in this chapter) coupled to an environment by a path integral goes back to Feynman and Vernon [76] and has consequently been applied to the spin-boson model [75, 79, 141, 160]. The approach consists of expressing an element of the reduced spin density matrix by a double path integral over classical spin paths using the so called influence functional [75, 76, 79]:

$$\langle \sigma_f | \rho_s(t) | \sigma_f' \rangle = \int \mathcal{D}\sigma \int \mathcal{D}\sigma' \mathcal{A}[\sigma] \mathcal{A}^*[\sigma'] \mathcal{F}[\sigma, \sigma']. \tag{2.66}$$

On the left hand side, an element of the reduced density matrix of the spin $\rho_s(t) = \mathrm{Tr}_{\mathrm{bath}} \rho(t)$ (i.e., the full density matrix of the entire system $\rho(t)$ with the bath degrees of freedom traced out) is determined using $|\sigma_f\rangle, |\sigma_f'\rangle \in \{|\uparrow\rangle, |\downarrow\rangle\}$. On the right hand side, this element is evaluated as a sum over classical spin paths $\sigma, \sigma' = \pm 1$ (reflecting the z-component of the spin under consideration). Intuitively, such a spin path can be thought of an evolution in time from $\sigma(\tau = 0) = \sigma_i$ to $\sigma(\tau = t) = \sigma_f$ via various spin flips. For the situation under consideration, initializing the spin in the state $|\uparrow\rangle$ corresponds to $\sigma_i, \sigma_i' = 1$ and evaluating the path integral in Eq. (2.66) for $\sigma_f, \sigma_f' = 1$ allows to evaluate the upper left element of the density matrix of the spin at time t. One would therefore consider spin paths from $\sigma_i = 1$ to $\sigma_f = 1$ only, thus necessarily involving an even number of spin flips.

The influence functional described by $\mathcal{F}[\sigma, \sigma']$ can be evaluated by integrating over the bosonic degrees of freedom and therefore encodes the influence of the bath on the spin dynamics. For a bath of quantum harmonic oscillators (as the one under consideration), it can be written in the form [75, 76, 79]

$$F[\sigma, \sigma'] = \exp\left(-\frac{1}{\pi} \int_{t_0}^{t} d\tau \int_{t_0}^{\tau} d\tau' [-iL_1(\tau - \tau')\xi(\tau)\eta(\tau') + L_2(\tau - \tau')\xi(\tau)\xi(\tau')] \right). \tag{2.67}$$

For this, we introduced the reparametrization $\eta(\tau) = \frac{1}{2}(\sigma(\tau) + \sigma'(\tau))$ and $\xi(\tau) = \frac{1}{2}(\sigma(\tau) - \sigma'(\tau))$ representing the symmetric and antisymmetric spin paths. The bath correlation functions are defined from [75]

$$\pi \langle R(t) R(0) \rangle = L_2(t) - iL_1(t), \tag{2.68}$$

and can be evaluated assuming a bath at equilibrium by

$$L_1(t) = \int_0^\infty d\omega J(\omega) \sin(\omega t), \tag{2.69a}$$

$$L_2(t) = \int_0^\infty d\omega J(\omega) \cos(\omega t) \coth\left(\frac{\beta\omega}{2}\right), \tag{2.69b}$$

where $R(t) = \sum_k g_k (b_k^\dagger + b_k)$ in our case. The functionals $\mathcal{A}[\sigma]$ encode the weight of a spin path under the free dynamics (i.e., given $\mathcal{H}_{\mathrm{spin}}$), where the field in z-direction contributes

through an offset, while the field in x-direction contributes by inducing spin flips and therefore allows to rewrite this path integral in the form of a double sum over spin flips.

In this framework, diagonal states in this double-path description (i.e., for which $\sigma = \sigma'$) are called 'sojourn' states corresponding to $\eta = \pm 1$ and $\xi = 0$, while off-diagonal states are called 'blip' states corresponding to $\xi = \pm 1$ and $\eta = 0$. Through the influence functional, a blip is coupled to all previous blips and sojourns, thus making the problem non-Markovian and difficult to solve[3]. In order to find analytical expressions for the elements of the density matrix, one thus has to resort to approximation schemes or numerical techniques. We briefly present both in the following, starting with the so called *non-interacting blip approximation (NIBA)* and consequently discussing a stochastic approach to tackle the spin dynamics from the real-time path integral in Eq. (2.66) numerically.

The non-interacting blip approximation (NIBA)

As the name suggests, the 'non-interacting blip approximation' (NIBA) consists in neglecting interactions between blips and blip-sojourn interactions except for neighboring ones in the influence functional Eq. (2.67) [64]. For a driven system, it leads to a set of equation describing the time evolution of the spin components [139, 141]:

$$\langle \dot{\sigma}^z(t) \rangle = \int_0^t dt' \left(K^{(-)}(t,t') - K^{(+)}(t,t') \langle \sigma^z(t') \rangle \right), \tag{2.70a}$$

$$\langle \sigma^x(t) \rangle = \int_0^t dt' \left(Y^{(+)}(t,t') + Y^{(-)}(t,t') \langle \sigma^z(t') \rangle \right), \tag{2.70b}$$

$$\langle \sigma^y(t) \rangle = -\frac{1}{H \sin(vt)} \langle \dot{\sigma}^z(t) \rangle, \tag{2.70c}$$

with the Kernels

$$K^{(+)}(t,t') = \Delta(t)\Delta(t') e^{-Q_2(t-t')} \cos(Q_1(t-t')) \cos(\zeta(t,t')), \tag{2.71a}$$

$$K^{(-)}(t,t') = \Delta(t)\Delta(t') e^{-Q_2(t-t')} \sin(Q_1(t-t')) \sin(\zeta(t,t')), \tag{2.71b}$$

and

$$Y^{(+)}(t,t') = \Delta(t)\Delta(t') e^{-Q_2(t-t')} \sin(Q_1(t-t')) \cos(\zeta(t,t')), \tag{2.72a}$$

$$Y^{(-)}(t,t') = \Delta(t)\Delta(t') e^{-Q_2(t-t')} \cos(Q_1(t-t')) \sin(\zeta(t,t')). \tag{2.72b}$$

The functions $Q_1(t)$ and $Q_2(t)$ are defined as the second integrals of the bath correlation functions $L_1(t)$ and $L_2(t)$ from Eqs. (2.69), which with an Ohmic spectral density ($J(\omega) =$

[3] In App. B.2.1, we rewrite the influence functional as Eq. (B.12), from which this is even more explicitly apparent.

$2\pi\alpha\omega e^{-\omega/\omega_c}$ according to Eq. (2.11)) and at $T = 0$ can be calculated as

$$Q_1(t) = 2\pi\alpha \arctan(\omega_c t), \tag{2.73a}$$
$$Q_2(t) = \pi\alpha \log\left(1 + \omega_c^2 t^2\right). \tag{2.73b}$$

For the specific time-dependence of the model under consideration from Eq. (2.1), we adapt $\Delta(t) = H\sin(vt)$ and $\zeta(t,t') = \int_{t'}^{t} dt'' H\cos(vt'')$. The Eqs. (2.70) can then be solved numerically, which is represented in Fig. 2.11 by the dotted lines.

Numerically exact stochastic approach

The influence functional in Eq. (2.67) can be evaluated numerically in a stochastic way [32, 75, 151] and therefore leads to a numerically exact method to evaluate Eq. (2.66). This involves expressing the influence functional as an average over many realizations of a stochastic field encoding the properties of the bath. Consequently, one can derive a stochastic Schrödinger equation for the reduced spin dynamics, thus allowing to determine the spin expectation values from an average over many realizations of this stochastic field. Details of this method are presented in App. B.2. The derivation presented there is justified in the limit where $\omega_c \gg H$ and $0 \leq \alpha < \frac{1}{2}$ [75, 79, 151].

This stochastic approach has been developed first for a spin-boson model with constant fields (i.e., a time-independent spin Hamiltonian) [75], where the results can be compared to analytical results. It has been shown that the results converge for sufficiently many realizations of the stochastic field to the correct time evolution of the spin expectation values [75]. The approach has consequently been adapted to time-dependent spin Hamiltonians [32, 137] and proven its versatility in the study of systems composed of two spins as well [138]. It allows to account for the effect of the influence functional in Eq. (2.66) in a numerically exact way [75]. Here, we use it to evaluate the driven dissipative dynamics of a spin-1/2 coupled to a bath in order to extract thermodynamic properties with regards to the quantum dynamo effect [33]. Furthermore, we benchmark the method in the driven case employing the following comparisons:

1. In the case of slow driving, i.e., a quasi-static evolution, the state of the spin should approach the ground state of the combined system. For this, we can compare to the exact solution of the model coming from a mapping to the anisotropic Kondo model. This will be discussed in the following and good agreement is seen in Fig. 2.8.

2. We compare the results from the stochastic approach to the NIBA results and discuss how the agreement between the two approaches is related to the limits of validity of the NIBA, which is shown in Fig. 2.11.

3. Finally, we also compare the results to an ED approach developed in [33], representing

the bath using a finite number of modes. This is shown in Fig. 2.10 and gives good qualitative agreement notably also for stronger coupling and larger driving velocities.

Mapping to the anisotropic Kondo model

There is an interesting correspondence between the Ohmic spin-boson model under consideration and the anisotropic Kondo model [157, 161]. This correspondence enables us to use exact results obtained for the Kondo model as a benchmark for our consideration of the driven spin-boson model, which we are going to use here. The time-independent spin boson model, i.e., Eq. (2.1) with

$$\mathcal{H}_{\text{spin}} = -\frac{\Delta}{2}\sigma^x - \frac{\epsilon}{2}\sigma^z, \tag{2.74}$$

can be mapped to the anisotropic Kondo model of a spin interacting with a fermionic bath [79, 80, 157, 161–163]. The Kondo model can be solved using the Bethe ansatz [158]. In particular, for $1-\alpha \gg \omega_c/\Delta$ and with only a small bias field ϵ acting on the spin, one can derive scaling forms of the spin expectation values. The results thus obtained are then valid for the driven model around the equator, i.e. when $vt = \pi/2 + n\pi$ with $n \in \mathbb{N}$ and for quasi-adiabatic driving speed. The dynamics is then controlled by the Kondo scale $T_K = \Delta\,(\Delta/D)^{\alpha/(1-\alpha)}$ [163] which has a similar form as the renormalized tunneling element from Eqs. (1.57) and (2.12). The high-energy cut-off D is related to ω_{c} by [145]

$$\left(\frac{D}{\omega_{\text{c}}}\right)^{2\alpha} = \frac{2\Gamma(3/2-\alpha)e^{-b}}{\sqrt{\pi}(1-2\alpha)\Gamma(1-2\alpha)\Gamma(1-\alpha)}, \tag{2.75}$$

with $b = \alpha\log(\alpha) + (1-\alpha)\log(1-\alpha)$. The observables then take the form [163]

$$\langle\sigma^x\rangle \approx \frac{1}{2\alpha-1}\frac{\Delta}{\omega_{\text{c}}} + C_1(\alpha)\frac{T_K}{\Delta}, \tag{2.76}$$

$$\langle\sigma^z\rangle \approx -\frac{2\,\mathrm{e}^{\frac{b}{2(1-\alpha)}}}{\sqrt{\pi}}\frac{\Gamma[1+1/(2-2\alpha)]}{\Gamma[1+\alpha/(2-2\alpha)]}\left(\frac{\epsilon}{T_K}\right), \tag{2.77}$$

where $C_1(\alpha) = \frac{e^{-b(2-2\alpha)}}{\sqrt{\pi}(1-\alpha)}\frac{\Gamma(1-1/(2-2\alpha))}{\Gamma(1-\alpha/(2-2\alpha))}$. These expressions allow for a comparison to the results from other approaches at the equator with $\theta = \pi/2$ or $t = \pi/(2v)$. A comparison of numerical results from the stochastic approach with quasi-adiabatic driving speed with Eq. (2.76) is shown in Fig. 2.8 and shows good agreement. In Sec. 2.3.3 we show similar results in Fig. 2.12a) for various driving speeds, showing changed behaviour at the equator for larger driving speed. Note that from the adiabaticity condition in Eq. (2.13), not only an increasing velocity, but also a decreased renormalized tunneling element Δ_r can lead to a breakdown of adiabaticity[4] and therefore to a deviation from the equilibrium result from

[4]The renormalized tunneling element decreases when α increases, cf. Eq. (2.12)

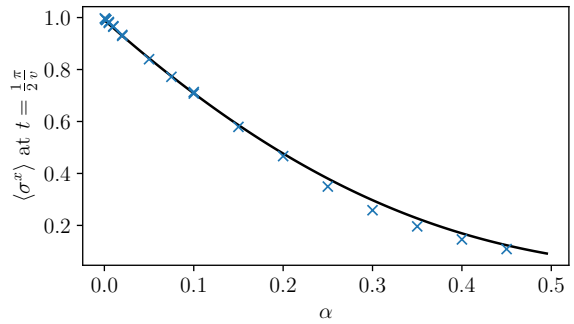

Figure 2.8: Comparison of the analytical result from Bethe ansatz in Eq. (2.76) with results for $\langle\sigma^z\rangle$ at $t = \pi/(2v)$ from the stochastic approach (see above and in App. B.2) with quasi-adiabatic driving speed $v = 0.04$ and $H = 1.0$ and the high-freqeuncy cut-off is at $\omega_c/H = 100.0$. For the stochastic approach, here we used a time step $\Delta t/t = 2^{-11}$ and averaged over $6 \cdot 10^5$ realizations of the stochastic field (cf. App. B.2).

the Bethe ansatz. The plot of Δ_r as a function of α shown in Fig. 2.12b) for comparison confirms that when the adiabaticity condition is not met, the results start to deviate.

The result in Eq. (2.76) predicts notably that at the equator, the expectation value $\langle\sigma^x\rangle$ will be decreased from its free value due to entanglement with the bath, which is confirmed from the numerical results.

GKLS Master equation

Another common approach to study the evolution of a quantum system coupled to its environment is to derive a Master equation for the evolution of the reduced system density matrix. A common type of such master equations describing the open system dynamics is the GKLS equation of the form [33, 61, 164]

$$\dot{\rho}_S = -i[\mathcal{H}_S(t) + \mathcal{H}_{\mathrm{LS}}(t), \rho_S] + \sum_i \mathcal{L}_i \rho_S, \tag{2.78}$$

where ρ_S is the reduced density matrix of the system, $\mathcal{H}_S(t)$ is the Hamiltonian of the system and $\mathcal{H}_{\mathrm{LS}}(t)$ is a Lamb-shift operator accounting for a renormalization of the unperturbed energy levels of the system Hamiltonian due to the coupling to the environment [61]. The last term in Eq. (2.78) accounts for different dissipative processes where we defined $\mathcal{L}_i \rho_S = \gamma_i \mathcal{D}[X_i]$ with the rate γ_i and the dissipation superoperator [33]

$$\mathcal{D}[X_i]\rho_S = X\rho_S X^\dagger - \tfrac{1}{2}(X^\dagger X\rho - \rho X^\dagger X).$$

Such an equation has been derived for the radially driven spin-boson model from microscopic grounds in [33] by Cyril Elouard. Since in the following, we will compare to these results, we describe some key results here and refer to [33] for the details. In the case under consideration, there are dissipative processes corresponding to relaxation and pure

dephasing. In the derivation and discussion, it is beneficial to switch to the frame rotating with the spin, in a similar way as described by the transformation in Eq. (2.5). Without coupling to the bath, the spin has two periodic orbits. Relaxation processes are associated with transitions to the energetically lower lying orbit. These processes have a rate proportional to $J(\Omega \pm v)$ (where $\Omega = \sqrt{H^2 + v^2}$ as defined in Sec. 2.1) and are thus associated to bath modes at frequencies $\Omega \pm v$. In addition, there are processes corresponding to pure dephasing in the basis of the two periodic orbits, associated to bath modes at frequency v. Interestingly, these processes yield a stable solution in the long-time limit that reads [33]

$$\langle \sigma^x(t) \rangle = \frac{H}{\Omega} \sin(vt), \tag{2.79a}$$

$$\langle \sigma^y(t) \rangle = \frac{v}{\Omega}, \tag{2.79b}$$

$$\langle \sigma^z(t) \rangle = \frac{H}{\Omega} \cos(vt). \tag{2.79c}$$

These results suggest that in the long time limit, the spin dynamics is stabilized along a periodic orbit on the Bloch sphere. Eqs. (2.79) are formally close to the free dynamics for slow driving (i.e., Eqs. (2.8)), with the difference that a finite constant y-component is acquired and the amplitudes in x- and y-directions are in turn reduced as a manifestation of dissipation. In the limit in which the GKLS equation works, the secondary oscillations are smoothed out after a long-time evolution, which is also seen from the numerical results in Figs. 2.11b) and e)[5]. The approximations usually made to derive the GKLS equation in the form of Eq. (2.78) are [61]:

- The *Born approximation*, which assumes that the coupling between the spin and the bath is weak, so that the total density matrix can be written as a tensor product of the density matrices of the two constituting subsystems, i.e.,

$$\rho \approx \rho_{\text{spin}} \otimes \rho_{\text{bath}}. \tag{2.80}$$

- The *Markov approximation*, which assumes that the observables of the environment vary on a much shorter time-scale than the spin.

- The derivation of the GKLS master equation usually takes place in the interaction picture. The *secular approximation* assumes that the evolution of the spin can be averaged over rapidly oscillating components (so-called *non-secular terms*) in the interaction picture, meaning that only those components varying slowly contribute to the dynamics.

[5] There we show the full solution of the GKLS approach, i.e., without taking the long-time limit, as developed in [33]

In the present model, these approximations require $J(\Omega \pm v),\ J(v) \ll k_B T \ll v, H, \omega_c$ [33]. This means that in order to ensure the derivation, the bath temperature T is non-zero, yet much smaller than the spin frequency and the driving velocity. This constitutes a key difference to the other approaches described in this section, with which we study the dynamics at zero temperature. According to these conditions, we expect agreement of the results from this approach with the other approaches at very weak coupling and higher velocities.

Exact diagonalization with a finite number of modes

To have a benchmark for the results with a continuous bath, we first consider a setup in which we can obtain numerical results through exact diagonalization: Considering a finite number of bath modes, in which we represent a part of the continuous spectrum by one discrete bosonic mode allows to evaluate the exact eigenstates and thus access all observables of the spin and the bath directly. In practice, we fix the couplings g_k from an Ohmic spectral density with a hard high-frequency cut-off ω_c:

$$J(\omega) = \begin{cases} 2\pi\alpha\omega & \omega \leq \omega_c \\ 0 & \omega > \omega_c. \end{cases} \tag{2.81}$$

Discretizing the spectral density, we then identify $g_k^2 = 2\alpha\omega_k\Delta\omega_k$ where $\Delta\omega_k$ is the width of the part of the spectrum that is represented by the mode k. The induced field on the spin is then given by Eq. (2.16), and the contribution for each mode is described by Eq. (2.22) (with $\omega \to \omega_k$ and $g \to g_k$), so that for weak coupling and slow driving, Eq. (2.23) equivalently holds. Therefore, also the approximations for modes with frequencies far below, far above and at resonance (cf. Eqs. (2.24)-(2.26)) hold and we see that the induced field will be dominated by the large frequency contributions, as those constitute the biggest part of the spectrum for slow driving.

Using the approximation $\langle\sigma^z(t)\rangle \sim \cos(vt)$ and a spectral density as in Eq. (2.81), we can integrate the contributions from Eq. (2.23) and obtain for $t > 0$ and $\omega_c t \gg 1$ [33]

$$h(t) = -\alpha\cos(vt)\left(2\omega_c + v\log\left(\frac{\omega_c - v}{\omega_c + v}\right)\right) - \alpha\pi v\sin(vt) \approx -2\alpha\omega_c\cos(vt) - \alpha\pi v\sin(vt), \tag{2.82}$$

where the last approximation is justified if $\omega_c \gg v$.

This result is consistent with Eqs. (2.59) obtained for an exponential cut-off, so we conclude that in this limit the induced field is the same for an Ohmic spectral function with an exponential and a hard cut-off in the continuum limit. In general, as discussed in Sec. 1.2.2 and App. D.1, the high-frequency modes equilibrate quickly and lead to a renormalization of the tunneling element, so as long as the normalization of the spectral

function remains fixed one thus not expect a big influence on the exact form of the cut-off. In particular, the form of the renormalized tunneling element can be evaluated with a hard cut-off to the same expression as given in Eq. (1.57) for an exponential cut-off. However, when working with the two forms of the spectral function in other setups and in order to evaluate other observables, one should always analyze the influence on the high-frequency part of the spectrum carefully.

Having discussed these techniques to study the spin dynamics in the presence of a bath, we will in the following show and discuss the results they yield.

2.3.3 Results for the Dynamo effect

Using the results of Secs. 2.3.1 and 2.3.2, we are in a position to study the dynamo effect numerically and analytically from the spin dynamics.

Exact diagonalisation

We will first check the consistency of the ED approach discussed above. Numerically, we can check that the contributions from modes with different frequencies are consistent with the analytic results from Eqs. (2.24)-(2.26) and that the total induced field at slow driving and weak coupling is given by Eq. (2.82). This is shown in Fig. 2.9a). As expected, we observe that the dominant contribution to the induced field (coming from the high-frequency modes equilibrated to the spin) tends to follow the spin. However, for the resonant mode, there is still a field opposing the change of the spin, i.e., the induced field coming from this particular mode has a large dynamic contribution. Since the contribution of this field to the total field is small, it also influences the spin to a smaller extent as was the case for the coupling to only one mode. We thus observe a contrast for the dynamo effect comparing the coupling of a spin to one and to many modes: In both cases, there is a dynamically induced field in the resonant mode, but when there is a broad spectrum of modes with (mainly) high frequency, those can effectively protect the spin dynamics from the effect of the dynamo field and therefore stabilize it. This then leads to an equivalent stabilization of the dynamo effect, which requires a rotation of the spin. In fact, we observed for the one mode dynamo in Sec. 2.2 that freezing of the spin leads to a diminution of the dynamo effect. The protection of the dynamo effect for coupling to a larger number of modes can be observed in Fig. 2.9b) from the definition of the dynamo energy in Eq. (2.62) and the associated efficiency with respect to the work done by driving the system, as defined in Eq. (2.30). Using exact diagonalisation, the observables of the bosonic modes can be evaluated and summed directly.

After every half period (i.e. at times $t = n\pi/v$ with $n \in \mathbb{N}$), the dynamo reaches large efficiencies (inset of Fig. 2.9b)), while in the same time the depth of the intervening valleys is decreasing. Instead of breaking down, the efficiency now approaches unity for longer

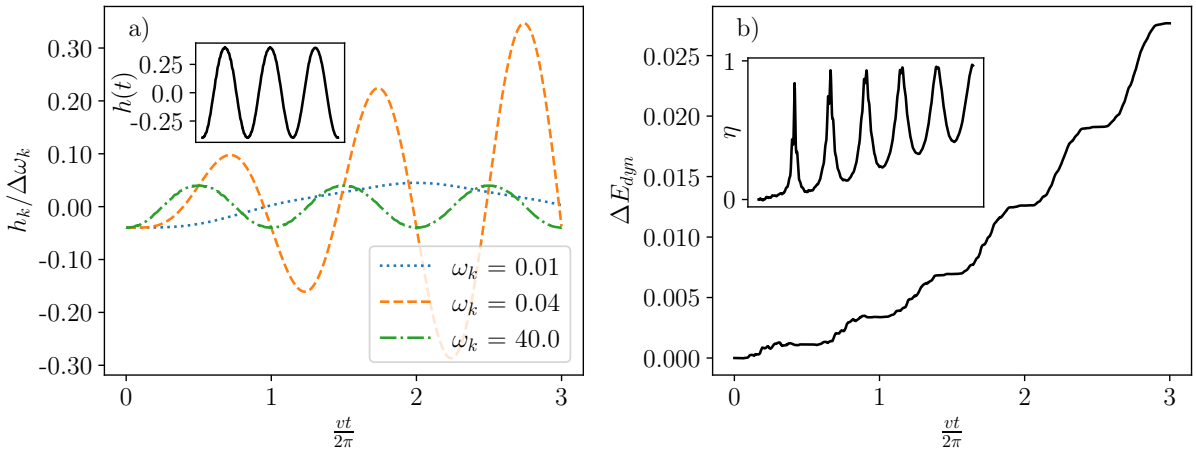

Figure 2.9: From [33]. Results from ED for a spin coupled to twelve modes with frequencies from 0.0 to 100.0 and a (discretized) linear spectral function with cut-off at $\omega_c/H = 100.0$ and a small coupling corresponding to $\alpha = 0.02$. The spin is driven with velocity $v = 0.04$ and the magnitude of the external field is $H = 1.0$. The Hilbert space of each mode is truncated above its maximal occupation. a) The induced field for three different modes. In the inset, the summed induced field is shown which is dominated by the high frequency modes. b) The dynamo energy ΔE_{dyn} and in the inset the efficiency η.

times, supporting the claim of a stabilisation of the dynamo effect. In a consistent way, the dynamo energy in this regime increases and dominates the energy of fluctuations, which we analyze in Appendix C.

The results for coupling to a finite number of modes hint how the dynamo effect can be understood for coupling to a continuous environment, in which we expect a similar protective effect of the high-frequency modes. This will be discussed in the follwong. We will first present different results found from the previously discussed approaches to solve the spin dynamics and consequently analyze the performance of the dynamo we find from them.

Comparison of results for spin dynamics for coupling to a bath

In this section, we will present and discuss results for the driven spin dynamics coupled to a bath, comparing the different approaches presented before:

- The numerical results from exact diagonalization.
- The stochastic approach (numerical results).
- The NIBA (numerical solution of the analytical Eqs. (2.70)).
- The analytical result from mapping to the anisotropic Kondo model at the equator for slow driving. In particular, we will compare Eq. (2.76) to the results of the stochastic approach at the equator.

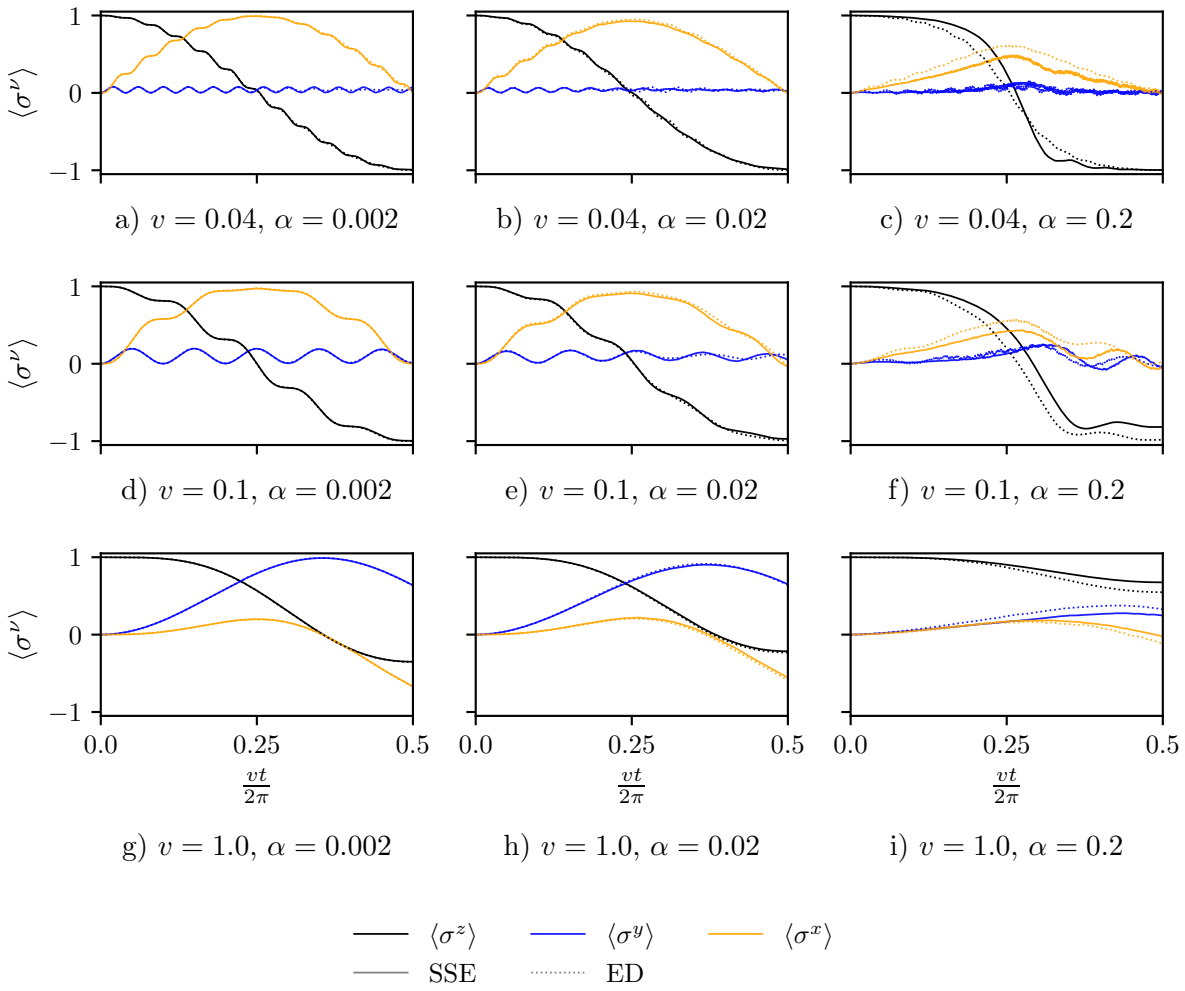

Figure 2.10: From [33]. Comparison of numerical results between ED (dotted line) and stochastic approach (solid line). The expectation values of $\langle\sigma^z\rangle$, $\langle\sigma^y\rangle$ and $\langle\sigma^x\rangle$ are shown in black, blue (gray) and yellow (light gray) in this order. Here, $H = 1.0$ and $\omega_c/H = 100.0$. For the ED result, we discretized the spectrum with a hard cut-off at ω_c into ten modes. Their Hilbert space was truncated such that the maximal occupation is well below the truncation.

- The results from the GKLS equation.

First, let us compare the results from ED to results obtained using the stochastic approach. The numerical results are shown in Fig. 2.10. We see that for all shown velocities, the ED agrees very well with the stochastic approach at weak coupling. At stronger coupling, there are deviations between the two but still there is qualitative agreement. For an increasing number of modes simulated in the ED, one would expect the results to correctly model the physical system under consideration. The results in Fig. 2.10 show that for small to intermediate coupling the results from ED with a small number of modes agree very well with the stochastic approach and therefore give an indication that on a qualitative level, both approaches in the considered range of parameters correctly reproduce the physical situation. Note that both approaches differ in the way how a

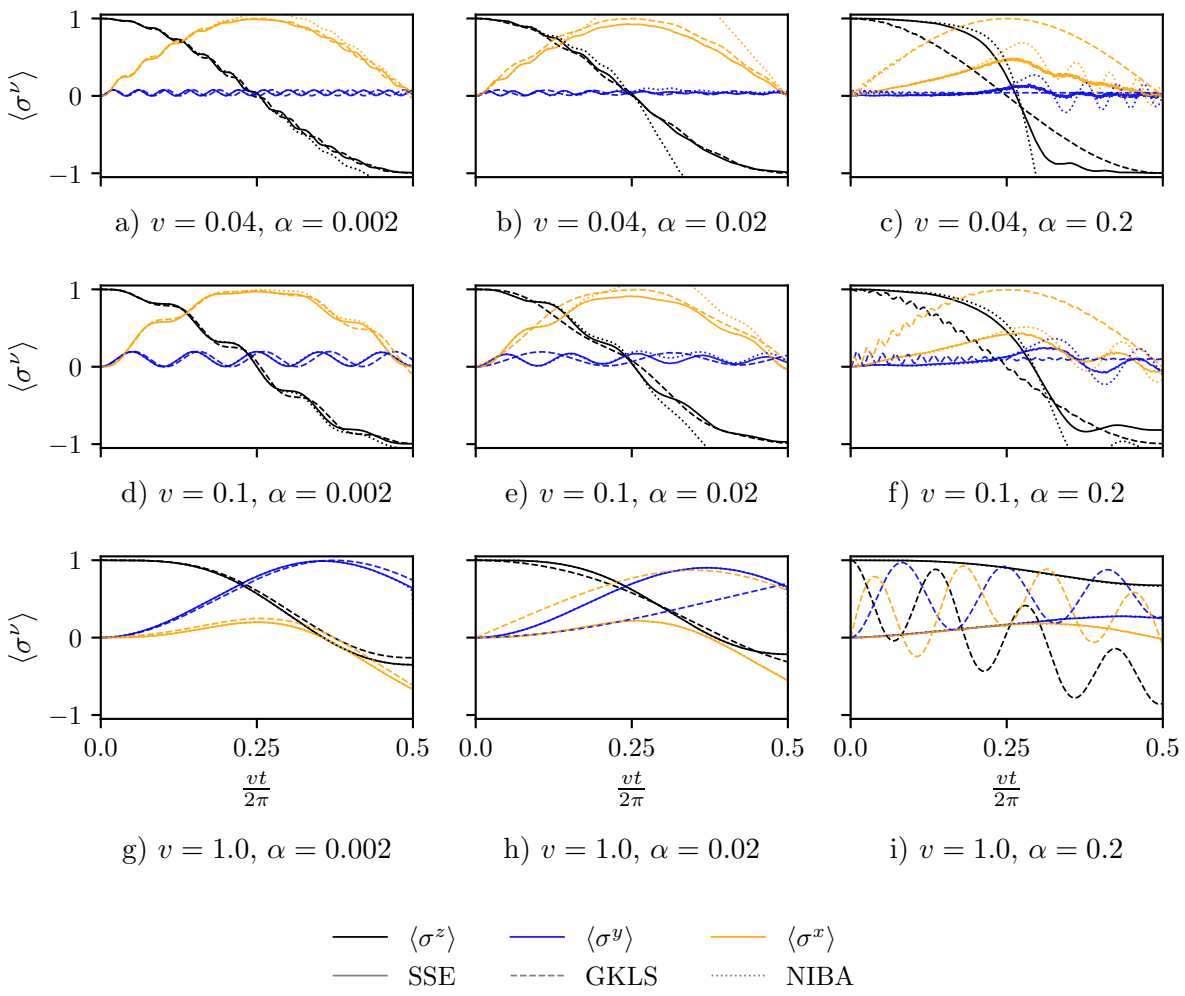

Figure 2.11: From [33]. Comparison of numerical results between stochastic approach, NIBA and GKLS approach. The expectation values of $\langle\sigma^z\rangle$, $\langle\sigma^y\rangle$ and $\langle\sigma^x\rangle$ are shown in black, blue and yellow in this order. Solid lines represent results from the stochastic approach, dashed lines represent results from the GKLS approach and dotted lines represent results from the NIBA. The chosen parameters are similar to those from Fig. 2.10.

cut-off is introduced to the spectral function. While the stochastic approach has been implemented with an exponential cut-off (i.e., a spectral function of the form of Eq. (2.11)), we use a hard cut-off (cf. Eq. (2.81)) in the ED for practical reasons. As we showed from Eq. (2.82), on an analytical level the results for the induced field coincide for small velocities and from the results in Fig. 2.10 we observe qualitative agreement also for larger velocities.

Next, let us compare results for the spin expectation values from the stochastic approach, the theoretical prediction from the NIBA and the GKLS master equation approach in Fig. 2.11. At quasi-adiabatic to intermediate driving speeds and at small coupling $\alpha = 0.002$, the spin follows the drive and shows secondary oscillations with period Ω, which is consistently reflected in the results of all three approaches. The secondary oscillations are with time increasingly suppressed which leads to a smoothing of the spin

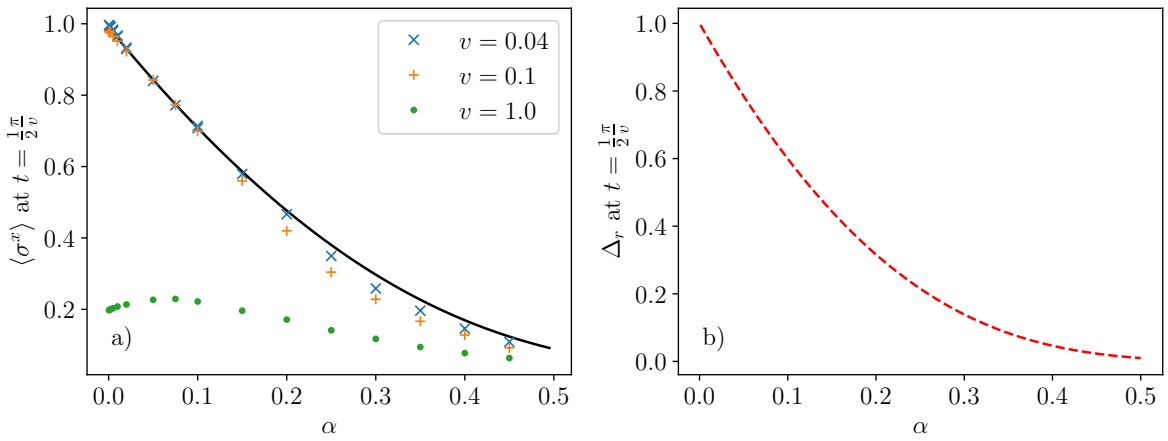

Figure 2.12: Adapted from [33]. a) Comparison of the SSE results at $t = \pi/(2v)$ (Different markers represent different velocities) with the result from Bethe ansatz Eq. (2.76) (solid line) for different velocities. We see that for quasi-adiabatic velocities, the value of $\langle \sigma^x \rangle$ at $t = \pi/(2v)$ agrees with the equilibrium theory, while for larger velocities and coupling strengths there are non-adiabatic effects. Except for the velocities giving in the legend, the parameters are the same as in Fig. 2.8. b) Visualization of Eq. (2.12) showing Δ_r for the parameters used in a) at the equator (i.e., $t = \pi/(2v)$) as a function of α.

dynamics. The expectation value $\langle \sigma^y \rangle$ approaches a constant value. The results from the NIBA start deviating when approaching $t = \pi/v$, i.e., when the external field is mainly pointing in x-direction. This is in agreement with the limit of validity of the NIBA, which cannot be justified for a large transverse field (compared to the bias field).

At $t = \pi/(2v)$ and for intermediate coupling strength (i.e., $\alpha = 0.02$), the external field points in x-direction and we find $\langle \sigma^x \rangle < 1$ from the stochastic approach, which is not captured by the NIBA and the GKLS approach. However, this was predicted by Eq. (2.76) from the mapping with the Kondo model and reflects the entanglement of the spin-bath ground state. In contrast, such an entanglement is neglected within the GKLS equation which assumes weak system-bath coupling. The comparison of the results from the stochastic approach to this formula is shown in Fig. 2.12 for different velocities, which demonstrates remarkable agreement at quasi-adiabatic driving speed.

For a larger coupling ($\alpha = 0.2$), the dynamics revealed by the stochastic approach differ: Secondary oscillations in $\langle \sigma^z \rangle$ are smoothed out and the shape of the curve is altered. Intuitively, this can be understood by the changed ground state with the renormalized tunneling element (given in Eq. (2.12)) due to the bath. Navigating adiabatically from the north to the south pole with a Hamiltonian

$$\mathcal{H} = -\frac{H}{2}\cos(vt)\sigma^z - \frac{\Delta_r(t)}{2}\sigma^x,$$

we can find the expectation value $\langle \sigma^z \rangle$ from the adiabatic ground state which leads to a qualitatively correct prediction in the range of α at question.

Note that from the Heisenberg equation of motion, we have $\langle \dot{\sigma}^z(t) \rangle = -H \sin(vt) \langle \sigma^y(t) \rangle$. It is interesting to observe that $\langle \sigma^y \rangle$ stays close to zero initially due to a smoothing of secondary oscillations in $\langle \sigma^z \rangle$ corresponding to a suppression of non-adiabatic effects, but then exhibits a "bump" around time $t = \pi/2v$. The expectation value $\langle \sigma^x \rangle$ approaches its unbiased value described by Eq. (2.76) in an almost linear fashion which close to the north pole is captured by the NIBA solution. We note that already at intermediate coupling, the GKLS approach breaks down, as a consequence notably of the assumption of a product state formed by the spin and the bath.

Finally, for higher velocities $v = H = 1.0$, at small values of α, the dynamics of $\langle \sigma^z \rangle$ is captured by the GKLS approach and agrees with the results of the stochastic approach. At higher values of α the two approaches start to differ but interestingly the NIBA now makes matching predictions throughout the half period of the drive shown in the figure. One of the situations in which the NIBA is working well is that of a large field in z-direction [139, 141]. We can thus hypothesize, that a large field is induced back onto the spin for the entire time of the drive due to the non-adiabatic response at larger velocities. We will make the nature of the induced field more explicit in the following section.

Dynamo performance

Using the results for the spin dynamics and its relation to the (dynamically) induced field in Eq. (2.58), we can now evaluate the dynamo energy (cf. Eq. (2.64)) and the work done by driving (cf. Eq. (2.61)) and thus the performance of the quantum dynamo for a driven spin coupled to a continuous bath. For the ED results, we already saw in Fig. 2.9 that at an intermediate coupling strength, the efficiency of the dynamo approaches unity in the long time limit.

In Fig. 2.13a), we show results from the numerically exact stochastic approach for a similar process as in Fig. 2.4c) for one mode but now with a continuous bath: Driving the system for half a period (from $t = 0$ to $t = \pi/v$), we numerically evaluate the work done to perform the drive and the averaged output power $\Delta E_{\mathrm{dyn}}(t_f)/t_f$. We then plot the ratio η against the averaged output power for different driving velocities. The result is qualitatively similar to the situation of one mode in the sense that for slow driving, we can reach a large conversion ratio at relatively small averaged output power. Increasing the velocity, we can increase the averaged output power at the cost of efficiency of this conversion mechanism. In Fig. 2.13b), we show the averaged output power as a function of the coupling strength α, for comparison.

Comparing Figs. 2.4c) and 2.13a), we note that for the same velocity, the maximally attained output power is higher (in absolute numbers) for the one-mode dynamo than for coupling to the Ohmic bath. This is related to a dilution of the effect: When coupling to

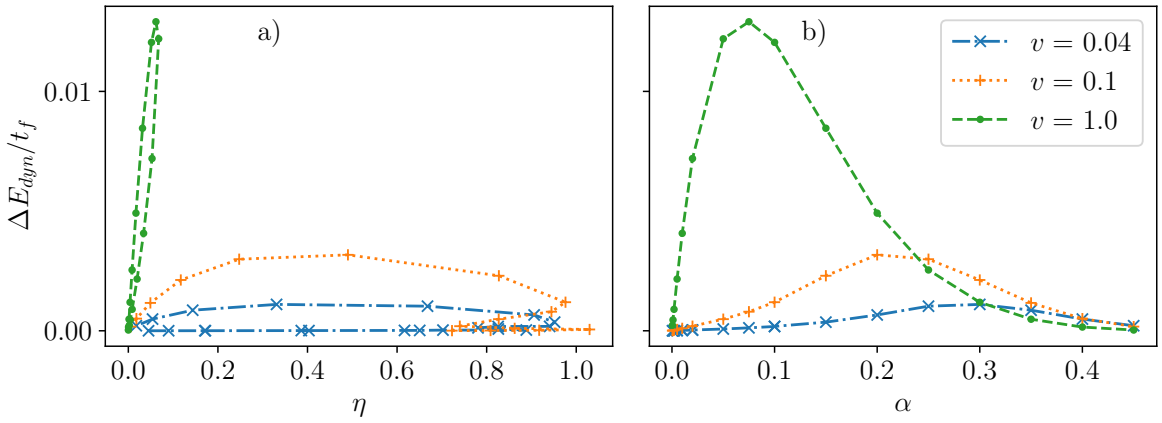

Figure 2.13: Adapted from [33]. a) Parametric plot of the averaged output power $\Delta E_{\rm dyn}(t_f)/t_f$ at $t_f = \pi/v$ as a function of $\eta = \Delta E_{\rm dyn}(t_f)/W_{\rm dr}(t_f)$ from results of the stochastic approach. b) The averaged output power as a function of α for comparison. Here, $H = 1.0$, $\omega/H_c = 100.0$ and α varies between 0.0 and 0.45.

many modes, the off-resonant modes can consume a fraction of the work done by driving[6].

We observe from Fig. 2.13 that at larger coupling, the dynamo effect breaks down with the averaged output power going to zero. Compared to the situation for one mode, the mechanism leading to this breakdown is different: Recall that for one mode, the dynamically induced field by a resonant mode becoming too strong fixes the spin, consequently leading to a breakdown of the dynamo effect. In a setup with a coupling to a continuous bath, according to Eq. (2.58) the dynamically induced field is still small compared to the driving field when the dynamo breaks down. Therefore, the mechanism is different in this case. As pointed out in [32], when coupling to a bath, the spin gets fixed for larger values of the coupling due to the creation of strong entanglement between the spin and the bath. This is consistent with the fact that at strong coupling, the fluctuation energy defined in Eq. (2.65) grows larger than the dynamo energy and contribute to the breakdown of the effect. A more detailed analysis of the latter is provided in App. C. Both for coupling to one resonant mode, as well as to a bath, the effect breaks down when the spin expectation value is fixed for a full period of the driving. For coupling to one mode, there is a direct connection between the dynamically accessed topology and the dynamo energy through Eq. (2.46). For the case of a coupling to continuous bath, we will discuss topological properties of the dynamo effect in Sec. 2.3.4.

When operating the dynamo for a longer time, the spin dynamics is protected by the field of the high-frequency modes which tend to follow the spin and by that keep the influence of the dynamically induced field small. While for coupling to one mode, a large dynamo field could build up over time (with an amplitude increasing linearly in time), at weak coupling the dynamo with a continuous bath shows a different behaviour with a

[6]We discuss this in more detail in the App. C

growing field only at the resonant mode.

The stochastic approach is based on the sampling of a stochastic field whose properties depend on the bath correlation and consequently requires to solve a stochastic Schrödinger equation in time, making it computationally expensive for long times. Therefore, the long time limit is more suitbaly adressed using the GKLS approach thanks to the convenient periodic orbit solution from Eqs. (2.79), valid at weak coupling at long times. The interaction with the drive in the formalism developed in [33] by Cyril Elouard can be thought of an emission of quanta with energy v. In the long-time limit, only the dephasing processes are active, for which the rate is $\gamma_{\text{deph}} = J(v)H^2/8\Omega^2$. Therefore, the work provided by the drive can be evaluated as [33]

$$W_{\text{dr},t\to\infty} = \int_0^t dt' v \frac{H^2}{8\Omega^2} J(v) = \pi\alpha v^2 t \frac{H^2}{4\Omega^2}. \tag{2.83}$$

On the other hand, the change in dynamo energy, using the periodic orbit solution in Eq. (2.79) can be evaluated from Eq. (2.64) as

$$\Delta E_{\text{dyn}} = \frac{\alpha\pi}{2}\frac{H^2v^2}{\Omega^2}\int_0^t dt' \sin^2(vt') = \frac{\alpha\pi}{2}\frac{H^2v^2}{\Omega^2}\frac{1}{2}\left(t - \frac{\sin(2vt)}{2v}\right) \xrightarrow[t\to\infty]{} \pi\alpha v^2 t\frac{H^2}{4\Omega^2}. \tag{2.84}$$

We see that this approach predicts a unit efficiency of the dynamo effect for long times. In the following, we will try to connect these results to the (effective) topological properties of the spin in a similar way as in Sec. 2.2.3 for one mode.

2.3.4 Topological properties

In this section, we will discuss inhowfar the results from Sec. 2.2.3 regarding the topological properties of a spin coupled to a single bosonic mode can be extended to the situation with a coupling to a continuous bath. It should be mentioned that general topological properties of a spin coupled to a bath have been discussed in [32]. One effect we can observe from Figs. 2.11 and 2.10 is the concentration of Berry curvature around the equator when coupling to a bath. This shows in the numerical results through a 'bump' in the expectation value $\langle\sigma^y\rangle$ around $t = \pi/(2v)$. In fact, $\langle\sigma^y\rangle$ has been used in experiments to measure the Chern number [35, 37], as it is related to the Berry curvature through [32, 34]

$$\frac{1}{2}\sin(vt)\langle\sigma^y(t)\rangle = \frac{v}{H}\mathcal{F}_{\phi=0,\theta} + \mathcal{O}\left(\frac{v^2}{H^2}\right). \tag{2.85}$$

The definition of C_{dyn} in Eq. (2.9) is actually equivalent to

$$C_{\text{dyn}} = \int_0^{\pi/v} dt \mathcal{F}_{\phi\theta(t)} = \frac{H}{2v}\int_0^{\pi/v} dt \sin(vt)\langle\sigma^y(t)\rangle. \tag{2.86}$$

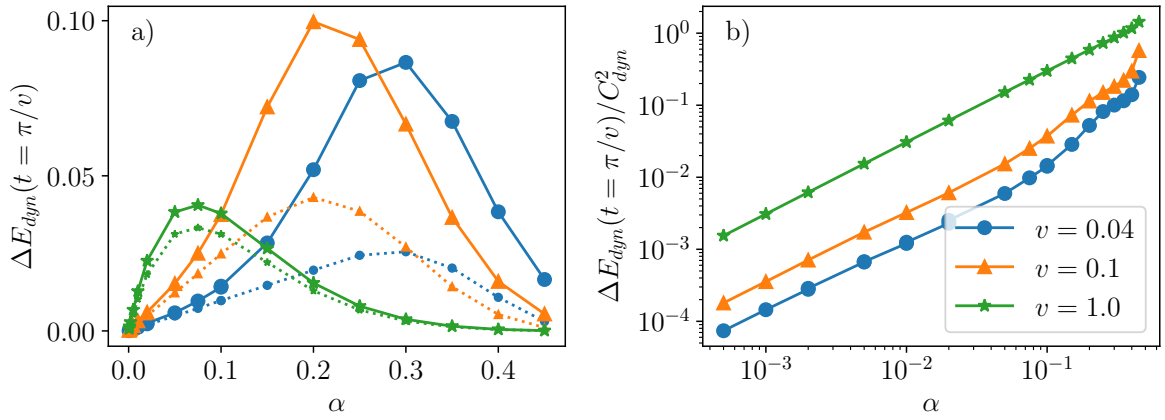

Figure 2.14: a) From [33]. The dynamo energy for coupling to a continuous bath after a drive from north to south pole from the stochastic approach (markers connected by solid lines) and from Eq. (2.89) with $C_{\rm dyn}$ evaluated from the same results of the stochastic approach (markers connected by dotted lines). b) Double logarithmic plot of $\Delta E_{\rm dyn}(t = \pi/v)/C^2_{\rm dyn}$ as a function of α from SSE, showing a linear relation, with deviations when $\alpha \to \frac{1}{2}$ and a velocity dependent offset. Here, $H = 1.0$ and $\omega_c/H = 100.0$.

Besides these general properties, we can also relate the properties of the dynamo effect to the dynamically accessed topology: Integrating Eq. (2.58) over half a period of the driving, we immediately find

$$\int_0^{\pi/v} h_{\rm dyn}(t) = 4\pi\alpha C_{\rm dyn}, \tag{2.87}$$

i.e., the integral of the induced field over half a period of the driving is proportional to the dynamically accessed Chern number. Note that assuming the adiabatic free spin dynamics $\langle\sigma^z(t)\rangle \sim \cos(vt)$ and using Eq. (2.58) for the dynamically induced field, we can evaluate the dynamo energy $\Delta E_{\rm dyn}$ accumulated between $t = 0$ and $t = \pi/v$ from Eq. (2.33) and find

$$\Delta E_{\rm dyn} = \frac{\alpha\pi^2 v}{4}. \tag{2.88}$$

Numerical results from the SSE approach are provided in Fig. 2.14. At small $\alpha \ll 1$, they suggest an extension of (2.88) as

$$\Delta E_{\rm dyn} \sim \frac{\alpha\pi^2 v}{4} C^2_{\rm dyn}. \tag{2.89}$$

For larger α, the graphs from numerical results and results using Eq. (2.88) deviate in Fig.2.14a), but interestingly the breakdown of the dynamo effect is still related to $C^2_{\rm dyn}$. This can be seen from Fig.2.14b), where we show a double logarithmic plot of the change in dynamo energy divided by $C^2_{\rm dyn}$ as a function of α. The results suggest that up to a velocity-dependent prefactor, Eq. (2.89) displays the correct dependence between $\Delta E_{\rm dyn}$,

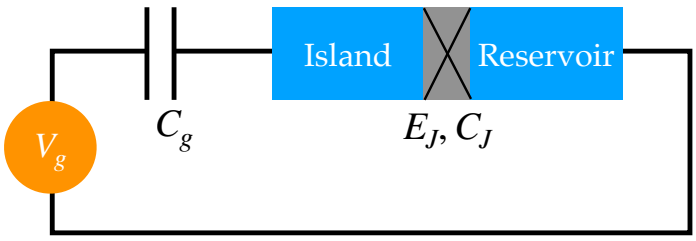

Figure 2.15: Adapted from [165,167]. Schematic of the charge qubit: The superconducting island and the superconducting electron reservoir (denoted by 'SC') are coupled by a Josephson junction. The island is capacitavely coupled to a gate voltage.

C_{dyn} and α for $\alpha \lesssim 0.2$. When α approaches $1/2$, for small velocities, there are deviations from this trend[7]. While at weak coupling the dynamo energy scales linearly in the velocity, for stronger couplings there is a trade-off between the linear factor of v in Eq. (2.89) and the square of the dynamically measured Chern number which decreases from $C_{\mathrm{dyn}} = 1$ for increasing velocities. This is qualitatively also seen in Fig. 2.14a).

2.4 Proposed experimental realization

In order to observe the quantum dynamo effect in an experimental setting, we will review used techniques and their applicability in the following. We first discuss the realization of a driven spin, to then comment on possible coupling to a single mode and a continuous bath.

2.4.1 Experimentally realizing a radially driven spin

A charge qubit

Experimentally, one can realize a spin-1/2 degree of freedom with a high degree of control using what is commonly called a *charge qubit* or *Cooper pair box (CPB)* [165–167]. It consists of a superconducting island and a superconducting electron reservoir that are coupled by a Josephson junction with energy E_J and capacitance C_J, as shown in Fig. 2.15. A gate voltage V_g is applied via a capacitance C_g [167]. The two-level system is implemented by the excess number of Cooper pairs in the island, which can be controlled to be either zero or one. Concretely, the system is implemented in the superconducting regime such that all electrons are paired to Cooper pairs. The system can then conveniently be described

[7] While one reason for this can certainly be found in the simplicity of the phenomenological justification of Eq. (2.89), possibly also the results of the SSE approach can show weaknesses, as they assume free bath correlation functions given in Eqs. (2.69). However, for stronger coupling, the influence of the dynamically induced field from modes near resonance becomes sizable. The derivation of the SSE presented in App. B.2 is valid for $0 \leq \alpha < \frac{1}{2}$ [75,79,151]. In order to describe the strong coupling limit, further efforts are thus in order. As here we are analyzing the quantum dynamo effect occuring at high efficiency for weak to intermediate coupling, we content ourselves with the given analysis.

by the number of Cooper pairs n on the island, leading to the Hamiltonian [167]

$$\mathcal{H}_{\text{CPB}} = \sum_n \left(4E_C(n - n_g)^2 \left|n\right\rangle \left\langle n\right| - \frac{1}{2} E_J \left(\left|n\right\rangle \left\langle n+1\right| + \text{h.c.} \right) \right). \tag{2.90}$$

Here, the single energy charging energy of the circuit in Fig. 2.15 is given by $E_C = e^2/(2(C_g + C_J))$, and the gate charge is $n_g = C_g V_g/(2e)$. When n_g is close to a half-integer value, the first term of the Hamiltonian becomes degenerate between two states with the number of Cooper pairs differing by one and an effective ground state description thus allows to disregard all other states. The system thus is effectively described by a two-level system. In order to realize the radially driven form from Eq. (2.2), we first notice that the z-component can be implemented by applying an additional radially varying gate voltage, i.e., $V_g = V_0 + \delta V \cos(\omega t)$. The term V_0 produces a constant bias field, similar to the M-term evoked in Sec. 2.2.3 [36, 167].

A way to also vary the field in x-direction in time consists in replacing the Josephson junction by two junctions in a loop configuration threaded by a magnetic flux, thus forming a SQUID. This then makes the hopping parameter (i.e., the second term) in the Hamiltonian (2.90) dependent on the cosine of the magnetic flux [167, 168]. Therefore, tuning the magnetic flux in time can realize the radial driving of the charge qubit.

From a Cooper pair box to transmons and g-mons

As described above, the realization of the Cooper pair box relies on setting $n_g \sim \frac{1}{2}$ to realize an effective two-level system. The energy difference to higher lying energy states is large at $n_g \sim \frac{1}{2}$ and depending on the value of E_J/E_C, can be more or less pronounced [169]. In the proposal [165], a ratio $E_J/E_C < 1$ had been realized, leading to an effective two-level description, but at the price of a high sensitivity to precisely tuning $n_g \sim \frac{1}{2}$. Dephasing due to deviations in n_g have thus motivated the development of the *transmon* [169, 170], which has a similar architecture as a Cooper pair box, but realizes a large quotient $E_J \gg E_C$. This leads to a reduced sensitivity to the precise value of n_g, while reducing the energy difference to higher lying energy states. However, the transmon design benefits from the fact that the sensitivity to deviations in the gate charge decreases exponentially when increasing the ratio $E_J \gg E_C$, while the differences to higher lying energy levels decrease only algebraically [169]. The transmon architecture has hence been further developed [171] and successfully employed to measure the topology of a radially driven spin-1/2 with the Hamiltonian (1.4) [37].

Thanks to its versatility and scalability, charge qubit realizations are an actively researched direction of quantum computation [172] and enjoy dynamic progress. Among recent developments are so-called *gmon-qubits* [173, 174] allowing a high-degree of control over the coupling between different qubits. We mention these techniques here, as such gmon-qubits have been used to experimentally measure the topology of a driven spin-

1/2 [35][8] and are thus also promising in order to observe the quantum dynamo effect experimentally. For that, a second ingredient - the coupling to an environment mode or bath - is necessary. We will therefore in the following comment on how this can be realized experimentally.

2.4.2 Coupling to bosonic modes

In order to realize the coupling to an environment or a single oscillator mode, different schemes for an experimental realization have been devised. Examples include the realization using Bose-Einstein condensates [175, 176], a Chiral Luttinger liquid [147, 148], microwave cavities [152, 153, 177] and a long transmission line [145, 146, 178]. Focussing on the realization using a transmission line, according to its properties and the coupling to the qubit, it can emulate both a cavity and a bosonic bath: With the qubit placed in the center of the transmission line and at low energies, one can approximate their interaction as that of a spin coupled to a single bosonic mode [178], reminiscent of the Jaynes-Cummings Hamiltonian [179]. This enables the realization of a spin strongly coupled to an oscillator mode [180].

On the other hand, when the qubit interacts with the entire transmission line, the latter effectively takes the form of a bosonic bath with a large number of modes [145, 146]. This allows the experimental realization of the spin-boson model, which has also been demonstrated experimentally for strong coupling and a driven setup [149, 150].

2.5 Conclusion

In this chapter, we have studied a dynamical resonance effect when coupling a periodically driven spin-1/2 to a bosonic environment, called the 'quantum dynamo effect'. In essence, the modes with frequency close to resonant with the driving velocity of the spin get coherently displaced, corresponding to a work-to-work conversion. We introduced the 'dynamo energy', measuring the energy stored in coherent displacement of the modes beyond the adiabatic displacement due to equilibration to the spin. This effect occurs in a regime where the spin dynamics is such that it can approximately follow the radial driving field. By adapting the notions of the topology of a spin-1/2 in a radial magnetic field from Sec. 1.1 for the dynamically driven case, we saw that the quantum dynamo effect is in fact linked to the dynamically accessed topological properties (in particular the quantity C_{dyn} defined in Eq. (2.9)) of the spin system. For coupling to one resonant mode, the effect is most pronounced, and we gave a phenomenological description of the relation between the dynamo energy and C_{dyn} in Eq. (2.46) which we verified using numerical ED. We

[8] There the authors have benefitted from an average coherence time of $\sim 10\mu$s, while the drive from north to south pole was realized in 600ns.

then extended the definitions for coupling to an Ohmic bath, for which we gave analytical arguments on how to identify the dynamo effect in an accessible way. We then used a range of approaches including exact diagonalization and a stochastic approach to study the dynamo effect in this setup. Due to the presence of the full spectrum of modes, the maximally attained output power is lower than for the case with one resonant mode, but can be tuned using a trade-off with the efficiency (see Fig. 2.13 and the corresponding discussion). We also compared to results from a GKLS approach developed in [33] and find agreement for weak coupling and larger driving velocities. Interestingly, both from exact diagonalization and the GKLS approach, we predicted that the efficiency of the effect improves for longer times of operation. The break down of the effect for larger coupling strength still seems to be connected to the change in the dynamically accessed topology, signalled by Eqs. (2.87) and (2.89), even though the latter gives only a tendency of the dynamo energy in this case and not a generally valid relation, as seen by comparing to numerical results in Fig. 2.14. Our work published under [33] offers perspectives on energy transfers in the quantum regime [25–27] and quantum thermodynamics [70–72, 74, 84], which are of great current interest for emerging applications. It explores a relation with effective topological properties and can thus find experimental implementations using recent techniques for measuring the topology of a spin-1/2 [35, 37] and coupling spins and bosonic degrees of freedom [149, 150, 152, 153, 177, 180].

Chapter 3

Fractional topology, disorder and Majorana fermions

After having studied the topology of a spin-1/2, possible ways to realize this model using a driving protocol and a dynamo effect related to this topological number, allowing for a work-to-work-conversion into a bath when implementing the driving, we now want to turn towards spin systems with larger extension.

As discussed in Sec. 1.1.3, for two interacting spins in a radial magnetic field, novel phases with fractional partial Chern numbers occur as a result of entanglement [12]. In the same time, we introduced the Kitaev wire in Sec. 1.1.2 and showed the occurence of gapless Majorana bound states at its edges. Having discussed the relation of the Hamiltonian in Eq. (1.27) of the Kitaev wire in momentum space to that of the spin in a radial field, it is natural to ask whether interacting fractional topological phases can occur also in two coupled wire systems and how this influences the Majorana bound states at the edges. This question has been answered in [51], where a fractional value of $C = 1/2$ has been demonstrated from DMRG for the double-critical Ising phase of two coupled wires [181]. From the analogy of two coupled spheres with two interacting Kitaev wires thus established, it is then interesting to ask whether Majorana bound states can be found in the sphere system as well and how stable they are [36]. This question of stability naturally brings up the topic of disorder and how robust these fractional interacting topological phases are with respect to it. In this chapter, we will first shine some more light on the robustness of $C_i = 1/2$ when disordering certain parameters of the system, and consequently study how this is related to the Majorana signatures of the model of two coupled spins.

Although their experimental evidence remains highly debated, Majorana fermions are maintaining extraordinary interest in the scientific community with steady experimental advances [44]. A recent work reports on the observation of Majorana bound states in a minimal systems composed of only two quantum dots [17], a configuration that has previously been called 'poor man Majorana bound states', as they are not topologically protected [182]. It is thus a topical question how the relation of the fractional topological

phase occuring in a system of two coupled spins found in [12] with Majorana fermions can be understood and what applications there are for such a system composed of two spins.

The contents of this chapter are part of a project on which I worked together with Karyn Le Hur, for which an article has been submitted to the preprint server arXiv and is in preparation for a journal submission [183]. This article also discusses perspectives for applications in quantum information, which were deepened during the Master's internship of Brian Chung Hang Cheung in our group. Karyn Le Hur has previously realized the relations of the fractional topological phase with Majorana fermions at the poles for the coupled spin system [36, 184] (see Sec. 3.2).

3.1 Fractional topology and disorder

As mentionned in Sec. 1.1.3, interactions between spins can lead to a fractionalization of the partial Chern number (per spin). Let us first study how this effect responds to the introduction of disorder. The occurence of a fractional topological number is intimately connected to the creation of an entangled state at the south pole of the sphere. To that end, we note that the Hamiltonian in Eq. (1.34) is diagonal at the poles in the tensor product basis. Therefore, a crucial necessary condition to achieve a fractional state in this case is the presence of a degenerate ground state subspace at the south pole [12]. For a system described by a Hamiltonian (1.34), we found under the conditions cited in Eq. (1.41) that the ground state at the south pole lies in the degenerate subspace $\{|\uparrow\downarrow\rangle, |\downarrow\uparrow\rangle\}$ due to the exchange symmetry between the two sites. The state found at the south pole when applying a drive and starting from the north pole (as realized in experiments [35, 37]) can be predicted using perturbation theory: Just before reaching the south pole, there are still transverse fields acting on each of the two spins, proportional to $\sin\theta$. Including their effect by applying effective Hamiltonian perturbation theory, it has been found that they give rise to an effective Hamiltonian [12]

$$\mathcal{H}_{\text{eff}} = -\frac{H^2}{4}\sin^2\theta \frac{r_z}{r_z^2 - \frac{1}{4}(H-M)^2}\begin{pmatrix} 1 & 1 \\ 1 & 1 \end{pmatrix}, \tag{3.1}$$

in the degenerate subspace $\{|\uparrow\downarrow\rangle, |\downarrow\uparrow\rangle\}$. This fixes the entangled state cited in Eq. (1.42)

$$|GS(\theta = \pi^-)\rangle = \frac{1}{\sqrt{2}}(|\uparrow\downarrow\rangle + |\downarrow\uparrow\rangle), \tag{3.2}$$

as the ground state just before the south pole and therefore also at the south pole for adiabatic driving.

In order to maintain an entangled state in the presence of disorder, we thus have two possibilities: We can either try to maintain a degenerate subspace at one of the poles, or

modify the system in such a way that the entanglement is enforced differently. We will in the following investigate how disorder can break the fractional phase to then restore it using the first option in Sec. 3.1.1 and study the second option in Sec. 3.1.2.

Mass disorder breaking fractional topology

Note that introducing an asymmetry between the two spins in the Hamiltonian changes the previous analysis. This can most easily be seen by making the angle-independent offset M site-dependent, i.e., modifying Eq. (1.4) into

$$\mathcal{H}_{\text{rad, i}}(\theta,\phi) = -\frac{H}{2}(\sin\theta\cos\phi\sigma_i^x + \sin\theta\sin\phi\sigma_i^y + \cos\theta\sigma_i^z) - \frac{M_i}{2}\sigma_i^z. \tag{3.3}$$

This lifts the degeneracy between the states $\{|\uparrow\downarrow\rangle, |\downarrow\uparrow\rangle\}$, which now have energies $\mp\frac{1}{2}(M_1 - M_2)$. The ground state at the south pole is thus changed into $|\uparrow\downarrow\rangle$ if $M_1 > M_2 > 0$ and into $|\downarrow\uparrow\rangle$ if $M_2 > M_1 > 0$. For a numerical example, we refer to Fig. 3.3 a).

Close to the south pole, the detuning between the masses defines the adiabaticity condition, in the sense that the driving can be called adiabatic if $v \ll |\frac{1}{2}(M_1 - M_2)|$. This raises a question relevant for experiments trying to realize the fractional state: As in experiments, there is a certain degree of error when tuning the system parameters, how precise does the tuning have to be in order to realize the fractional state?

Following the above consideration, one could be inclined to argue that if there is a small mass asymmetry, the fractional state can still be observed as long as $v \gg |\frac{1}{2}(M_1 - M_2)|$. However, this would actively (and in a way deliberately) violate adiabaticity and thus not probe the true topology of each subsystem: Instead of the true $(1,0)/(0,1)$ topology (where (C_1, C_2) are the partial Chern numbers of each spin), one artificially would measure a *dynamically accessed* $(\frac{1}{2},\frac{1}{2})$ topology. This picks up the discussion of C_{dyn} from Sec. 2.1 (for a system made up of two interacting spins instead of one spin interacting with a bath) and underlines the importance of clearly distinguishing it from C.

In the following, we will discuss how the partial Chern number of each spin behaves and can be accessed in the presence of disorder, focussing on a site-dependent mass M_i.

3.1.1 Vanishing disorder at the south pole

As pointed put above, a necessary condition for the fractional state to occur is the presence of a degenerate ground state subspace at the south pole. In the presence of a site-dependent mass term M_i, a straight-forward way to restore the degeneracy at the south pole is thus to suppress the disorder at the south pole, i.e., setting

$$M_i = M + f_{\text{dis}}(\theta)\delta M_i, \tag{3.4}$$

where $f_{\text{dis}}(\theta)$ is a real function vanishing at the south pole ($f_{\text{dis}}(\pi) = 0$) and with $|f_{\text{dis}}(\theta)| \leq 1$. Whether or not the fractional state is destroyed by this form of disorder depends on the behaviour of the function $f_{\text{dis}}(\theta)$ close to the south pole:

The off-diagonal elements of the effective Hamiltonian in the degenerate subspace for the disorder-free case from Eq. (3.1) favour the entangled state and are evolving as $\sin^2\theta \propto |_{\theta\to\pi^-} - (\theta-\pi)^2$ when driving θ from 0 to π. The additional term coming from the disorder in this subspace reads

$$\mathcal{H}_{\text{dis}} = -\frac{f(\theta)}{2}\begin{pmatrix}\delta M_1 - \delta M_2 & 0\\ 0 & -\delta M_1 + \delta M_2\end{pmatrix}. \tag{3.5}$$

We can therefore assert that the disorder function $f_{\text{dis}}(\theta)$ vanishing slower than quadratically in θ leads to a breakdown of the fractional phase: When approaching the south pole, at a certain critical angle, the disorder Hamiltonian will dominate over the effective interaction Hamiltonian (3.1). If the disorder vanishes faster than quadratically in θ, the fractional phase will persist. If the disorder vanishes quadratically, the effective interaction and the disorder intervene at similar orders. To discuss a concrete case, we discuss in the following an example where we set

$$f(\theta) = \sin^\gamma(\theta), \tag{3.6}$$

where γ is a parameter. For $\gamma < 2$, we expect the fractional phase to break down. At $\gamma = 2$ and for small deviations in the masses, the dominant effect of the disorder in the effective Hamiltonian for the quasi-degenerate subspace will with this form of $f(\theta)$ lead to

$$\mathcal{H}_{\text{eff}} = -\sin^2\theta\begin{pmatrix}(\delta M_1 - \delta M_2) & \frac{rd^2}{r^2-(d-M)^2}\\ \frac{rd^2}{r^2-(d-M)^2} & -(\delta M_1 - \delta M_2)\end{pmatrix}. \tag{3.7}$$

Note that this is similar to the Hamiltonian of a single 'sphere', i.e., a spin in a radial magnetic field, at a fixed angle ρ:

$$\mathcal{H}_{\text{eff}} = -\sin^2\theta\sqrt{(\delta M_1 - \delta M_2)^2 + \left(\frac{rd^2}{r^2-(d-M)^2}\right)^2}\begin{pmatrix}\cos\rho & \sin\rho\\ \sin\rho & -\cos\rho\end{pmatrix}, \tag{3.8}$$

where we defined

$$\cos\rho = \frac{\delta M_1 - \delta M_2}{\sqrt{(\delta M_1 - \delta M_2)^2 + \left(\frac{rd^2}{r^2-(d-M)^2}\right)^2}}. \tag{3.9}$$

We can interpret this Hamiltonian as that of a single spin near the equator of a radial parameter space, where the mass imbalance introduces a deviation from the equator. The ground state is

$$|GS\rangle = \cos\frac{\rho}{2}|\uparrow\downarrow\rangle + \sin\frac{\rho}{2}|\downarrow\uparrow\rangle. \tag{3.10}$$

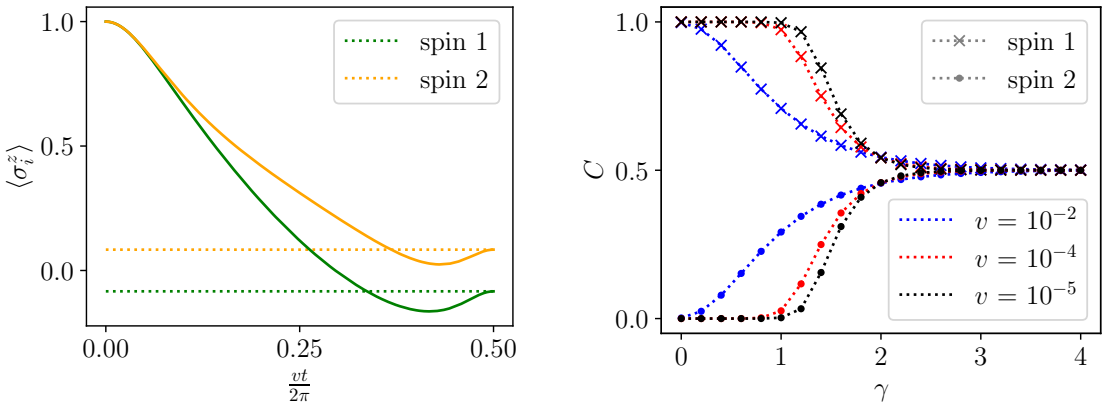

(a) $\gamma = 2$, $v = 10^{-4}$ (b) C-γ dependence for various v

Figure 3.1: a) Expectation values $\langle\sigma_i^z\rangle$ for a single drive (solid lines) with comparison to the resul from Eq. (3.11) at the south pole (dotted lines). Further parameters are $H = 2.0$, $(M_1, M_2) = (1.1, 1.3)$, $r_z = 1.0$. b) C_i evaluated for a range of γ and for a drive with different velocities.

Therefore, for $\gamma = 2$, we can evaluate

$$\langle\sigma^z_{1/2}(\theta = \pi)\rangle = \pm\cos\rho = \pm\frac{\delta M_1 - \delta M_2}{\sqrt{(\delta M_1 - \delta M_2)^2 + \left(\frac{rd^2}{r^2-(d-M)^2}\right)^2}}. \tag{3.11}$$

We see that the mass disorder vanishing quadratically introduces a shift of the partial Chern number from the fractional value, vanishing with the mass difference between the two spheres.

For $\gamma > 2$, the disordered term vanishes faster than the effective coupling introduced by the transverse fields when approaching the south pole and thus the fractional phase persists. In Fig. 3.1 we study the disordered model with disorder vanishing at the south pole as $f(\theta) = \sin^\gamma\theta$ numerically using ED. In Fig. 3.1a), we show a drive from north to south pole with $\gamma = 2$. The dotted lines there show the analytical prediction at the south pole from Eq. (3.11), which agrees with the numerical results. In Fig. 3.1b), we show the dependence of C_i for $i = 1, 2$ on the parameter γ. This confirms our prediction that for $\gamma > 2$, the fractional topological numbers are restored. However, there remains a dependence on the velocity: For smaller velocities, the crossover around $\gamma = 2$ becomes increasingly steeper. Note that since C is evaluated from a driving protocol with finite velocity, it should be understood in the sense of C_{dyn} defined in Eq. (2.9).

In the following, we will discuss the case with $\gamma = 2$ in a bit more detail, as it bridges with the situation of a transverse coupling, that we will discuss afterwards.

Stochastic properties

Assuming the mass deviations δM_i are random variables and thus interpreting them as a form of disorder, we can evaluate the disorder average of the partial Chern number. We will in the following denote the disorder average of a random variable X by $\overline{X}$. Assuming the mass deviations have a mean of zero, $\overline{\delta M_i} = 0$, and a standard deviation $\sigma_i = \sqrt{\overline{\delta M_i^2} - \overline{\delta M_i}^2}$, the different situations discussed from above lead to different properties:

Consider first the disorder-free situation (i.e., setting $f_{\text{dis}}(\theta) = 0$). As discussed in Sec. 1.1.3, we find partial Chern numbers $(C_1, C_2) = (\frac{1}{2}, \frac{1}{2})$. Straightforwardly, we can then also evaluate $C_i^2 = \frac{1}{4}$.

Now, for the situation with disordered masses having the same weight at all angles (technically, this corresponds to setting $f_{\text{dis}}(\theta) = 1$), we find partial Chern numbers (C_1, C_2) as $(0, 1)$ or $(1, 0)$ depending on the realization. Note that this leads to $\overline{C_i} = \frac{1}{2}$ and $\overline{C_i^2} = \frac{1}{2}$. In an experimental realization, this situation could thus be distinguished from the setup giving fractional topology by evaluating $\overline{C_i^2}$.

Note that this way of distinguishing the disordered and the clean case on the one hand relies on first evaluating the quantum mechanical expectation value and consequently taking the disorder average. This would mean that it is practicable when the disorder configuration varies slowly compared to the time-scale of one experiment. On the other hand, there are interesting perspectives of the measure C_i^2 with regards to applications for a quantum dynamo (cf. Chap. 2) or also with regards to light-matter interaction [36, 41]: In Eq. (2.46), we found a relation of the change of dynamo energy for a single radially driven spin coupled to a bath with C_{dyn}^2. In [41], it has been argued how C^2 can be measured for a single sphere from the interaction with circularly polarized light. Therefore, even though both of these applications have been studied for a single sphere, it seems promising to study similar relations also in interacting systems, which would then also allow to distinguish the response to disorder. Here, we focus on the effects on the partial topology from disorder.

Then, with an angle-dependent function $f_{\text{dis}}(\theta)$ vanishing at the south pole, we showed in the previous section that the behaviour depends on how quickly the disorder is suppressed when approaching the south pole. If this suppression is slower than quadratic, we restore the disordered case. However, if the suppression is faster than quadratic, this correctly mimicks the clean case.

If the suppression of disorder around the south pole decreases quadratically, using Eq. (3.11) and Eq. (1.15), we find $\overline{C_i} = \frac{1}{2}$ and for small values of disorder (i.e., $(\delta M_1 - \delta M_2)^2 \ll \left(\frac{rd^2}{r^2-(d-M)^2}\right)^2$), we can approximate

$$\overline{C_i^2} \approx \frac{1}{4}\left(1 + \overline{(\delta M_1 - \delta M_2)^2}\left(\frac{r^2-(d-M)^2}{rd^2}\right)^2\right) = \frac{1}{4} + (\sigma_1^2 + \sigma_2^2)\left(\frac{r^2-(d-M)^2}{4rd^2}\right)^2, \tag{3.12}$$

where σ_i^2 is the variance of the disordered δM_i. We see that we restore $\overline{C_i^2} \approx \frac{1}{4}$ with a deviation scaling in the square of the standard deviations σ_i of the mass disorder. We therefore conclude that for small disorder values, the clean case can be mimicked experimentally using this type of disorder. The case with $f_{\text{dis}} = \sin^2\theta$ close to the south pole presented here gives rise to an effective Hamiltonian similar to that of two spins coupled according to Eq. (1.34) with an additional xy-coupling. We will see in the following how this setup can equivalently be used to stabilize a fractional phase against disorder, builiding on the analysis from above.

3.1.2 Effect of a transverse coupling

Addition of a transverse coupling to the system of two spins giving rise to fractional partial topology in Eq. (1.34) has first been considered in [12]. The coupling takes the form

$$\mathcal{H}_{xy} = r_{xy}(\sigma_1^x\sigma_2^x + \sigma_1^y\sigma_2^y) = 2r_{xy}(\sigma_1^+\sigma_2^- + \sigma_1^-\sigma_2^+). \tag{3.13}$$

We emphasize here that this coupling preserves the $\mathbb{Z}_2$ exchange symmetry between the sites and a global symmetry of rotation around the z-axis of the Hamiltonian, which are crucial conditions to observe a fractional topological state. Upon a first glimpse, it is also clear that a negative r_{xy} will make the state $|\psi\rangle = \frac{1}{\sqrt{2}}(|\uparrow\downarrow\rangle + |\downarrow\uparrow\rangle)$ energetically more favorable and that this coupling in general favors entanglement between the two sites. In the following, we will make this more precise, to then see how this coupling can improve the stability of the fractional state with respect to disorder and even give rise to an extended fractional phase.

The clean case

As pointed out out in [12], the Hamiltonian (1.34) together with the xy-coupling from Eq. (3.13) can conveniently be written in the added momentum basis of the two spin-1/2. This gives rise to the following singlet-triplet form of the Hamiltonian (for $\phi = 0$) [12]:

$$\mathcal{H} = -(2r_{xy} + r_z)\,|0,0\rangle\langle 0,0| + \begin{pmatrix} r_z - (H\cos\theta + M) & -\frac{H}{\sqrt{2}}\sin\theta & 0 \\ -\frac{H}{\sqrt{2}}\sin\theta & 2r_{xy} - r_z & -\frac{H}{\sqrt{2}}\sin\theta \\ 0 & -\frac{H}{\sqrt{2}}\sin\theta & r_z + H\cos\theta + M \end{pmatrix}. \tag{3.14}$$

The matrix describing the triplet sector is written in the basis $\{|1,1\rangle, |1,0\rangle, |1,-1\rangle\}$ and the basis of added angular momentum states is defined in the usual way by $|0,0\rangle = \frac{1}{\sqrt{2}}(|\uparrow\downarrow\rangle - |\downarrow\uparrow\rangle)$, $|1,1\rangle = |\uparrow\uparrow\rangle$, $|1,0\rangle = \frac{1}{\sqrt{2}}(|\uparrow\downarrow\rangle + |\downarrow\uparrow\rangle)$ and $|1,-1\rangle = |\downarrow\downarrow\rangle$. In this form, a decoupling between the singlet and the triplet sector of the Hamiltonian becomes apparent - initialized in one of the sectors, no transitions to the other are allowed. This important fact has the consequence that a fractional topological state can arise only if the state

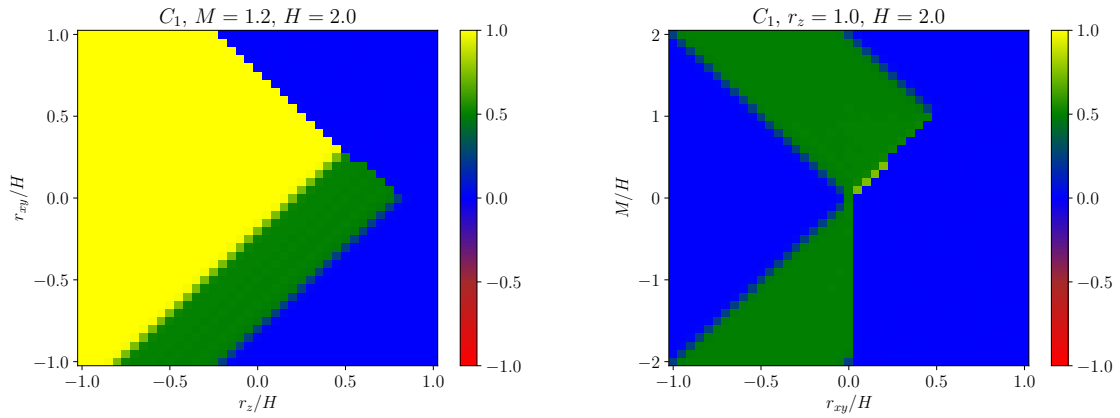

(a) r_{xy}-r_z-plane (b) M-r_{xy}-plane

Figure 3.2: Phase diagram from ED for sphere 1 for driving from north to south pole along the $\phi = 0$ meridian with $H = 2.0$ and $v = 0.005$ and the other parameters as indicated.

$|1,0\rangle$ is the ground state at the south pole. When the singlet state $|0,0\rangle$ independently would be the ground state at the south pole, the system driven from the north pole will end in an excited state at the south pole. In other words, the lowest lying energy state accessed through the dynamic driving protocol is always chosen from the triplet sector of the Hamiltonian. A detailed analysis yields the condition [12]

$$r_z - \frac{H}{2} - \frac{M}{2} < r_{xy} < \min\left(\frac{H}{2} + \frac{M}{2} - r_z, r_z - \left|\frac{H}{2} - \frac{M}{2}\right|\right), \tag{3.15}$$

to find $C = \frac{1}{2}$ without disorder, corresponding to a transition from $|1,1\rangle$ to $|1,0\rangle$. A numerical verification of the topological phase diagram in the r_{xy}-r_z-plane and in the M-r_{xy}-plane can be seen in Fig. 3.2.

We observe that instead of a ground state degeneracy at the south pole, we now find a unique ground state which preserves the $\mathbb{Z}_2$ exchange symmetry in the $C = \frac{1}{2}$ phase. We trivially also find $C^2 = \frac{1}{4}$, as for the clean case without a transverse coupling (i.e., the situation described in the introductory Sec. 1.1.3) In the following we will study the changes to the topology when introducing static disorder to this setup.

Adding static disorder

We introduce disorder between the two sites as a deviation of the mass term. We set

$$M_i = M + \delta M_i, \tag{3.16}$$

which corresponds to Eq. (3.4) with $f(\theta) = 1$, i.e., we are studying a setup in which the disorder does not intervene differently at different angles. This mass imbalance between the two sites introduces a new term in the singlet-triplet representation of the Hamiltonian,

which we now write in the basis $\{|0,0\rangle, |1,1\rangle, |1,0\rangle, |1,-1\rangle\}$ and for $\phi = 0$:

$$\mathcal{H} = \begin{pmatrix} -(2r_{xy}+r_z) & 0 & \frac{M_2-M_1}{2} & 0 \\ 0 & r_z - \left(H\cos\theta + \frac{M_1+M_2}{2}\right) & -\frac{H}{\sqrt{2}}\sin\theta & 0 \\ \frac{M_2-M_1}{2} & -\frac{H}{\sqrt{2}}\sin\theta & 2r_{xy}-r_z & -\frac{H}{\sqrt{2}}\sin\theta \\ 0 & 0 & -\frac{H}{\sqrt{2}}\sin\theta & r_z + H\cos\theta + \frac{M_1+M_2}{2} \end{pmatrix}. \tag{3.17}$$

Note that the mass difference enables transitions between the singlet and the triplet sector of the Hamiltonian, therefore the singlet state cannot be excluded from the ground state subspace at the south pole when initializing the system in the triplet sector at the north pole and consequently driving downwards. An important consequence of this is the extension of the fractional topological phase, as we will see in the following section.

From the Hamiltonian in Eq. (3.17), we can find the eigenstates at the north and the south pole in order to evaluate the topology from Eq. (1.15). Calling $\Delta M = M_1 - M_2 = \delta M_1 - \delta M_2$, we can evaluate the eigensystems *to first order in* ΔM. At the north pole, we find the following eigenenergies with the respective eigenstates:

$-H - \frac{M_1}{2} - \frac{M_2}{2} + r_z$	$\|\uparrow\uparrow\rangle$
$H + \frac{M_1}{2} + \frac{M_2}{2} + r_z$	$\|\downarrow\downarrow\rangle$
$-\sqrt{\frac{(\Delta M)^2}{4} + 4r_{xy}^2} - r_z$	$\frac{1}{\sqrt{2}}\left(\left(-\mathrm{sgn}(r_{xy}) - \frac{\Delta M}{8r_{xy}}\right)\|\uparrow\downarrow\rangle + \left(1 - \frac{\Delta M}{8\|r_{xy}\|}\right)\|\downarrow\uparrow\rangle\right)$
$\sqrt{\frac{(\Delta M)^2}{4} + 4r_{xy}^2} - r_z$	$\frac{1}{\sqrt{2}}\left(\left(\mathrm{sgn}(r_{xy}) - \frac{\Delta M}{8r_{xy}}\right)\|\uparrow\downarrow\rangle + \left(1 + \frac{\Delta M}{8\|r_{xy}\|}\right)\|\downarrow\uparrow\rangle\right)$

Table 3.1: Eigensystem of the Hamiltonian in Eq. (3.17) in the disordered case at the north pole with $\theta = 0$.

On the other hand, at the south pole, we find:

$H - \frac{M_1}{2} - \frac{M_2}{2} + r_z$	$\|\uparrow\uparrow\rangle$
$-H + \frac{M_1}{2} + \frac{M_2}{2} + r_z$	$\|\downarrow\downarrow\rangle$
$-\sqrt{\frac{(\Delta M)^2}{4} + 4r_{xy}^2} - r_z$	$\frac{1}{\sqrt{2}}\left(\left(-\mathrm{sgn}(r_{xy}) - \frac{\Delta M}{8r_{xy}}\right)\|\uparrow\downarrow\rangle + \left(1 - \frac{\Delta M}{8\|r_{xy}\|}\right)\|\downarrow\uparrow\rangle\right)$
$\sqrt{\frac{(\Delta M)^2}{4} + 4r_{xy}^2} - r_z$	$\frac{1}{\sqrt{2}}\left(\left(\mathrm{sgn}(r_{xy}) - \frac{\Delta M}{8r_{xy}}\right)\|\uparrow\downarrow\rangle + \left(1 + \frac{\Delta M}{8\|r_{xy}\|}\right)\|\downarrow\uparrow\rangle\right)$

Table 3.2: Eigensystem of the Hamiltonian in Eq. (3.17) in the disordered case at the south pole with $\theta = \pi$.

To find a phase similar to the $C_i = \frac{1}{2}$-phase encountered without disorder, we see that it would be preferential to have the state $|\uparrow\uparrow\rangle$ at the north pole and the state from the third line of Table 3.2 at the south pole. Note that the latter for vanishing disorder ($\Delta M \to 0$) converges to $\frac{1}{\sqrt{2}}\left(-\mathrm{sgn}(r_{xy})|\uparrow\downarrow\rangle + |\downarrow\uparrow\rangle\right)$ so that $C_i \xrightarrow[\Delta M\to 0]{} \frac{1}{2}$. The state in the fourth line has always larger energy than the state in the third line. From the Hamiltonian matrix in Eq. (3.17) we see that the singlet and triplet sectors are coupled by a term introduced by the mass imbalance, i.e., $\frac{M_1-M_2}{2}|0,0\rangle\langle 1,0| + \text{h.c.}$. This implies that the selection rules

on transitions between these sectors are lifted. We will discuss this in more detail with regards to an extension of the fractional phase in Sec. 3.1.3

From a comparison of the eigenenergies in Table 3.1, it is clear that the ground state at the north pole will be the state $|\uparrow\uparrow\rangle$ if

$$H + \frac{M_1}{2} + \frac{M_2}{2} > \max\left(0, 2r_z + \sqrt{\frac{\Delta M^2}{4} + 4r_{xy}^2}\right). \tag{3.18a}$$

At the south pole the ground state will be the state from the third line in Table 3.2 if

$$\sqrt{\frac{\Delta M^2}{4} + 4r_{xy}^2} > -2r_z + \left|H - \frac{M_1}{2} - \frac{M_2}{2}\right|. \tag{3.18b}$$

Eqs. (3.18) define a regime closely resembling the $C = \frac{1}{2}$ phase in presence of a small mass disorder.

The Hamiltonian with disorder is still rotationally invariant upon a rotation around the z-axis for both spins. Therefore, Eq. (1.15) is still applicable to find the partial quantities C_i. Note however that the $\mathbb{Z}_2$ exchange symmetry between the two sites is broken by the disorder, therefore they should still sum up to an integer value but are not necessarily fractionalized individually anymore. We will therefore refer to them as 'disordered partial Chern markers' in the following. We observe

$$C_{1/2} = \frac{1}{2} \mp \frac{\Delta M}{8|r_{xy}|}. \tag{3.19}$$

Therefore, the partial Chern number picks up a correction to first order in $\Delta M/r_{xy}$ for one realization of disorder. If the realization of such disorder is according to

$$\overline{\delta M_i} = 0, \tag{3.20a}$$

$$\sqrt{\overline{\delta M_i^2} - \overline{\delta M_i}^2} = \sigma_i, \tag{3.20b}$$

we still find $\overline{C}_i = 1/2$ as disorder average. Note moreover that in contrast to the case with $r_{xy} = 0$,

$$C_{1/2}^2 = \frac{1}{4} \mp \frac{\Delta M}{4|r_{xy}|}. \tag{3.21}$$

to first order so that $\overline{C_{1/2}^2} = \frac{1}{4}$, similar to the disorder-free case.

We can therefore conclude that when a transverse coupling between the spins is activated, tuning the disorder to smaller values allows to mimick the $C = \frac{1}{2}$ case more closely while maintaining the adiabatic driving condition. This can therefore be useful in experiments facing imperfect conditions to stabilize the fractional phase, which we will see in the following.

Experimental realization of a ferromagnetic transverse interaction

The realization of a transverse xy-coupling of the form from Eq. (3.13) can be experimentally realized by coupling the interacting spins to a cavity [36]. This gives rise to a Hamiltonian

$$\mathcal{H}_{\text{cavity}} = \sum_{i=1}^{2} \frac{g_i}{2}(\sigma_i^- a^\dagger + \sigma_i^+ a) + \omega a^\dagger a. \tag{3.22}$$

To simplify this Hamiltonian, it is beneficial to apply a unitary transformation shifting the cavity mode according to

$$\tilde{a} = a + \sum_{i=1}^{2} \frac{g_i}{2}\sigma_i^-. \tag{3.23}$$

This allows to rewrite the Hamiltonian as

$$\mathcal{H}_{\text{cavity}} = \omega \tilde{a}^\dagger \tilde{a} - \frac{g_1 g_2}{4\omega}(\sigma_1^+\sigma_2^- + \sigma_1^-\sigma_2^+) - \sum_i \frac{g_i^2}{4\omega}(\sigma_i^z + \mathbb{1}_2). \tag{3.24}$$

In the symmetric case with $g_1 = g_2 = g$, we see that from an identification with Eq. (3.13), we find

$$r_{xy} = -\frac{g^2}{8\omega}, \tag{3.25}$$

we therefore conclude that coupling to the cavity induces a ferromagnetic interaction. In addition, we find a renormalization of the mass term according to

$$\tilde{M}_i = M_i + \frac{g_i^2}{2\omega}. \tag{3.26}$$

Care needs thus to be taken that this shift in the mass term does not drive a transition out of the fractional topological phase. In addition, the form of the induced coupling from Eq. (3.25) also imposes requirements on the parameters g and ω, so that the condition (3.15) to reach the fractional phase can be fulfilled.

In relation to the quantum dynamo effect described in the previous section, and in particular to the one-mode dynamo from Sec. 2.2, we further remark that a similar effect can occur when the interaction between the system and the bosonic mode is described by the Hamiltonian (3.22). In this case, we have two spins coupled to one common mode mediating an interaction [185–187]. In order to maintain adiabaticity of the driving of the two spins, we require in addition $v \ll \omega$, which corresponds to the case of a rapidly equilibrating mode described by Eq. (2.25) for a single spin coupled in z-direction. For a single spin, this implied an evolution of the spin close to the free case. Here we conclude that for $v \ll \omega$, the spins will evolve adiabatically with the effective interaction Hamiltonian from Eq. (3.24) with little additional effects (in particular, no dynamo effect will occur). Another way to view this requirement is from the different time-scales of equilibration: If $v \ll \omega$, the cavity mode equilibrates quickly to the spins and its state is determined by

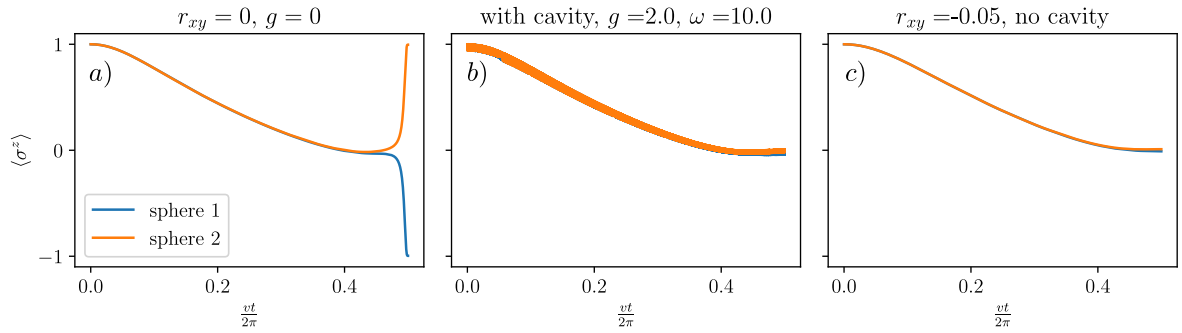

Figure 3.3: Numerical results for the $\langle \sigma_i^z \rangle$ expectation values in time for driving from north to south pole. a) Situation without a transverse coupling or a cavity, obtained for $H = 2.0$, $(M_1, M_2) = (1.6, 1.602)$, $r_z = 1.0$ and $v = 10^{-5}$. b) A similar setup, but now coupled to a cavity as in Eq. (3.22) with $g = 2.0$ and $\omega = 10.0$. The cavity was initialized in an empty state and simulated with an occupation number cut-off at $N_b = 10$ and we checked that the maximally reached occupation stays well below this value. This corresponds to preparation (2) in the language of Chap. 2. c) The situation without the cavity, but a transverse coupling $\tilde{r}_{xy}$ and a renormalized mass according to Eqs. (3.25) and (3.26) instead.

that of the spins. Due to its fast equilibration, it can effectively mediate an interaction. As we stated in the discussion around Eq. (2.24), in the opposite case $v \gg \omega$, the cavity mode would evolve almost freely and would thus be less effective in mediating an interaction.

The effective interaction introduced by coupling to a cavity mode can be verified numerically. We present results from ED without coupling to a cavity in Fig. 3.3a), with coupling to a cavity in Fig. 3.3b) and compare them to those of an interacting spin model with $\tilde{r}_{xy}$ and $\tilde{M}_i$ according to Eqs. (3.25) and (3.26) in Fig. 3.3c). We verify that the coupling to a cavity can indeed be described by an effective transverse coupling and a renormalization of the mass by comparing Figs. 3.3b) and c). A comparison to Fig. 3.3a), showing the situation with neither a transverse coupling nor a cavity, demonstrates how the coupling to a cavity can stabilize the fractional phase [36], which due to a small mass disorder between the two sites would not be observed for the setup shown here. The main difference between the Fig. 3.3b) and c) are the secondary oscillations, which are slightly more pronounced for the coupling to a cavity.

We emphasize that the discussed realization allows to implement a ferromagnetic xy-coupling. This is useful for the case without disorder, in which the fractional phase occurs when an entangled state is formed at the south pole, which is then stabilized by a ferromagnetic xy-coupling. An antiferromagnetic coupling would favor the singlet state with vanishing total spin at the south pole. As discussed above, singlet-triplet transitions are ruled out by the Hamiltonian (3.14) in the clean case. However, we have also seen how this selection rule is lifted when disorder is introduced in the form of a mass assymetry $M_1 \neq M_2$. We will discuss in the following how this allows to almost double the size of

the fractional phase in the presence of disorder.

3.1.3 Extending the fractional phase

In Eq. (3.15), we cited the conditions described in [12] to find a fractional $C_i = 1/2$ phase in the clean case where no transitions to the singlet sector are possible. Note that this gave the phase diagram shown in Fig. 3.2 in the r_{xy}-r_z-plane with a stripe-like region of $C_i = 1/2$, located mainly in the half plane with $r_{xy} < 0$, but extending slightly into the half-plane with $r_{xy} > 0$. Instead of evaluating which state from the triplet sector will have the lowest energy at the south pole, one can also try and evaluate the ground state of the full Hamiltonian. At the poles, the Hamiltonian (3.14) (without disorder) is diagonal in the basis of added spin and has the following eigenenergies [12]:

State	energy at north pole	energy at south pole
$\|0,0\rangle$	$-2r_{xy} - r_z$	$-2r_{xy} - r_z$
$\|1,1\rangle$	$r_z - H - M$	$r_z + H - M$
$\|1,0\rangle$	$2r_{xy} - r_z$	$2r_{xy} - r_z$
$\|1,-1\rangle$	$r_z + H + M$	$r_z - H + M$

Table 3.3: Eigensystem of the Hamiltonian in Eq. (3.14) at the north and the south pole.

The state $|1,1\rangle$ is the ground state at the north pole if[1] $2r_z - H - M < 2r_{xy} < -2r_z + H + M$ [12]. The fractional $C_i = 1/2$ then occurs when $\langle \sigma_i^z(\theta = \pi)\rangle = 0$. This is fulfilled when the state at the south pole is $|1,0\rangle$, but also when it is $|0,0\rangle$. This occurs when $2r_{xy} < 2r_z - |H - M|$ and $-2r_{xy} < 2r_z - |H - M|$ respectively. Only considering the energetics, the two states at the south pole are selected simply by the sign of r_{xy}: If $r_{xy} > 0$, we find the singlet state $|0,0\rangle$, while if $r_{xy} < 0$ we find the state $|1,0\rangle$. In summary, we find that *considering only the ground states at the poles* and *neglecting selection rules* for the moment, fractional phases are theoretically possible in the phase space region described by

$$H + M > \max\left(0, 2r_z + 2|r_{xy}|\right), \tag{3.27a}$$

$$2|r_{xy}| > -2r_z + |H - M|. \tag{3.27b}$$

Note that this is equivalent to Eqs. (3.18) for $\Delta M \to 0$. As can be seen from the Hamiltonian in the presence of a mass asymmetry in Eq. (3.17), transitions are possible between the two sectors at a rate proportional to the difference in the masses. This can be checked numerically using ED, which is shown in Fig. 3.4. From the comparison of the energy levels in the clean and the disordered case in Fig. 3.4a), we see that in the clean case there is a crossing of the initially lowest lying band (purple in the figure) and the initially second lowest band (cyan in the figure, corresponding to the singlet state, whose energy

[1] We are assuming H, M and r_z are positive.

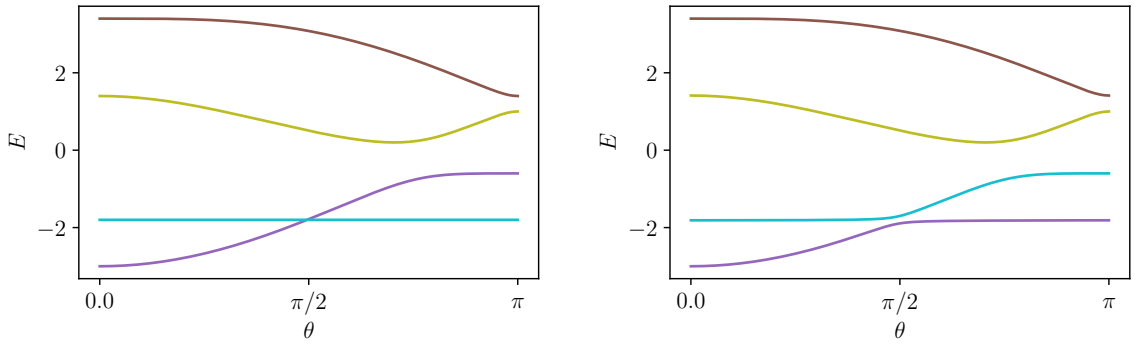

(a) Energy levels, clean case

(b) Energy levels, disordered case

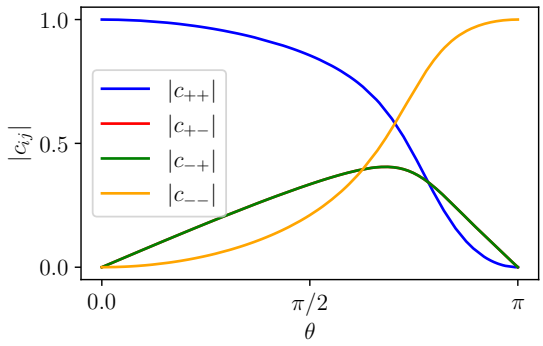

(c) wave function components, clean case

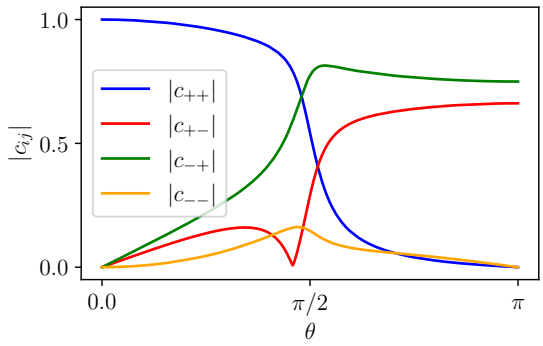

(d) wave function components, disordered case

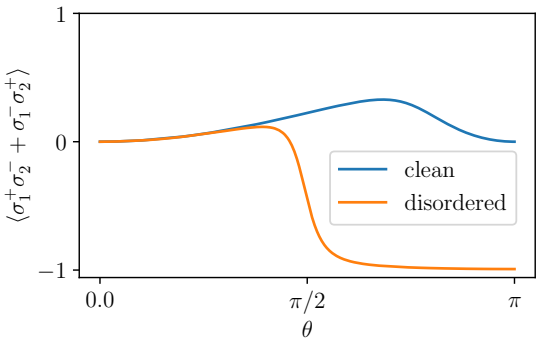

(e) Comparison of $\left\langle \sigma_1^+\sigma_2^- + \sigma_1^-\sigma_2^+ \right\rangle$

Figure 3.4: Comparison of energy levels ((a) and (b)) and wave function components in the time-evolved state starting from the ground state at the north pole ((c) and (d)) for the clean case ((a) and (c)) and with a mass disorder ((b) and (d)). In (e), we compare the expectation value $\left\langle \sigma_1^+\sigma_2^- + \sigma_1^-\sigma_2^+ \right\rangle$ for the time-evolved state starting from the ground state at the north pole for the clean and the disordered case. Used parameters are $H = 2.0$, $r_z = 0.2$, $r_{xy} = 0.8$, furthermore $M = 1.2$ for (a), (c) and the clean graph in (e), $(M_1, M_2) = (1.0, 1.4)$ for (b), (d) and the disordered graph in (e) and $v = 0.001$ for (c),(d) and (e), where $\theta = vt$.

remains constant throughout the drive). However, the system cannot transition due to the selection rule discussed above and in [12], that forbids transitions between the singlet and the triplet sector and causes the system to remain in the purple band. Along this band,

the wave function varies smoothly from $|\uparrow\uparrow\rangle$ to $|\downarrow\downarrow\rangle$, as can be verified from Fig. 3.4c), where we plot the absolute values of the wave function components for a drive starting from the ground state at the north pole. This can be compared to the disordered case in Figs. 3.4b) and d). There we introduced a mass imbalance $\Delta M = M_1 - M_2$ between the two sites. We see that this modifies the band structure by opening a gap between the two lowest lying bands. This leads to a transition of the wave function initialized in the ground state at the north pole to a state close to the singlet state at the south pole. In Figs. 3.4b) and d), $\Delta M/r_{xy} = 1/2$ and the mass imbalance is therefore relatively large, given the consideration around Eq. (3.19). This was chosen deliberately to clearly demonstrate the effects around the transition to the singlet state. As seen from the consideration of the energetics at the two poles in Sec. 3.1.2, the ground state at the south pole with $r_{xy} > 0$ and disorder to first order in $\Delta M/r_{xy}$ is

$$|GS(\pi)\rangle = \frac{1}{\sqrt{2}}\left(-\left(1+\frac{\Delta M}{8r_{xy}}\right)|\uparrow\downarrow\rangle + \left(1-\frac{\Delta M}{8|r_{xy}|}\right)|\downarrow\uparrow\rangle\right). \tag{3.28}$$

Therefore a relatively large disorder causes a deviation from the singlet state, but the state at the south pole remains smoothly connected to it by taking the limit $\Delta M \to 0$. This deviation is seen in the wave function components in Fig. 3.4d) at $\theta = \pi$ and it decreases with the mass imbalance.

The comparison of the small gap opened and the driving velocity now gives the necessary conditions for adiabaticity: If the velocity is much smaller than the gap opened, the system remains in the ground state, while otherwise, a non-adiabatic transition may occur and the system has a finite probability to end up in the cyan band. In Fig. 3.4, we focus on the adiabatic case[2].

Fig. 3.4e) shows that in the disordered case, the ground state at the south pole for the disordered case is indeed close to the singlet state from following the expectation value $\left\langle \sigma_1^+\sigma_2^- + \sigma_1^-\sigma_2^+ \right\rangle$ in time. This quantity approaches -1 for the case shown in Fig. 3.4e). Calculating it from the form of the wave function in Eq. (3.28), we find

$$\left\langle \sigma_1^+\sigma_2^- + \sigma_1^-\sigma_2^+ \right\rangle = -1 + \left(\frac{\Delta M}{8r_{xy}}\right)^2, \tag{3.29}$$

in good agreement with the numerical results[3]. The fact that this quantity varies only to second order in $\Delta M/r_{xy}$ while transitions to the singlet sector are enabled with a rate proportional to ΔM makes it interesting for applications, as we will see in Sec. 3.3.

From the discussion of these results, we conclude that the result from Eq. (3.19) for

[2]The velocity $v/H = 0.5{\cdot}10^{-3}$ is much smaller than the gap quantified numerically by $\Delta E/H \approx 93{\cdot}10^{-3}$ for the situation shown in Fig. 3.4b).

[3]With the parameters used in Fig. 3.4e), we find $\left\langle \sigma_1^+\sigma_2^- + \sigma_1^-\sigma_2^+ \right\rangle \sim -0.996$, while from the ED shown there, we evaluate it to ~ -0.992.

the disordered partial Chern marker C_i holds across the region described by Eqs. (3.27). There is a correction of the fractional value of the order of $\Delta M/r_{xy}$ which can be controlled by either scaling up the transverse coupling between the spins or scaling down the mass difference. Crucially, we then find for a mass disorder following a distribution described by a normal distribution, i.e., by Eqs. (3.20),

$$\overline{C_i} = \frac{1}{2}, \tag{3.30a}$$

$$\overline{C_i^2} = \frac{1}{4}, \tag{3.30b}$$

thus mimicking the clean case when $\Delta M/r_{xy} \to 0$.

The possibility to reach the singlet state at the south pole opened by the mass imbalance is at the core of this mechanism. From here, we can state that the possibility to reproduce (upon averaging over disorder configurations) a fractional phase for antiferromagnetic coupling in the presence of disorder effectively extends this phase. Introducing a small asymmetry can thus be seen as inducing a fractionalization of the averaged disordered partial Chern marker. In Fig. 3.5a) and b), we show a numerical check of the r_{xy}-r_z-plane and the M-r_{xy}-plane of the disordered partial Chern marker as a disorder average, revealing the extended fractional phase from a comparison to the clean case shown in Fig. 3.2. In Fig. 3.5c) and d), we show the same regions in phase space, but now as a phase diagram for $\overline{C_1^2}$, confirming in particular Eq. (3.30b). The dependence of this extension on the presence of disorder allows to think about interesting applications in the realm of quantum information storage and manipulation, which we will discuss in Sec. 3.3. For this it is convenient to introduce a description of the system under study in terms of Majorana fermions, which we will describe in the following.

3.2 Fractional topology and Majorana fermions

In this section, we want to give an interpretation of the fractional topology per spin in terms of Majorana fermions. We first recap some results from the clean case, to then discuss how they carry over to the disordered situation.

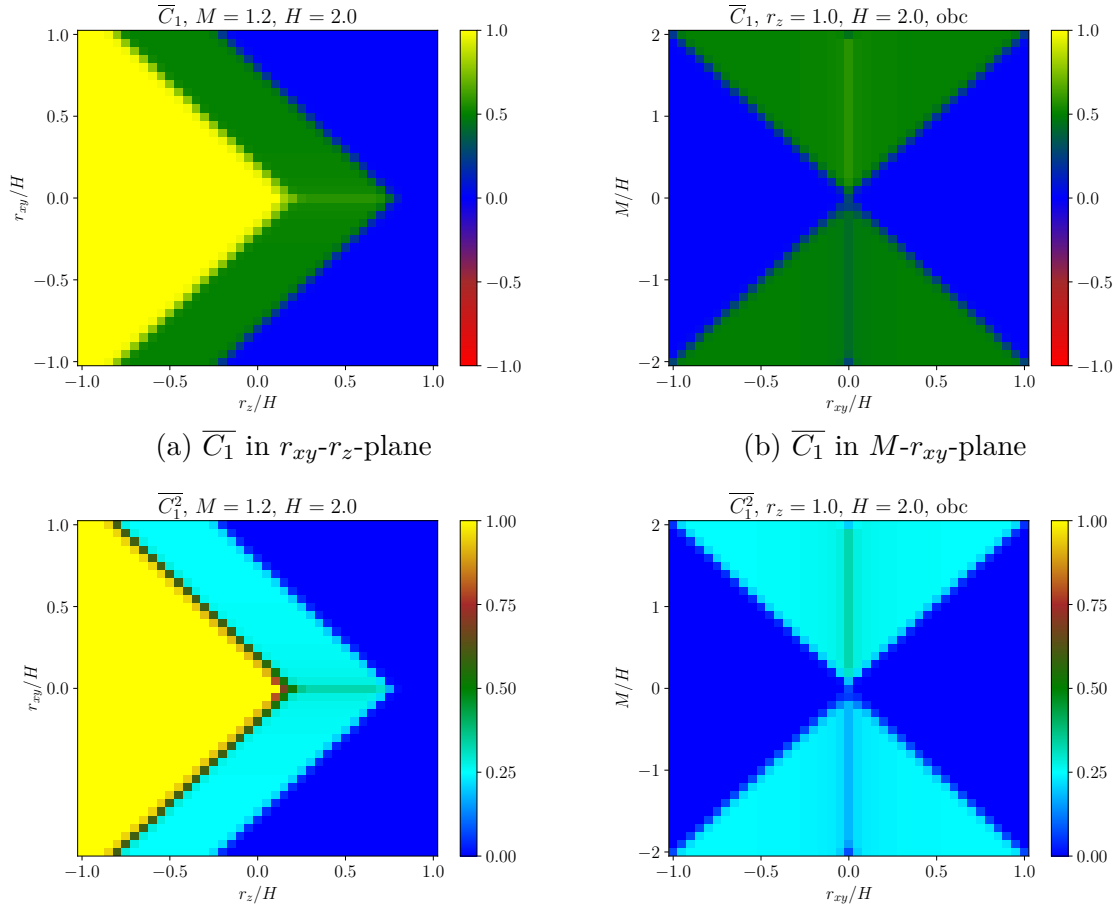

(a) $\overline{C_1}$ in r_{xy}-r_z-plane

(b) $\overline{C_1}$ in M-r_{xy}-plane

(c) $\overline{C_1^2}$ in r_{xy}-r_z-plane

(d) $\overline{C_1^2}$ in M-r_{xy}-plane

Figure 3.5: Averaged phase diagrams from ED for sphere 1 for driving from north to south pole along the $\phi = 0$ meridian with $H = 2.0$ and $v = 0.005$ and the other parameters as indicated, showing $\overline{C_1}$ in a) and b), and $\overline{C_1^2}$ in c) and d). The phase diagrams were obtained by averaging the disordered partial Chern marker at each point in parameter space over 40 different configurations of the mass disorder drawn from a normal distribution, which was of the form of Eqs. (3.20) with $\overline{\delta M_i} = 0$ and $\sigma_i = 0.05$.

3.2.1 The clean case

At the north pole

In order to interpret the Hamiltonian in terms of Majorana fermions, we first employ a Jordan-Wigner transformation of the standard form [121, 188]

$$\sigma_i^z = 2n_i - 1, \tag{3.31a}$$

$$\sigma_i^y = -i \prod_{j<i} (1 - 2n_j)(c_i^\dagger - c_i), \tag{3.31b}$$

$$\sigma_i^x = \prod_{j<i} (1 - 2n_j)(c_i^\dagger + c_i). \tag{3.31c}$$

The operators c_i fulfill fermionic anticommutation relations and we defined $n_i = c_i^\dagger c_i$. The Hamiltonian at the north pole then reads (with $M_1 = M_2$) [36]

$$\mathcal{H}(\theta = 0) = -(H + M)(n_1 + n_2 - 1) + r_z(2n_1 - 1)(2n_2 - 1). \tag{3.32}$$

Consequently, we can decompose each of these fermions into a real and an imaginary part similarly to the consideration of the Kitaev wire in Eq. (1.33) discussed in Sec. 1.1.2, which will give us two Majorana fermions on each site that we call α_i and η_i [14, 36, 52]. We define similarly to Eq. (1.30)

$$\eta_i = \frac{c_i^\dagger + c_i}{\sqrt{2}}, \tag{3.33a}$$

$$\alpha_i = \frac{c_i^\dagger - c_i}{\sqrt{2}i}. \tag{3.33b}$$

The operators η_i and α_i fulfill the fermionic anticommutation relations from Eq. (1.31). From the definition in Eqs. (3.33), we find $2n_i - 1 = 2i\alpha_i\eta_i$ and thus we rewrite the Hamiltonian as

$$\mathcal{H}(\theta = 0) = -\left(\frac{H}{2} + \frac{M}{2}\right)(2i\alpha_1\eta_1 + 2i\alpha_2\eta_2) + r_z(2i\alpha_1\eta_1)(2i\alpha_2\eta_2). \tag{3.34}$$

Note that the Hamiltonian commutes with the parity operators $\mathcal{P}_i = 2i\alpha_i\eta_i$, i.e., $[\mathcal{H}, \mathcal{P}_i] = 0$, whose eigenvalues are thus good quantum numbers. They are squaring to one, i.e., $(2i\alpha_i\eta_i)^2 = 1$, so they have possible eigenvalues $\mathcal{P}_i |\psi_{ij}\rangle = \pm |\psi_{ij}\rangle$, where $|\psi_{ij}\rangle$ is a common eigentstate of the Hamiltonian and the parity operator $\mathcal{P}_i$ and $j = \pm$. From here, we see that if $\frac{H}{2} + \frac{M}{2} > r_z$, the ground state will fulfill $2i\alpha_i\eta_i |GS\rangle = + |GS\rangle$. To reach $C_i = \frac{1}{2}$, we required the condition from Eq. (1.41) for the situation without disorder, which then fixes these two parities to be positive. This corresponds to two Majorana fermions bound together on each site, or, stated differently, one local Dirac fermion on each site, similar to the trivial phase of the Kitaev wire. This is consistent with the ground state being $|\uparrow\uparrow\rangle$ on the north pole.

A transverse coupling according to Eq. (3.13) reads in terms of the Jordan-Wigner fermions $\mathcal{H}_{xy} = 2r_{xy}(c_1^\dagger c_2 + c_2^\dagger c_1)$ and therefore, in terms of the Majorana fermions:

$$\mathcal{H}_{xy} = 2r_{xy}(2i\alpha_1\eta_2 - 2i\eta_1\alpha_2). \tag{3.35}$$

Note that the Hamiltonian now does not commute with the local parity operators $\mathcal{P}_i = 2i\alpha_i\eta_i$ anymore. Instead, it commutes with the sum of both parities, i.e.,

$$[\mathcal{H}(\theta = 0) + \mathcal{H}_{xy}, 2i\alpha_1\eta_1 + 2i\alpha_2\eta_2] = 0 \tag{3.36}$$

This is equivalent to the statement that in a free fermionic model (which the Hamiltonian corresponds to in terms of the c_i-fermions), the total particle number is preserved. Under the condition identified in Eq. (3.15), the ground state at the north pole is that with $\langle 2i\alpha_1\eta_1 + 2i\alpha_2\eta_2\rangle = 2$, which can only be achieved when for $i = 1, 2$, $\langle 2i\alpha_i\eta_i\rangle = 1$. Therefore, we can conclude that the ground state at the north pole will have two locally bound Majorana fermions on each site[4]. In the following we will explore how a different Majorana signature can be found at the south pole in relation to the fractional phase.

At the south pole

A the south pole, with $r_{xy} = 0$ and under the condition $r_z > \frac{H}{2} - \frac{M}{2}$, the ground state is found in the degenerate subspace $\{|\uparrow\downarrow\rangle, |\downarrow\uparrow\rangle\}$. Close to the south pole, the effective Hamiltonian derived from perturbation theory in Eq. (3.1) can in terms of the spin operators be written as [36]

$$H_{\text{eff}}^{\{|\uparrow\downarrow\rangle,|\downarrow\uparrow\rangle\}}(\theta = \pi^-) = r_z\sigma_1^z\sigma_2^z - \frac{H^2}{4}\sin^2\theta\frac{r_z}{r_z^2 - \frac{1}{4}(H-M)^2}\sigma_1^x\sigma_2^x. \tag{3.37}$$

Using the Jordan-Wigner transformation from Eqs. (3.31), a consequent rewriting in terms of Majorana fermions from Eqs. (3.33) and changing the order of the Majorana operators using the anticommutation relations gives

$$H_{\text{eff}}^{\{|\uparrow\downarrow\rangle,|\downarrow\uparrow\rangle\}}(\theta = \pi^-) = r_z(2i\alpha_1\eta_2)(2i\eta_1\alpha_2) - \frac{H^2}{4}\sin^2\theta\frac{r_z}{r_z^2 - \frac{1}{4}(H-M)^2}(2i\alpha_1\eta_2). \tag{3.38}$$

This Hamiltonian commutes with the two non-local Majorana parity operators $\tilde{\mathcal{P}}_1 = 2i\alpha_1\eta_2$ and $\tilde{\mathcal{P}}_2 = 2i\eta_1\alpha_2$ and these two parity operators commute with each other. Both $\tilde{\mathcal{P}}_1$ and $\tilde{\mathcal{P}}_2$ square to one, therefore their eigenvalues are ± 1. From the first term in Eq. (3.38), we see that for $r_z > 0$, the ground state of the Hamiltonian will have opposite eigenvalues of these two parities, i.e., $2i\alpha_1\eta_2 |GS\rangle = -2i\eta_1\alpha_2 |GS\rangle = \pm |GS\rangle$. The second term, however, fixes $2i\alpha_1\eta_2 |GS\rangle = |GS\rangle$. Therefore, we find

$$2i\alpha_1\eta_2 |GS\rangle = -2i\eta_1\alpha_2 |GS\rangle = |GS\rangle . \tag{3.39}$$

This implies that two Majorana fermions are bound across the two sites, thus reflecting the entanglement of the ground state at the south pole. This allows an interpretation of the fractional $C_i = \frac{1}{2}$-phase in terms of the pairing of Majorana fermions: While two Majorana fermions are bound at each site on the north pole, they reach a non-local pairing at the south pole. This interpretation is shown pictorially in Fig. 3.6. Note that this scheme consistently remains valid when turning on an r_{xy}-coupling. From the transverse coupling Hamiltonian in Eq. (3.13) using the Jordan-Wigner transformation (3.31), we

[4]This of course corresponds to the state $|\uparrow\uparrow\rangle$ in the spin language.

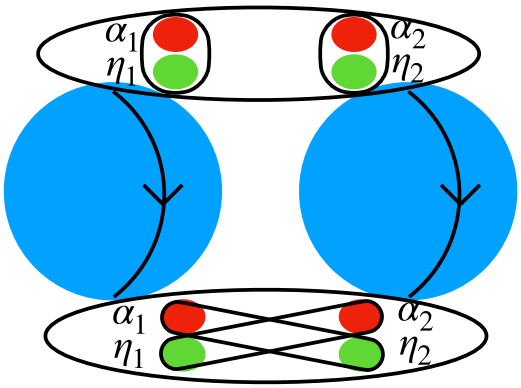

Figure 3.6: Schematic view of the interpretation of the fractional phase in terms of the Majorana fermions from Eqs. (3.33). The pairing is local on the north pole, but non-local on the south pole, driving along a Meridian thus leads to a crossover in these signatures.

find the term already cited in Eq. (3.35). This is already written in terms of the non-local parities $2i\alpha_1\eta_2$ and $2i\eta_1\alpha_2$. If $r_z > 0$ and $r_{xy} < 0$, the ground state therefore consistently remains fulfilling the condition from Eq. (3.39) above. In this way, the antiferromagnetic transverse coupling reinforces the Majorana pairing shown in Fig. 3.6.

As we will see in the following, a rotation of the basis at the south pole allows to see that two of the Majorana fermions at the south pole will be coupled non-locally, while two others will be energetically free if $r_{xy} = 0$. This can give rise to interesting applications of the setup under configuration for quantum information storage and manipulation. Before discussing these perspectives, let us study the influence of disorder in the masses on the Majorana structure introduced in the present section.

3.2.2 Disordered case

Disorder through a mass imbalance as introduces around Eq. (3.16) intervenes as

$$\mathcal{H}_{\text{dis}} = -\frac{\delta M_1}{2} 2i\alpha_1\eta_1 - \frac{\delta M_2}{2} 2i\alpha_2\eta_2. \tag{3.40}$$

At the north pole

At the north pole, the full Hamiltonian still commutes with the sum of the local parity operators, i.e., we can generalize Eq. (3.36) to include the disorder contribution (3.40) on the left side of the commutator. Then, as discussed in Sec. 3.1.2 using the spin language, if the disorder has a small variance and a zero average, it is possible to assure the state $|\uparrow\uparrow\rangle$ as ground state at the north pole, corresponding to a local pairing of the two Majorana fermions on each site, i.e., $2i\alpha_1\eta_1 |GS\rangle = 2i\alpha_2\eta_2 |GS\rangle = |GS\rangle$. This continues to hold true when adding a transverse coupling but remaining in the parameter range given in

Eq. (3.27).

At the south pole

At the south pole, the situation is more subtle: The disorder part of the Hamiltonian (3.40) does not commute with the non-local parities $2i\alpha_1\eta_2$ and $2i\eta_1\alpha_2$. The response of the Majorana signature to the addition of disorder then underlines the crucial differences between the cases with and without a transverse coupling pointed out in Sec. 3.1.2 in the spin language:

Firstly, for the case with $r_{xy} = 0$, the full Hamiltonian close to the south pole[5] commutes with both of the local parities $2i\alpha_i\eta_i$. The r_z-coupling favours opposite sign of the two parities when acting on the ground state, but the key point is that in this case, two Majorana fermions are being bounded locally at each site. This corresponds to the breaking of the $C_i = \frac{1}{2}$ phase into a phase with $(C_1, C_2) = (1, 0)$ or $(C_1, C_2) = (0, 1)$, as described in Sec. 3.1.

For the case with $r_{xy} \neq 0$, the full Hamiltonian at the south pole in the $\{|\uparrow\downarrow\rangle\, |\downarrow\uparrow\rangle\}$-subspace reads in terms of the Majorana fermions introduced in Eq. (3.33)

$$\mathcal{H}^{\{|\uparrow\downarrow\rangle,|\downarrow\uparrow\rangle\}}(\theta = \pi) = r_z(2i\alpha_1\eta_2)(2i\eta_1\alpha_2)+2r_{xy}(2i\alpha_1\eta_2-2i\eta_1\alpha_2)-\frac{\delta M_1}{2}2i\alpha_1\eta_1-\frac{\delta M_2}{2}2i\alpha_2\eta_2. \tag{3.41}$$

Without the r_{xy}-term, the Hamiltonian right at the south pole would commute with the local parities $2i\alpha_i\eta_i$, but the r_{xy} term breaks this symmetry and introduces a degree of superposition of the locally and non-locally entangled parity states. In particular, when δM_i goes to zero, we come back to the situation shown in Fig. 3.6, corresponding to a maximally entangled state.

In the following, we will introduce an alternative mapping to Majorana fermions at the south pole, allowing to understand the situation there in a different way and also giving an interesting view towards applications in quantum information.

Alternative mapping at the south pole

In order to understand the situation at the south pole with disorder better and give perspectives with regards to applications, we introduce a rotated basis for the mapping to

[5]Close to the south pole, we include the perturbative term as in Eq. (3.38), which commutes with the local parities.

Majorana fermions: Consider a rotated Jordan-Wigner transformation of the form [36]

$$\sigma_i^z = -i\prod_{j<i}(1-2n_j^d)(d_i^\dagger - d_i), \tag{3.42a}$$

$$\sigma_i^y = 1-2n_i^d, \tag{3.42b}$$

$$\sigma_i^x = \prod_{j<i}(1-2n_j^d)(d_i^\dagger + d_i). \tag{3.42c}$$

Then we introduce new Majorana operators by

$$\zeta_i = \frac{d_i^\dagger + d_i}{\sqrt{2}}, \tag{3.43a}$$

$$\beta_i = \frac{d_i^\dagger - d_i}{\sqrt{2}i}. \tag{3.43b}$$

The Hamiltonian from Eq. (3.41) in terms of these new Majorana fermions reads

$$\mathcal{H}^{\{|\uparrow\downarrow\rangle,|\downarrow\uparrow\rangle\}}(\theta=\pi) = -r_z(2i\zeta_1\beta_2) + r_{xy}(2i\beta_1\zeta_2 + (2i\zeta_1\beta_1)(2i\zeta_2\beta_2)) \\ - \frac{\delta M_1}{2}\sqrt{2}\beta_1 - \frac{\delta M_2}{2}(2i\zeta_1\beta_1)\sqrt{2}\beta_2. \tag{3.44}$$

We observe that for $\delta M_i \to 0$, the Hamiltonian commutes with the non-local parities $2i\zeta_1\beta_2$ and $2i\beta_1\zeta_2$ and the ground state will for $r_z > 0$ and $r_{xy} < 0$ satisfy

$$2i\zeta_1\beta_2\,|GS\rangle = 2i\beta_1\zeta_2\,|GS\rangle = |GS\rangle\,. \tag{3.45}$$

This implies a non-local binding of the Majorana fermions across the two different sites. Note that for $r_{xy} > 0$, we obtain

$$2i\zeta_1\beta_2\,|GS\rangle = -2i\beta_1\zeta_2\,|GS\rangle = |GS\rangle\,, \tag{3.46}$$

implying that the same signature occurs in the region of phase space that was made accessible by the disorder in Sec. 3.1.3, but with one parity operator taking an opposite eigenvalue. From the form of the mass-disorder terms proportional to δM_i, we see that both of them involve an odd number of Majorana fermion operators. Thus, we can immediately conclude that they do not contribute to first order in $\delta M_i/r_{xy}$ and $\delta M_i/r_z$. Therefore, we conclude that in a perturbative sense, the non-local Majorana structure is maintained if the ground state lies in the $\{|\uparrow\downarrow\rangle\,, |\downarrow\uparrow\rangle\}$-subspace. Note that this condition is violated if $r_{xy} = 0$, as discussed in Sec. 3.1, such that in this case the mapping to the Majorana structure breaks down when adding disorder. In Fig. 3.4e, we have plotted the value of $\left\langle \sigma_1^+\sigma_2^- + \sigma_1^-\sigma_2^+ \right\rangle$ in time, which corresponds in Majorana language to $\langle 2i\beta_1\zeta_2 + (2i\zeta_1\beta_1)(2i\zeta_2\beta_2)\rangle$. In this way we can verify that a deviation from the parities with disorder occurs only to second order

in $\delta M_i/r_{xy}$ (cf. Eq. (3.29) and its discussion).

If $r_{xy} = 0$ and *without disorder*, the Majorana fermions from Eqs. (3.43) can be used to rewrite the effective Hamiltonian close to the south pole from Eq. (3.37) obtained from perturbation theory as

$$\mathcal{H}_{\text{eff}}^{\{|\uparrow\downarrow\rangle,|\downarrow\uparrow\rangle\}}(\theta = \pi^-) = -r_z(2i\zeta_1\beta_2) - \frac{H^2}{4}\sin^2\theta\frac{r_z}{r_z^2 - \frac{1}{4}(H-M)^2}(2i\beta_1\zeta_2). \tag{3.47}$$

We see that for $r_z > 0$ the ground state still satisfies $2i\zeta_1\beta_2\,|GS\rangle = |GS\rangle$ and if $\theta \lesssim \pi$, $2i\beta_1\zeta_2\,|GS\rangle = |GS\rangle$. However, in this case, when $\theta = \pi$ is reached using the driving protocol $\theta = vt$ introduced in Chap. 2, the Majorana fermions β_1 and ζ_2 become essentially free in an energetic sense: Their entanglement properties can be changed without an energy cost[6]. We will exploit this in the following to lay out potential applications of this setup to the storage and modification of quantum information.

3.3 Applications for quantum information

As mentionned above, using a setup without transverse coupling, from the mapping to Majorana fermions laid out in Eq. (3.43), we find two gapless Majorana zero-modes at the south pole. This allows to reinterprete the non-local Majorana parity $2i\beta_1\zeta_2$ as the z-component of a parity qubit. It has been proposed that the unpaired Majorana edge modes of a long fermionic chain can be used to store quantum information in a topological way, which can be thought of as a parity qubit [14]. This way of thinking about a protected qubit enjoys great interest in theoretical and experimental research, as it is stable towards local perturbations [16, 47, 52, 182, 189]. Setups where the qubit is realized on two sites only have been proposed and are studied as realizations of singlet-triplet qubits similar to the situation of the Hamiltonian at the south pole discussed in this chapter [182, 190–192] and have recently been realized experimentally [17]. Here we will show how the setup of two driven coupled spins allows to create and manipulate a parity qubit, how this can be seen both from the spin language and in terms of Majorana fermions and which role disorder and the fractional topology play for this.

3.3.1 A parity qubit

As mentioned above, we can interprete the Majorana parity as the z-component of a quantum spin degree of freedom. For simplicity, we call $P_z = 2i\beta_1\zeta_2$. We already used the fact that the eigenvalues of this operator are ± 1. If we translate the parity operator back

[6] When driving from north to south pole, the parity will of course remain fixed at $2i\beta_1\zeta_2\,|GS\rangle = |GS\rangle$ due to adiabatic connectedness. What we mean here is that acting with a new Hamiltonian at the south pole, we now have the freedom to modify this bound without paying an energy cost.

into the spin language using Eqs. (3.43) and (3.42), we find

$$P_z = 2i\beta_1\zeta_2 \leftrightarrow (d_1^\dagger - d_1)(d_2^\dagger + d_2) \leftrightarrow \sigma_1^x\sigma_2^x. \tag{3.48}$$

From this correspondence, we can conclude that the eigenstates of $P_z\,|p_z = \pm\rangle = \pm\,|p_z = \pm\rangle$ with eigenvalue $p_z = \pm 1$ in the spin language are

$$|p_z = \pm\rangle \leftrightarrow \frac{1}{\sqrt{2}}\left(|\uparrow\downarrow\rangle \pm |\downarrow\uparrow\rangle\right). \tag{3.49}$$

We see that the two different Majorana parities corresponding to different eigenstates of the operator P_z correspond precisely to the entangled states which we called $|1,0\rangle$ and $|0,0\rangle$ in Sec. 3.1.2, referring to the basis of two added spin-$\frac{1}{2}$. In said Sec. 3.1.2, we concluded that a mass asymmetry allows to access the singlet state which otherwise is not accessible when initializing the system in a ferromagnetic state. Therefore, the consideration of a small asymmetry (or disorder) will reveal important features of the parity qubit proposed here. From this correspondence and the mapping between the Majorana fermions and the spin system, it is then straightforward to construct the spin algebra:

$$P_x = |p_z = -1\rangle\langle p_z = +1| + |p_z = +1\rangle\langle p_z = -1| \leftrightarrow \frac{\sigma_1^z - \sigma_2^z}{2} \leftrightarrow \frac{\beta_1}{\sqrt{2}}(1 + 2i\zeta_1\beta_2), \tag{3.50}$$

$$P_y = i\,|p_z = -1\rangle\langle p_z = +1| - i\,|p_z = +1\rangle\langle p_z = -1| \leftrightarrow \frac{\sigma_1^x\sigma_2^y - \sigma_1^y\sigma_2^x}{2} \leftrightarrow -\frac{\zeta_2}{\sqrt{2}}(1 + 2i\zeta_1\beta_2). \tag{3.51}$$

3.3.2 Preparing states of a parity qubit

As we showed in the previous section, the ground state space at the south pole can be identified as that of a parity qubit. We now want to demonstrate how the protocol defining the (partial) topology of the two spin-1/2 can be used to prepare states of such a parity qubit in a controlled way. For this, we consider the z-direction as our computational basis. Using the considerations from the previous section and from Sec. 3.1.2, the ground state at the south pole will be a fully entangled state if $C_i = \frac{1}{2}$. If in addition $r_{xy} < 0$, the state will be $|p_z = +1\rangle$ (or, equivalently, $|1,0\rangle$ in spin language). On the other hand, if $r_{xy} > 0$ and there is a small detuning between the masses at both sites, the state at the south pole will approach $|p_z = -1\rangle$ (or, equivalently, $|0,0\rangle$ in spin language). As the latter case is enabled by the presence of disorder, there will be a correction to the state in $\Delta M/r_{xy}$, which can however be tuned to arbitrarily small values if there is sufficient experimental control over the mass imbalance ΔM and r_{xy}[7].

The setup of two coupled spheres can thus be used to create a non-local parity qubit

[7]The requirement to take care of is that the driving speed v to go from the north to the south pole remains much smaller than ΔM.

state at the south pole oriented along the z-direction (in the basis of the parity qubit) from a product state at the north pole. The creation of entanglement using this protocol is directly related to the fractionalization of the partial Chern numbers C_i. We can thus conclude that a high fidelity of the state preparation manifests itself with $C_i \to 1/2$. This application requires a finite amount of disorder between the two sites, we can thus argue that it includes the influence of disorder in a controlled way.

Let us mention that from Eq. (3.50), our protocol also allows to prepare states of the parity qubit oriented in x-direction. In the spin language, these corresponds to the states $|\uparrow\downarrow\rangle$ and $|\downarrow\uparrow\rangle$. As discussed in Sec. 3.1, these correspond to integer partial topological numbers, with the sum $C_1 + C_2 = 1$ maintained at one. These states can be achieved at the south pole by setting $r_{xy} = 0$ and adding a small detuning between the masses of both sites. This then corresponds to locally binding two Majorana fermions at each site.

The fractionalization of the partial Chern number C_i is a measure of entanglement between both sites and allows for the application to a parity qubit created at the south pole inherently requiring such formation of entanglement.

3.3.3 A Pauli-X gate

Finally, let us show how a Pauli-X gate could be constructed using the parity qubit and the considerations regarding the transverse coupling. As we have seen, disorder is needed in order to access the ground state manifold of the parity qubit. The sign of the transverse coupling determines the state at the south pole. One can therefore hypothesize a situation of changing sign of this coupling to switch between the two states of the qubit. This leads to the following protocol:

1. Preparing the system with parameters for the $C_i = 1/2$-phase, a transverse coupling r_{xy} and a small mass detuning ΔM.

2. Driving from the north to the south pole in order to create the parity qubit and ascribe a state $|p_z = \pm\rangle$ to it.

3. Staying at the south pole, one can now switch the sign of r_{xy} adiabatically in order to flip the state of the parity qubit with high fidelity. This can be realized, e.g., by setting $r_{xy}|_{t>\frac{\pi}{v}} \to r_{xy} \cos\left(\omega t - \frac{\pi}{v}\right)$, with $\omega \ll \Delta M$ to maintain adiabaticity.

This then allows to flip the state of the parity qubit at the south pole with high fidelity, as can be seen from Fig. 3.7. This protocol can thus be seen as an application of the $C_i = 1/2$ phase formed when driving from the north to the south pole: At the south pole, it allows to create and manipulate a parity qubit which can prospectively be used to store quantum information with good coherence properties due to its non-local nature. Varying the r_{xy}-coupling in time, as shown in Fig. 3.7, then induces transitions to the singlet state,

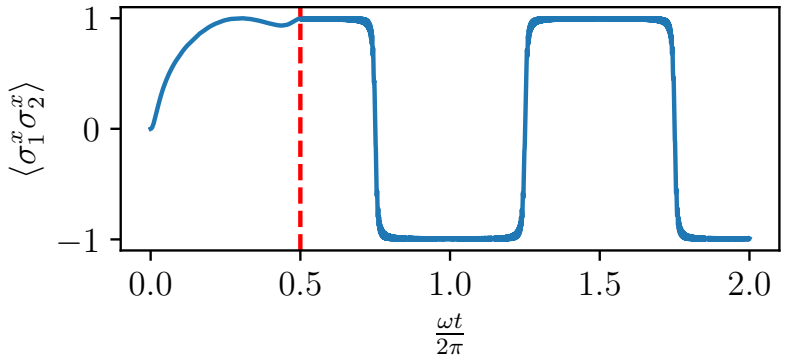

Figure 3.7: Application of the two-spheres model as a Pauli X-gate. The system is prepared at the north pole in the ground state $|\uparrow\uparrow\rangle$ and consequently driven to the south pole (shown by the red dashed line), where it is in the entangled state $\frac{1}{\sqrt{2}}(|\uparrow\downarrow\rangle + |\downarrow\uparrow\rangle)$. The r_{xy} coupling is then varied in time, thus flipping the state to $\frac{1}{\sqrt{2}}(|\uparrow\downarrow\rangle - |\downarrow\uparrow\rangle)$. A periodic variation of r_{xy} leads to a formation of plateaus in the parity $\langle\sigma_1^x\sigma_2^x\rangle$ or equivalently $\langle 2i\beta_1\zeta_2\rangle$. Here, $H = 2.0$, $(M_1, M_2) = (0.6, 0.62)$, $r_z = 1.0$, $r_{xy} = -0.1$ initially and is then varied $r_{xy}|_{t>\frac{\pi}{v}} \to r_{xy}\cos\left(\omega t - \frac{\pi}{v}\right)$ with $\omega = v = 10^{-4}$.

if a finite amount of disorder is present. In this way, this setup can be understood as a disorder-enabled Pauli-X gate.

3.4 Conclusion

In this chapter, we have studied a model of two coupled spins in a radial magnetic field in the light of its recently discovered novel fractional topological phases [12]. We have in particular studied the interplay of these phases with disorder and broken symmetries. We have discussed that a broken $\mathbb{Z}_2$ symmetry in the model of Eq. (1.34) leads to a deviation from the fractional phase, with the partial topological numbers (C_1, C_2) going from $(\frac{1}{2}, \frac{1}{2})$ to $(1, 0)$ or $(0, 1)$. Then we have seen how adding a transverse coupling can restore properties of the system mimicking these of the clean fractional phase upon averaging over weak disorder. Interestingly, disorder also enables new transitions in the spin system, leading to the occurence of an averaged fractional phase in new regions of phase space. This is a different mechanism than for the topological Anderson insulator discussed in Sec. 1.3.2 and opens new perspectives on how disorder in interacting systems can change effective topological properties.

We have then discussed an interpretation of the fractional phases in terms of Majorana fermions [36] and its relation with the transverse coupling, the disorder and the extended fractional phase. This opened a view on applications, in which the Majorana fermions at the south pole can be used to store information [17, 182].

As mentioned in the introductory Sec. 1.1.2, the spin model can be seen as an analogue

of other condensed matter models as a Haldane layer or a Kitaev wire. It is well justified to ask about the occurence of the fractional phases and applications of the formalism described in Sec. 1.1.3 also in these analogous models when coupling two similar systems together. This has been discussed for two Haldane layers [12, 13] and two Kitaev wires [51] and remains an active question of research in our group. Here, we have studied the spin model in its own right, as new effects can be straightforwardly understood in this platform, and, as Chap. 2 and also Sec. 3.3 of the present chapter showed, yield interesting implications and applications. The relevance of this model is furthermore underlined by experimental progress on it [35,37]. In general, spin systems constitute a topical platform to describe and understand new physical effects in the realm of complex quantum systems (in particular, in one dimension), as they are accessible from a numerical and an experimental point of view and yield direct connections to potential applications. We have so far already seen spin systems in the context of (effective) topological properties, quantum open system dynamics, quantum energy and quantum thermodynamics (cf. Chap. 2) and in relation to fractional topology, disorder, Majorana fermions and quantum information in the present chapter. As such, one-dimensional coupled spin systems are also a commonly used platform to study *localization phenomena*, introduced in Sec. 1.3. In the following two chapters, we will focus on such effects in an effective spin chain in different regimes, and put a special emphasis on implementability and detection of these phenomena, as well as their interplay with global and local properties of the system.

Chapter 4

From bosonic ladders to spin chains

The models introduced in this thesis so far, ranging from interacting spin models, over one- and two-dimensional fermionic models to models for open quantum systems, all had unique features justifying their discussion in the light of fundamental physical understanding in its own right. An important challenge and in the same time a fascinating aspect of theoretical condensed matter physics is however finding unifying features across different models, allowing to understand them in a more universal way and in the same time linking to experimental progress and applications. The discussion of topological properties in interacting systems from Sec. 1.1 and Chapter 3 indeed opened perspectives on other condensed matter models such as the Haldane model, or the Kitaev wire, as discussed in Sec. 1.1.2.

On a more general level, there are attempts for topological systems to organize them in a systematic fashion in the form of a classification table, according to their symmetries and dimensionality and assigning the occurence of topological invariants [193–195]. The Kitaev wire is a p-wave superconductor [14] in one dimension, the model as stated in Eq. (1.24) has a combined time-reversal and particle-hole symmetry (thus a chiral symmetry, similarly as the SSH model from Eq. (1.62)) [195]. The interesting topological properties of the Kitaev wire discussed in Sec. 1.1.2 require only the particle-hole symmetry, which is then associated with the $\mathbb{Z}_2$ winding number from Eq. (1.29).

The Kitaev wire is a topological superconductor. Superconductivity more generally is a phenomenon that has been discovered experimentally in materials and discussed theoretically many years before [196–198]. This can be seen as an allegory for the new power of theoretical physics in condensed matter: Rather than 'only' explaining experimental observation (a task that is very challenging and cumbersome in itself), the theoretical study of abstract models for new phenomena can also spur experimental interest. Superconductivity was first discovered experimentally [196], then described theoretically by Bardeen–Cooper–Schrieffer (BCS) theory [198], which then allowed Kitaev to hypothesize the p-wave superconducting wire hosting Majorana edge states [14]. This last step was done before experimental evidence of these exotic edge states was found, which, as we

mentioned before, remains in fact controversial until today.

In the spirit of discovering new properties in lower dimensions, while remaining inspired by established concepts, we will in this chapter introduce a model in a one-dimensional geometry that exhibits effects analogous to the Meissner effect in three-dimensional superconductors [197]. To underline the phenomenological journey across different models, we will show under what conditions this platform can serve as an analogue to spin models and how it can be used to implement and test disorder and localization physics.

Novel experimental techniques to artificially create condensed matter systems in laboratories have enabled and fueled research of quantum systems revealing new exotic properties and collective phenomena. One of these techniques that has gained a lot of popularity in recent years due to its high degree of control over parameters uses cold atomic gases in optical lattices [199–202]. This allows to realize a wide range of lattice models, such as the Bose-Hubbard model [199, 200, 203] or various spin chain models [204], for example. In addition, synthetic gauge fields can be implemented using periodic modulation - so called *Floquet engineering* - of the Hamiltonian [205–207], which allows to study topological models such as the Haldane model [9, 208–210] discussed in Sec. 1.1.2 and gives itself rise to new physical phenomena, such as anomalous Floquet toplogical phases [211]. Furthermore, Floquet modulation of the Hamiltonian allows to simulate $\mathbb{Z}_2$ lattice gauge theories [212–214].

The bosonic ladder model introduced in this chapter can be implemented using cold atoms. It is linked to recent studies of the simulation of $\mathbb{Z}_2$ lattice gauge theories in bosonic ladders [213–215]. The model features Peierls phases (which can be implemented using Floquet engineering) and thus allows to define a current observable and study physical properties of the system, in particular the localization behaviour when a second particle species - rendered as impurities - is introduced to the system. This current shows some analogies with the Meissner effect, which we are going to introduce in the following section.

This chapter is based on results published in [216]. I have started working on this project during my Master's under the guidance and supervision of Karyn Le Hur and with the help of Fan Yang. Karyn Le Hur has worked with collaborators on the Meissner effect in a bosonic ladder system before [217, 218] and initiated this project. I developed analytical calculations extending these previous results to the situation where a second particle species populates the lattice, acting as impurities. These included different approximation schemes, perturbative techniques, as well as bosonization and a renormalization group analysis. Furthermore, I developed numerical methods to test the physical effect using exact diagonalization and a fitting of the cut-off of a sum over momentum states.

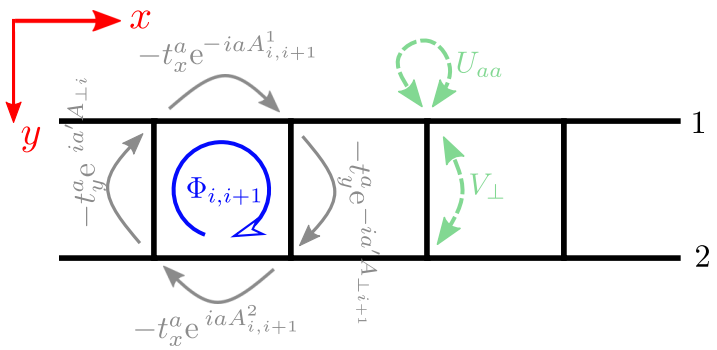

Figure 4.1: From [216]. A one-dimensional ladder geometry.

4.1 Meissner effect in a bosonic ladder

In 1933, Walther Meissner and Robert Ochsenfeldt found that a superconductor can screen a magnetic field that is exerted onto it [197]. The macroscopic explanation of this Meissner effect through the London equations [219] relates the external magnetic field to a current density forming on the surface of the superconductor and countering the external field up to a material-dependent critical field strength. Later it was found that certain so-called type-II superconductors actually have two critical field strengths: upon crossing the first one, they transition from the superconducting phase to a vortex phase, in which the magnetic field can enter the superconductor through a lattice of vortices of quantized currents [220, 221]. This is similar to the vortices of quantized circulation forming in a superfluid [222, 223].

In the following section, we will explain how an analogue of this effect in a bosonic two-leg ladder geometry can arise.

4.1.1 Superfluid phase

We are considering a bosonic ladder geometry as shown in Fig. 4.1. Subject to a magnetic field, what we call an analogue of the Meissner effect is the formation of surface currents along the 'edge' (i.e., the legs) of the ladder, which are proportional to the negative magnetic flux. In the superfluid phase of the bosonic hopping model, i.e., when tunneling amplitudes between sites are much larger than local potentials and the wavefunctions of the particles have large extensions, this effect has been predicted theoretically [224] and verified experimentally [225]. The Hamiltonian corresponding to the setup shown in Fig. 4.1 can be written as

$$\mathcal{H}_a = -t_x^a \sum_{\alpha,i} \mathrm{e}^{iaA^\alpha_{i,i+1}} a^\dagger_{\alpha i} a_{\alpha,i+1} - t_y^a \sum_i \mathrm{e}^{-ia' A_{\perp i}} a^\dagger_{2i} a_{1i} + \mathrm{h.c.} \\ + \frac{U_{aa}}{2} \sum_{\alpha,i} n^a_{\alpha i}(n^a_{\alpha i} - 1) + V_\perp \sum_i n^a_{1i} n^a_{2i} - \mu \sum_{\alpha,i} n^a_{\alpha i}. \quad (4.1)$$

We are using a subscript 'a' for the particles, in order to distinguish them from the impurities which we will introduce in Sec. 4.2 with a subscript 'f'. We will in this chapter also refer to the particles with creation operator $a_i^\dagger$ as *a-particles*. They can hop along the legs and the rungs of the ladder with amplitudes t_x^a and t_y^a respectively. There is an on-site potential U_{aa} and an intrarung potential $V_\perp$ assigning an energy cost for two particles residing on the same site or on the same rung, respectively. Finally, there is a chemical potential μ.

The effect of a uniform magnetic field (or $\mathcal{U}(1)$ gauge field) in a bosonic model can be introduced by performing a Peierls substitution [226]. In a general way and following [217], we keep the possiblity to have different components of the magnetic vector potential along the legs and the rungs of the ladder, which thus enter as $A_{i,i+1}$ and $A_{\perp i}$ in the respective Peierls phases, together with the respective lattice spacings a and a'. The flux per plaquette can then be calculated from a contour integral around a plaquette. We obtain the following relation with the components of the vector potential [217, 224]:

$$\Phi_{i,i+1} = \oint \mathbf{A} \cdot d\mathbf{l} = -a(A^1_{i,i+1} - A^2_{i,i+1}) - a'(A_{\perp i+1} - A_{\perp i}). \tag{4.2}$$

In the superfluid phase, we write the bosonic operators in the phase-angle representation, i.e., $a^\dagger_{\alpha i} = \sqrt{n_{\alpha i}} \mathrm{e}^{i\Theta_{\alpha i}}$ and at commensurate filling the interrung hopping-term proportional to t_y^a then takes the form of a Josphson coupling term between the two rungs [217]. The minimization of the variational energy with respect to the expectation values $\langle \Theta_{\alpha i} \rangle$ then leads to a pinning of these phases to $A_{\perp i} a' + \Theta_{1i} - \Theta_{2i} = 2\pi l$ with $l \in \mathbb{Z}$ when t_y^a is the dominant energy scale in the system [217].

We can define a local current on each rung as the time-derivative of the relative density operator, i.e., at a site i

$$j_i = \frac{\mathrm{d}(n_{1i} - n_{2i})}{\mathrm{d}t} = i[\mathcal{H}_a, n_{1i} - n_{2i}] = j_{i,\perp} + j_{i,\parallel}. \tag{4.3}$$

This gives a perpendicular and a parallel component, i.e., a current along the rung flowing from one leg to the other and a contriubtion flowing in or out of the rung. Evaluating the commutator, we define [217]

$$j_{i,\parallel} = i t_x^a (\mathrm{e}^{iaA^1_{i,i+1}} a^\dagger_{1i} a_{1,i+1} + \mathrm{e}^{iaA^2_{i,i+1}} a^\dagger_{2i} a_{2,i+1}) + \mathrm{h.c.}, \tag{4.4a}$$

$$j_{i,\perp} = -2 i t_y^a (\mathrm{e}^{ia' A_{\perp i}} a^\dagger_{1i} a_{2i}) + \mathrm{h.c.}. \tag{4.4b}$$

Then, for weak coupling between the rungs, using the pinning of the phase in the superfluid

phase discussed above, one can find [217]

$$\langle j_{i,\parallel}\rangle = -2nt_x^a((A^1_{i,i+1} - A^2_{i,i+1})a + (A_{\perp i+1} - A_{\perp i})a') = -2nt_x^a\Phi_{i,i+1}, \tag{4.5a}$$

$$\langle j_{i,\perp}\rangle = 0. \tag{4.5b}$$

This derivation shows how a surface current comes about in the introduced setup. In [224] it has been shown from studying the low-energy properties of the system that at a critical field strength, current vortices develop, which lead do a decreasing screening current. While the development of a screening current along the legs is somewhat intuitive in the superfluid phase, the effect persists even in the Mott insulating phase of the model. We will study this more closely in the following section.

4.1.2 Rung-Mott phase

In the rung-Mott insulating phase, the particles are localized at a rung due to strong interactions. Applying an electromagnetic field (here represented by the $\mathcal{U}(1)$ gauge field) to an insulating phase, one would intuitively not expect the formation of currents as seen in the superfluid phase. However, due to spin-charge separation in the Mott insulating phase, one can yet observe a spin current with an insulating charge sector [217]. This will be made more explicit in this section.

The model described by Eq. (4.1), in the limit of decoupled rungs with $t_x^a = 0$ and at commensurate filling, is in the rung-Mott phase for $U_{aa} - V_\perp \gg t_y^a$ and $V_\perp + t_y^a > \mu > -t_a^y$ [216,217], as can be shown from a consideration of the energetics in that case. Reintroducing t_x^a, it can be shown, e.g. using numerical techniques[1], that the rung-Mott phase occurs in a tip-like region in the t_x^a-μ-plane of the phase diagram [217]. We are focussing on the rung-Mott phase with one particle per rung and a small interrung hopping t_x^a. Then each particle on a rung can be identified with an effective spin-1/2 degree of freedom, marking yet another example of the usefulness of working in different languages in condensed matter setups. Identifying the particle residing on the upper leg with 'spin up' and on the lower leg with 'spin down', we can identify the bosonic operators with Pauli operators. Formally, this corresponds to the Schiwnger-boson representation of the spin $SU(2)$ algebra that reads [227]

$$\sigma_i^x = a_{1i}^\dagger a_{2i} + a_{1i}a_{2i}^\dagger, \tag{4.6a}$$

$$\sigma_i^y = -ia_{1i}^\dagger a_{2i} + ia_{1i}a_{2i}^\dagger, \tag{4.6b}$$

$$\sigma_i^z = a_{1i}^\dagger a_{1i} - a_{2i}^\dagger a_{2i}. \tag{4.6c}$$

In this language, the hopping along the legs can then be reintroduced to second order

[1] In [217], the authors have used a density matrix renormalization group approach.

in perturbation theory. Hopping from one rung to another leads to an energy cost of either $V_\perp$ or U_{aa}, which we assume to be large. Therefore, only second order processes between two rungs will contribute, in which one particle hops to a neighbouring rung, from which one of the two particles then hops to the now unoccupied rung. In summary, using Eqs. (4.6) for the hopping term along the rungs (i.e., proportional to t_y^a) and the effective Hamiltonian from perturbation theory, we find the effective spin model

$$\mathcal{H}_a = \sum_i - \left(2J_{xy}\sigma_i^+\sigma_{i+1}^- \mathrm{e}^{iaA_{i,i+1}^{\parallel}} + \text{h.c.} + J_z\sigma_i^z\sigma_{i+1}^z - g\left(\sigma_i^x \cos(a'A_{\perp i}) - \sigma_i^y \sin(a'A_{\perp i})\right)\right). \tag{4.7}$$

We called $J_{xy} = (t_x^a)^2/V_\perp$ and $J_z = (t_x^a)^2(1/V_\perp - 2/U_{aa})$, $g = t_y^a$, $A_{i,i+1}^{\parallel} = A_{i,i+1}^1 - A_{i,i+1}^2$ and we neglected a constant energy shift $-(t_x^a)^2(2/U_{aa} + 1/V_\perp)$.

The model in Eq. (4.7) defines an effective spin model in the rung-Mott phase from the original bosonic ladder model in Eq. (4.1), allowing to study the Meissner effect in this phase, but moreover provides a platform to propose the study of localization phenomena in spin chains. This will be the topic of the next sections. The model corresponds to a gauged XXZ-chain in a transverse field.

As for the Meissner effect, we can straightforwardly evaluate the derivative of the relative density operator on each rung to find the current operator which reads $j_i = i[\mathcal{H}_a, \sigma_i^z]$. We find contributions along the rungs (proportional to g) and along the legs (proportional to J_{xy}) and can identify the latter as the Meissner current. For each rung, assuming $g \gg J_{xy}, J_z$, the spin sector is in a superfluid phase, so that it is justified to adopt a phase-angle representation and from minimization of the energy, we can find the ground state in the limit of decoupled rungs to evaluate [217] [217]

$$\left\langle j_{\parallel,i} \right\rangle = -2J_{xy}\Phi_{i,i+1}, \tag{4.8a}$$

$$\langle j_{\perp,i} \rangle = 0. \tag{4.8b}$$

This has a form closely reminiscent of Eqs. (4.5). We can therefore again identify an analogue of the Meissner effect. In the following section, we want to see how this is modified under addition of a second particle species.

4.2 Meissner effect with a second particle species - Localization of the current

We now want to introduce a second particle species to the system, in order to see new effects in relation with the Meissner current and the $\mathcal{U}(1)$ gauge symmetry of the a-particles. Bosonic ladders with several particle species have recently gained attention as model systems to realize lattice gauge theories [213, 214, 228]. Another possibility arising from

this class of models and the system described by Eq. (4.7) in particular is to study the localization of one particle species as a response to the properties of the other, thus effectively rendering the latter as impurities. We will discuss all of these aspects in the following sections.

On the level of the bosonic Hamiltonian in Eq. (4.1), we can introduce a second particle species living on the same lattice in a similar way as the previously introduced a-particles. Let us call them 'f-particles' and for now consider them to be static, i.e. they remain on the same site at all times. On general grounds, we introduce a density-dependent interaction of the form

$$\mathcal{H}_{int}^{af} = U_{af} \sum_{\alpha,i} n_{\alpha,i}^{a} n_{\alpha,i}^{f}. \tag{4.9}$$

The f-particles can play several roles: On the one hand, they can lead to flux attachment for the a-particles [213, 214], which is a key to realize lattice gauge theories[2]. On the other hand, they in general introduce an additional potential scale felt by the a-particles, thus changing the physical properties of the system. Having introduced the $\mathcal{U}(1)$ gauge field through a Peierls substitution, we can use the arising Meissner current as an indicator for this changed behaviour. In particular, we here want to interpret them as impurities and study the localization behaviour of the a-particles. We are thus requiring:

- There is exactly one f-particle on each rung. This is implemented by a huge intrarung potential (i.e., a term $V_{\perp}^{f} n_{1,i}^{f} n_{2,i}^{f}$ with $V_{\perp}^{f} \to \infty$) and a half-filling for the f-particles.
- There is at most one single f-particle on each site. This is achieved by a huge on-site interaction energy of the f-particles (i.e., a term $U_{ff} n_{\alpha,i}^{f} n_{\alpha,i}^{f}$ with $U_{ff} \to \infty$).
- Each f-particle is localized on a randomly chosen site.

Under these conditions, we can then directly adopt a Schwinger-boson representation for the f-particles as well and upon neglecting a constant energy shift rewrite the interaction part of the Hamiltonian in spin language as [216]

$$\mathcal{H}_{int} = U_{af} \sum_{i} \sigma_i^z \tau_i^z. \tag{4.10}$$

Here, τ_i^z should be thought of as a classical number taking values ± 1.

4.2.1 Weakly coupled rungs

In the limit of weekly coupled rungs with the effective magnetic field formed by g and U_{af} at each rung being much larger than J_{xy} and J_z, we can solve for the ground state at each rung independently (thus rendering the rungs as effectively uncoupled). This corresponds to finding the ground state of a single spin on the Bloch sphere and gives [216]

[2] We will link our considerations with these interesting developments in Sec. 4.3.2

$$\langle \sigma_i^x \rangle = \frac{\cos(a' A_{\perp i})}{\sqrt{1 + (\tau_i^z U_{af}/(2g))^2}}, \tag{4.11a}$$

$$\langle \sigma_i^y \rangle = -\frac{\sin(a' A_{\perp i})}{\sqrt{1 + (\tau_i^z U_{af}/(2g))^2}}, \tag{4.11b}$$

$$\langle \sigma_i^z \rangle = -\tau_i^z \frac{U_{af}/(2g)}{\sqrt{1 + (\tau_i^z U_{af}/(2g))^2}}. \tag{4.11c}$$

We can then use these results to evaluate the expectation values of the parallel and the perpendicular current operators.

Localization of the current

We identify the components of the current $j_i = j_{\perp,i} + j_{\parallel,i}$ in spin language as [217]

$$j_{\perp,i} = -2g(\sigma_i^x \sin(a' A_{\perp i}) + \sigma_i^y \cos(a' A_{\perp i})), \tag{4.12a}$$

$$\begin{aligned} j_{\parallel,i} =& -4iJ_{xy}(\mathrm{e}^{iaA^{\parallel}_{i,i+1}} \sigma_i^+ \sigma_{i+1}^- - \mathrm{e}^{-iaA^{\parallel}_{i,i+1}} \sigma_i^- \sigma_{i+1}^+), \\ =& 2J_{xy}\left((\sigma_i^x \sigma_{i+1}^x + \sigma_i^y \sigma_{i+1}^y) \sin\left(aA^{\parallel}_{i,i+1}\right) + (\sigma_i^y \sigma_{i+1}^x - \sigma_i^x \sigma_{i+1}^y) \cos\left(aA^{\parallel}_{i,i+1}\right) \right). \end{aligned} \tag{4.12b}$$

Assuming weak coupling of the rungs, we can approximate $\left\langle \sigma_i^\alpha \sigma_{i+1}^\beta \right\rangle \approx \langle \sigma_i^\alpha \rangle \left\langle \sigma_{i+1}^\beta \right\rangle$ and thus plug in the results from Eqs. (4.11) to obtain

$$\left\langle j_{\parallel,i} \right\rangle = -2J_{xy} \frac{1}{1 + (U_{af}/2g)^2} \sin \Phi_{i,i+1}. \tag{4.13}$$

We can interpret this result as a localization of the Meissner current, which occurs here in a polynomial fashion. Therefore, we conclude that the Meissner effect in the Mott phase still occurs in the presence of impurities. We interpret the polynomial localization of the current as a weak localization. The validity of this formula for weakly-coupled rungs can be checked by comparing to results of numerical exact diagonalization, which shows good agreement, as can be seen from Fig. 4.2.

Symmetry effects

To conclude the consideration of the weak-coupling limit with a second particle species playing the role of disorder, let us comment on global and local symmetries of the system. Firstly, as already mentionned above, in the decoupled rung limit and for vanishing gauge fields, the disordered system has a local symmetry described by the operator [216]

$$\mathcal{G}_i = (\cos(a' A_{\perp i}) \sigma_i^x - \sin(a' A_{\perp i}) \sigma_i^y) \otimes \mathbb{Z}_2, \tag{4.14}$$

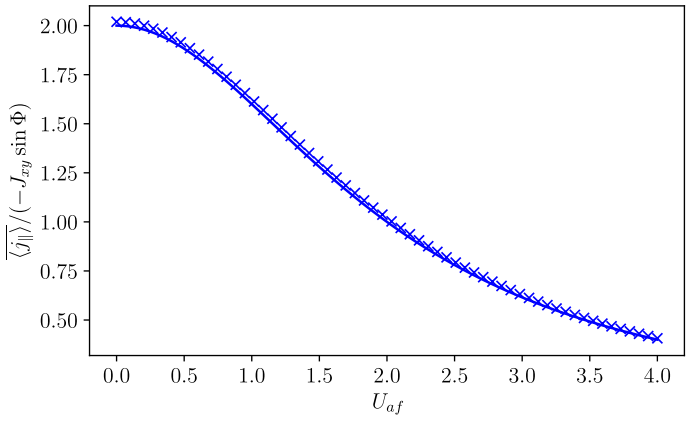

Figure 4.2: From [216]. The parallel current $\langle j_{i,\parallel}\rangle$ as a function of the coupling term U_{af} normalized by $-\sin\Phi$ and J_{xy} from ED (crosses) averaged over all configurations of disorder and Eq. (4.13). The parameters used for this simulation were $J_{xy} = 0.01$, $J_z = 0.01$, $g = 1.0$, $a'A_{\perp i} = aA^{\parallel}_{i,i+1} = 0.01$ for all sites i leading to $\Phi = \Phi_{i,i+1} = -aA^{\parallel}_{i,i+1} = -0.01$. The simulation was done for a chain with eight sites and periodic boundary conditions. The current was measured between two neighbouring sites i, $i+1$.

where $\mathbb{Z}_2$ denotes the transformation $\tau_i^z \to -\tau_i^z$ for the classical impurities[3].

This implies that the current is insensitive to the concrete realization of disorder in this limit. Turning on the interactions breaks this symmetry and thus the current observable will start to respond to the concrete realization of disorder. Therefore, we are showing disorder averages in Fig. 4.2. Throughout this chapter, if not stated differently, we express expectation values as $\langle\cdot\rangle$, while we denote disorder averages of a quantity A over different realizations of τ_i^z by a bar, i.e. $\overline{A}$.

Note that turning on the interactions, the local symmetries break down, but there is still a global symmetry corresponding to exchanging the legs of the ladder, described in the spin language by an operator [216]

$$\mathcal{R} = \prod_i \sigma_i^x \mathcal{O} \otimes \mathbb{Z}_2. \tag{4.15}$$

Here, we introduced the operator $\mathcal{O}$ which changes the direction of the magnetic field in the Hamiltonian, i.e., $\mathcal{O} f(A_{\perp i}, A^{\parallel}_{i,i+1})\,|\Psi\rangle = f(-A_{\perp i}, -A^{\parallel}_{i,i+1})\mathcal{O}\,|\Psi\rangle$ for any state $|\Psi\rangle$[4]. This exchange symmetry follows naturally from the symmetry of the ladder geometry and survives also in the strong coupling limit. We will consider this limit in the following section.

[3] In the quantum description, this would correspond to the operator τ_i^x. We will describe this case in Sec. 4.3.2. Here we used this notation to emphasize that τ_i^z are classical variables.

[4] The operator $\mathcal{O}$ is equivalent to taking the complex conjugate of the exponential functions involving the vector potential. Therefore, it acts as $\mathcal{O}\cos(a'A_{\perp i}) = \cos(a'A_{\perp i})\mathcal{O}$, $\mathcal{O}\sin(a'A_{\perp i}) = -\sin(a'A_{\perp i})\mathcal{O}$, $\mathcal{O}e^{iaA^{\parallel}_{i,i+1}} = e^{-iaA^{\parallel}_{i,i+1}}\mathcal{O}$ but $\mathcal{O}\sigma_i^y = \sigma_i^y\mathcal{O}$ [216].

4.2.2 Strong xy-coupling

We now turn to the case of a transverse field g that is negligible compared to the interaction strength. This gives rise to the Hamiltonian

$$\mathcal{H}_a = \sum_i \left(-2J_{xy} \mathrm{e}^{iaA^{\parallel}_{i,i+1}} \sigma^+_i \sigma^-_{i+1} + \text{h.c.} + J_z \sigma^z_i \sigma^z_{i+1} + \frac{U_{af}}{2} \sigma^z_i \tau^z_i \right), \tag{4.16}$$

corresponding to a gauged XXZ-model in a disordered longitudinal field, where the disorder potential is realized by a binary potential, i.e., $\tau^z_i = \pm\tau^z_i$. The XXZ-model from Eq. (4.16) (usually with $A^{\parallel}_{i,i+1} = 0$ and the disorder drawn from a uniform distribution) is one of the standard models to study disorder and localization phenomena. Indeed, as we will see, in the non-interacting case (i.e., $J_z = 0$), the model can be mapped to free fermions in a disorder potential, which is then similar to the seminal work of Anderson on localization in disordered media [86] that we discussed in Sec. 1.3.1. Including the interactions in J_z, the model is commonly studied in the realm of many-body localization [119, 120, 122, 125, 126, 229, 230]. In the following sections, we will present several techniques to study the model with a binary potential and a gauged hopping term and see how the Meissner current can be used as a signature for the localization [216].

We will first study the case of a strong xy-coupling, but without interactions in z-direction. We then turn to the case with interactions in Sec. 4.2.3. In Chapter 5, we finally investigate the many-body localization occuring in this model.

Solutions for specific disorder configurations

We emphasize that an important advantage of the model in Eq. (4.16) (as compared to a model with uniform disorder and without a gauge field) is on the one hand the possiblity to measure a current as an indicator of localization, but on the other hand the controlable way in which the disorder can be realized by coupling to a second particle species. The latter allows to, for example, consider all possible configurations of disorder when studying small systems numerically or, potentially, experimentally (cf. Sec. 4.4). For some specific configurations, namely where all impurities are on the same leg and for a staggered configuration of impurities, we can find exact results that we will present in the following paragraphs.

Starting with a configuration where all impurities are on the same leg so that $\tau^z_i = \tau^z = \pm 1$, we employ the Jordan-Wigner transformation [121, 188] already introduced in Eq. (3.31). At $J_z = 0$, we then obtain from the Hamiltonian in Eq. (4.16)

$$\mathcal{H}_a = -2J_{xy} \sum_i \mathrm{e}^{iaA^{\parallel}_{i,i+1}} c^\dagger_i c_{i+1} + \text{h.c.} + \frac{U_{af}}{2} \sum_i (2n_i - 1)\tau^z_i. \tag{4.17}$$

When using periodic boundary conditions, there is an extra term which after the Jordan-

Wigner transformation gives a contribution depending on the parity of the total fermion number [216]. This only influences the choice of frequencies in momentum space, so the differences should vanish in the thermodynamic limit. Fourier transforming using

$$c_j = \frac{1}{\sqrt{N}} \sum_k \mathrm{e}^{-ikaj} c_k,$$

the Hamiltonian in momentum space reads

$$\mathcal{H}_a = \sum_k \omega(k) c_k^\dagger c_k, \tag{4.18}$$

with $\omega = -4J_{xy}\cos\left(ak - aA^{\parallel}_{i,i+1}\right) + U_{af}\tau^z$ and a the lattice spacing of the spin chain (corresponding to the lattice spacing along the legs of the ladder geometry). The current can in this fermion basis be written as

$$j_{\parallel,i} = -4iJ_{xy}(\mathrm{e}^{iaA^{\parallel}_{i,i+1}}\, c_i^\dagger c_{i+1} - \mathrm{e}^{-iaA^{\parallel}_{i,i+1}}\, c_i c_{i+1}^\dagger), \tag{4.19}$$

and we can therefore write

$$\left\langle j_{\parallel,i} \right\rangle = \frac{2}{N} \frac{\partial E}{\partial (aA^{\parallel}_{i,i+1})}, \tag{4.20}$$

to calculate the current [216]. Here, $E = \langle \mathcal{H}_a \rangle$ Inquiring about the ground state, we see from Eq. (4.18) that negative energy states will be occupied, i.e.

$$4J_{xy}\cos\left(ak - aA^{\parallel}_{i,i+1}\right) > U_{af}\tau^z,$$

so that k must be between $k_\pm = A^{\parallel}_{i,i+1} \pm \arccos\left(\frac{U_{af}\tau_i^z}{4J_{xy}}\right)/a$ [216]. From above consideration, we then find the current per site in the continuum limit from

$$\begin{aligned}\left\langle j_{\parallel,i} \right\rangle &= -4J_{xy}\frac{2}{N}\sum_k \sin\left(ak - aA^{\parallel}_{i,i+1}\right)\left\langle c_k^\dagger c_k \right\rangle = -\frac{4J_{xy}}{\pi}\int_{k_-}^{k_+} dk \sin\left(ak - aA^{\parallel}_{i,i+1}\right), \\ &= \frac{4J_{xy}}{\pi}\cos\left(ak - aA^{\parallel}_{i,i+1}\right)\Big|_{k_-}^{k_+} = 0.\end{aligned} \tag{4.21}$$

In a finite size system, we can yet find a nonvanishing current since (for an odd fermion number), the allowed momentum values $2\pi r/L$ with $r = -N/2, -N/2+1, ...N/2-1$ (i.e., they are centered around 0), while the energy band is shifted by $aA^{\parallel}_{i,i+1}$. Hence, in the non-continuous case, a better estimate can be achieved by integrating exactly between the

outermost values that are still occupied. This changes the integration boundaries to

$$\tilde{k}_- = k_- - \left(k_- \mod \frac{2\pi}{L}\right),$$
$$\tilde{k}_+ = k_+ - \left(k_+ \mod \frac{2\pi}{L}\right),$$

and we obtain the current

$$\left\langle j_{\parallel,i}\right\rangle \approx \frac{4J_{xy}}{\pi}\left[\frac{U_{af}\tau_i^z}{4J_{xy}}\left(-2\sin\left(aA^{\parallel}_{i,i+1}\right)\sin\alpha\right) + \sqrt{1-\left(\frac{U_{af}\tau_i^z}{4J_{xy}}\right)^2}\left(2\sin\left(aA^{\parallel}_{i,i+1}\right)\cos\alpha\right)\right], \tag{4.22}$$

where $\alpha = \arccos\left(\frac{U_{af}\tau_i^z}{4J_{xy}}\right) \mod \frac{2\pi}{L}$. For large L, $\alpha \to 0$ and we find

$$\left\langle j_{\parallel,i}\right\rangle = 8\frac{J_{xy}}{\pi}\sqrt{1-\left(\frac{U_{af}\tau_i^z}{4J_{xy}}\right)^2}\sin\left(aA^{\parallel}_{i,i+1}\right). \tag{4.23}$$

From a comparison to exact diagonalization shown in Fig. 4.3, we see that this formula correctly captures a steep localization of the current at $U_{af} \sim 4J_{xy}$. The step-like behavior for a small system reflects the evoked fact that the occupied states are discrete and only when U_{af} has changed enough to change the sign of the energy of the outermost occupied state, the current localizes by 'one more step'.

On the other hand, with an alternating configuration of the impurities (i.e., the disorder part in the fermionic model taking the form $U_{af}\sum_j(-1)^j n_j = U_{af}\sum_j \mathrm{e}^{i\pi j}n_j$), the Hamiltonian can still be written in momentum space and now gives in BdG form [216]

$$\mathcal{H}_a = \sum_{k<0}(c_k^\dagger\, c_{k+\frac{\pi}{a}}^\dagger)\begin{pmatrix} -4J_{xy}\cos\left(ak - aA^{\parallel}_{i,i+1}\right) & U_{af} \\ U_{af} & -4J_{xy}\cos\left(ak - aA^{\parallel}_{i,i+1} + \pi\right)\end{pmatrix}\begin{pmatrix} c_k \\ c_{k+\frac{\pi}{a}}\end{pmatrix}. \tag{4.24}$$

The staggered potential gives rise to a shift in momentum of π/a. This Hamiltonian can be diagonalized to readily find the ground state energy and from there, using Eq. (4.20), the current can be found as

$$\left\langle j_{\parallel,i}\right\rangle = -\frac{2}{N}\sum_k \frac{16J_{xy}^2\cos\left(ak - aA^{\parallel}_{i,i+1}\right)\sin\left(ak - aA^{\parallel}_{i,i+1}\right)}{\sqrt{U_{af}^2 + 16J_{xy}^2\cos^2(ak - aA^{\parallel}_{i,i+1})}}, \tag{4.25}$$

where k ranges over half of the Brillouin zone. This result can be checked numerically against the results from exact diagonalization for small systems, which is shown in Fig. 4.3. There we also show the result when averaging over all configurations of disorder[5], also

[5] As the disorder here has only two possible configurations on each site, the number of possible global configurations is 2^N with N being the length of the chain.

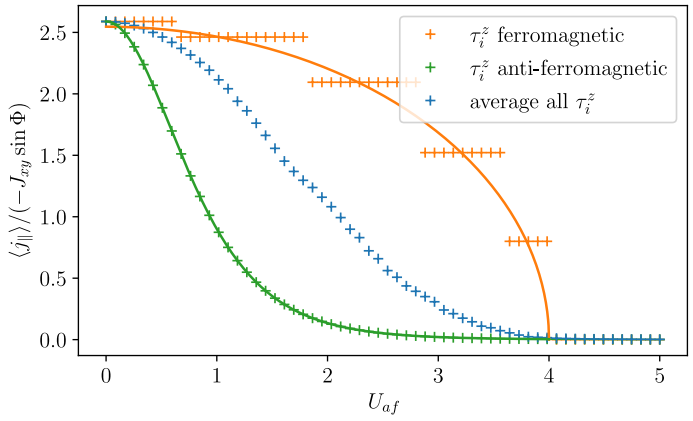

Figure 4.3: Adapted from [216]. The expectation value of the parallel current is shown as a function of the coupling strength to impurities U_{af}. The markers show the results from ED with a ferromagnetic (orange), anti-ferromagnetic (green) and disordered (blue) configuration of impurities. For the latter, the result is obtained by taking a disorder average over all possible configurations. The orange line shows the analytical result from Eq. (4.23) and the green line the result from Eq. (4.25). The used parameters are $N = 10$, $J_{xy} = 1.0$, $J_z = g = 0.0$, $aA^{\parallel}_{i,i+1} = 0.01$ and we used periodic boundary conditions.

showing a strong localization at large values of the disorder strength, i.e., vanishing rapidly beyond values of the disorder strength of $U_{af} \sim 4$.

To make this more precise and to consider also the interacting case with $J_z \neq 0$ (cf. Sec. 4.2.3), we need to bosonize the fermionic Hamiltonian. This technique will be introduced in the following section for the case of a staggered potential.

Bosonization

To solve for the dynamics with a staggered potential, an interesting alternative way is to bosonize the Hamiltonian in Eq. (4.17). This allows to account for the coupling in z-direction as well, which in the fermionic language reads $J_z(2n_i - 1)(2n_{i+1} - 1)$, thus including four-body interactions. A staggered impurity configuration gives rise to a term $\frac{U_{af}}{2} \sum_i (-1)^i (2n_i - 1)$. In total, we are starting from the Hamiltonian

$$\mathcal{H}_a = -2J_{xy} \sum_i c_i^\dagger c_{i+1} + \text{h.c.} + J_z \sum_i (2n_i - 1)(2n_{i+1} - 1) + \frac{U_{af}}{2} \sum_i (-1)^i (2n_i - 1). \quad (4.26)$$

Note that for simplicity, we here set $A^{\parallel}_{i,i+1} = 0$ assuming that it is small, but its effect can be reintroduced by a renormalization of J_{xy} [216]. Restricting to the low energy limit, we can linearize the spectrum around the Fermi momenta $\pm k_F$ and therefore define left- and right-moving fermions described by operators $c_{L/R}(x), c^\dagger_{L/R}(x)$ respectively. Defining operators describing the phase and the density fluctuations which we call $\tilde{\theta}$ and $\tilde{\phi}$ respectively, we

can in the continuum limit write [203, 231]

$$c_R^\dagger(x) = \frac{U_R}{\sqrt{2\pi a}} e^{i\tilde{\theta}(x)} e^{ik_F x} e^{i\tilde{\phi}}, \tag{4.27a}$$

$$c_L^\dagger(x) = \frac{U_L}{\sqrt{2\pi a}} e^{i\tilde{\theta}(x)} e^{-ik_F x} e^{-i\tilde{\phi}}, \tag{4.27b}$$

where $U_{R/L}$ are the Klein factors [231] ensuring fermionic anticommutation relations by $U_R U_L = i$. The details of this procedure and the precise definitions of the fields $\tilde{\theta}$ and $\tilde{\phi}$ can be found in Appendix E. Following the procedure laid out in Appendix E, we find the following bosonized Hamiltonian for the case of a staggered impurity configuration [216]:

$$\mathcal{H}_a = \frac{v}{2\pi} \int dx \left(\frac{1}{K} (\partial_x \tilde{\phi})^2 + K (\partial_x \tilde{\theta})^2 \right) - \frac{1}{\pi} \int dx \frac{U_{af}}{a} \sin\left(2\tilde{\phi}\right). \tag{4.28}$$

Here, $v/a = \sqrt{(4J_{xy})^2 + 32 J_z J_{xy}/\pi}$ and $K = \sqrt{4J_{xy}/(4J_{xy} + 8J_z/\pi)}$. This now has the form of a sine-Gordon model [231, 232]. The last term plays the role of a sine-Gordon term and we will in the following section treat it perturbatively to make predictions about the localization of the current in this case.

Renormalization group analysis

Assuming $U_{af} \ll J_{xy}$, we now want to write down the Renormalization Group (RG) equation for U_{af} using the standard methodology [232] applied in [216]. Assume we scale the lattice parameter $a \to a' = a e^{dl} \approx a(1 + dl)$. From this it follows that $dl = \log(a'/a)$. We demand that the partition function remains unchanged under this transformation, which gives [216]

$$\frac{U_{af}^2(a)}{a^2} a^{2K} = \frac{U_{af}^2(a')}{a'^2} a'^{2K}.$$

We then redefine the dimensionless quantity $g_{af} = U_{af} a/v$ such that

$$g_{af}^2 a^{2K-4} = g_{af}^2(a') a'^{2K-4}.$$

Upon scaling the lattice constant in the way described above, we find

$$\frac{\mathrm{d}g_{af}}{\mathrm{d}l} = (2 - K) g_{af}. \tag{4.29}$$

Now for the simple case of $J_z = 0$ we have $K = 1$. Therefore, upon increasing l, we also enhance g_{af}. Define $g_{af}(l^*)$, at which this term is for general K of the same order as the hopping term. Solving the differential equation (4.29) by integrating from a to l we get

$$\frac{g_{af}(l)}{g_{af}(a)} = \left(\frac{a(l)}{a} \right)^{2-K}. \tag{4.30}$$

We fix l^* at which the impurities-matter term is strongly renormalized and becomes comparable to the kinetic energy, which gives

$$g_{af}(l^*) = \frac{J_{xy}a}{v}, \tag{4.31}$$

and therefore:

$$l^* \sim a\left(\frac{v}{aU_{af}}\right)^{\frac{1}{2-K}}. \tag{4.32}$$

The expression (4.32) quantifies the gap opened by a sine-Gordon term, which arises from the staggered magnetic. In order to use it for the calculation of the current, note that without disorder and in the non-interacting case with $J_z = 0$, we can use the diagonal form of the Hamiltonian in momentum space similar to Eq. (4.18), i.e.,

$$\mathcal{H}_a = -4J_{xy}\sum_k \cos\Big(ak - aA^{\parallel}_{i,i+1}\Big))c_k^\dagger c_k. \tag{4.33}$$

Using Eq. (4.20), we then readily find

$$\left\langle j_{\parallel,i}\right\rangle = \frac{2}{N}\frac{\partial E}{\partial aA^{\parallel}_{i,i+1}} = -4J_{xy}\frac{2}{N}\sum_k \sin\left(ak - aA^{\parallel}_{i,i+1}\right)\left\langle c_k^\dagger c_k\right\rangle. \tag{4.34}$$

The sum ranges over accessible momentum states, spaced depending on the boundary conditions up to the Fermi momenta $k_F = \pi/(2a)$ (for the non-interacting, disorder-free case). Disorder will open a gap quantified by l^*. We therefore account for its effect by introducing a cut-off of the sum (4.34) so that it ranges only over momenta with absolute values smaller than $|k_F - (l^*)^{-1}|$. This can be done numerically to obtain a prediction for the behaviour of the current with a staggered magnetic field. The approximative nature of Eqs. (4.32) can be accounted for by fitting a free prefactor C, i.e. for $K = 1$ we fit C in

$$l^* = Ca\left(\frac{v}{aU_{af}}\right). \tag{4.35}$$

The results of this procedure and a comparison to results from exact diagonalization are shown in Fig. 4.4 by the violet curve. Using the bosonization framework, we can then account for interaction effects through the Luttinger parameter K in Eq. (4.32). Decreasing K (corresponding to an antiferromagnetic coupling $J_z > 0$) leads to a decrease in l^*, therefore the gap increases and there are more terms which are cut off from the sum in Eq. (4.34). This effect is stronger than the increase in v coming from an antiferromagnetic coupling J_z, as can be seen from simulation results shown in Fig. 4.4 by the brown crosses. Therefore an antiferromagnetic coupling of the σ_i^z-spins in this regime supports the localization of the current, which is seen from the red crosses in Fig. 4.4 from ED. In the bosonization approach, the effect of the interaction enters through the Luttinger

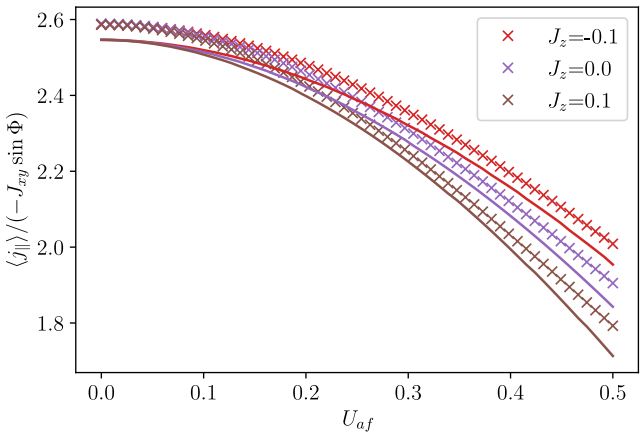

Figure 4.4: From [216]. The parallel current with a staggered impurity distribution as a function of U_{af} from ED (crosses) and fitting of the gap (Eq. (4.36), C is a free fitting parameter) opened by disorder in the sum from Eq. (4.34) (truncated at $|k_F - (l^*)^{-1}|$). We set $J_{xy} = 1.0$, $g = 0.0$ and $aA^{\parallel}_{i,i+1} = 0.001$ with periodic boundary conditions. The ED data (crosses) was obtained for a chain with ten sites. The truncated sum (solid lines) was evaluated on a large system with scaled lattice constant in order to get a smooth result.

parameter K and fitting

$$l^* = Ca \left(\frac{v}{aU_{af}} \right)^{\frac{1}{2-K}}, \tag{4.36}$$

i.e., optimizing for the parameter C. Summarizing from Fig. 4.4 and Eq. (4.36), a ferromagnetic coupling ($J_z < 0$) tends to hinder the localization in this setup, while an antiferromagnetic coupling ($J_z > 0$) supports the localization, which is consistent with the result from the bosonization approach [216]. In the following section, we will comment on how a bosonization approach can also be used to adress the case of a similar spin chain with Gaussian disorder and apply the results to our setup.

4.2.3 Strong coupling with interactions

Bosonization and RG analysis

The interacting case of an XXZ-chain with Gaussian disorder is a well-established model and using bosonization, one can similarly find a sine-Gordon model for this case. An RG equation of a form similar to that for staggered impurities presented in Eq. (4.29) can then be found. Translated to our setup it reads [232]

$$\frac{\mathrm{d}g_{af}}{\mathrm{d}l} = (3 - 2K) g_{af}. \tag{4.37}$$

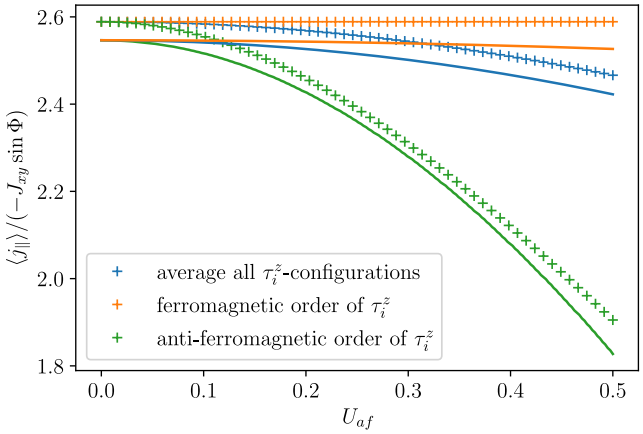

Figure 4.5: From [216]. The crosses show ED results for a system with $N = 10$ sites and ferromagnetic, antiferromagnetic and averaged over all τ_i^z-configurations with $aA^{\parallel}_{i,i+1} = 0.001$, $J_{xy} = 1.0$, $J_z = 0.0$ and periodic boundary conditions. The blue and the green solid lines show Eq. (4.34) with l^* fitted from Eq. (4.36) and Eq. (4.38) respectively. To obtain the fit, we sum over 4000 states to obtain a smooth curve. The resulting fitting parameter C in Eq.(4.36) was evaluated to $C = 0.1624$ and C_G from Eq. (4.38) to $C_G = 0.3993$.

This then leads to an estimate of the localization length given by

$$l^* = C_G a \left(\frac{v}{a U_{af}} \right)^{\frac{1}{3-2K}} , \tag{4.38}$$

where C_G is a fitting paramter that can be determined by fitting with numerical data in a similar way as for the case of staggered impurities above.

Note that although in our setup given by Eq. (4.16), we use a different form of disorder given by a two-peak potential, in the limit of large system sizes we expect the results obtained from Gaussian disorder to be applicable in the spirit of the central limit theorem [232]. Indeed, already for the relatively small systems under study in Fig. 4.5, we find a good agreement of this approach with ED results at low values of disorder, which we will present below.

Numerical results

In Fig. 4.5, we show results from ED for a ferromagnetic (orange) and an antiferromagnetic (green) setup of impurities, as well as an average over all possible configurations of τ_i^z (blue). For the green and the blue curve, we compare to results from the bosonization approaches for the respective setup described above. In the chosen range of disorder strength U_{af}, the results match the ED results closely, except for a small offset also present in the impurity-free case with $U_{af} = 0$, which can be ascribed to a mismatch of the highest occupied state in the band and the Fermi momentum due to the finite system size [216].

The study of the current from a truncated sum in momentum space with the truncation

depending on the disorder strength shows how the localization mechanism in the case of strong coupling between the sites of the chain differs compared to the weakly coupled setup described in Sec. 4.2.1. While there we found a power-law localization for each rung separately, here we find a cut-off of the sum in momentum space determining the current expectation value which for increasing disorder strength leads to a strong localization of the current, that can additionally be favoured by an anti-ferromagnetic J_z interaction between the sites.

After having studied the τ-spin degree of freedom derived from the impurities on the ladder as static disorder, we will now bridge with the recent literature describing ways to engineer $\mathbb{Z}_2$ lattice gauge theories in a similar ladder setup [213, 214]. For this, we will render the impurities as mobile quantum objects and see how the localization properties of the a-particles (or σ-spins, equivalently) respond to this.

4.3 Behaviour with mobile impurities

4.3.1 Modification of localization in weakly coupled rungs

The situation where the impurities (f-particles/τ-spins) were fixed to their site at all times allowed us to interprete their effect as a type of disorder leading to a localization of the a-particles/σ-spins. We now want to see how adding an additional ingredient changes these results. Concretely, we now want to consider the situation where the impurities can also hop from one leg to the other, while remaining localized on their respective rung. This is inspired by the experiments described in [213, 214], where a similar setup was used to study $\mathbb{Z}_2$ lattice gauge theories experimentally in a bosonic ladder setup. We will first describe the response of the Meissner current in the weak coupling limit and then digress on the effect of a $\mathbb{Z}_2$ lattice gauge theory on a double well which arises at each rung in this setup.

Response of the Meissner current

The dynamics of the f-particles constrained to hopping along a rung corresponds to addition of a term $-g_f(f_{2i}^\dagger f_{1i} + f_{1i}^\dagger f_{2i})$, which using a Schwinger-boson representation for f-particles in an equivalent way as for the a-particles (i.e., as in Eqs. (4.6)), gives rise to addition of a term $-g_f\tau_i^x$ to the Hamiltonian (4.7).

We focus on the case of weakly-coupled rungs, as in Sec. 4.2.1 for the case of static impurities, but now including hopping of the f-particles along the rungs. The Hamiltonian can then again be diagonalized on each rung and the ground state can be written down, from which expectation values can be evaluated directly. Invoking a mean-field approximation

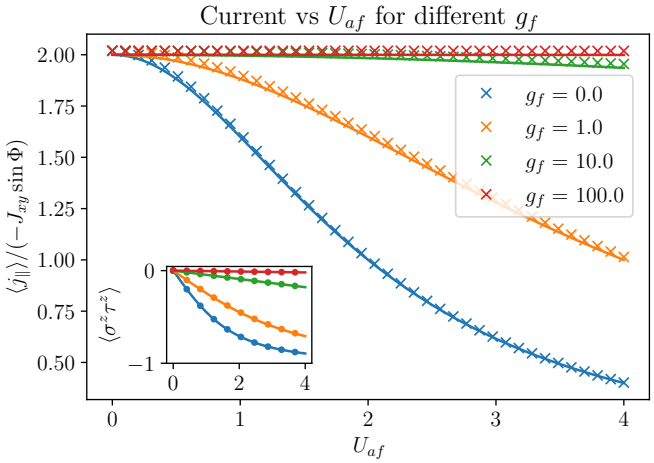

Figure 4.6: From [216]. The expectation value of the parallel current with mobile impurities with various tunneling coefficients along the rungs g_f from ED (crosses) and Eq. (4.39) (solid lines). The inset shows the expectation value of $\sigma_i^z \tau_i^z$ from ED (dots) and from Eq. (4.40), for the same values of g_f. The results are obtained from a chain with six sites and open boundary conditions and $J_{xy} = J_z = 0.01$, $g = 1.0$, $a' A_{\perp i} = a A^{\parallel}_{i,i+1} = 0.01$ for all sites i.

for the correlations necessary to compute the parallel current in Eq. (4.12b), we obtain

$$\langle j_\parallel \rangle = -2 J_{xy} \frac{1}{1 + \left(\frac{U_{af}/2}{g + g_f} \right)^2} \sin \Phi_{i,i+1}. \tag{4.39}$$

We compare this result to ED simulations in Fig. 4.6. The form of Eq. (4.39) shows that the current localizes in a power-law profile similar to a static f-particle configuration, but a large value of g_f protects it against the effects of strong coupling between a- and f-particles (i.e., large values of U_{af}). This effective protection of the current from localization by the g_f term is also confirmed from the numerical results in Fig. 4.6. Phenomenologically, a large parameter g_f tends to align the $\vec{\tau}$-spins in x-direction, which in turn reduces the influence of the U_{af}-term, as seen from the inset in Fig. 4.6, thus explaining this protection from localization. Mathematically, the correlation in z-direction between the two spin species can be evaluated as [216]

$$\langle \sigma_i^z \tau_i^z \rangle = - \frac{U_{af}}{\sqrt{4(g + g_f)^2 + U_{af}^2}}, \tag{4.40}$$

which is confirmed numerically by the inset of Fig. 4.6.

In the following section, we will study how this protection from localization in the case of quantum impurities can be interpreted using $\mathbb{Z}_2$ lattice gauge theory in a double well.

4.3.2 Symmetries and $\mathbb{Z}_2$ lattice gauge theory on a double well

The global symmetry of the system under consideration under exchange of the two legs of the ladder is still conserved when the impurities are mobile. The operator $\mathcal{R}$ introduced in Eq. (4.15) describing this global symmetry now takes the form

$$\mathcal{R} = \prod_i \sigma_i^x \mathcal{O} \otimes \tau_i^x, \tag{4.41}$$

with $\mathcal{H}_a = \mathcal{R}\mathcal{H}_a\mathcal{R}^{-1}$ and acting with τ_i^x corresponds to inverting the two legs of the ladder for the impurity degrees of freedom.

For decoupled rungs with $J_{xy} = J_z = 0$, we can again define a local symmetry operator [216]

$$\mathcal{G}_i = (\cos(a' A_{\perp i})\sigma_i^x - \sin(a' A_{\perp i})\sigma_i^y) \otimes \tau_i^x, \tag{4.42}$$

commuting with the Hamiltonian. For each of the decoupled rungs, the situation is then comparable to a model for $\mathbb{Z}_2$ lattice gauge theory (LGT) in a double well [213, 215]. To see this more clearly, we rotate the spin degrees of freedom according to $\gamma_i^x = \sigma_i^z$ and $\gamma_i^z = \cos(a' A_{\perp i})\sigma_i^x - \sin(a' A_{\perp i})\sigma_i^y$. Then the local symmetry in the decoupled rung limit simply reads $\mathcal{G}_i = \gamma_i^z \otimes \tau_i^x$. Each rung then corresponds to a $\mathbb{Z}_2$ LGT on a double well with τ_i^z as a $\mathbb{Z}_2$ gauge field and τ_i^x playing the role of a $\mathbb{Z}_2$ electric field [213, 215]. The Hamiltonian of one rung reads

$$\mathcal{H}_{a,i} = -g\gamma_i^z - g_f\tau_i^x + U_{af}\gamma_i^x\tau_i^z, \tag{4.43}$$

we see that for $U_{af} = 0$, we would have the $\vec{\gamma}$-spin oriented in z-direction and the $\vec{\tau}$-spin oriented in x-direction, which would lead to an eigenvalue $+1$ of the operator $\mathcal{G}_i$. With non-zero U_{af}, the dynamics of both spins are coupled, but since $\mathcal{G}_i$ commutes with the Hamiltonian, its eigenvalue is conserved, therefore flipping γ_i^z requires flipping τ_i^x as well, which comes with an energy cost proportional to g_f [214]. This shows how a large parameter g_f can through the coupling of both spins effectively stabilize the $\vec{\gamma}$-spin in the z-direction in the limit of weakly coupled rungs. Transforming back to the $\vec{\sigma}$-variables, this implies that a large g_f term supports the orientation of the $\vec{\sigma}$-spin in the direction given by the g term, i.e., in the xy-plane in which they are not coupled to the impurities. Therefore, g_f stabilizes the superfluid spin current and we thus expect it to hinder the localization.

To complete the analogy with [213–215], we can define a charge for each site of the double well (which correspond to the different legs) from the operator γ_i^z by expressing it through a boson tunnelling between the two sites with $\gamma_i^z = \tilde{n}_{1,i} - \tilde{n}_{2,i}$. Here $\tilde{n}_{\alpha,i}$ is the number operator on the respective site of the rung i and the charge would be defined by $Q_\alpha = (-1)^\alpha \gamma_i^z$. We could then define the two conserved local symmetry operators

$\mathcal{G}_{i,\alpha} = Q_\alpha \otimes \tau_i^x$ as in [215]. However, since for the situation of one particle in a double well Q_1 and Q_2 are related by $Q_1 Q_2 = -1$ (similarly to [213]), we drew conclusions about the influence of this $\mathbb{Z}_2$ LGT on a double well directly using the symmetry operator $\mathcal{G}_i$. These considerations only hold for decoupled rungs. When $J_{xy}, J_z \neq 0$, our model cannot be described by $\mathbb{Z}_2$ LGT as the operators $\mathcal{G}_i$ do not commute with the Hamiltonian in that case. Instead, the model then shows the global $\mathbb{Z}_2$-symmetry associated with the operator $\mathcal{R}$ as described above.

Further insights about the role of $\mathbb{Z}_2$ LGT on a double-well in the decoupled limit and when activating a small interaction through the J_z term can be reached by considering the vison operator. In the realm of $\mathbb{Z}_2$ LGT, the vison operator or magnetic field operator is usually defined by $B_p = \prod_{l \in \partial p} \tau_l^z$ (with ∂p referring here to the closed path on a given unit cell) [213]. In our case, we identified a minimal $\mathbb{Z}_2$ LGT for each of the decoupled rungs representing a double well. In general, for one-dimensional $\mathbb{Z}_2$ LGT, the magnetic plaquette term can not be defined [215]. However, considering the ladder as a whole, we can define the operator $B_p = \tau_j^z \tau_{j+1}^z$ (where the plaquette p is defined between two rungs j and $j+1$) phenomenologically in the same form as above and use it to describe the situation for the f-particles.

As we have seen, for the simple case of decoupled rungs, we can evaluate observables analytically. The Hamiltonian can be diagonalized on each rung and the ground state can be written down, from which expectation values can be evaluated directly. For the limit of decoupled rungs, when $g_f \neq 0$ we have $\langle \tau_i^z \rangle = 0$ and therefore $\langle \tau_i^z \tau_{i+1}^z \rangle = \langle \tau_i^z \otimes \tau_{i+1}^z \rangle = 0$. This implies that B_p is disordered and has a zero expectation value on a square unit cell, the state corresponds to a vison condensate [213]. For $g_f = 0$, in the decoupled rung limit we get a degenerate ground state with $\langle \tau_i^z \rangle = \pm 1$, so we get a static configuration of B_p. Turning on a small positive value of J_z, an anti-ferromagnetic configuration of the $\vec{\sigma}$-spins is favored which is through the U_{af}-coupling transmitted to the $\vec{\tau}$-spins. Therefore, in this case we get a static configuration with $B_p = -1$. These arguments from $\mathbb{Z}_2$ LGT in a double well confirm the conclusions drawn for the localization of the current from Eq. (4.39) and Fig. 4.6: A coupling to mobile impurities can protect the localization of the current by hindering flips of the spin through a $\mathbb{Z}_2$ electric field (coming form rendering the impurities as mobile quantum objects, i.e., introducing τ_i^x), hindering entanglement between the $\vec{\sigma}$-spins and the impurities and therefore preserving superfluidity of the spin-sector.

In the following section, we will see how the system responds to large interactions between the two considered particle species.

4.3.3 Four-body model

When U_{af} is of the same order as U_{aa} and $V_\perp$ in Eq. (4.1) and we allow for hopping of the f-particles in all directions (and not only along the rungs), we have to account for this

when doing the perturbation theory to derive the effective spin model. If we consider the Hamiltonian without any hopping and at half filling, the ground state is on each rung two-fold degenerate with one a- and one f-particle on different sites of each rung. For a detailed account of all the perturbative terms arising in this situation, we refer to Appendix D of [216]. Here we will discuss the resulting Hamiltonian phenomenologically. Reintroducing the hopping of a-particles perturbatively again produces second-order Ising interactions such as $J_z^a \sigma_i^z \sigma_{i+1}^z$ with J_z^a different from J_z in the previous sections. Now, introducing a hopping for the impurities along both legs and rungs with $-t_x^f \sum_{\alpha,i} f_{\alpha i}^\dagger f_{\alpha,i+1} - t_y^f \sum_i f_{2i}^\dagger f_{1i} + \text{h.c.}$ with $\alpha = 1, 2$, we get a similar term

$$J_z^f \tau_i^z \tau_{i+1}^z. \tag{4.44}$$

The hopping term t_y^f can be identified with the parameter g_f in the spin language of Sec. 4.3. The interchange of an a- and an f-particle along a rung is accounted for by a term

$$-g^{af} \mathrm{e}^{ia' A_{\perp i}} \sigma_i^+ \tau_i^- + \text{h.c.}. \tag{4.45}$$

Finally to fourth order, we also have contributions of the form

$$-J_{xy}^{\parallel} \mathrm{e}^{ia(A_{i,i+1}^1 - A_{i,i+1}^2)} \sigma_i^+ \tau_i^- \sigma_{i+1}^- \tau_{i+1}^+ + \text{h.c.}. \tag{4.46}$$

The effective Hamiltonian can then be written as [216]

$$\begin{aligned} \mathcal{H} = -J_{xy}^{\parallel} \sum_i \mathrm{e}^{ia(A_{i,i+1}^1 - A_{i,i+1}^2)} \sigma_i^+ \tau_i^- \sigma_{i+1}^- \tau_{i+1}^+ + \text{h.c.} + J_z^a \sum_i \sigma_i^z \sigma_{i+1}^z \\ + J_z^f \sum_i \tau_i^z \tau_{i+1}^z - g^{af} \sum_i \mathrm{e}^{ia' A_{\perp i}} \sigma_i^+ \tau_i^- + \text{h.c.}. \end{aligned} \tag{4.47}$$

From here, we can in a similar way as in Eqs. 4.12 evaluate current as the relative density operator and then - again along the lines of Sec 4.2.1 evaluate the parallel component for the case of weakly coupled rungs. This limit corresponds with the model in Eq. (4.47) to a dominant g^{af} term. We can then analogously find

$$\langle j_\parallel \rangle = -2 J_{xy}^{\parallel} \sin \Phi_{i,i+1}. \tag{4.48}$$

Note that this is again similar to the form of Eq. (4.5a) and Eq. (4.8a), but with a reduced prefactor. In fact, the prefactor has been found from perturbation theory to be [216]

$$\begin{aligned} J_{xy}^{\parallel} = \frac{8(t_x^a)^2 (t_y^f)^2}{U_{af} + V_\perp} \left(\frac{1}{U_{af}^2} + \frac{1}{U_{af}(U_{af} + V_\perp)} + \frac{1}{2(U_{af} + V_\perp)^2} \right) \\ + \frac{8(t_x^a)^2 (t_x^f)^2}{(U_{af} + V_\perp)^2} \left(\frac{1}{2U_{af}} + \frac{1}{2V_\perp} + \frac{1}{2U_{af} + 2V_\perp} \right). \end{aligned} \tag{4.49}$$

This analysis shows that as long as we consider weakly-coupled rungs, the system can be described through local observables as a result of the dominant transverse magnetic field in the spin representation. The system still shows an analogue of the Meissner effect with a parallel current decreasing in a polynomial fashion in the coupling strength U_{af}. Note that because of the mobile character of the impurities, they cannot be understood as static disorder. The model thus shows some similarities with models studied in the light of disorder-free localization [233–235].

To conclude this chapter, it remains to show how the studied system can be realized experimentally. For this, we will first come back to the discussion of ultracold atoms from the beginning of the chapter and consequently also discuss quantum circuits, leaning on the discussion from Sec. 2.4.

4.4 Experimental realization

After having demonstrated theoretically how a model of two bosonic particle species on a ladder can be used to study different regimes of localization and disorder physics (in relation to effective $\mathbb{Z}_2$ LGT on a double well when the impurities can hop along the rungs) using the response of a Meissner current, we aim to conclude this chapter commenting on experimental realizations. For this, we will focus on the main ideas and principles used for setting up these realizations.

4.4.1 Ultracold atoms

Firstly, it should be emphasized that an analogue of the Meissner effect in a bosonic ladder with one particle species and in the superfluid phase has been observed experimentally [225]. As mentioned, populating such a geometry with a second particle species has been proposed as a possibility of modelling $\mathbb{Z}_2$ LGT experimentally using ultracold atoms [213–215]. As the setup in Eq. (4.1) and the coupling to a second particle species in Eq. (4.9) closely resemble the form used in [213, 214], the results found in this chapter could be verified experimentally using similar techniques.

The basic building block of such realizations consists in a Bose-Einstein condensate in a periodic potential made up by lasers (i.e., an optical lattice) [199, 200]. This then allows to realize the different hopping parameters and potentials for one particle species. More recently, these experiments have benefitted from new techniques to artificially realize the effect of a magnetic field, i.e. mimicking the Peierls phases in the Hamiltonian in Eq. (4.1). Such artificial gauge fields can be realized using laser-assisted tunneling and described using a Floquet protocol [205–207, 213, 236].

Artificial gauge fields in a double well

To explain this technique on an elementary level, let us first go back to a single particle on a single rung or double well, to then generalize it to the setup studied in this chapter. The key ingredient to obtain a Peierls phase for hopping between the two sites is to introduce both a static and a periodically modulated potential difference between both sites. This gives rise to the following Hamiltonian:

$$\mathcal{H}_{\text{double well}} = -t_y^a(a_2^\dagger a_1 + a_1^\dagger a_2) + (\Delta_{2,1} + A_{2,1}\cos(\omega t + \phi))n_2. \tag{4.50}$$

Performing a unitary transformation using the operator

$$R_{2,1} = \exp\Big(i(\Delta_{2,1}t + \frac{A_{2,1}}{\omega}\sin(\omega t + \phi))n_2\Big),$$

we obtain according to $\tilde{H} = RHR^\dagger + i(\partial_t R)R^\dagger$:

$$\tilde{\mathcal{H}}_{\text{double well}} = -t_y^a \exp\Big(i(\Delta_{2,1}t + \frac{A_{2,1}}{\omega}\sin(\omega t + \phi))\Big)a_2^\dagger a_1 + \text{h.c.}. \tag{4.51}$$

This Hamiltonian is periodic in time, therefore we can use Floquet's theorem to evaluate the time-evolution operator for an integer multiple of the period. For this, we define an effective Floquet Hamiltonian to zeroth order in $1/\omega$ by averaging over one period [213, 236, 237]. Assuming the period is short, we can replace the Hamiltonian by this effective Hamiltonian. Averaging the Hamiltonian (4.51) over one period of the driving, we obtain from the average of the time-dependent phase [213]

$$-t_y^a\frac{\omega}{2\pi}\int_{\frac{-\pi-\phi}{\omega}}^{\frac{\pi-\phi}{\omega}} \exp\Big(i(\Delta_{2,1}t' + \frac{A}{\omega}\sin(\omega t' + \phi))\Big)dt' = -t_y^a\mathcal{J}_1(A/\omega)\mathrm{e}^{-i\phi},$$

under the resonance condition $\Delta_{2,1} = \omega$. Here, $\mathcal{J}_1(x)$ is the Bessel function of the first kind of first order. In that way, we obtain the effective hopping Hamiltonian [213, 238]

$$\tilde{\mathcal{H}}_{\text{double well}} = -t_y^a\mathcal{J}_1(A/\omega)(\mathrm{e}^{-i\phi}a_2^\dagger a_1 + \mathrm{e}^{i\phi}a_1^\dagger a_2), \tag{4.52}$$

where ϕ now mimicks a gauge field and can thus be used to simulate a vector potential, which can be seen by comparing its role in eq. (4.52) with the Peierls phases in the Hamiltonian (4.1). We emphasize that this worked thanks to the particular resonance condition we invoked, requiring the static potential offset to be equal to the driving frequency.

Artificial gauge fields in an effective spin model

A similar procedure can be used to obtain the Peierls phases in the Hamiltonian in Eq. (4.1). Assume we start from the Hamiltonian of the two interacting particle species, but without the gauge field, i.e.,

$$\mathcal{H}_a = -t_x^a \sum_{\alpha,i} a_{\alpha i}^\dagger a_{\alpha,i+1} - t_y^a \sum_i a_{2i}^\dagger a_{1i} + \text{h.c.} \\ + \frac{U_{aa}}{2} \sum_{\alpha,i} n_{\alpha i}^a (n_{\alpha i}^a - 1) + V_\perp \sum_i n_{1i}^a n_{2i}^a - \mu \sum_{\alpha,i} n_{\alpha i}^a + \frac{U_{af}}{2} (n_2^a - n_1^a)\tau_i^z. \quad (4.53)$$

Here we rendered the f-particles as static with one particle per rung and therefore introduced them in effective spin language (using τ_i^z) directly. In the atomic limit ($t_x^a = 0$) and if τ_i^z is a classical variable taking only the values ± 1, the Mott phase is then achieved for

$$V_\perp + \sqrt{(t_y^a)^2 + (U_{af}/2)^2} > \mu > -\sqrt{(t_y^a)^2 + (U_{af}/2)^2}.$$

If we now add a static potential offset and a periodic driving by

$$\sum_{\alpha,j} (j + \alpha - 1)(\Delta + \Delta^\omega(t)) n_j^\alpha,$$

with $\Delta^\omega(t) = A\cos(\omega t + \phi)$, each link on the ladder behaves like a double well described above, since the difference of driving and offset between any two sites is $\Delta + \Delta^\omega(t)$. Therefore, the hopping processes along each link will be renormalized in the same way as for one single double well and we will get back the Hamiltonian (4.1) with the gauge fields realized as $aA_{i,i+1}^\alpha = a' A_{\perp i} = \phi$. We can then do the perturbation theory as described in Sec. 4.1.2, but we need to assume that $U_{af} \ll U_{aa}, V_\perp$ in order to perform the perturbation theory in t_x^a as before[6]. In this framework, we can then obtain Hamiltonian (4.7). This method to obtain the effective hopping Hamiltonian allows to think about implementing different artificial gauge fields in both directions [239]. One can then consider setups where the difference in static potential offset between two sites along the legs is not the same as along the rungs and in addition a driving with multiple frequencies is realized in order to achieve a greater freedom in the renormalizations in both directions [213, 236].

4.4.2 Quantum circuits

The model studied in this chapter has been inspired by recent theoretical and experimental progress regarding ultracold atoms [207,213,225], that allows to directly implement hopping Hamiltonians as Eq. (4.1). However, even before these advances, realisations of bosonic two-leg ladders using quantum circuits have been discussed extensively [240–242]. For the

[6]Otherwise, we come back to the situation described in Sec. 4.3.3

concrete model from Eq. (4.1) with the a-particles only, a realization using two Josephson junction arrays has been proposed in [217, 218]. Each site is realized by a superconducting resonator, composed of an inductive and a capacitive element. On each individual chain, a capacitive coupling to ground gives rise to a term mimicking the on-site energy U_{aa} while the inductive element mimicks hopping along the chain [218]. A Josephson tunnel element can be used to couple the two arrays at each corresponding site, leading to a tunneling term mimicking t_y^a (from the Josephson element) and a potential term mimicking $V_\perp$ from the capacitive element.

A second particle species could then in principle be realized by realizing a second ladder for the f-particles in a similar way. Coupling two respective sites of each ladder capacitively would give a potential similar to $U_{af} n^a_{\alpha,i} n^f_{\alpha,i}$, thus mimicking the interspecies Hubbard interaction from Eq. (4.9).

In summary, there are several ways to potentially realize the system studied in this chapter, which makes it an interesting platform to study the interplay of disorder and related symmetries with an applied $\mathcal{U}(1)$ gauge field and the associated Meissner current. In the following chapter, we will see how this platform can also be used to test intriguing effects related to *many-body localization*.

4.5 Conclusion

In this chapter, we studied a one-dimensional bosonic system, which hosts a superfluid to Mott transition and can in the rung-Mott phase (i.e., with one particle per rung of the ladder) be described by an effective spin chain. The effect of a magnetic field can be introduced by a Peierls substitution and allows to define a local current from the relative density operator. An analogue of the Meissner effect can be seen in the superfluid phase by a vanishing perpendicular current and a parallel current proportional to the flux [224, 225] and a similar effect occurs in the rung-Mott phase due to the persistence of superfluidity in the spin sector [217, 218].

Adding a second particle species, that one can consider as impurities, leads to a localization of this current [216]. We study this phenomenon in various limits. For weakly coupled rungs, the current localizes in a polynomial fashion and we interprete it as a weak localization, in which the Meissner effect still occurs. With a strong transverse coupling, the model maps to the one-dimensional Anderson problem described in Sec. 1.3.1 and with periodic boundary conditions one expects a persistent current because of the magnetic flux applied [243]. We checked numerically that the disorder-averaged current in this limit indeed localizes strongly at large disorder and provided analytical results for two particular configurations (ferromagnetic/antiferromagnetic configuration of impurities, cf. Fig. 4.3). We then included interactions for the case of antiferromagnetically configured impurities and show that an antiferromagnetic interaction supports the localization in

this case. This is in fact also true for the more general case of Gaussian disorder [232], to which we fit the results as well. This result is consistent with the prediction of stronger Anderson localization for repulsive interactions established by Giamarchi and Schulz [19].

We have furthermore studied a situation in which the impurities have a quantum character themselves and are allowed to tunnel along the rungs. Studying this modification in the limit of weakly coupled rungs, we saw that this hinders the localization of the particles, which can be understood from a relation to $\mathbb{Z}_2$ lattice gauge theory on a double well [213, 214]. In the limit of a strong interaction between the particles and the impurities, we showed how a different spin model can be derived, for which we demonstrated the continued occurence of an analogue of the Meissner effect.

The model we studied is realizable with cold atoms or quantum circuits. The parallel component of the local current could in these setups be measured dynamically and used as an indicator of the response to disorder and the localization properties, as done here in a numerical way. This opens the question on whether this current can also serve as a witness to the many-body localization transition introduced in Sec. 1.4. This will be the subject of the following chapter.

Chapter 5

Many-body localization in an effective spin chain

In Chap. 4, we have seen how the local current defined from an applied $\mathcal{U}(1)$ gauge field can be used to study localization properties of an effective spin system. It is then natural to ask whether it can be used in a similar way as a witness to a many-body localization transition. For this, we will continue to study the effective spin model from Eq. (4.7), where disorder is defined through a random spatial distribution of impurities, thus corresponding to a positive or a negative value of the potential. A comparable binary disorder potential has been studied in the context of many-body localization (MBL) [244, 245], motivated by its realizability with ultracold atoms. Here, the goal is to study the MBL phase with a binary disorder under more general conditions, in particular, including a gauge field and a finite transverse magnetic field, while testing for different probes that we will introduce below.

We will first introduce the relevant probes to test a many-body localized system in Sec. 5.1. Consequently, in Sec. 5.2 we will see how these definitions play out in the context of the effective spin model from Eq. (4.7). As introduced in the introductory Sec. 1.4.1, an established way of testing an MBL transition is to study the scaling of the entanglement entropy in time. We will present a numerical study of this property to identify the MBL phase and compare also to the scaling of the bipartite fluctuations, which is a probe more easily accessible experimentally, as we will introduce below. Finally, by comparing the long-time evolution of these quantities to that of the Meissner current introduced in Chapter 4, we will conclude about the MBL transition in this system and how the current can be seen as an indicator of the latter.

This chapter is based on work published in [216]. The bipartite fluctuations as a tool to identify entanglement have been established by Karyn Le Hur and collaborators before [131, 246]. For this work, I used the entanglement entropy and the bipartite fluctuations as probes to study the MBL phase of the model numerically under supervision of Karyn Le Hur. I furthermore developed and implemented the codes and evaluated the shown results.

5.1 Probes for MBL

As mentioned in the introductory Sec. 1.4, probing many-body localized phases remains a challenging experimental task [22, 120, 122, 247]. Here we will focus on two established probes that are commonly studied numerically in the context of MBL, which are the bipartite fluctuations and the entanglement entropy [120, 126]. A commonly studied model in the realm of MBL is the XXZ-model in a random longitudinal field [119, 120, 248, 249]. It has the Hamiltonian introduced in Eq. (1.65), which reads

$$\mathcal{H}_{\mathrm{XXZ}} = \sum_i \left(J_{\mathrm{xy}}(\sigma_i^x \sigma_{i+1}^x + \sigma_i^y \sigma_{i+1}^y) + J_z \sigma_i^z \sigma_{i+1}^z + h_i \sigma_i^z \right), \tag{5.1}$$

where h_i is a random variable, often chosen to be drawn from a uniform distribution, i.e. $h_i \in [-h_c, h_c]$ with $h_c > 0$. Note that this corresponds precisely to Eq. (4.7) with $A^{\parallel}_{i,i+1} = 0$, $g = 0$ and a longitudinal random field $h_i = \frac{U_{af}}{2}\tau_i^z$ (which in the case of Chap. 4 corresponds to a Bernoulli random variable). We will now introduce the bipartite fluctuations and the entanglement entropy for the model in Eq. (5.1).

5.1.1 Bipartite fluctuations

An important idea for both the bipartite fluctuations and the entanglement is the division of the full system into two partitions, as shown in Fig. 1.4. The bipartite fluctuations of the spin in a state $|\psi\rangle$ read for a subsystem of size l [131, 246]

$$\mathcal{F}(l) = \langle\psi| \left(S_l^z\right)^2 |\psi\rangle - \langle\psi| S_l^z |\psi\rangle^2, \tag{5.2}$$

with $S_l^z = \sum_{i=1}^{l} \frac{1}{2}\sigma_i^z$.

The bipartite fluctuations are an indicator of entanglement in many-body systems [131, 246] and are well suited to study many-body physics in condensed matter systems numerically [125, 126] or using quantum simulation [250], as they are more easily accessible than the entanglement entropy defined in Eq. (1.66), which we will discuss below in Sec. 5.1.2 As an example, we first address the situation of the weakly-coupled rungs limit for the model we introduced in Eq. (4.7) where we can also solve the dynamics using the decoupled-rungs approximation from Sec. 4.2.1.

Weakly coupled rungs

When $g \gg J_{xy}, J_z$, the ground state can be found by diagonalizing simultaneously on each rung, as described in Sec. 4.2.1. We can then calculate the bipartite fluctuation in the ground state as

$$\mathcal{F}(l) = \frac{l}{4} \frac{1}{1 + (U_{af}/2g)^2}. \tag{5.3}$$

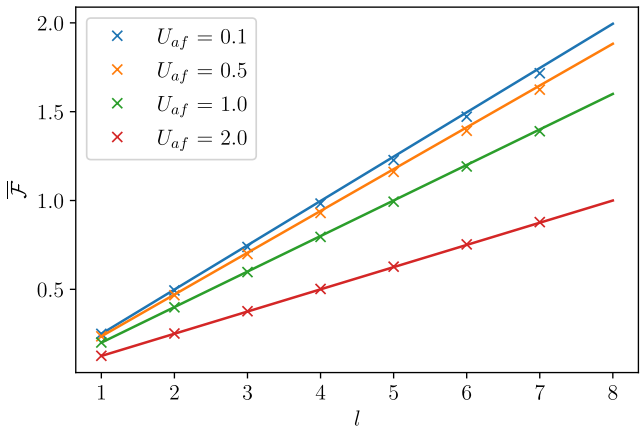

Figure 5.1: From [216]. ED results (crosses) for the bipartite fluctuation as a function of the subsystem size in the weakly-coupled rungs limit for a range of U_{af} values. The size of the full system is fixed to $N = 8$ and we use $J_{xy} = J_z = 0.01$, $g = 1.0$, $aA^{\parallel}_{i,i+1} = 0.01$ and open boundary conditions. The bipartite fluctuation $\overline{\mathcal{F}}$ was evaluated as an average over all possible configurations of τ^z_i. The solid line shows a comparison to Eq. (5.3). The bipartite fluctuation grows linearly with the subsystem size.

The bipartite fluctuations here scale linearly with the subsystem size. Interestingly, up to a prefactor, it is equal to the parallel current from Eq. (4.12b). The localization on a single rung can thus be seen from the bipartite fluctuation and the Meissner current equivalently. Note that Eq. (5.3) is independent of the disorder configuration since the localization occurs on each rung independently. In Fig. 5.1, we show the scaling of the bipartite fluctuation with the subsystem size as an average over disorder configurations which we call $\bar{\mathcal{F}}$, confirming Eq. (5.3) in this limit.

Ground state of the XXZ-chain

In order to study many-body localization in the full spin model from Eq. (4.7), we need to consider interactions. For this, we will consider the J_{xy} and J_z interactions at the so called Heisenberg point $J_{xy} = -J_z$, in order to compare to previously established results in the literature [125, 126, 131, 249]. When deriving the Hamiltonian (4.7) from the bosonic ladder model, we had $J_{xy} > 0$ or $-J_{xy} < 0$. Here, we thus redefine $J_{xy} \to -J_{xy}$ in Eq. (4.7) corresponding now to ferromagnetic couplings. Note that the cases of ferromagnetic and antiferromagnetic interactions can be mapped onto each other by rotating around the z-axis for every second spin. In the model of Eq. (4.7), we can set $J_{xy} = -0.25$, $J_z = 0.25$ and $g = 0$ to make the connection with Ref. [126]. Here, we study the bipartite fluctuations when tracing half of the system, from the ground state. In the ground state, the bipartite fluctuations can then be evaluated numerically and for a range of J_z we obtain the results shown in Fig. 5.2.

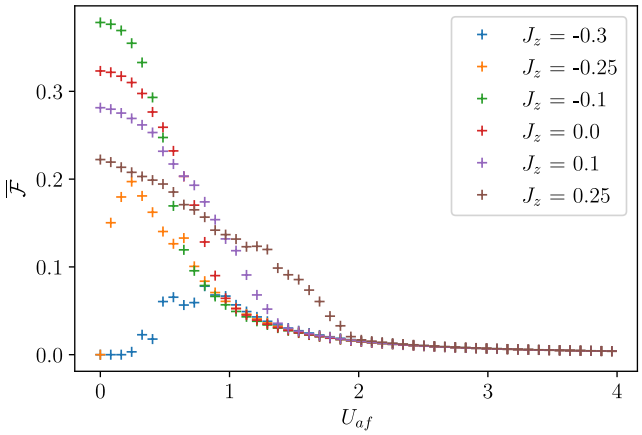

Figure 5.2: From [216]. Bipartite fluctuations averaged over all realizations of τ_i^z for $N = 8$ with periodic boundary conditions, the bipartition boundary being in the center of the chain (i.e. $l = N/2$). Here, we set $J_{xy} = -0.25$ and $g = 0.0$, so that the curve with $J_z = 0.25$ bridges with the results in [126]. We furthermore set $aA^{\parallel}_{i,i+1} = 0.001$.

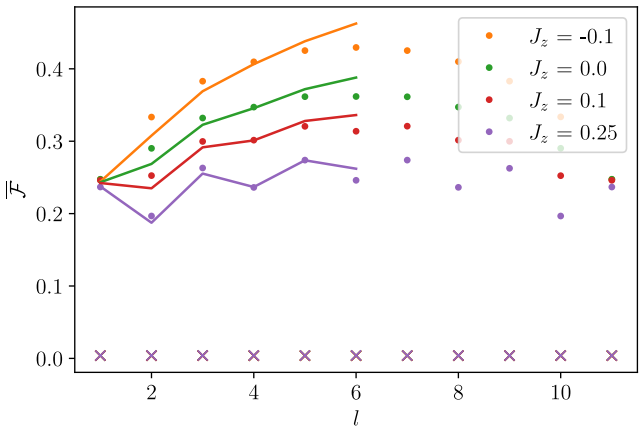

Figure 5.3: From [216]. Scaling of the average bipartite fluctuations with the subsytem size for different values of J_z and U_{af}. The dots show simulation results in the gapless phase with $U_{af} = 0.1$ and the solid lines a fit of equation (5.4). The crosses show results for $U_{af} = 4.0$. Different values of J_z are represented by different colors. The bipartite fluctuation was evaluated for 1000 randomly chosen configurations of τ_i^z and consequently averaged over. These simulations were performed for a chain with 12 sites and periodic boundary conditions, other parameters are as in Fig. 5.2.

The gapless phase of the XXZ-model in Eq. (4.7) is realized for $-1 < -J_z/J_{xy} \leq 1$. In this phase, the low energy physics without disorder is described by the Luttinger liquid theory [232]. In the region $-1 < -J_z/J_{xy} < 1$, the scaling of the fluctuations with the subsystem size can be evaluated when $U_{af} \to 0$ and reads [131, 246]

$$\mathcal{F}(l) = \frac{K}{\pi^2} \ln(l) + \frac{f_2}{\pi^2} - A_1 \frac{(-1)^l}{\pi^2 l^{2K}}, \tag{5.4}$$

where the Luttinger parameter K is now determined from the Bethe ansatz solution[1]

$$K = \frac{1}{2} \left(1 - \frac{\cos^{-1} \Delta}{\pi} \right)^{-1}, \tag{5.5}$$

with here $\Delta = -J_z/J_{xy}$. The $\ln l$ contribution in the fluctuations comes from gapless modes in the effective fermions theory achieved by the Jordan-Wigner transformation. We will therefore refer to this phase at weak-coupling with impurities, i.e. starting from $U_{af} = 0$, as gapless phase. When $\Delta \leq -1$, Eq. (5.4) is not valid. Instead, the ferromagnetic Ising phase shows a classical order and the bipartite fluctuations should then be zero when $U_{af} = 0$. The Heisenberg point $\Delta = 1$ is also special since in the bosonized framework there is a marginal operator at this point so that the spin correlations acquire a correction [131, 232] and for $\Delta > 1$ the system becomes gapped and Eq. (5.4) needs to be modified [232, 246].

Including the effects of disorder through U_{af}, a phase transition to a localized phase is anticipated while for small values of disorder the scaling of the bipartite fluctuation with subsystem size for the disorder-free case from Eq. (5.4) should still hold (at least qualitatively) as long as we are in the gapless phase with visible bipartite fluctuations. We verify that disorder induces a transition to a localized phase by plotting the disorder-averaged bipartite fluctuation $\overline{\mathcal{F}}$ against the disorder strength U_{af} for different values of J_z in Fig. 5.2. For $-1 < -J_z/J_{xy} < 1$, the behaviour is qualitatively the same with a sharp transition to the localized phase for a critical value of disorder strength U_{af} depending on J_z. The curve with $J_z = -0.25$ is in the ferromagnetic phase, consequently its behaviour is different for $U_{af} = 0$ and the bipartite fluctuation vanishes. It is interesting to observe in Fig. 5.2 that for increasing values of disorder the behaviour of this curve can still be compared to the other curves qualitatively.

In the gapless phase (i.e. at small disorder), interestingly already for small systems sizes, we can fit the parameters f_2 and A_1 from Eq. (5.4) to the results from the simulation, which is shown in Fig. 5.3. The simulation results for the gapless phase are here represented by dots, the results from fitting to Eq. (5.4) for $U_{af} = 0.1$ are shown by solid lines. In the strongly localized regime, results for a large value of disorder U_{af} lead to a vanishing bipartite fluctuation for all values of J_z (represented by crosses in the figure). For the

[1] The form of the Luttinger parameter given below Eq. (4.28) is only valid in the perturbative region $|J_z| \ll |J_{xy}|$.

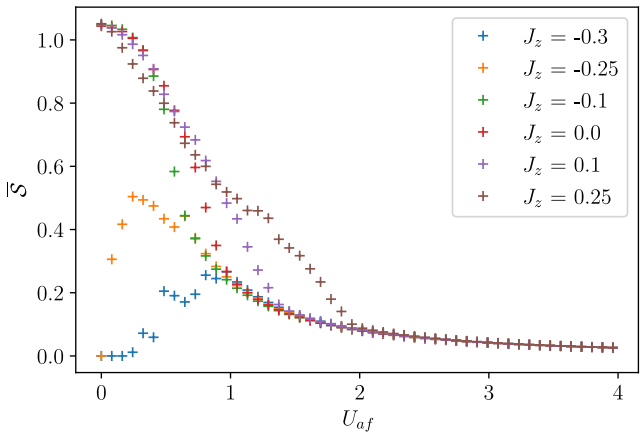

Figure 5.4: The entanglement entropy averaged over all realizations of τ_i^z for $N = 8$ with periodic boundary conditions, the bipartition boundary being in the center of the chain (i.e. $l = N/2$). The parameters are similar to Fig. 5.2 and bridge also with Ref. [126].

considered situation, we observe that the curve with $J_z = 0.25$ corresponding to the Heisenberg point could be also fitted with Eq. (5.4) in Fig. 5.3 even though corrections are present in the form of the A_1 term [131].

5.1.2 Entanglement entropy

Definition of the entanglement entropy

The entanglement entropy S between two subsystems, as introduced in Eq. (1.66), is defined by

$$S = -\operatorname{Tr} \rho_A \ln \rho_A, \tag{5.6}$$

where $\rho_A = \operatorname{Tr}_B (|\psi\rangle \langle\psi|)$ is the density matrix of the ground state with the degrees of freedom of the composite subsystem (i.e., the subsystem B in Fig. 1.4) traced out. Using this definition, we can evaluate the entanglement entropy numerically.

Ground state properties

In the interacting model, similar to Sec. 5.1.1, we can plot the entanglement entropy in the ground state averaged over all disorder configurations as a function of the disorder strength and for various interaction strengths. The result, shown in Fig. 5.4, reveals similar features to Fig. 5.2 in the sense that there is a sharp transition in the entanglement entropy for larger values of disorder.

In order to find a clear indication of the MBL phase, we have to depart from the ground state description. Therefore, we will in the following study the long-time evolution of the bipartite fluctuations and the entanglement entropy. The latter will give a clear criterion to identify the MBL phase [126].

5.2 MBL in an effective spin model with $U(1)$ gauge fields

5.2.1 Long-time evolution of the bipartite fluctuations

In order to detect an MBL phase in the model described by Eq. (4.7), we have to depart from the time-independent ground state description. The bipartite fluctuations can be a witness[2] of an MBL phase when studying its scaling in time and with the system size [126, 251].

To make the connection with [126], we study the bipartite fluctuation in time when starting from a global quench of the system. For this, we prepare the system of $\vec{\sigma}$-spins in the Néel state in z-direction $|\uparrow\downarrow\uparrow\downarrow ... \uparrow\downarrow\rangle$ and evolve in time with the Hamiltonian (4.7) with $J_{xy} = -0.25$, $J_z = 0.25$ and $aA^{\parallel}_{i,i+1} = 0.01$. We then evaluate the bipartite fluctuations of the half chain (i.e. $l = N/2$) as an average over all configurations of disorder defined by $\tau^z_i = \pm 1$. We then compare qualitatively to the results obtained in [126], where the authors simulated a system with similar interaction strengths, but without the gauge field, without a transverse field (i.e., at $g = 0$) and with disorder drawn from a uniform distribution.

For $g = 0.0$, we observe a similar behaviour as in Ref. [126]: With weak disorder, when initializing the system in the Néel state, the bipartite fluctuations of the half chain averaged over all possible disorder configurations (that we call $\overline{\mathcal{F}}$) saturate to a finite value after a rapid growth (see Fig. 5.5a). In the localized phase with strong disorder (i.e. large values of U_{af}), the bipartite fluctuations show a rapid growth at short times, after which they saturate (see Fig. 5.5b).

This situation remains qualitatively similar when adding the transverse field with $g = 0.1$. In the two lower panels of Fig. 5.5, we show the results for the the bipartite fluctuation at $g = 0.1$ with relatively weak disorder $U_{af} = 1.0$ (see Fig. 5.5c) and with strong disorder in the localized phase with $U_{af} = 10.0$ (see Fig. 5.5d). For both $g = 0.0$ and $g = 0.1$, at long times we find the volume-law scaling with system size for weak disorder, and a constant saturation value (i.e., an area-law scaling) at strong disorder, also consistent with [126]. In the following section, we will do a similar comparison to the results in [126] showing the entanglement entropy.

[2] In the sense that it is an entanglement witness, meaning that entanglement will manifest itself in a large value of the bipartite fluctuations. For a sufficient criterion of an MBL phase, one has however to refer to the entanglement entropy, as there are situations where the bipartite fluctuations do not capture the transition to an MBL phase [251].

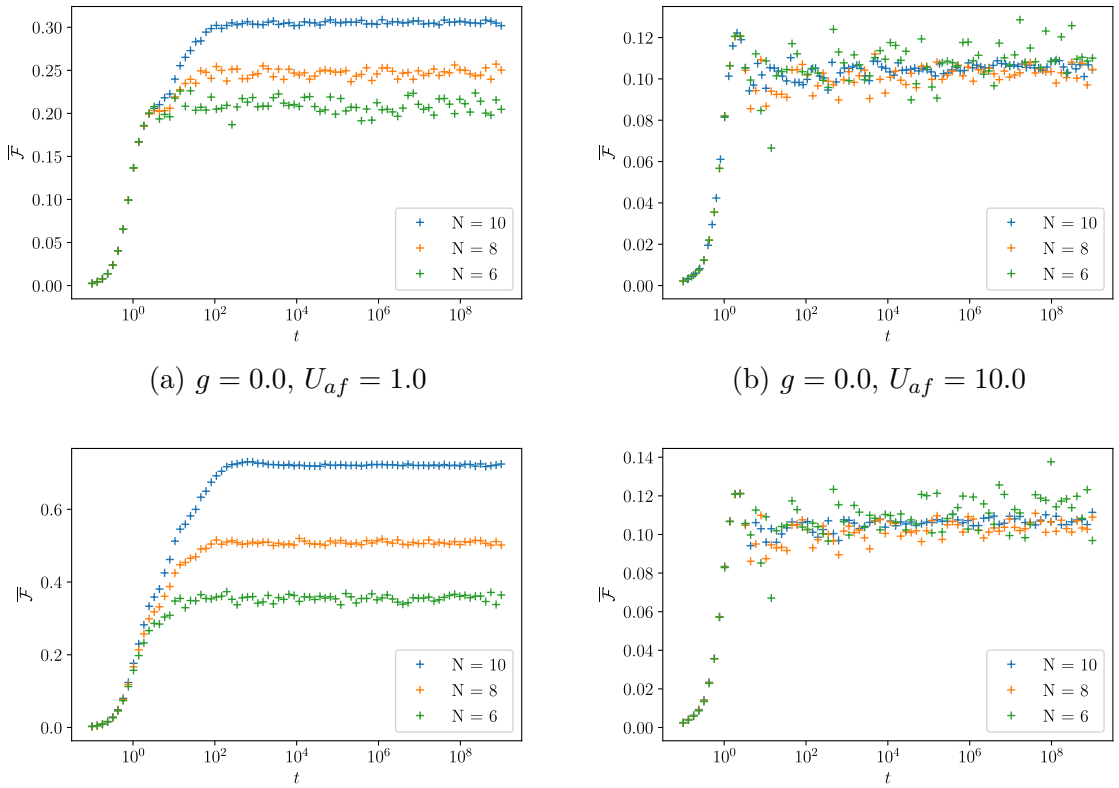

(a) $g = 0.0$, $U_{af} = 1.0$

(b) $g = 0.0$, $U_{af} = 10.0$

(c) $g = 0.1$, $U_{af} = 1.0$

(d) $g = 0.1$, $U_{af} = 10.0$

Figure 5.5: Adapted from [216]. Bipartite fluctuation for the half chain (i.e. $l = N/2$) starting from the Néel state with $g = 0.0$ (upper line) and $g = 0.1$ (lower line), for different values of disorder ($U_{af} = 1.0$ on the left and $U_{af} = 10.0$ on the right). Here we show an average over all possible configurations of disorder with open boundary conditions. The parameters are $J_{xy} = -0.25$, $J_z = 0.25$, $g = 0.1$ and $aA^{\parallel}_{i,i+1} = 0.01$.

5.2.2 Detecting the MBL phase from the entanglement entropy

To detect the MBL phase, we are attempting to measure the entanglement entropy after a global quench in time. A slow growth holds as a sufficient criterion to identify an MBL phase [22, 126, 129]. To implement this, we use a similar protocol as described in Sec. 5.2.1: Starting from a global quench, we evolve the system in time for all different disorder configurations and finally take the disorder average. Keeping the parameters used in Sec. 5.2.1 (i.e., $J_{xy} = -0.25$, $J_z = 0.25$ and $aA^{\parallel}_{i,i+1} = 0.01$) to compare to Ref. [126] and starting from the Néel state in z-direction, we find the results shown in Fig. 5.6.

At weak disorder, we find a volume-law scaling at long times of the entanglement entropy, i.e., $S = \alpha N$ after a long time evolution, where the maximal value for α is $\ln(2)/2$ when partitioning the system into two half-chains [126]. At strong disorder, we find the characteristic slow growth of the entanglement entropy after an initial fast increase [126, 129]. The latter is a characteristic property of an MBL phase. We find this behaviour at both $g = 0.0$ and $g = 0.1$, with the special form of a binary disorder

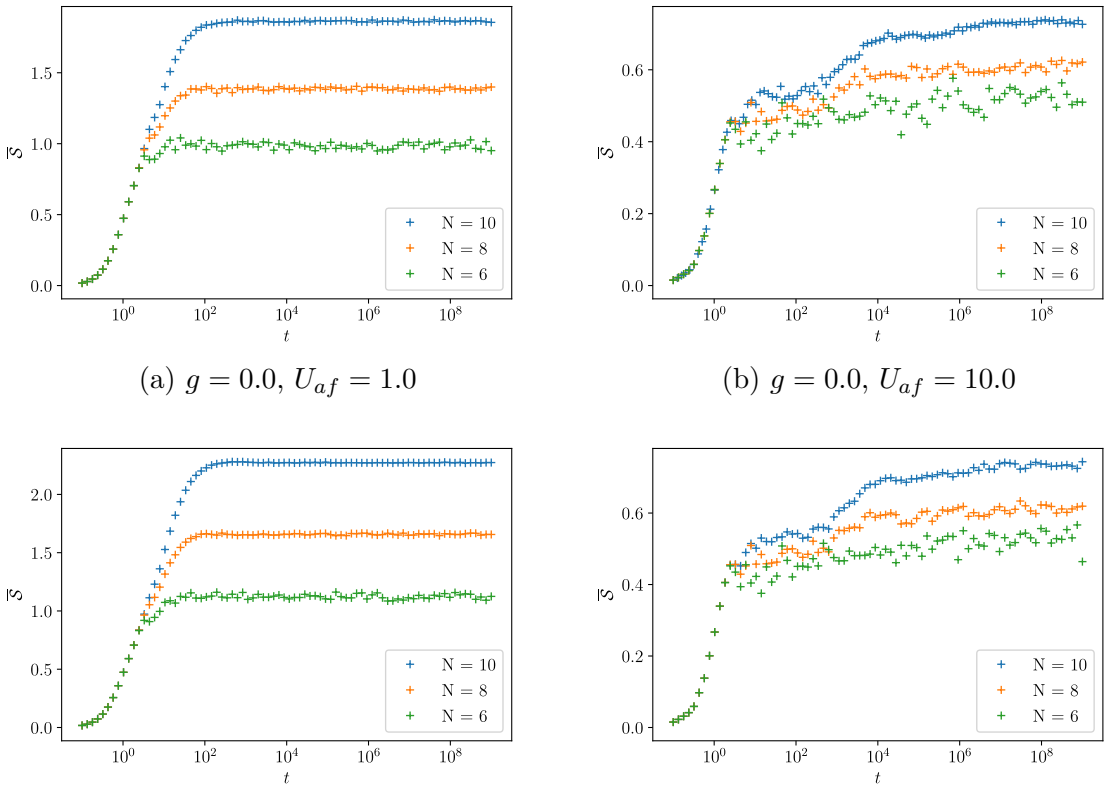

(a) $g = 0.0$, $U_{af} = 1.0$

(b) $g = 0.0$, $U_{af} = 10.0$

(c) $g = 0.1$, $U_{af} = 1.0$

(d) $g = 0.1$, $U_{af} = 10.0$

Figure 5.6: Adapted from [216]. Entanglement entropy for the half chain (i.e. $l = N/2$) starting from the Néel state with $g = 0.0$ (upper line) and $g = 0.1$ (lower line), for different values of disorder ($U_{af} = 1.0$ on the left and $U_{af} = 10.0$ on the right). Here we show an average over all possible configurations of disorder with open boundary conditions. The parameters are the same as in Fig. 5.5.

potential and complex xy-interaction coefficients. We therefore conclude that at strong disorder, the model introduced in Eq. (4.7) undergoes a transition to an MBL phase, which is stable upon adding a $\mathcal{U}(1)$ gauge field and a small transverse magnetic field g. In the following section, we will study the asymptotic behaviour after a long time in more detail and in particular also examine the local current introduced in Eq. (4.3), which can now be measured dynamically.

5.2.3 Localization of the dynamical parallel current

In order to complete the comparison with [126], we also check the asymptotic behaviour at long times of the bipartite fluctuations, the entanglement entropy and finally also the dynamically measured current. The current at a site i, defined from Eq. (4.3), can in the spin language be determined by simply measuring the time derivative of $\langle \sigma_i^z \rangle$, i.e., $\langle j_i \rangle = \langle \dot{\sigma}_i^z \rangle$ and is thus a local observable easily accessible. Therefore, we evolve the system with a given disorder configuration for a long time and consequently evaluate

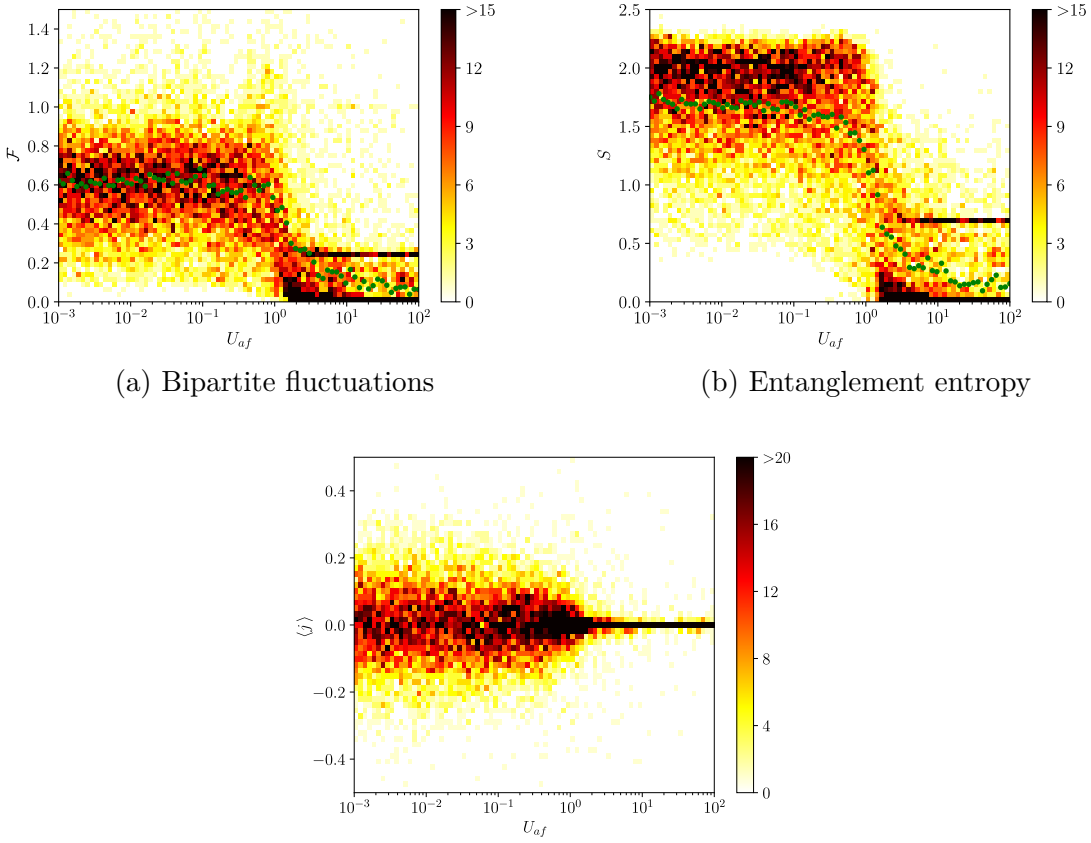

(a) Bipartite fluctuations

(b) Entanglement entropy

(c) Local current

Figure 5.7: Adapted from [216]. Histograms of (a) the bipartite fluctuations, (b) the entanglement entropy for a half chain and (c) the local current evaluated between the two sites at the center of the chain as a function of U_{af} for all configurations of disorder. The color shows the number of disorder configurations with an observable in the respective range. The system was initalized in the Néel state and consequently evolved in time until $t = 10^{16}$, at which the respective quantity was evaluated. The green dots show a disorder average. The parameters are $J_{xy} = -0.25$, $J_z = 0.25$, $g = 0.1$, $aA^{\parallel}_{i,i+1} = 0.01$ and $N = 8$.

the observables numerically. The results of this procedure in the form of histograms for all different configurations of disorder with the bipartite fluctuations, the entanglement entropy and the local current evaluated for different values of the disorder strength U_{af} are shown in Fig. 5.7. The results for the entanglement entropy and the bipartite fluctuations show a localization of these quantities at strong disorder with a clear transition value, in agreement with the existence of an MBL transition and previously established results [126]. Note that at large values of disorder, both the entanglement entropy and the bipartite fluctuations vanish for most of the disorder configurations, with a second peak occuring corresponding to the cutting of a singlet at the bipartition boundary [126, 252, 253]. The transition is also observed from the sharpness of the peaks in the bipartite fluctuations and the entanglement entropy: While at small disorder values, the quantities have a finite mean with a larger variance, they clearly focus to the two peaks with little variance after

the transition. The results are qualitatively similar with $g = 0.0$ (not shown).

Interestingly, this transition can also be observed in the local current: While at smaller disorder values, it strongly flucutates around its mean for different disorder configurations, it becomes focussed with small variance after the transition. We thus conclude this chapter, summarizing that we found a many-body localized phase in the model introduced in Eq. (4.7), which is stable towards adding a gauge field at the xy-coupling term, a small transverse field and also with respect to a peaked disorder potential. The existence of the MBL phase is proven by the scaling in time of the entanglement entropy, but witnessed equivalently by the bipartite fluctuations and the long-time distribution of the local current. We emphasize that this is a local measurable quantity, accessible in experimental setups described in Sec. 4.4.

5.3 Conclusion and outlook

In this chapter, we have studied a gauged XXZ-model with binary disorder and a finite transverse magnetic field. Studying the scaling of the bipartite fluctuations and the entanglement entropy of the half-chain in time, we find results in agreement with previous studies of an XXZ-chain with uniform disorder [126]: With weak disorder, we find a fast saturation to a volume law of both the entanglement entropy and the bipartite fluctuations. For strong disorder, the bipartite fluctuations saturate to an area law, while the entanglement entropy shows the characteristic slow growth. We thus conclude from the scaling of the entanglement entropy that an MBL transition occurs and see that the bipartite fluctuations are also a witness.

After a long time evolution, we see that both the entanglement entropy and the bipartite fluctuations show a transition for increasing disorder. Interestingly, this transition can also be seen in the expectation value of the local current: While its average value remains unchanged, its variance when considering many different disorder configurations, also serves as a witness of this MBL transition.

The analysis in this chapter has shown that the MBL phase is stable towards the special type of implemented disorder, a $\mathcal{U}(1)$ gauge field and a transverse magnetic field. Combining these findings with the partial topological properties of interacting spins discussed in Sec. 1.1.3 and Chap. 3, as well as with the dynamical protocol studied in Chap. 2, it is an interesting question whether the (many-body) localization properties of the spin chain interact with the partial topology of each spin. To study this question, the following conditions necessarily need to be satisfied:

1. The MBL phase is preserved upon applying a periodic driving.

2. The partial topology can be defined for systems with $N > 2$ and in presence of disorder.

3. The definition of partial topology makes sense for a system with finite energy.

For each of these conditions, we note the current state of advancement from the scientific community and our own current activities:

1. This question has been adressed in [254]. There it has been found that an MBL phase persists with periodic driving at high frequencies. Since in the setup for studying the topology of a spin-1/2 dynamically, one attempts to reach quasi-adiabatic driving speeds, this implies that the study of dynamically accessed quantities as C_{dyn} defined in Eq. (2.9) is more straightforward in this context. However, a larger disorder strength can lead to an MBL transistion also in a slowly driven system [254].

2. The occurence of fractional partial Chern numbers for longer systems has been adressed in [12]. There it has been argued, that in a chain with periodic boundary conditions and an odd number of sites N and in a chain with open boundary conditions and an even number of sites, fractional partial Chern numbers can occur. Using the arguments from Sec. 3.1, a transverse coupling is expected to support these states when adding weak disorder.

3. This point is a major concern when trying to study the partial topology in relation with an MBL phase: For the latter, as done in the analysis in this chapter, one initializes the system in a state that is not necessarily an eigenstate and studies the thermalization properties. However, for studying a (partial) topological quantity, as done in Chap. 3, one evolves the system quasi-adiabatically in an eigenstate (or, in the case of Chap. 3, the ground state) of the system. As these two approaches are in a way opposing each other, an interesting option is to use other probes of MBL, such as the energy level statistics of the Hamiltonian. It is an interesting question, whether doing such a study in time would then allow to make a connection with the partial topological properties of each spin.

While our efforts in these directions have not yet been conclusive, this study could potentially serve as an interesting link between MBL and topological properties [229, 255], relevant for applications trying to harness the potential of topological states, while in the same time operating in a disordered context.

Chapter 6

Conclusion

In this thesis, we have considered topological properties, effects of driven-dissipative dynamics and disorder physics in spin systems. From the general definitions introduced in Sec. 1.1, one can study a topological invariant of a spin-1/2 in a radial magnetic field, which provides a formalism that can be extended to a spin coupled to an environment (cf. Chap. 2) and to interacting systems (cf. Sec. 1.1.3 and Chap. 3). In addition, this model gives a formalism to think about topological invariants in other systems (see Sec. 1.1.2), such as the Haldane model [9, 35, 37], or the p-wave supercoducting wire [51–53].

In Chap. 2, we have then studied a new effect arising when implementing this prescription of a topological invariant using a dynamical protocol and coupling the system to an Ohmic environment. This effect, called the 'quantum dynamo effect' [32, 33], occurs for environment modes close to resonance with the driving velocity and leads to their coherent displacement, thus corresponding to a work transfer into the bath. This bridges with recent results in the rapidly developing field of quantum thermodynamics [24–27, 67]. We analyzed this effect in detail for a spin coupled to one mode and to an Ohmic bath using analytical techniques, energetic definitions and numerical approaches, notably exact diagonalization and a stochastic Schrödinger equation approach (cf. App. B). In this way, we could find the conditions under which this effect can operate at high efficiency. Curiously, it is related to the dynamically accessed topological properties of the driven spin. This work thus opens interesting perspectives for applications with energy transfers on the quantum scale [74].

We then continued to study topological properties of spins in Chap. 3, but this time with interactions. Such a setup has been shown to give rise to a fractionalization of the partial Chern number [12]. Here we studied the interplay of these fractional numbers to the introduction of an asymmetry due to disorder. We found that this asymmetry, while leaving the global topology invariant, can lead to a shift from a phase with a 1/2 fractional topology for each spin to a phase with an integer and a trivial topology for one of the two sites respectively. However, the introduction of a transverse coupling between the spins, maintaining the global rotational symmetry, allows to mimick the fractional phase in the

presence of disorder in the sense of a disorder average. The disorder in this case has the peculiar effect of extending this fractional phase. The mechanism underlying this extension is a transition to an entangled singlet state enabled by the disorder. It is therefore a different effect than the topological Anderson insulator, as its origin is inherently dynamical. The symmetry breaking due to disorder thus is a two-sided mechanism: On the one hand, it leads to a finite deviation from the fractionalized topological numbers, on the other hand it enables their accessibility in another region of phase space. Interpreting the two-spin setup in terms of Majorana fermions [36] allows to think about the discussed physical effects in terms of Majorana parities and interpret the fractional numbers as different Majorana signatures at the two opposite poles. This opens perspectives for applications as a parity qubit [14, 182, 189], which bridges with recent experimental progress [17].

In order to study localization phenomena in more extended spin systems and with a focus on their realization and detection, we introduced a one-dimensional bosonic lattice model in Chap. 4, which can be mapped onto a spin model in a certain limit giving rise to a rung-Mott phase. There, we investigate the role of a $\mathcal{U}(1)$ gauge field, allowing to define a current in an analogue of the Meissner effect [197, 217, 224, 225] and its interplay with a special form of disorder introduced by a second particle species [216]. By studying different limits of interaction in this effective spin model, we observe that the current defined from the analogous Meissner effect can be seen as an indicator for localization due to the interaction with the second particle species. Furthermore, when the second particle species acquires a quantum dynamics as well, we showed through a relation to $\mathbb{Z}_2$ lattice gauge theories on a double well [214, 215] how this can hinder the localization of the current and also considered the limit of very strong coupling to the impurities, in which an effective spin model featuring four-body interactions can be derived. The relation with recent works on the relation of such one-dimensional condensed matter systems with $\mathbb{Z}_2$ lattice gauge theories opens perspectives on realizations of this setup [213, 214].

Finally, in Chap. 5 we inquired about the possibility to realize a many-body localized (MBL) phase in the model introduced in Chap. 4. Formally, the model we introduced has been widely studied in this context [119, 120, 126, 249]. We examined the effect of a binary disorder due to the coupling to impurities, application of a $\mathcal{U}(1)$ gauge field and a finite transverse field. By studying the entanglement entropy, we can identify the occurence and stability of an MBL phase in our model, which is also witnessed by the bipartite fluctuations [131, 246] and the current defined in Chap. 4, already for relatively short systems. The study of the localization properties of such spin systems together with the formalism introduced in Sec. 1.1 for defining the topology of a single spin-1/2 opens interesting perspectives on studying their interplay. As MBL naturally bridges with thermal properties of quantum systems, this can then potentially also be linked with the discussion of thermodynamic properties and the quantum dynamo effect discussed in Chap. 2.

Bibliography

[1] Lev D. Landau. On the theory of phase transitions. I. *Zhurnal Eksperimental'noi i Teoreticheskoi Fiziki*, 11:19–32, 1937. URL: http://archive.ujp.bitp.kiev.ua/files/journals/53/si/53SI08p.pdf.

[2] M. Zahid Hasan and Charles L. Kane. Colloquium: Topological insulators. *Reviews of Modern Physics*, 82(4):3045, 2010. URL: 10.1103/RevModPhys.82.3045.

[3] Jerome Cayssol. Introduction to Dirac materials and topological insulators. *Comptes Rendus Physique*, 14(9-10):760–778, 2013. doi:10.1016/j.crhy.2013.09.012.

[4] Klaus v. Klitzing, Gerhard Dorda, and Michael Pepper. New method for high-accuracy determination of the fine-structure constant based on quantized Hall resistance. *Physical Review Letters*, 45(6):494, 1980. doi:10.1103/PhysRevLett.45.494.

[5] Robert B. Laughlin. Quantized Hall conductivity in two dimensions. *Physical Review B*, 23(10):5632, 1981. doi:10.1007/978-94-010-9709-3_14.

[6] Bertrand I. Halperin. Quantized Hall conductance, current-carrying edge states, and the existence of extended states in a two-dimensional disordered potential. *Physical Review B*, 25(4):2185, 1982. doi:10.1007/978-94-010-9709-3_15.

[7] David J. Thouless, Mahito Kohmoto, M. Peter Nightingale, and Marcel den Nijs. Quantized Hall conductance in a two-dimensional periodic potential. *Physical Review Letters*, 49(6):405, 1982. doi:10.1016/0378-4371(84)90239-5.

[8] Michael V. Berry. Quantal phase factors accompanying adiabatic changes. *Proceedings of the Royal Society of London. A. Mathematical and Physical Sciences*, 392(1802):45–57, 1984. doi:10.1142/9789813221215_0006.

[9] F. Duncan M. Haldane. Model for a quantum Hall effect without Landau levels: Condensed-matter realization of the "parity anomaly". *Physical Review Letters*, 61(18):2015, 1988. doi:10.1103/PhysRevLett.61.2015.

[10] Gregor Jotzu, Michael Messer, Rémi Desbuquois, Martin Lebrat, Thomas Uehlinger, Daniel Greif, and Tilman Esslinger. Experimental realization of the topological Haldane model with ultracold fermions. *Nature*, 515(7526):237–240, 2014. doi:10.1038/nature13915.

[11] Peng Cheng, Philipp W. Klein, Kirill Plekhanov, Klaus Sengstock, Monika Aidelsburger, Christof Weitenberg, and Karyn Le Hur. Topological proximity effects in a Haldane graphene bilayer system. *Physical Review B*, 100(8):081107, 2019. doi:10.1103/PhysRevB.100.081107.

[12] Joel Hutchinson and Karyn Le Hur. Quantum entangled fractional topology and curvatures. *Communications Physics*, 4(1):1–9, 2021. doi:10.1038/s42005-021-00641-0.

[13] Karyn Le Hur and Sariah Al Saati. Topological nodal ring semimetal in graphene. *Physical Review B*, 107(16):165407, 2023. doi:10.1103/PhysRevB.107.165407.

[14] Alexei Y. Kitaev. Unpaired Majorana fermions in quantum wires. *Physics-Uspekhi*, 44(10S):131, 2001. doi:10.1070/1063-7869/44/10S/S29.

[15] Alexei Y. Kitaev. Fault-tolerant quantum computation by anyons. *Annals of Physics*, 303(1):2–30, 2003. doi:10.1016/S0003-4916(02)00018-0.

[16] Chetan Nayak, Steven H. Simon, Ady Stern, Michael Freedman, and Sankar Das Sarma. Non-Abelian anyons and topological quantum computation. *Reviews of Modern Physics*, 80(3):1083, 2008. doi:10.1103/RevModPhys.80.1083.

[17] Tom Dvir, Guanzhong Wang, Nick van Loo, Chun-Xiao Liu, Grzegorz P. Mazur, Alberto Bordin, Sebastiaan L. D. Ten Haaf, Ji-Yin Wang, David van Driel, Francesco Zatelli, et al. Realization of a minimal Kitaev chain in coupled quantum dots. *Nature*, 614(7948):445–450, 2023. doi:10.1038/s41586-022-05585-1.

[18] Philip W. Anderson. Local moments and localized states. *Science*, 201(4353):307–316, 1978. doi:10.1126/science.201.4353.307.

[19] Thierry Giamarchi and Heinz J. Schulz. Anderson localization and interactions in one-dimensional metals. *Physical Review B*, 37(1):325, 1988. doi:10.1103/PhysRevB.37.325.

[20] Boris L. Altshuler, Yuval Gefen, Alex Kamenev, and Leonid S. Levitov. Quasiparticle lifetime in a finite system: A nonperturbative approach. *Physical Review Letters*, 78(14):2803, 1997. doi:10.1103/PhysRevLett.78.2803.

[21] Igor V. Gornyi, Alexander D. Mirlin, and Dmitry G. Polyakov. Interacting electrons in disordered wires: Anderson localization and low-T transport. *Physical Review Letters*, 95(20):206603, 2005. doi:10.1103/PhysRevLett.95.206603.

[22] Dmitry A. Abanin, Ehud Altman, Immanuel Bloch, and Maksym Serbyn. Colloquium: Many-body localization, thermalization, and entanglement. *Reviews of Modern Physics*, 91(2):021001, 2019. doi:10.1103/RevModPhys.91.021001.

[23] Christoph Berke, Evangelos Varvelis, Simon Trebst, Alexander Altland, and David P. DiVincenzo. Transmon platform for quantum computing challenged by chaotic fluctuations. *Nature Communications*, 13(1):2495, 2022. doi:10.1038/s41467-022-29940-y.

[24] Philipp Strasberg and Andreas Winter. First and second law of quantum thermodynamics: a consistent derivation based on a microscopic definition of entropy. *Physical Review X Quantum*, 2(3):030202, 2021. doi:10.1103/PRXQuantum.2.030202.

[25] Juliette Monsel, Marco Fellous-Asiani, Benjamin Huard, and Alexia Auffeves. The Energetic Cost of Work Extraction. *Physical Review Letters*, 124(13):130601, March 2020. doi:10.1103/PhysRevLett.124.130601.

[26] Maria Maffei, Patrice A. Camati, and Alexia Auffeves. Probing nonclassical light fields with energetic witnesses in waveguide quantum electrodynamics. *Physical Review Research*, 3(3):L032073, September 2021. doi:10.1103/PhysRevResearch.3.L032073.

[27] Cyril Elouard and Camille L. Latune. Extending the laws of thermodynamics for arbitrary autonomous quantum systems. *Physical Review X Quantum*, 4(2):020309, 2023. doi:10.1103/PRXQuantum.4.020309.

[28] Iulia M. Georgescu, Sahel Ashhab, and Franco Nori. Quantum simulation. *Reviews of Modern Physics*, 86(1):153, 2014. doi:10.1103/RevModPhys.86.153.

[29] Hendrick A. Kramers and Gregory H. Wannier. Statistics of the two-dimensional ferromagnet. Part I. *Physical Review*, 60(3):252, 1941. doi:10.1103/PhysRev.60.252.

[30] Franz J. Wegner. Duality in generalized Ising models and phase transitions without local order parameters. *Journal of Mathematical Physics*, 12(10):2259–2272, 1971. doi:10.1063/1.1665530.

[31] Franz J. Wegner. Duality in generalized ising models. In *Topological Aspects of Condensed Matter Physics: Lecture Notes of the Les Houches Summer School:*

Volume 103, August 2014, pages 219–240. Oxford University Press, 2017. doi:10.1093/acprof:oso/9780198785781.003.0005.

[32] Loïc Henriet, Antonio Sclocchi, Peter P Orth, and Karyn Le Hur. Topology of a dissipative spin: Dynamical Chern number, bath-induced nonadiabaticity, and a quantum dynamo effect. *Physical Review B*, 95(5):054307, 2017. doi:10.1103/PhysRevB.95.054307.

[33] Ephraim Bernhardt, Cyril Elouard, and Karyn Le Hur. Topologically protected quantum dynamo effect in a driven spin-boson model. *Physical Review A*, 107(2):022219, 2023. doi:10.1103/PhysRevA.107.022219.

[34] Vladimir Gritsev and A. Polkovnikov. Dynamical quantum Hall effect in the parameter space. *Proceedings of the National Academy of Sciences*, 109(17):6457–6462, 2012. doi:10.1073/pnas.1116693109.

[35] Pedram Roushan, C. Neill, Yu Chen, M. Kolodrubetz, C. Quintana, N. Leung, M. Fang, R. Barends, B. Campbell, Z. Chen, et al. Observation of topological transitions in interacting quantum circuits. *Nature*, 515(7526):241–244, 2014. doi:10.1038/nature13891.

[36] Karyn Le Hur. Topological matter and fractional entangled geometry. *arXiv preprint arXiv:2209.15381*, 2022. doi:10.48550/arXiv.2209.15381.

[37] M. D. Schroer, M. H. Kolodrubetz, W. F. Kindel, M. Sandberg, J. Gao, M. R. Vissers, D. P. Pappas, Anatoli Polkovnikov, and K. W. Lehnert. Measuring a topological transition in an artificial spin-1/2 system. *Physical Review Letters*, 113(5):050402, 2014. doi:10.1103/PhysRevLett.113.050402.

[38] Philip Richard Wallace. The band theory of graphite. *Physical Review*, 71(9):622, 1947. doi:10.1103/PhysRev.71.622.

[39] A. H. Castro Neto, Francisco Guinea, Nuno M. R. Peres, Kostya S. Novoselov, and Andre K. Geim. The electronic properties of graphene. *Reviews of Modern Physics*, 81(1):109, 2009. doi:10.1002/pssb.200776208.

[40] Gordon W. Semenoff. Condensed-matter simulation of a three-dimensional anomaly. *Physical Review Letters*, 53(26):2449, 1984. doi:10.1103/PhysRevLett.53.2449.

[41] Karyn Le Hur. Global and local topological quantized responses from geometry, light, and time. *Physical Review B*, 105(12):125106, 2022. doi:10.1103/PhysRevB.105.125106.

[42] N. Fläschner, D. Vogel, M. Tarnowski, B. S. Rem, D.-S. Lühmann, Markus Heyl, J. C. Budich, L. Mathey, Klaus Sengstock, and C. Weitenberg. Observation of dynamical vortices after quenches in a system with topology. *Nature Physics*, 14(3):265–268, 2018. doi:10.1038/s41567-017-0013-8.

[43] Jason Alicea, Yuval Oreg, Gil Refael, Felix Von Oppen, and Matthew P.A. Fisher. Non-Abelian statistics and topological quantum information processing in 1D wire networks. *Nature Physics*, 7(5):412–417, 2011. doi:10.1038/nphys1915.

[44] Xiao Mi, M. Sonner, M. Y. Niu, K. W. Lee, B. Foxen, R. Acharya, I. Aleiner, T. I. Andersen, F. Arute, K. Arya, et al. Noise-resilient edge modes on a chain of superconducting qubits. *Science*, 378(6621):785–790, 2022. doi:10.1126/science.abq5769.

[45] Yuval Oreg, Gil Refael, and Felix Von Oppen. Helical liquids and Majorana bound states in quantum wires. *Physical Review Letters*, 105(17):177002, 2010. doi:10.1103/PhysRevLett.105.177002.

[46] Roman M. Lutchyn, Jay D. Sau, and S. Das Sarma. Majorana fermions and a topological phase transition in semiconductor-superconductor heterostructures. *Physical Review Letters*, 105(7):077001, 2010. doi:10.1103/PhysRevLett.105.077001.

[47] Martin Leijnse and Karsten Flensberg. Introduction to topological superconductivity and Majorana fermions. *Semiconductor Science and Technology*, 27(12):124003, 2012. doi:10.1088/0268-1242/27/12/124003.

[48] Vincent Mourik, Kun Zuo, Sergey M. Frolov, S. R. Plissard, Erik P. A. M. Bakkers, and Leo P. Kouwenhoven. Signatures of Majorana fermions in hybrid superconductor-semiconductor nanowire devices. *Science*, 336(6084):1003–1007, 2012. doi:10.1126/science.1222360.

[49] M.T. Deng, S. Vaitiekėnas, Esben Bork Hansen, Jeroen Danon, M. Leijnse, Karsten Flensberg, Jesper Nygård, P. Krogstrup, and Charles M. Marcus. Majorana bound state in a coupled quantum-dot hybrid-nanowire system. *Science*, 354(6319):1557–1562, 2016. doi:10.1126/science.aaf3961.

[50] Roman M. Lutchyn, Erik P. A. M. Bakkers, Leo P. Kouwenhoven, Peter Krogstrup, Charles M. Marcus, and Yuval Oreg. Majorana zero modes in superconductor–semiconductor heterostructures. *Nature Reviews Materials*, 3(5):52–68, 2018. doi:10.1038/s41578-018-0003-1.

[51] Frederick del Pozo, Loïc Herviou, and Karyn Le Hur. Fractional topology in interacting one-dimensional superconductors. *Physical Review B*, 107(15):155134, 2023. doi:10.1103/PhysRevB.107.155134.

[52] Jason Alicea. New directions in the pursuit of Majorana fermions in solid state systems. *Reports on Progress in Physics*, 75(7):076501, 2012. doi:10.1088/0034-4885/75/7/076501.

[53] Masatoshi Sato and Yoichi Ando. Topological superconductors: a review. *Reports on Progress in Physics*, 80(7):076501, 2017. doi:10.1088/1361-6633/aa6ac7.

[54] Ettore Majorana. Teoria simmetrica dell'elettrone e del positrone. *Il Nuovo Cimento (1924-1942)*, 14:171–184, 1937. doi:10.1007/BF02961314.

[55] N. B. Kopnin and M. M. Salomaa. Mutual friction in superfluid ^{3}He: Effects of bound states in the vortex core. *Physical Review B*, 44(17):9667, 1991. doi:10.1103/PhysRevB.44.9667.

[56] Nicholas Read and Dmitry Green. Paired states of fermions in two dimensions with breaking of parity and time-reversal symmetries and the fractional quantum Hall effect. *Physical Review B*, 61(15):10267, 2000. doi:10.1103/PhysRevB.61.10267.

[57] Karyn Le Hur. Kondo effect in a one-dimensional d-wave superconductor. *Europhysics Letters*, (6):768. doi:10.1209/epl/i2000-00217-9.

[58] Serge Florens, Davide Venturelli, and R. Narayanan. Quantum phase transition in the spin boson model. In *Quantum Quenching, Annealing and Computation*, pages 145–162. Springer, 2010. doi:10.1007/978-3-642-11470-0_6.

[59] Albert Einstein, Boris Podolsky, and Nathan Rosen. Can quantum-mechanical description of physical reality be considered complete? *Physical Review*, 47(10):777, 1935. doi:10.1007/978-3-322-91080-6_6.

[60] John S. Bell. On the Einstein-Podolsky-Rosen paradox. *Physics Physique Fizika*, 1(3):195, 1964. doi:10.1017/CBO9780511815676.004.

[61] Heinz-Peter Breuer and Francesco Petruccione. *The theory of open quantum systems*. Oxford University Press, 2007. doi:10.1093/acprof:oso/9780199213900.001.0001.

[62] John von Neumann. Wahrscheinlichkeitstheoretischer Aufbau der Quantenmechanik. *Nachrichten von der Gesellschaft der Wissenschaften zu Göttingen, Mathematisch-Physikalische Klasse*, pages 245–272, 1927. URL: http://dml.mathdoc.fr/item/GDZPPN002507277.

[63] Lev D. Landau and Evgenii M. Lifshitz. Statistical physics. In *Statistical Physics*, volume 5 of *Course of Theoretical Physics*. Pergamon, 3rd edition, 1980. doi:10.1016/B978-0-08-023039-9.50007-X.

[64] Ulrich Weiss. *Quantum dissipative systems*. World Scientific, 4th edition, 2012. doi:10.1142/8334.

[65] Peter Talkner and Peter Hänggi. Colloquium: Statistical mechanics and thermodynamics at strong coupling: Quantum and classical. *Reviews of Modern Physics*, 92(4):041002, 2020. doi:10.1103/RevModPhys.92.041002.

[66] Ronnie Kosloff. Quantum thermodynamics: A dynamical viewpoint. *Entropy*, 15(6):2100–2128, 2013. doi:10.3390/e15062100.

[67] Robert Alicki and Ronnie Kosloff. Introduction to quantum thermodynamics: History and prospects. *Thermodynamics in the Quantum Regime: Fundamental Aspects and New Directions*, pages 1–33, 2018. doi:10.1007/978-3-319-99046-0_1.

[68] Alexia Auffèves. A short story of quantum and information thermodynamics. *SciPost Physics Lecture Notes*, page 27, 2021. doi:10.21468/SciPostPhysLectNotes.27.

[69] Sebastian Deffner and Steve Campbell. *Quantum Thermodynamics: An introduction to the thermodynamics of quantum information*. Morgan & Claypool Publishers, 2019. doi:10.1088/2053-2571/ab21c6.

[70] Robert S. Whitney, Rafael Sánchez, and Janine Splettstoesser. Quantum thermodynamics of nanoscale thermoelectrics and electronic devices. *Thermodynamics in the Quantum Regime: Fundamental Aspects and New Directions*, pages 175–206, 2018. doi:10.1007/978-3-319-99046-0_7.

[71] Nathan M. Myers, Obinna Abah, and Sebastian Deffner. Quantum thermodynamic devices: From theoretical proposals to experimental reality. *AVS Quantum Science*, 4(2):027101, 2022. doi:10.1116/5.0083192.

[72] Daniel J. Bedingham and Owen J.E. Maroney. The thermodynamic cost of quantum operations. *New Journal of Physics*, 18(11):113050, 2016. doi:10.1088/1367-2630/18/11/113050.

[73] Jeremy Stevens, Daniel Szombati, Maria Maffei, Cyril Elouard, Reouven Assouly, Nathanaël Cottet, Rémy Dassonneville, Quentin Ficheux, Stefan Zeppetzauer, Audrey Bienfait, et al. Energetics of a single qubit gate. *Physical Review Letters*, 129(11):110601, 2022. doi:10.1103/PhysRevLett.129.110601.

[74] Alexia Auffèves. Quantum technologies need a quantum energy initiative. *Physical Review X Quantum*, 3(2):020101, 2022. doi:10.1103/PRXQuantum.3.020101.

[75] Peter P. Orth, Adilet Imambekov, and Karyn Le Hur. Nonperturbative stochastic method for driven spin-boson model. *Physical Review B*, 87(1):014305, 2013. doi:10.1103/PhysRevB.87.014305.

[76] Richard P. Feynman and Frank L. Vernon. The theory of a general quantum system interacting with a linear dissipative system. *Annals of Physics*, 24:118–173, 1963. doi:10.1016/0003-4916(63)90068-X.

[77] Amir O. Caldeira and Anthony J. Leggett. Influence of dissipation on quantum tunneling in macroscopic systems. *Physical Review Letters*, 46(4):211, 1981. doi:10.1103/PhysRevLett.46.211.

[78] Amir O. Caldeira and Anthony J. Leggett. Quantum tunnelling in a dissipative system. *Annals of Physics*, 149(2):374–456, 1983. doi:10.1016/0003-4916(83)90202-6.

[79] Anthony J. Leggett, Sudip Chakravarty, Alan T. Dorsey, Matthew P. A. Fisher, Anupam Garg, and Wilhelm Zwerger. Dynamics of the dissipative two-state system. *Reviews of Modern Physics*, 59(1):1, 1987. doi:10.1103/RevModPhys.59.1.

[80] Karyn Le Hur. Quantum Phase Transitions in Spin-Boson Systems: Dissipation and Light Phenomena. In L. Carr, editor, *Understanding Quantum Phase Transitions*. CRC Press, Taylor & Francis, 2010. doi:10.1201/b10273.

[81] Robert Silbey and Robert A. Harris. Variational calculation of the dynamics of a two level system interacting with a bath. *The Journal of Chemical Physics*, 80(6):2615–2617, 1984. doi:10.1063/1.447055.

[82] Tobias Brandes. Coherent and collective quantum optical effects in mesoscopic systems. *Physics Reports*, 408(5-6):315–474, 2005. doi:10.1016/j.physrep.2004.12.002.

[83] Karyn Le Hur. Entanglement entropy, decoherence, and quantum phase transitions of a dissipative two-level system. *Annals of Physics*, 323(9):2208–2240, 2008. doi:10.1016/j.aop.2007.12.003.

[84] N. Williams, K. Le Hur, and A. Jordan. Effective thermodynamics of strongly coupled qubits. *Journal of Physics A: Mathematical and Theoretical*, 44:385003, 2011. doi:10.1088/1751-8113/44/38/385003.

[85] Julio Gea-Banacloche. Minimum energy requirements for quantum computation. *Physical Review Letters*, 89(21):217901, November 2002. doi:10.1103/PhysRevLett.89.217901.

[86] Philip W. Anderson. Absence of diffusion in certain random lattices. *Physical Review*, 109(5):1492, 1958. doi:10.1103/PhysRev.109.1492.

[87] Nevill F. Mott and W. D. Twose. The theory of impurity conduction. *Advances in Physics*, 10(38):107–163, 1961. doi:10.1142/9789812794086_0020.

[88] Elihu Abrahams, Philip W. Anderson, Donald C. Licciardello, and Tiruppattur V. Ramakrishnan. Scaling theory of localization: Absence of quantum diffusion in two dimensions. *Physical Review Letters*, 42(10):673, 1979. doi:10.1142/9789812567154_0042.

[89] Ad Lagendijk, Bart van Tiggelen, and Diederik S. Wiersma. Fifty years of Anderson localization. *Physics Today*, 62(8):24–29, 2009. doi:10.1063/1.3206091.

[90] Elihu Abrahams. *50 years of Anderson Localization*. World Scientific, 2010. doi:10.1142/7663.

[91] Laurent Sanchez-Palencia, David Clément, Pierre Lugan, Philippe Bouyer, Georgy V. Shlyapnikov, and Alain Aspect. Anderson localization of expanding Bose-Einstein condensates in random potentials. *Physical Review Letters*, 98(21):210401, 2007. doi:10.1103/PhysRevLett.98.210401.

[92] Juliette Billy, Vincent Josse, Zhanchun Zuo, Alain Bernard, Ben Hambrecht, Pierre Lugan, David Clément, Laurent Sanchez-Palencia, Philippe Bouyer, and Alain Aspect. Direct observation of Anderson localization of matter waves in a controlled disorder. *Nature*, 453(7197):891–894, 2008. doi:10.1038/nature07000.

[93] Julien Chabé, Gabriel Lemarié, Benoît Grémaud, Dominique Delande, Pascal Szriftgiser, and Jean Claude Garreau. Experimental observation of the Anderson metal-insulator transition with atomic matter waves. *Physical Review Letters*, 101(25):255702, 2008. doi:10.1103/PhysRevLett.101.255702.

[94] Alain Aspect and Massimo Inguscio. Anderson localization of ultracold atoms. *Physics Today*, 62(8):30, 2009. doi:10.1063/1.3206092.

[95] Patrick A. Lee and Daniel S. Fisher. Anderson localization in two dimensions. *Physical Review Letters*, 47(12):882, 1981. doi:10.1103/PhysRevLett.47.882.

[96] Gerald Schubert, Jens Schleede, Krzysztof Byczuk, Holger Fehske, and Dieter Vollhardt. Distribution of the local density of states as a criterion for Anderson localization: Numerically exact results for various lattices in two and three dimensions. *Physical Review B*, 81(15):155106, 2010. doi:10.1103/PhysRevB.81.155106.

[97] Cord A. Müller and Dominique Delande. Disorder and interference: Localization phenomena. In Christian Miniatura, Leong-Chuan Kwek, Martial Ducloy, Benoît Grémaud, Berthold-Georg Englert, Leticia Cugliandolo, Artur Ekert, and Kok Khoo Phua, editors, *Ultracold Gases and Quantum Information: Lecture Notes of the Les Houches Summer School in Singapore: Volume 91, July 2009*, chapter 9. Oxford University Press, 2011. doi:10.1093/acprof:oso/9780199603657.003.0009.

[98] Daniel Bruns, Rafael Haenel, and Gary Tom. Anderson localization, 2017. URL: https://phas.ubc.ca/~berciu/TEACHING/PHYS502/PROJECTS/17AL.pdf.

[99] Nevill Mott. The mobility edge since 1967. *Journal of Physics C: Solid State Physics*, 20(21):3075, 1987. doi:10.1088/0022-3719/20/21/008.

[100] Diederik S. Wiersma, Paolo Bartolini, Ad Lagendijk, and Roberto Righini. Localization of light in a disordered medium. *Nature*, 390(6661):671–673, 1997. doi:10.1038/37757.

[101] Richard L. Weaver. Anderson localization of ultrasound. *Wave Motion*, 12(2):129–142, 1990. doi:10.1016/0165-2125(90)90034-2.

[102] R. E. Prange. Quantized Hall resistance and the measurement of the fine-structure constant. *Physical Review B*, 23(9):4802, 1981. doi:10.1007/978-94-010-9709-3_13.

[103] A. M. M. Pruisken. Universal singularities in the integral quantum Hall effect. *Physical Review Letters*, 61(11):1297, 1988. doi:10.1103/PhysRevLett.61.1297.

[104] John T. Chalker. The integer quantum Hall effect and Anderson localisation. In A. Comtet, T. Jolicœur, S. Ouvry, and F. David, editors, *Aspects topologiques de la physique en basse dimension. Topological aspects of low dimensional systems: Session LXIX. 7–31 July 1998*, pages 879–893. Springer Berlin Heidelberg, 2002. doi:10.1007/3-540-46637-1_13.

[105] Shivaji L. Sondhi, S. M. Girvin, J. P. Carini, and Dan Shahar. Continuous quantum phase transitions. *Reviews of Modern Physics*, 69(1):315, 1997. doi:10.1103/RevModPhys.69.315.

[106] C. W. Groth, M. Wimmer, A. R. Akhmerov, J. Tworzydło, and C. W. J. Beenakker. Theory of the topological Anderson insulator. *Physical Review Letters*, 103(19):196805, 2009. doi:10.1103/PhysRevLett.103.196805.

[107] Jian Li, Rui-Lin Chu, Jainendra K. Jain, and Shun-Qing Shen. Topological Anderson insulator. *Physical Review Letters*, 102(13):136806, 2009. doi:10.1007/978-3-642-32858-9_11.

[108] Eric J. Meier, Fangzhao Alex An, Alexandre Dauphin, Maria Maffei, Pietro Massignan, Taylor L. Hughes, and Bryce Gadway. Observation of the topological Anderson insulator in disordered atomic wires. *Science*, 362(6417):929–933, 2018. doi:10.1126/science.aat3406.

[109] Wu-Pei Su, John Robert Schrieffer, and Alan J. Heeger. Solitons in polyacetylene. *Physical Review Letters*, 42(25):1698, 1979. doi:10.1103/PhysRevLett.42.1698.

[110] János K. Asbóth, László Oroszlány, and András Pályi. A short course on topological insulators. *Lecture Notes in Physics*, 919:166, 2016. doi:10.1007/978-3-319-25607-8.

[111] Charles Poli, Matthieu Bellec, Ulrich Kuhl, Fabrice Mortessagne, and Henning Schomerus. Selective enhancement of topologically induced interface states in a dielectric resonator chain. *Nature Communications*, 6(1):6710, 2015. doi:10.1038/ncomms7710.

[112] Eric J. Meier, Fangzhao Alex An, and Bryce Gadway. Observation of the topological soliton state in the Su–Schrieffer–Heeger model. *Nature Communications*, 7(1):13986, 2016. doi:10.1038/ncomms13986.

[113] Philippe St-Jean, V. Goblot, Elisabeth Galopin, A. Lemaître, T. Ozawa, Luc Le Gratiet, Isabelle Sagnes, J. Bloch, and A. Amo. Lasing in topological edge states of a one-dimensional lattice. *Nature Photonics*, 11(10):651–656, 2017. doi:10.1038/s41566-017-0006-2.

[114] Filippo Cardano, Alessio D'Errico, Alexandre Dauphin, Maria Maffei, Bruno Piccirillo, Corrado de Lisio, Giulio De Filippis, Vittorio Cataudella, Enrico Santamato, Lorenzo Marrucci, et al. Detection of Zak phases and topological invariants in a chiral quantum walk of twisted photons. *Nature Communications*, 8(1):15516, 2017. doi:10.1038/ncomms15516.

[115] Zhi-Qiang Zhang, Bing-Lan Wu, Juntao Song, and Hua Jiang. Topological Anderson insulator in electric circuits. *Physical Review B*, 100(18):184202, 2019. doi:10.1103/PhysRevB.100.184202.

[116] Igor L. Aleiner, Boris L. Altshuler, and Georgy V. Shlyapnikov. A finite-temperature phase transition for disordered weakly interacting bosons in one dimension. *Nature Physics*, 6(11):900–904, 2010. doi:10.1038/nphys1758.

[117] Giulio Bertoli, Vincent P. Michal, Boris L. Altshuler, and Georgy V. Shlyapnikov. Finite-temperature disordered bosons in two dimensions. *Physical Review Letters*, 121(3):030403, 2018. doi:10.1103/PhysRevLett.121.030403.

[118] Jr-Chiun Yu, Shaurya Bhave, Lee Reeve, Bo Song, and Ulrich Schneider. Observing the two-dimensional Bose glass in an optical quasicrystal. *arXiv preprint arXiv:2303.00737*, 2023. doi:10.48550/arXiv.2303.00737.

[119] Arijeet Pal and David A. Huse. Many-body localization phase transition. *Physical Review B*, 82(17):174411, 2010. doi:10.1103/PhysRevB.82.174411.

[120] Fabien Alet and Nicolas Laflorencie. Many-body localization: An introduction and selected topics. *Comptes Rendus Physique*, 19(6):498–525, 2018. doi:10.1016/j.crhy.2018.03.003.

[121] Pascual Jordan and Eugene Paul Wigner. Über das Paulische Äquivalenzverbot. *Zeitschrift für Physik*, 47:631–651, 1928. doi:10.1007/BF01331938.

[122] Dmitry A. Abanin and Zlatko Papić. Recent progress in many-body localization. *Annalen der Physik*, 529(7):1700169, 2017. doi:10.1002/andp.201700169.

[123] Mark Srednicki. Chaos and quantum thermalization. *Physical Review E*, 50(2):888, 1994. doi:10.1103/PhysRevE.50.888.

[124] Denis M. Basko, Igor L. Aleiner, and Boris L. Altshuler. Metal–insulator transition in a weakly interacting many-electron system with localized single-particle states. *Annals of physics*, 321(5):1126–1205, 2006. doi:10.1016/j.aop.2005.11.014.

[125] David J. Luitz, Nicolas Laflorencie, and Fabien Alet. Many-body localization edge in the random-field Heisenberg chain. *Physical Review B*, 91(8):081103, 2015. doi:10.1103/PhysRevB.91.081103.

[126] Rajeev Singh, Jens H. Bardarson, and Frank Pollmann. Signatures of the many-body localization transition in the dynamics of entanglement and bipartite fluctuations. *New Journal of Physics*, 18(2):023046, 2016. doi:10.1088/1367-2630/18/2/023046.

[127] Maksym Serbyn, Zlatko Papić, and Dmitry A. Abanin. Local conservation laws and the structure of the many-body localized states. *Physical Review Letters*, 111(12):127201, 2013. doi:10.1103/PhysRevLett.111.127201.

[128] David A. Huse, Rahul Nandkishore, and Vadim Oganesyan. Phenomenology of fully many-body-localized systems. *Physical Review B*, 90(17):174202, 2014. doi:10.1103/PhysRevB.90.174202.

[129] Maksym Serbyn, Zlatko Papić, and Dmitry A. Abanin. Universal slow growth of entanglement in interacting strongly disordered systems. *Physical Review Letters*, 110(26):260601, 2013. doi:10.1103/PhysRevLett.110.260601.

[130] Jens H. Bardarson, Frank Pollmann, and Joel E. Moore. Unbounded growth of entanglement in models of many-body localization. *Physical Review Letters*, 109(1):017202, 2012. doi:10.1103/PhysRevLett.109.017202.

[131] H. Francis Song, Stephan Rachel, and Karyn Le Hur. General relation between entanglement and fluctuations in one dimension. *Physical Review B*, 82(1):012405, 2010. doi:10.1103/PhysRevB.82.012405.

[132] Michael Schreiber, Sean S. Hodgman, Pranjal Bordia, Henrik P. Lüschen, Mark H. Fischer, Ronen Vosk, Ehud Altman, Ulrich Schneider, and Immanuel Bloch. Observation of many-body localization of interacting fermions in a quasirandom optical lattice. *Science*, 349(6250):842–845, 2015. doi:10.1126/science.aaa7432.

[133] Piotr Sierant and Jakub Zakrzewski. Challenges to observation of many-body localization. *Physical Review B*, 105(22):224203, 2022. doi:10.1103/PhysRevB.105.224203.

[134] Tuure Orell, Alexios A. Michailidis, Maksym Serbyn, and Matti Silveri. Probing the many-body localization phase transition with superconducting circuits. *Physical Review B*, 100(13):134504, 2019. doi:10.1103/PhysRevB.100.134504.

[135] Ming Gong, Gentil D. de Moraes Neto, Chen Zha, Yulin Wu, Hao Rong, Yangsen Ye, Shaowei Li, Qingling Zhu, Shiyu Wang, Youwei Zhao, et al. Experimental characterization of the quantum many-body localization transition. *Physical Review Research*, 3(3):033043, 2021. doi:10.1103/PhysRevResearch.3.033043.

[136] Ken Xuan Wei, Chandrasekhar Ramanathan, and Paola Cappellaro. Exploring localization in nuclear spin chains. *Physical Review Letters*, 120(7):070501, 2018. doi:10.1103/PhysRevLett.120.070501.

[137] Loïc Henriet, Zoran Ristivojevic, Peter P. Orth, and Karyn Le Hur. Quantum dynamics of the driven and dissipative Rabi model. *Physical Review A*, 90(2):023820, 2014. doi:10.1103/PhysRevA.90.023820.

[138] Loïc Henriet and Karyn Le Hur. Quantum sweeps, synchronization, and Kibble-Zurek physics in dissipative quantum spin systems. *Physical Review B*, 93(6):064411, 2016. doi:10.1103/PhysRevB.93.064411.

[139] Milena Grifoni, Maura Sassetti, and Ulrich Weiss. Exact master equations for driven dissipative tight-binding models. *Physical Review E*, 53(3):R2033, 1996. doi:10.1103/physreve.53.r2033.

[140] Milena Grifoni, Manfred Winterstetter, and Ulrich Weiss. Coherences and populations in the driven damped two-state system. *Physical Review E*, 56(1):334, 1997. doi:10.1103/PhysRevE.56.334.

[141] Milena Grifoni and Peter Hänggi. Driven quantum tunneling. *Physics Reports*, 304(5-6):229–354, 1998. doi:10.1016/S0370-1573(98)00022-2.

[142] Thomas Weißl, Bruno Küng, Étienne Dumur, Alexey K. Feofanov, Iulian Matei, Cécile Naud, Olivier Buisson, Frank W. J. Hekking, and Wiebke Guichard. Kerr

coefficients of plasma resonances in Josephson junction chains. *Physical Review B*, 92(10):104508, 2015. doi:10.1103/PhysRevB.92.104508.

[143] K. V. Samokhin. Lifetime of excitations in a clean Luttinger liquid. *Journal of Physics: Condensed Matter*, 10(31):L533, 1998. doi:10.1088/0953-8984/10/31/002.

[144] Karyn Le Hur, Bertrand I. Halperin, and Amir Yacoby. Charge fractionalization in nonchiral Luttinger systems. *Annals of Physics*, 323(12):3037–3058, 2008. doi:10.1016/j.aop.2008.04.006.

[145] Pascal Cedraschi, Vadim V. Ponomarenko, and Markus Büttiker. Zero-point fluctuations and the quenching of the persistent current in normal metal rings. *Physical Review Letters*, 84(2):346, 2000. doi:10.1103/PhysRevLett.84.346.

[146] Pascal Cedraschi and Markus Büttiker. Quantum coherence of the ground state of a mesoscopic ring. *Annals of Physics*, 289(1):1–23, 2001. doi:10.1006/aphy.2001.6116.

[147] A. Furusaki and K. A. Matveev. Occupation of a resonant level coupled to a chiral Luttinger liquid. *Physical Review Letters*, 88(22):226404, 2002. doi:10.1103/PhysRevLett.88.226404.

[148] Karyn Le Hur and Mei-Rong Li. Unification of electromagnetic noise and Luttinger liquid via a quantum dot. *Physical Review B*, 72(7):073305, 2005. doi:10.1103/PhysRevB.72.073305.

[149] P. Forn-Díaz, J. José García-Ripoll, Borja Peropadre, J.-L. Orgiazzi, M. A. Yurtalan, R. Belyansky, Christopher M. Wilson, and A. Lupascu. Ultrastrong coupling of a single artificial atom to an electromagnetic continuum in the nonperturbative regime. *Nature Physics*, 13(1):39–43, 2017. doi:10.1038/nphys3905.

[150] Luca Magazzù, Pol Forn-Díaz, Ron Belyansky, J.-L. Orgiazzi, M. A. Yurtalan, Martin R. Otto, Adrian Lupascu, C. M. Wilson, and Milena Grifoni. Probing the strongly driven spin-boson model in a superconducting quantum circuit. *Nature Communications*, 9(1):1–8, 2018. doi:10.1038/s41467-018-03626-w.

[151] Loïc Henriet. *Non-equilibrium dynamics of many body quantum systems*. PhD thesis, Université Paris Saclay, 2016. URL: https://pastel.hal.science/tel-01525432.

[152] Jean-Michel Raimond, Michel Brune, and Serge Haroche. Manipulating quantum entanglement with atoms and photons in a cavity. *Reviews of Modern Physics*, 73(3):565, 2001. doi:10.1103/RevModPhys.73.565.

[153] J. J. Viennot, M. C. Dartiailh, Audrey Cottet, and Takis Kontos. Coherent coupling of a single spin to microwave cavity photons. *Science*, 349(6246):408–411, 2015. doi:10.1126/science.aaa3786.

[154] Alfred G. Redfield. On the theory of relaxation processes. *IBM Journal of Research and Development*, 1(1):19–31, 1957. doi:10.1016/B978-1-4832-3114-3.50007-6.

[155] Neill Lambert, Shahnawaz Ahmed, Mauro Cirio, and Franco Nori. Modelling the ultra-strongly coupled spin-boson model with unphysical modes. *Nature Communications*, 10(1):1–9, 2019. doi:10.1038/s41467-019-11656-1.

[156] Sebastian Wenderoth, H.-P. Breuer, and Michael Thoss. Non-Markovian effects in the spin-boson model at zero temperature. *Physical Review A*, 104(1):012213, 2021. doi:10.1103/PhysRevA.104.012213.

[157] F. Guinea, V. Hakim, and A. Muramatsu. Bosonization of a two-level system with dissipation. *Physical Review B*, 32(7):4410, 1985. doi:10.1103/physrevb.32.4410.

[158] V. V. Ponomarenko. Resonant tunneling and low-energy impurity behavior in a resonant-level model. *Physical Review B*, 48(8):5265, 1993. doi:10.1103/physrevb.48.5265.

[159] Claude Cohen-Tannoudji, Jacques Dupont-Roc, and Gilbert Grynberg. *Atom-Photon Interactions: Basic Process and Applications*. Wiley-VCH, 2010. doi:10.1002/9783527617197.

[160] Milena Grifoni, Elisabetta Paladino, and Ulrich Weiss. Dissipation, decoherence and preparation effects in the spin-boson system. *The European Physical Journal B-Condensed Matter and Complex Systems*, 10:719–729, 1999. doi:10.1007/s100510050903.

[161] Sudip Chakravarty. Quantum fluctuations in the tunneling between superconductors. *Physical Review Letters*, 49(9):681, 1982. doi:10.1103/PhysRevLett.49.681.

[162] A. J. Bray and M. A. Moore. Influence of dissipation on quantum coherence. *Physical Review Letters*, 49(21):1545, 1982. doi:10.1103/PhysRevLett.49.1545.

[163] Angela Kopp and Karyn Le Hur. Universal and measurable entanglement entropy in the spin-boson model. *Physical Review Letters*, 98(22):220401, 2007. doi:10.1103/PhysRevLett.98.220401.

[164] Daniel Manzano. A short introduction to the Lindblad master equation. *AIP Advances*, 10(2), 2020. doi:10.1063/1.5115323.

[165] Vincent Bouchiat, Denis Vion, Philippe Joyez, Daniel Esteve, and M. H. Devoret. Quantum coherence with a single Cooper pair. *Physica Scripta*, 1998(T76):165, 1998. doi:10.1238/Physica.Topical.076a00165.

[166] Yasunobu Nakamura, Yu A. Pashkin, and J. S. Tsai. Coherent control of macroscopic quantum states in a single-Cooper-pair box. *Nature*, 398(6730):786–788, 1999. doi:10.1038/19718.

[167] Yuriy Makhlin, Gerd Schön, and Alexander Shnirman. Quantum-state engineering with Josephson-junction devices. *Reviews of Modern Physics*, 73(2):357, 2001. doi:10.1103/RevModPhys.73.357.

[168] Yuriy Makhlin, Gerd Schön, and Alexander Shnirman. Josephson-junction qubits with controlled couplings. *Nature*, 398(6725):305–307, 1999. doi:10.1038/18613.

[169] Jens Koch, M. Yu Terri, Jay Gambetta, Andrew A. Houck, David I. Schuster, Johannes Majer, Alexandre Blais, Michel H. Devoret, Steven M. Girvin, and Robert J. Schoelkopf. Charge-insensitive qubit design derived from the Cooper pair box. *Physical Review A*, 76(4):042319, 2007. doi:10.1103/PhysRevA.76.042319.

[170] Andrew A. Houck, Jens Koch, Michel H. Devoret, Steven M. Girvin, and Robert J. Schoelkopf. Life after charge noise: recent results with transmon qubits. *Quantum Information Processing*, 8:105–115, 2009. doi:10.1007/s11128-009-0100-6.

[171] Josephine B. Chang, Michael R. Vissers, Antonio D. Córcoles, Martin Sandberg, Jiansong Gao, David W. Abraham, Jerry M. Chow, Jay M. Gambetta, Mary Beth Rothwell, George A. Keefe, et al. Improved superconducting qubit coherence using titanium nitride. *Applied Physics Letters*, 103(1):012602, 2013. doi:10.1063/1.4813269.

[172] Morten Kjaergaard, Mollie E. Schwartz, Jochen Braumüller, Philip Krantz, Joel I.-J. Wang, Simon Gustavsson, and William D. Oliver. Superconducting qubits: Current state of play. *Annual Review of Condensed Matter Physics*, 11:369–395, 2020. doi:10.1146/annurev-conmatphys-031119-050605.

[173] Yu Chen, C. Neill, Pedram Roushan, Nelson Leung, Michael Fang, Rami Barends, Julian Kelly, Brooks Campbell, Z. Chen, Benjamin Chiaro, et al. Qubit architecture with high coherence and fast tunable coupling. *Physical Review Letters*, 113(22):220502, 2014. doi:10.1103/PhysRevLett.113.220502.

[174] Michael R. Geller, Emmanuel Donate, Yu Chen, Michael T. Fang, Nelson Leung, Charles Neill, Pedram Roushan, and John M. Martinis. Tunable coupler for superconducting Xmon qubits: Perturbative nonlinear model. *Physical Review A*, 92(1):012320, 2015. doi:10.1103/PhysRevA.92.012320.

[175] Peter P. Orth, Ivan Stanic, and Karyn Le Hur. Dissipative quantum Ising model in a cold-atom spin-boson mixture. *Physical Review A*, 77(5):051601, 2008. doi:10.1103/PhysRevA.77.051601.

[176] Alessio Recati, Peter O. Fedichev, Wilhelm Zwerger, Jan von Delft, and Peter Zoller. Atomic quantum dots coupled to a reservoir of a superfluid Bose-Einstein condensate. *Physical Review Letters*, 94(4):040404, 2005. doi:10.1103/PhysRevLett.94.040404.

[177] J. J. Viennot, M. R. Delbecq, M. C. Dartiailh, Audrey Cottet, and T. Kontos. Out-of-equilibrium charge dynamics in a hybrid circuit quantum electrodynamics architecture. *Physical Review B*, 89(16):165404, 2014. doi:10.1103/PhysRevB.89.165404.

[178] Alexandre Blais, Ren-Shou Huang, Andreas Wallraff, Steven M. Girvin, and Robert. J. Schoelkopf. Cavity quantum electrodynamics for superconducting electrical circuits: An architecture for quantum computation. *Physical Review A*, 69(6):062320, 2004. doi:10.1103/PhysRevA.69.062320.

[179] Edwin T. Jaynes and Frederick W. Cummings. Comparison of quantum and semiclassical radiation theories with application to the beam maser. *Proceedings of the IEEE*, 51(1):89–109, 1963. doi:10.1109/PROC.1963.1664.

[180] Fumiki Yoshihara, Tomoko Fuse, Sahel Ashhab, Kosuke Kakuyanagi, Shiro Saito, and Kouichi Semba. Superconducting qubit–oscillator circuit beyond the ultrastrong-coupling regime. *Nature Physics*, 13(1):44–47, 2017. doi:10.1038/nphys3906.

[181] Loïc Herviou, Christophe Mora, and Karyn Le Hur. Phase diagram and entanglement of two interacting topological Kitaev chains. *Physical Review B*, 93(16):165142, 2016. doi:10.1103/PhysRevB.93.165142.

[182] Martin Leijnse and Karsten Flensberg. Parity qubits and poor man's Majorana bound states in double quantum dots. *Physical Review B*, 86(13):134528, 2012. doi:10.1103/PhysRevB.86.134528.

[183] Ephraim Bernhardt, Brian C. H. Cheung, and Karyn Le Hur. Majorana fermions and quantum information with fractional topology and disorder. *arXiv preprint arXiv:2309.03127*, 2023. doi:10.48550/arXiv.2309.03127.

[184] Karyn Le Hur. One-half topological number in entangled quantum physics. *arXiv preprint arXiv.2308.14062*, 2023. doi:10.48550/arXiv.2308.14062.

[185] Guido Burkard and Atac Imamoglu. Ultra-long-distance interaction between spin qubits. *Physical Review B*, 74(4):041307, 2006. doi:10.1103/PhysRevB.74.041307.

[186] Oliver Gywat, Florian Meier, Daniel Loss, and David D. Awschalom. Dynamics of coupled qubits interacting with an off-resonant cavity. *Physical Review B*, 73(12):125336, 2006. doi:10.1103/PhysRevB.73.125336.

[187] Johannes Majer, J. M. Chow, J. M. Gambetta, Jens Koch, B. R. Johnson, J. A. Schreier, L. Frunzio, D. I. Schuster, Andrew Addison Houck, Andreas Wallraff, et al. Coupling superconducting qubits via a cavity bus. *Nature*, 449(7161):443–447, 2007. doi:10.1038/nature06184.

[188] Elliott Lieb, Theodore Schultz, and Daniel Mattis. Two soluble models of an antiferromagnetic chain. *Annals of Physics*, 16(3):407–466, 1961. doi:10.1007/978-3-662-06390-3_35.

[189] Athanasios Tsintzis, Rubén Seoane Souto, and Martin Leijnse. Creating and detecting poor man's Majorana bound states in interacting quantum dots. *Physical Review B*, 106(20):L201404, 2022. doi:10.1103/PhysRevB.106.L201404.

[190] Sebastian Mehl, Hendrik Bluhm, and David P. DiVincenzo. Fault-tolerant quantum computation for singlet-triplet qubits with leakage errors. *Physical Review B*, 91(8):085419, 2015. doi:10.1103/PhysRevB.91.085419.

[191] Daniel Jirovec, Andrea Hofmann, Andrea Ballabio, Philipp M. Mutter, Giulio Tavani, Marc Botifoll, Alessandro Crippa, Josip Kukucka, Oliver Sagi, Frederico Martins, et al. A singlet-triplet hole spin qubit in planar Ge. *Nature Materials*, 20(8):1106–1112, 2021. doi:10.1038/s41563-021-01022-2.

[192] Maria Spethmann, Stefano Bosco, Andrea Hofmann, Jelena Klinovaja, and Daniel Loss. High-fidelity two-qubit gates of hybrid superconducting-semiconducting singlet-triplet qubits. *arXiv preprint arXiv:2304.05086*, 2023. doi:10.48550/arXiv.2304.05086.

[193] Alexander Altland and Martin R. Zirnbauer. Nonstandard symmetry classes in mesoscopic normal-superconducting hybrid structures. *Physical Review B*, 55(2):1142, 1997. doi:10.1103/PhysRevB.55.1142.

[194] Alexei Y. Kitaev. Periodic table for topological insulators and superconductors. In *AIP conference proceedings*, volume 1134, pages 22–30. American Institute of Physics, 2009. doi:10.1063/1.3149495.

[195] Andrei Bernevig and Titus Neupert. Topological superconductors and category theory. In *Topological Aspects of Condensed Matter Physics: Lecture Notes of the Les Houches Summer School: Volume 103, August 2014*, pages 63–121. Oxford University Press, 2017. doi:10.1093/acprof:oso/9780198785781.003.0002.

[196] H. Kamerlingh Onnes. Further experiments with liquid helium. C. On the change of electric resistance of pure metals at very low temperatures etc. IV. The resistance of pure mercury at helium temperatures. In *Through Measurement to Knowledge: The Selected Papers of Heike Kamerlingh Onnes 1853–1926*, pages 261–263. Springer, 1991. doi:10.1007/978-94-009-2079-8_15.

[197] Walther Meissner and Robert Ochsenfeld. Ein neuer Effekt bei Eintritt der Supraleitfähigkeit. *Naturwissenschaften*, 21(44):787–788, 1933. doi:10.1007/BF01504252.

[198] John Bardeen, Leon N. Cooper, and John R. Schrieffer. Theory of superconductivity. *Physical Review*, 108(5):1175, 1957. doi:10.1063/1.3047438.

[199] Dieter Jaksch, Christoph Bruder, Juan Ignacio Cirac, Crispin W. Gardiner, and Peter Zoller. Cold bosonic atoms in optical lattices. *Physical Review Letters*, 81(15):3108, 1998. doi:10.1103/PhysRevLett.81.3108.

[200] Markus Greiner, Olaf Mandel, Tilman Esslinger, Theodor W. Hänsch, and Immanuel Bloch. Quantum phase transition from a superfluid to a Mott insulator in a gas of ultracold atoms. *Nature*, 415(6867):39, 2002. doi:10.1038/415039a.

[201] Immanuel Bloch, Jean Dalibard, and Wilhelm Zwerger. Many-body physics with ultracold gases. *Reviews of Modern Physics*, 80(3):885, 2008. doi:10.1103/RevModPhys.80.885.

[202] Immanuel Bloch, Jean Dalibard, and Sylvain Nascimbene. Quantum simulations with ultracold quantum gases. *Nature Physics*, 8(4):267–276, 2012. doi:10.1038/nphys2259.

[203] Matthew P. A. Fisher, Peter B. Weichman, Geoffrey Grinstein, and Daniel S. Fisher. Boson localization and the superfluid-insulator transition. *Physical Review B*, 40(1):546, 1989. doi:10.1063/1.38820.

[204] Jonathan Simon, Waseem S. Bakr, Ruichao Ma, M. Eric Tai, Philipp M. Preiss, and Markus Greiner. Quantum simulation of antiferromagnetic spin chains in an optical lattice. *Nature*, 472(7343):307–312, 2011. doi:10.1038/nature09994.

[205] Nathan Goldman and Jean Dalibard. Periodically driven quantum systems: effective Hamiltonians and engineered gauge fields. *Physical Review X*, 4(3):031027, 2014. doi:10.1103/PhysRevX.4.031027.

[206] Marin Bukov, Luca D'Alessio, and Anatoli Polkovnikov. Universal high-frequency behavior of periodically driven systems: from dynamical stabilization to Floquet engineering. *Advances in Physics*, 64(2):139–226, 2015. doi:10.1080/00018732.2015.1055918.

[207] Christof Weitenberg and Juliette Simonet. Tailoring quantum gases by Floquet engineering. *Nature Physics*, 17(12):1342–1348, 2021. doi:10.1038/s41567-021-01316-x.

[208] Duc Thanh Tran, Alexandre Dauphin, Adolfo G. Grushin, Peter Zoller, and Nathan Goldman. Probing topology by "heating": Quantized circular dichroism in ultracold atoms. *Science Advances*, 3(8):e1701207, 2017. doi:10.1126/sciadv.1701207.

[209] Kirill Plekhanov, Guillaume Roux, and Karyn Le Hur. Floquet engineering of Haldane Chern insulators and chiral bosonic phase transitions. *Physical Review B*, 95(4):045102, 2017. doi:10.1103/PhysRevB.95.045102.

[210] Luca Asteria, Duc Thanh Tran, Tomoki Ozawa, Matthias Tarnowski, Benno S. Rem, Nick Fläschner, Klaus Sengstock, Nathan Goldman, and Christof Weitenberg. Measuring quantized circular dichroism in ultracold topological matter. *Nature Physics*, 15(5):449–454, 2019. doi:10.1038/s41567-019-0417-8.

[211] Karen Wintersperger, Christoph Braun, F. Nur Ünal, André Eckardt, Marco Di Liberto, Nathan Goldman, Immanuel Bloch, and Monika Aidelsburger. Realization of an anomalous Floquet topological system with ultracold atoms. *Nature Physics*, 16(10):1058–1063, 2020. doi:10.1038/s41567-020-0949-y.

[212] U.-J. Wiese. Ultracold quantum gases and lattice systems: quantum simulation of lattice gauge theories. *Annalen der Physik*, 525(10-11):777–796, 2013. doi:10.1002/andp.201300104.

[213] Luca Barbiero, Christian Schweizer, Monika Aidelsburger, Eugene Demler, Nathan Goldman, and Fabian Grusdt. Coupling ultracold matter to dynamical gauge fields in optical lattices: From flux-attachment to $\mathbb{Z}_2$ lattice gauge theories. *Science*, (5):p. Eaav7444, 2019. doi:10.1126/sciadv.aav7444.

[214] Christian Schweizer, Fabian Grusdt, Moritz Berngruber, Luca Barbiero, Eugene Demler, Nathan Goldman, Immanuel Bloch, and Monika Aidelsburger. Floquet approach to $\mathbb{Z}_2$ lattice gauge theories with ultracold atoms in optical lattices. *Nature Physics*, 15:1168–1173, 2019. doi:10.1038/s41567-019-0649-7.

[215] Christian Schweizer. *Minimal instances for $\mathbb{Z}_2$ lattice gauge theories and spin pumps*. PhD thesis, LMU München, 2019. doi:10.5282/edoc.24871.

[216] Ephraim Bernhardt, Fan Yang, and Karyn Le Hur. Localization dynamics from static and mobile impurities. *Physical Review B*, 104(11):115113, 2021. doi:10.1103/PhysRevB.104.115113.

[217] Alexandru Petrescu and Karyn Le Hur. Bosonic Mott insulator with Meissner currents. *Physical Review Letters*, 111(15):150601, 2013. doi:10.1103/PhysRevLett.111.150601.

[218] Alexandru Petrescu and Karyn Le Hur. Chiral Mott insulators, Meissner effect, and Laughlin states in quantum ladders. *Physical Review B*, 91(5):054520, 2015. doi:10.1103/PhysRevB.91.054520.

[219] Fritz London and Heinz London. The electromagnetic equations of the supraconductor. *Proceedings of the Royal Society of London. Series A-Mathematical and Physical Sciences*, 149(866):71–88, 1935. doi:10.1098/rspa.1935.0048.

[220] Vitaly L. Ginzburg and Lev D. Landau. On the theory of superconductivity. *Soviet Physics–Journal of Experimental and Theoretical Physics*, 20:1064–1082, 1950. doi:10.1007/978-3-540-68008-6_4.

[221] Alexei A. Abrikosov. The magnetic properties of superconducting alloys. *Journal of Physics and Chemistry of Solids*, 2(3):199–208, 1957. doi:10.1016/0022-3697(57)90083-5.

[222] Lars Onsager. Statistical hydrodynamics. *Il Nuovo Cimento*, 6:279–287, 1949. doi:10.1007/BF02780991.

[223] Richard P. Feynman. Application of quantum mechanics to liquid helium. In C.J. Gorter, editor, *Progress in low temperature physics*, volume 1, chapter 2, pages 17–53. Elsevier, 1955. doi:10.1016/B978-0-08-015816-7.50021-3.

[224] E. Orignac and T. Giamarchi. Meissner effect in a bosonic ladder. *Physical Review B*, 64(14):144515, 2001. doi:10.1103/PhysRevB.64.144515.

[225] Marcos Atala, Monika Aidelsburger, Michael Lohse, Julio T. Barreiro, Belén Paredes, and Immanuel Bloch. Observation of chiral currents with ultracold atoms in bosonic ladders. *Nature Physics*, 10(8):588, 2014. doi:10.1038/nphys2998.

[226] Douglas R. Hofstadter. Energy levels and wave functions of Bloch electrons in rational and irrational magnetic fields. *Physical Review B*, 14(6):2239, 1976. doi:10.1007/978-94-010-9709-3_19.

[227] J. S. Schwinger. Lectures on angular momentum. In L. C. Biedenharn and H. van Dam, editors, *Selected Papers on the Quantum Theory of Angular Momentum*. Academic Press, 1965. doi:10.2172/4389568.

[228] Monika Aidelsburger, Luca Barbiero, Alejandro Bermudez, Titas Chanda, Alexandre Dauphin, Daniel González-Cuadra, Przemysław R. Grzybowski, Simon Hands, Fred

Jendrzejewski, Johannes Jünemann, et al. Cold atoms meet lattice gauge theory. *Philosophical Transactions of the Royal Society A*, 380(2216):20210064, 2022. doi:10.1098/rsta.2021.0064.

[229] S. A. Parameswaran and Romain Vasseur. Many-body localization, symmetry and topology. *Reports on Progress in Physics*, 81(8):082501, 2018. doi:10.1088/1361-6633/aac9ed.

[230] Ehud Altman and Ronen Vosk. Universal dynamics and renormalization in many-body-localized systems. *Annual Reiew of Condensed Matter Physics*, 6(1):383–409, 2015. doi:10.1146/annurev-conmatphys-031214-014701.

[231] E. Miranda. Introduction to bosonization. *Brazilian Journal of Physics*, 33(1):3–35, 2003. doi:10.1590/S0103-97332003000100002.

[232] Thierry Giamarchi. *Quantum Physics in One Dimension*. Oxford University Press, 2003. doi:10.1093/acprof:oso/9780198525004.001.0001.

[233] Adam Smith, Johannes Knolle, Dmitry L. Kovrizhin, and Roderich Moessner. Disorder-free localization. *Physical Review Letters*, 118:266601, 2017. doi:10.1007/978-3-030-20851-6.

[234] Adam Smith, Johannes Knolle, Roderich Moessner, and L. Dmitry Kovrizhin. Absence of ergodicity without quenched disorder: From quantum disentangled liquids to many-body localization. *Physical Review Letters*, 119:176601, 2017. doi:10.1103/PhysRevLett.119.176601.

[235] N. Y. Yao, C. Laumann, J. I. Cirac, M. D. Lukin, and J. E. Moore. Quasi many-body localization in translation invariant systems. *Physical Review Letters*, 117:240601, 2016. doi:10.1103/PhysRevLett.117.240601.

[236] Nathan Goldman, Jean Dalibard, Monika Aidelsburger, and Nigel R. Cooper. Periodically driven quantum matter: The case of resonant modulations. *Physical Review A*, 91(3):033632, 2015. doi:10.1103/PhysRevA.91.033632.

[237] T. P. Grozdanov and M. J. Raković. Quantum system driven by rapidly varying periodic perturbation. *Physical Review A*, 38(4):1739, 1988. doi:10.1103/PhysRevA.38.1739.

[238] Andrey R. Kolovsky. Creating artificial magnetic fields for cold atoms by photon-assisted tunneling. *Europhysics Letters*, 93(2):20003, 2011. doi:10.1209/0295-5075/93/20003.

[239] Botao Wang, Xiao-Yu Dong, F. Nur Ünal, and André Eckardt. Robust and ultrafast state preparation by ramping artificial gauge potentials. *New Journal of Physics*, 23(6):063017, 2021. doi:10.1088/1367-2630/abf9b2.

[240] C. J. Lobb. What can (and can't) be measured in superconducting networks. *Physica B: Condensed Matter*, 152(1-2):1–6, 1988. doi:10.1016/0921-4526(88)90059-2.

[241] Enzo Granato. Phase transitions in Josephson-junction ladders in a magnetic field. *Physical Review B*, 42(7):4797, 1990. doi:10.1103/PhysRevB.42.4797.

[242] Colin Denniston and Chao Tang. Phases of Josephson junction ladders. *Physical Review Letters*, 75(21):3930, 1995. doi:10.1103/PhysRevLett.75.3930.

[243] Heinz J. Schulz, Gianaurelio Cuniberti, and Pierbiagio Pieri. Fermi liquids and Luttinger liquids. In *Field Theories For Low-Dimensional Condensed Matter Systems: Spin Systems And Strongly Correlated Electrons*, pages 9–81. Springer, 2000. doi:10.1007/978-3-662-04273-1_2.

[244] Felix Andraschko, Tilman Enss, and Jesko Sirker. Purification and many-body localization in cold atomic gases. *Physical Review Letters*, 113(21):217201, 2014. doi:10.1103/PhysRevLett.113.217201.

[245] Baoming Tang, Deepak Iyer, and Marcos Rigol. Quantum quenches and many-body localization in the thermodynamic limit. *Physical Review B*, 91(16):161109, 2015. doi:10.1103/PhysRevB.91.161109.

[246] H. Francis Song, Stephan Rachel, Christian Flindt, Israel Klich, Nicolas Laflorencie, and Karyn Le Hur. Bipartite fluctuations as a probe of many-body entanglement. *Physical Review B*, 85(3):035409, 2012. doi:10.1103/PhysRevB.85.035409.

[247] Marcel Goihl, Mathis Friesdorf, Albert H. Werner, Winton Brown, and Jens Eisert. Experimentally accessible witnesses of many-body localization. *Quantum Reports*, 1(1):50–62, 2019. doi:10.3390/quantum1010006.

[248] David A. Huse, Rahul Nandkishore, Vadim Oganesyan, Arijeet Pal, and Shivaji L. Sondhi. Localization-protected quantum order. *Physical Review B*, 88(1):014206, 2013. doi:10.1103/PhysRevB.88.014206.

[249] Marko Žnidarič, Tomaž Prosen, and Peter Prelovšek. Many-body localization in the Heisenberg XXZ magnet in a random field. *Physical Review B*, 77(6):064426, 2008. doi:10.1103/PhysRevB.77.064426.

[250] Adam Smith, M. S. Kim, Frank Pollmann, and Johannes Knolle. Simulating quantum many-body dynamics on a current digital quantum computer. *npj Quantum Information*, 5(1):106, 2019. doi:10.1038/s41534-019-0217-0.

[251] Michael Iversen, N. S. Srivatsa, and Anne E. B. Nielsen. Escaping many-body localization in an exact eigenstate. *Physical Review B*, 106(21):214201, 2022. doi:10.1103/PhysRevB.106.214201.

[252] Nicolas Laflorencie. Scaling of entanglement entropy in the random singlet phase. *Physical Review B*, 72(14):140408, 2005. doi:10.1103/PhysRevB.72.140408.

[253] Bela Bauer and Chetan Nayak. Area laws in a many-body localized state and its implications for topological order. *Journal of Statistical Mechanics: Theory and Experiment*, 2013(09):P09005, 2013. doi:10.1088/1742-5468/2013/09/P09005.

[254] Dmitry A. Abanin, Wojciech De Roeck, and François Huveneers. Theory of many-body localization in periodically driven systems. *Annals of Physics*, 372:1–11, 2016. doi:10.1016/j.aop.2016.03.010.

[255] Nicolas Laflorencie, Gabriel Lemarié, and Nicolas Macé. Topological order in random interacting Ising-Majorana chains stabilized by many-body localization. *Physical Review Research*, 4(3):L032016, 2022. doi:10.1103/PhysRevResearch.4.L032016.

[256] J. Robert Johansson, P. D. Nation, and Franco Nori. QuTiP: An open-source python framework for the dynamics of open quantum systems. *Computer Physics Communications*, 183(8):1760–1772, 2012. doi:10.1016/j.cpc.2012.02.021.

[257] John G.F. Francis. The QR transformation a unitary analogue to the LR transformation—part 1. *The Computer Journal*, 4(3):265–271, 1961. doi:10.1093/comjnl/4.3.265.

[258] Jürgen T. Stockburger and Hermann Grabert. Exact c-number representation of non-Markovian quantum dissipation. *Physical Review Letters*, 88(17):170407, 2002. doi:10.1103/PhysRevLett.88.170407.

[259] Werner Koch, Frank Großmann, Jürgen T. Stockburger, and Joachim Ankerhold. Non-Markovian dissipative semiclassical dynamics. *Physical Review Letters*, 100(23):230402, 2008. doi:10.1103/PhysRevLett.100.230402.

[260] Peter P. Orth, Adilet Imambekov, and Karyn Le Hur. Universality in dissipative Landau-Zener transitions. *Physical Review A*, 82(3):032118, 2010. doi:10.1103/PhysRevA.82.032118.

[261] Matteo Carrega, Paolo Solinas, Maura Sassetti, and Ulrich Weiss. Energy exchange in driven open quantum systems at strong coupling. *Physical Review Letters*, 116(24):240403, 2016. doi:10.1103/PhysRevLett.116.240403.

[262] Gordei Borisovich Lesovik, Andrey V. Lebedev, and Adilet Onlasynovich Imambekov. Dynamics of a two-level system interacting with a random classical field. *Journal of Experimental and Theoretical Physics Letters*, 75:474–478, 2002. doi:10.1134/1.1494045.

[263] Karyn Le Hur, Loïc Henriet, Loïc Herviou, Kirill Plekhanov, Alexandru Petrescu, Tal Goren, Marco Schiro, Christophe Mora, and Peter P. Orth. Driven dissipative dynamics and topology of quantum impurity systems. *Comptes Rendus Physique*, 19(6):451–483, 2018. doi:10.1016/j.crhy.2018.04.003.

[264] A. Luther and I. Peschel. Single-particle states, Kohn anomaly, and pairing fluctuations in one dimension. *Physical Review B*, 9(7):2911, 1974. doi:10.1007/BFb0113395.

[265] F. Duncan M. Haldane. Luttinger liquid theory of one-dimensional quantum fluids. I. Properties of the Luttinger model and their extension to the general 1D interacting spinless Fermi gas. *Journal of Physics C: Solid State Physics*, 14(19):2585, 1981. doi:10.1088/0022-3719/14/19/010.

Appendix A

Résumé en français

Cette thèse de doctorat porte sur l'étude du désordre, de la localisation, de l'interaction avec un environnement et de la topologie dans des systèmes quantiques à plusieurs corps, en particulier dans les systèmes de spin. Elle vise à étudier cette interface à la fois d'un point de vue fondamental et afin de développer des perspectives en ce qui concerne les applications dans la technologie quantique. Cette thèse se concentre particulièrement sur les systèmes de spin, qui constituent une plateforme accessible pour sonder les effets mentionnés ci-dessus et sont également intéressants du point de vue des réalisations expérimentales et des applications. Pour un spin-1/2 dans un champ magnétique radial, la topologie peut être définie à partir des pôles de la variété d'état fondamental. Ce modèle est analogue à plusieurs autres modèles de la matière condensés, tels que le modèle de Haldane ou le fil de Kitaev. La définition de la topologie dans le modèle de spin peut être étendue aux systèmes en interaction composés de plusieurs spins et aux systèmes ouverts couplés à un environnement.

Expérimentalement, cette topologie peut être mesurée en utilisant un protocole dynamique pilotant le champ magnétique agissant sur le spin au cours du temps. Pour cette configuration, la thèse étudie un 'effet de dynamo quantique', se produisant comme une conséquence de la dynamique dissipative entraînée lors du couplage à un environnement. Il existe une relation curieuse entre cet effet et la 'topologie accédée dynamiquement' du spin. Cette thèse étudie et définit les propriétés thermodynamiques de cet effet correspondant à une conversion de travail à travail, déplaçant de manière cohérente certains modes de l'environnement et ouvrant ainsi des perspectives pour le transfert d'énergie à l'échelle quantique à travers un environnement. Les définitions et les mesures sont comparées à l'aide de différentes techniques analytiques et numériques pour évaluer la dynamique dissipative entraînée.

Dans les systèmes en interaction composés de plusieurs spins, la topologie de chaque spin peut être étudiée et il a été montré précédemment qu'elle peut donner des valeurs fractionnaires en fonction de la symétrie du modèle. Cette thèse met l'accent sur le comportement de cette phase topologique fractionnaire lors de l'introduction du désordre

et montre que ce dernier peut conduire à son extension. Une interprétation de ces effets en termes de fermions de Majorana est discutée et permet d'envisager des applications en information quantique.

Les effets du désordre et de la physique de la localisation sont examinés en profondeur pour un modèle qui peut être réalisé à partir d'atomes froids et qui, dans une certaine limite, peut également être représenté par un modèle de spin. Une forme particulière de désordre peut être réalisée dans ce système par le biais d'un couplage avec une deuxième espèce de particule. Dans ce cas, il existe un lien intéressant avec les théories de jauge sur réseau $\mathbb{Z}_2$ lorsque les impuretés introduisant le désordre dans le système acquièrent elles-mêmes une dynamique quantique. Cette thèse étudie l'interaction d'un champ de jauge $\mathcal{U}(1)$ appliqué permettant de définir un courant local avec cette forme particulière de désordre et propose en particulier d'utiliser ce courant comme indicateur des propriétés de localisation. Une étude numérique utilisant la diagonalisation exacte démontre la présence d'une phase localisée à N-corps dans ce modèle. Elle est identifiée à partir du comportement de l'entropie d'intrication et attestée par les fluctuations bipartites et le courant local.

La thèse ouvre des perspectives pour une compréhension fondamentale de l'interaction de la topologie, de la dynamique des systèmes ouverts et des effets de désordre dans les systèmes quantiques et fait le lien avec les réalisations expérimentales et les applications.

L'étude des propriétés topologiques des systèmes de matière condensée a attiré beaucoup d'attention ces dernières années. Au cœur de cet intérêt se trouve le fait que les phases topologiques ne peuvent pas être expliquées par la théorie traditionnelle de la rupture spontanée de symétrie formulée par Landau [1, 2]. Les phases topologiques constituent donc de nouvelles phases de la matière, ce qui rend leur étude pertinente du point de vue de l'intérêt physique fondamental. Comme le suggère le nom 'topologique', ces propriétés ne dépendent pas de changements locaux, mais sont plutôt évaluées comme une propriété globale du système [2]. L'intérêt qu'elles suscitent est en outre alimenté par des propriétés exotiques qui sont prometteuses pour des applications technologiques: Une caractéristique commune des phases topologiques est une correspondance 'cœur-bord' (bulk-edge), dans laquelle les propriétés topologiques du cœur se manifestent par l'apparition d'états topologiquement protégés à la frontière du système [3]. Un exemple est celui des isolants topologiques, qui sont isolants dans leurs cœurs, mais qui présentent des modes de bord conducteurs, qui sont en fait liés aux propriétés topologiques du cœur [2].

Un exemple concret et fondamental est l'effet Hall quantique découvert expérimentalement en 1980 [4]. Dans un gaz d'électrons bidimensionnel soumis à un fort champ magnétique, on a constaté que la résistance de Hall transversale (et donc aussi la conductance de Hall σ_{xy}) développe des plateaux quantifiés par des nombres entiers. La stabilité remarquable de ces plateaux laisse entrevoir leur origine topologique. La relation trouvée

expérimentalement est la suivante

$$\sigma_{xy} = \nu \frac{e^2}{h}, \tag{A.1}$$

où e est la charge élémentaire, h est la constante de Planck et ν est un nombre entier. Des considérations théoriques sur cet effet particulier ont suivi [5–7]. La structure des bandes d'un gaz d'électrons bidimensionnel dans un champ magnétique intense est décrite par des niveaux de Landau, avec des bandes interdites entre eux. On peut montrer que la conductivité transversale due à une bande est liée à sa topologie: En particulier, l'entier ν observé expérimentalement est donné par la somme d'un invariant topologique - le fameux nombre de Chern - pour chaque bande occupée, c'est-à-dire [2, 7]

$$\nu = \sum_{\alpha} C_{\alpha}, \tag{A.2}$$

avec

$$C_{\alpha} = \frac{1}{2\pi} \int d\vec{k} \mathcal{F}^{\alpha}_{\vec{k}}. \tag{A.3}$$

Ici, $\mathcal{F}^{\alpha}_{\vec{k}} = \vec{\nabla} \mathcal{A}^{\alpha}_{\vec{k}}$ est la courbure de Berry de la bande α définie à partir de la connexion de Berry $\mathcal{A}^{\alpha}_{\vec{k}} = i \left\langle \psi^{\alpha}(\vec{k}) \right| \vec{\nabla}_{\vec{k}} \left| \psi^{\alpha}(\vec{k}) \right\rangle$ avec $\left| \psi^{\alpha}(\vec{k}) \right\rangle$ la fonction d'onde de Bloch [8] et l'intégration s'étend sur la première zone de Brillouin. De même que l'intégrale de la courbure de Gauss définit le genre d'une surface, le nombre de Chern est un invariant défini à partir d'une intégration de la courbure de Berry sur la zone de Brillouin. Ceci démontre la nature topologique de l'effet Hall quantique.

En 1988, Haldane a réalisé qu'un effet Hall quantique similaire pouvait également se produire dans un modèle de réseau, à savoir le graphène avec des sauts complexes supplémentaires entre voisins suivants les plus proches [9]. Dans cette configuration, que nous décrirons brièvement dans la Sec. 1.1.2, des états de bord chiraux peuvent être obtenus explicitement comme une manifestation de la correspondance cœur-bord mentionnée ci-dessus [2]. En tant que modèle de réseau, une caractéristique attrayante du modèle de Haldane est qu'il peut être réalisé à l'aide d'implémentations accordables [10], ce qui le rend intéressant à la fois pour les vérifications expérimentales des propriétés topologiques, mais aussi pour les développements théoriques ultérieurs de celles-ci (voir par exemple [11–13]). Un autre exemple de la correspondance cœur-bord est celui d'un fil supraconducteur topologique, que nous présenterons également dans la Sec. 1.1.2. Il possède une phase topologique, dans laquelle il présente des modes de bord exotiques de Majorana [14].

Les phases de la matière quantique dotées de propriétés topologiques sont attrayantes, car ces propriétés sont stables face aux perturbations locales et au désordre, et donc

intéressantes pour les applications technologiques [2]. En particulier, le fil supraconducteur mentionné ci-dessus présente un grand intérêt pour les applications potentielles de l'informatique quantique topologique [15–17]. Pour revenir à l'exemple de l'effet Hall quantique mentionné ci-dessus, on peut d'une part montrer que la quantification de la conductance transversale par des nombres entiers est stable lorsqu'on ajoute un petit désordre [6]. D'autre part, et de manière moins intuitive, le désordre joue un rôle crucial dans l'apparition des plateaux de Hall quantique en localisant des états qui ne contribuent pas à la conductivité (voir Sec. 1.3.1). L'interaction entre les propriétés topologiques et le désordre est donc un domaine complexe, qui donne lieu à des propriétés subtiles, comme nous le discutons également au Chap. 3.

L'étude des effets de désordre dans les systèmes quantiques a elle-même donné lieu à une variété de nouveaux phénomènes et phases curieux. La localisation d'Anderson [18], un phénomène se produisant pour les particules dans un environnement 'sale', intrinsèquement en raison du caractère ondulatoire des particules quantiques, a été une étape importante dans ce domaine. Nous nous concentrons sur les effets de localisation dans un système quantique particulier conçu pour une réalisation expérimentale dans le chapitre 4. Depuis les travaux d'Anderson, l'étude de configurations plus complexes avec des interactions entre particules [19–21] a ouvert la voie à la découverte d'un phénomène appelé 'localisation à N-corps', décrivant des systèmes fermés qui ne se thermalisent pas après une longue évolution temporelle. Remarquablement, ce phénomène est le seul mécanisme connu qui présente cette caractéristique de non-thermalisation de manière robuste [22]. La compréhension de cette phase est essentielle pour concevoir des applications dans les technologies quantiques fonctionnant dans le régime désordonné en présence d'interactions [23]. Nous présentons une étude des propriétés de localisation à N-corps d'un système de spin particulier au chapitre 5.

Cependant, la nécessité de comprendre les notions thermodynamiques dans le domaine quantique afin de permettre des applications fonctionnelles est plus générale. Même si les lois de la thermodynamique, formulées pour les systèmes classiques, peuvent être généralisées aux environnements quantiques sous certaines restrictions [24], il existe des configurations quantiques qui ne sont pas décrites par ces conditions [25, 26] et des généralisations sont souhaitables [27]. Au chapitre 2, nous examinons un effet 'dynamo quantique', qui décrit une situation dans laquelle un système dynamique couplé à un bain peut, sous certaines conditions, transférer du travail dans le bain. Curieusement, cette configuration et cet effet présentent des parallèles avec un invariant topologique qui peut être défini pour un spin dans un champ magnétique radial, mais qui est en fait un modèle ayant plusieurs analogues dans la matière condensée, comme le modèle de Haldane mentionné plus haut.

Appendix B

Summary of numerical methods

In this thesis, we have developed and utilized a variety of numerical methods, on the one hand in order to check the validity of analytical results, on the other hand also to get a better understanding of the properties of the examined physical systems in order to then define directions of further investigation. In the following, we will first give a simple overview over exact diagonalization (ED) techniques (used to obtain results throughout this thesis) and consequently give an introduction to the stochastic Schrödinger equation approach to solve the spin dynamics in the spin-boson model, which has been used in Chap. 2

B.1 Exact diagonalization

In simple terms, exact diagonalization is employed to solve the Schrödinger equation corresponding to a quantum system exactly by diagonalizing a matrix representation of the Hamiltonian in a certain basis. This explains the term 'exact diagonalization', as basically one attempts to diagonalize the Hamiltonian matrix numerically. In practice, it is convenient to use the package QuTip [256], which simplifies the representation of the operators in terms of matrices and provides a variety of tools to analyze the results.

B.1.1 Time-independent problems

The simplest case is that where the Hamiltonian operator does not depend on time and one simply aims to find its eigenvalues and corresponding eigenstates. This can be realized using, e.g., the QR algorithm, decomposing the matrix into an orthogonal and an upper triangular matrix [257]. In practice, for spin systems as the one considered in Eq. (1.4), one often chooses the eigenstates of the σ^z matrix as basis vectors, which corresponds to the usual Pauli matrices as representations for the spin operators. This gives a 2-by-2 matrix for a single spin, corresponding to the two-dimensional Hilbert space of the spin. The situation is slightly more complicated for two coupled spins, as in Eq. (1.34).

Operators acting on a single spin are promoted to operators in the Hilbert space of the two spins by forming a tensor product with the identity operator in the other subspace. The Hamiltonian should thus be written as

$$\mathcal{H} = \mathcal{H}_{\text{rad},1} \otimes \mathbb{1}_2 + \mathbb{1}_1 \otimes \mathcal{H}_{\text{rad},2} + r_z \sigma_1^z \otimes \sigma_2^z, \tag{B.1}$$

where $\mathbb{1}_i$ denotes the identity operator in the subspace of the i-th spin. In terms of matrices, a tensor product operator can be represented by the Kronecker product of the two matrices.

More generally, in order to diagonalize the Hamiltonian of spin chains, as the one from Eq. (4.7), one needs to promote local operators to the Hilbert space of the entire system, i.e., for a local operator A acting on the i-th spin, one has

$$A_i = \mathbb{1}_1 \otimes \cdots \otimes \mathbb{1}_{i-1} \otimes A \otimes \mathbb{1}_{i+1} \cdots . \tag{B.2}$$

Interaction terms are written in a similar way with the tensor product of two local operators embedded in the full Hilbert space. The size of the Hilbert space increases rapidly with the system size. For N coupled spin-1/2, the Hilbert space size is 2^N. This explains why ED can be used only for small systems - increasing the system size, the size of the Hamiltonian matrix grows exponentially.

The same principle works when considering a spin coupled to a number of bosonic modes, i.e., when discretizing Eq. (2.1) as described in Sec. 2.3.3. Coupling of the spin to the j-th bath mode would be expressed through an operator

$$\frac{\sigma^z}{2} g_j (b_j^\dagger + b^j) = \frac{\sigma^z}{2} \otimes \mathbb{1}_1 \otimes \cdots \otimes \mathbb{1}_{j-1} \otimes g_j (b_j^\dagger + b^j) \otimes \mathbb{1}_{j+1} \otimes \cdots , \tag{B.3}$$

where $\mathbb{1}_i$ is the identity operator acting on the j-th mode. Note that the subspaces for the bosonic modes in general have sizes larger than two and in practice should be chosen such that they are well above the maximally reached occupation.

This recaps how the Hamiltonian can be set up in order to implement a numerical exact diagonalization for a time-independent problem. In the following, we will discuss time-dependent problems and cases, where one is interested in the time-evolution of an initial state.

B.1.2 Time evolution and time-dependence with ED

To evaluate the unitary time-evolution of an initial state, one needs to solve the time-dependent Schrödinger equation

$$i\partial_t |\psi(t)\rangle = H(t) |\psi(t)\rangle . \tag{B.4}$$

In order to solve it numerically, one needs to discretize the time axis, which is done by partitioning it as $(t_0, t_1, ..., t_{N-1}, t_N)$ into N intervals of length Δt . The simplest method to discretize the differential on the left hand side is the Euler scheme, that gives $\partial_t |\psi(t)\rangle = (|\psi(t_{n+1})\rangle - |\psi(t_n)\rangle)/\Delta t$, where a discrete time step Δt needs to be fixed. Consequently, one can obtain an iterative formula by considering the right hand side of Eq. (B.4) at a discrete time as well: Choosing $H(t_n)|\psi(t_n)\rangle$, one speaks of a 'forward Euler' or 'explicit Euler' scheme. Here, we rather choose the 'backward Euler' or 'implicit Euler' scheme setting $H(t_{n+1})|\psi(t_{n+1})\rangle$ due to its favorable stability. Then one obtains the iterative prescription

$$|\psi(t_{n+1})\rangle = (\mathbb{1} + i\Delta t H(t_{n+1}))^{-1} |\psi(t_n)\rangle , \tag{B.5}$$

thus amounting to inverting the matrix $\mathbb{1} + i\Delta t H(t_{n+1})$. In practice, more refined implicit schemes based on discretization of the Schrödinger equation are available in QuTip and are used for solving the time dynamics. This has been used in Chaps. 2, 3 and 5.

If the Hamiltonian is time-independent and one is mainly interested in a time-evolved state at one certain later instant of time, another possibility to evaluate a time-evolved state consists in directly using the time-evolution operator. This relies on the solution of Eq. (B.4) of the form

$$|\psi(t)\rangle = e^{-iHt} |\psi(0)\rangle . \tag{B.6}$$

This way relies on computing a matrix exponential and has been used in Chap. 5 to obtain Fig. 5.7, where we evaluated expectation values only for one certain time.

B.2 Stochastic Schrödinger Equation for the spin-boson model

When coupling a system to a bath, this implies the presence of an infinite amount of degrees of freedom. Since ED reaches its limits already for a few coupled degrees of freedom, other methods are needed to study open system dynamics, as done in Chap. 2 and in particular in Sec. 2.3. As mentioned there, the spin dynamics can be expressed using the influence functional to account for the bath effects [76, 79] through the path integral in Eq. (2.66). This formulation has lead to several numerical approaches [75, 137, 138, 258–261]. In Sec. 2.3, we use the numerically exact stochastic Schrödinger equation (SSE) approach which had previously been developed in our group [75, 137, 138, 151] to study the thermodynamic properties of the quantum dynamo effect. In this section, we will summarize the theory underlying this numerical approach and the concrete implementation realized during this PhD.

B.2.1 Rewriting the influence functional

As described in Sec. 2.3.2, one expresses elements of the reduced density matrix of the spin as a double path integral over classical spin paths through Eq. (2.66). In this section, we will exemplify the calculation of the upper diagonal matrix element of the reduced spin density matrix (i.e., initializing the spin with $\sigma_i, \sigma_i' = 1$ and evaluating the path integral for $\sigma_f, \sigma_f' = 1$).

We are starting from the expression of the influence functional given by Eq. (2.67), which we print here again:

$$F[\sigma, \sigma'] = \exp\left(-\frac{1}{\pi}\int_{t_0}^{t} d\tau \int_{t_0}^{\tau} d\tau' [-iL_1(\tau - \tau')\xi(\tau)\eta(\tau') + L_2(\tau - \tau')\xi(\tau)\xi(\tau')]\right). \quad \text{(B.7)}$$

It uses the reparametrization $\eta(\tau) = \frac{1}{2}(\sigma(\tau) + \sigma'(\tau))$ and $\xi(\tau) = \frac{1}{2}(\sigma(\tau) - \sigma'(\tau))$, representing the symmetric and antisymmetric spin paths. Also, the bath correlation functions were defined by

$$L_1(t) = \int_0^\infty d\omega J(\omega) \sin(\omega t), \quad \text{(B.8)}$$

$$L_2(t) = \int_0^\infty d\omega J(\omega) \cos(\omega t) \coth\left(\frac{\beta\omega}{2}\right). \quad \text{(B.9)}$$

We first reparametrize the spin paths in terms of the times at which a (classical) spin along one of the two paths $\sigma(t)$ or $\sigma'(t)$ is flipped, that is the system switches between a sojourn ($\eta = \pm 1$ and $\xi = 0$) and a blip ($\xi = \pm 1$ and $\eta = 0$). Writing

$$\xi(t) = \sum_{j=1}^{2n} \Xi_j \theta(t - t_j), \quad \text{(B.10)}$$

$$\eta(t) = \sum_{j=0}^{2n} \Upsilon_j \theta(t - t_j), \quad \text{(B.11)}$$

with $\{\Xi_1, \Xi_2, ..., \Xi_{2n}\} = \{\xi_1, -\xi_1, ..., -\xi_n\}$ and $\{\Upsilon_1, \Upsilon_2, ..., \Upsilon_{2n}\} = \{\eta_0, -\eta_0, ...\eta_n\}$, the influence functional in Eq. (B.7) can be written in the simple form

$$F_n[\{\Xi_j\}, \{\Upsilon_j\}, \{t_j\}] = \mathcal{Q}_1 \mathcal{Q}_2, \quad \text{(B.12)}$$

with

$$\mathcal{Q}_1 = \exp\left(\frac{i}{\pi} \sum_{j>k\geq 0}^{2n} \Xi_j \Upsilon_k Q_1(t_j - t_k)\right), \quad \text{(B.13)}$$

$$\mathcal{Q}_2 = \exp\left(\frac{1}{\pi} \sum_{j>k\geq 1}^{2n} \Xi_j \Xi_k Q_2(t_j - t_k)\right). \quad \text{(B.14)}$$

The functions $Q_1(t)$ and $Q_2(t)$ are the second integrals of the bath correlation functions $L_1(t)$ and $L_2(t)$, which for an Ohmic spectral density and $T = 0$ read

$$Q_1(t) = 2\pi\alpha \arctan(\omega_c t), \tag{B.15a}$$
$$Q_2(t) = \pi\alpha \log\left(1 + \omega_c^2 t^2\right), \tag{B.15b}$$

as given in Eqs. (2.73) of the main text.

We see that through the influence functional in Eq. (B.12), a blip is coupled to all previous blips and sojourns, thus making the problem non-Markovian and difficult to solve. In order to find analytical expressions for the elements of the density matrix, one thus has to resort to approximation schemes or numerical techniques. The NIBA, whose results were given in Eqs. (2.70) of the main text, can be justified from here by neglecting interactions between blips and blip-sojourn interactions except for neighboring ones [64]. In this chapter, we rather seek to explain how Eq. (B.12) can be used to develop a stochastic approach to tackle the spin dynamics from the real-time path integral numerically.

B.2.2 A stochastic Schrödinger equation

To simplifiy the notation, let us call the upper left element of the density matrix

$$p(t) = \langle\uparrow|\rho_s(t)|\uparrow\rangle = \frac{1 + \langle\sigma^z(t)\rangle}{2}, \tag{B.16}$$

and write out the effect of $\int \mathcal{D}\sigma\mathcal{A}[\sigma]$ in Eq. (B.7), which are given by [33]

$$\begin{aligned}\int \mathcal{D}\sigma\mathcal{A}[\sigma] = \sum_{n=0}^{\infty} \int_0^t dt_n \frac{-iH\sin(vt_n)}{2} \int_0^{t_n} dt_{n-1} \frac{-iH\sin(vt_{n-1})}{2} \times \cdots \\ \cdots \times \int_0^{t_2} dt_1 \frac{-iH\sin(vt_1)}{2} \times \exp\left(-i\int_0^t d\tau \frac{H\cos(v\tau)}{2}\sigma(\tau)\,|_{\{t_1,t_2,\ldots,t_n\}}\right).\end{aligned} \tag{B.17}$$

It can be shown that one then finds [33, 75, 151]

$$p(t) = 1 + \sum_{n=1}^{\infty} \int_0^t dt_{2n} \frac{iH\sin(vt_{2n})}{2} \times \ldots \times \int_0^{t_2} dt_1 \frac{iH\sin(vt_1)}{2} \sum_{(\Xi_j,\Upsilon_j)} F_n H_n. \tag{B.18}$$

Here, the spin part of the Hamiltonian contributes by flipping the spin (which allows to rewrite the path integral as a series of spin flips) and through the bias-dependent factor H_n which is given by

$$H_n = \exp\left(-i\sum_{j=1}^{2n} \Xi_j \int_0^{t_j} H\cos(vt')dt'\right). \tag{B.19}$$

To simplify the influence functional further from Eq. (B.12), let us first note that for large ω_c, we can safely approximate $Q_1(t) \approx \pi^2\alpha$ [75]. Next, let us define a stochastic field $h_s(t)$ satisfying [151]

$$\overline{h_s(t)} = 0, \tag{B.20a}$$

$$\overline{h_s(t)h_s(s)} = \frac{1}{\pi}Q_2(t-s) + l_1, \tag{B.20b}$$

with l_1 a complex constant. This allows to rewrite Eq. (B.12) through (B.14):

$$F_n = \mathcal{Q}_1\mathcal{Q}_2, \tag{B.21}$$

$$= \exp\left(i\alpha\pi \sum_{j>k\geq 0}^{2n} \Xi_j \Upsilon_k\right) \exp\left(\sum_{j>k\geq 1}^{2n} \Xi_j\Xi_k(\overline{h(t_j)h(t_k)} - l_1)\right), \tag{B.22}$$

$$= \exp\left(i\alpha\pi \sum_{k=0}^{n-1} \xi_{k+1}\eta_k\right)\overline{\exp\left(\sum_{j=1}^{2n} h_s(t_j)\Xi_j\right)}. \tag{B.23}$$

One could now introduce a second stochastic field capturing $Q_1(t)$ fully [137], thus departing from the approximation made above. While this should in principle lead to more precise results, it has for the present work led to significantly worse convergence and therefore was not used to obtain the results in Chap. 2. One can rewrite the expression for $p(t)$ in Eq. (B.18) as an average over realizations of this stochastic field by [151]

$$p(t) = \overline{\sum_{n=0}^{\infty} \int_0^t dt_{2n} \frac{iH\sin(vt_{2n})}{2} \times \ldots \times \int_0^{t_2} dt_1 \frac{iH\sin(vt_1)}{2} \prod_{j=1}^{2n} V(t_j)}, \tag{B.24}$$

where $V(t)$ is a 4-by-4 matrix defined in the space of classical double spin states $|\uparrow\uparrow\rangle$, $|\uparrow\downarrow\rangle$, $|\downarrow\uparrow\rangle$, $|\downarrow\downarrow\rangle$ by [75, 151, 262]

$$V(t) = \frac{H\sin(vt)}{2}\begin{pmatrix} 0 & e^{-h} & -e^{h} & 0 \\ e^{i\pi\alpha}e^{h} & 0 & 0 & -e^{-i\pi\alpha}e^{h} \\ -e^{-i\pi\alpha}e^{-h} & 0 & 0 & e^{i\pi\alpha}e^{-h} \\ 0 & -e^{-h} & e^{h} & 0 \end{pmatrix}, \tag{B.25}$$

and $h(t)$ is defined from Eq. (B.19) and $h_s(t)$ by

$$h(t) = h_s - i\int_0^t H\cos(vt')dt'. \tag{B.26}$$

Finally, in this space, using a time-ordered exponential one can write [75, 151]

$$p(t) = \overline{\langle\Phi_f|\,\mathcal{T}e^{-i\int_0^t dt' V(t')}\,|\Phi_i\rangle} = \overline{\langle\Phi_f|\Phi(t)\rangle}, \tag{B.27}$$

where $\left|\Phi_{i/f}\right\rangle$ are states in this four-dimensional space, which for the situation we are considering (i.e., computation of the upper diagonal element of the reduced spin density matrix) are represented by $(1,0,0,0)^T$ [75]. The equation above defines $|\Phi(t)\rangle$ as the solution to

$$i\partial_t |\Phi\rangle = V(t) |\Phi\rangle . \tag{B.28}$$

This has the form of a Schrödinger equation for one realization of the stochastic field, one therefore speaks of the *stochastic Schrödinger equation (SSE)*. Note that $V(t)$ is not Hermitian, for a single realization of the stochastic field, the evolution of the state vector $|\Phi(t)\rangle$ is therefore not unitary [75]. Solving Eq. (B.28) allows to evaluate one realization of $p(t)$. Averaging over many realizations of the stochastic field, one then finds the value of the upper diagonal density matrix element. Note that

$$\langle \sigma^z(t) \rangle = 2p(t) - 1. \tag{B.29}$$

To find expectation values of $\sigma^{x/y}$, we need to evaluate off-diagonal elements of the density matrix. Those have contributions from paths which make $2n-1$ transitions. Therefore, we need to modify the parametrization of the paths to account for that and modify the expression of the influence functional such that paths end after $2n-1$ transitions in a blip state. Essentially, it is as if the system stepped back one time step from a final sojourn state, therefore in order to find $[\rho_s(t)]_{12}$, we need to project out the second component multiplied by $e^{-h(t)}$. Eventually, it holds that $[\rho_s(t)]_{ij} = \overline{\langle \Sigma_{ij} | \Phi(t) \rangle}$ where $\langle \Sigma_{11}| = (1,0,0,0)$, $\langle \Sigma_{12}| = (0, e^{-h(t)}, 0, 0)$, $\langle \Sigma_{21}| = (0,0,e^{h(t)},0)$ and $\langle \Sigma_{22}| = (0,0,0,1)$ [151].

We finally comment on the realization of the stochastic field. To realize the field $h_s(t)$ with the properties (B.20), we decompose $Q_2(t)$ in a Fourier series. For this, realize that Q_2 is a symmetric function. We can define $\tau = t/t_f$ so that $Q_2(\tau t_f)$ is defined on $\tau \in [-1,1]$. If we extend this to make $Q_2(\tau t_f)$ a periodic function, it is justified to write it as a Fourier series. We can write [151]

$$\frac{Q_2(\tau t_f)}{\pi} = \frac{g_0}{2} + \sum_{m=1}^{\infty} g_m \cos(m\pi\tau), \tag{B.30}$$

because of the symmetry. Then we can define $h_s(t)$ in terms of the Fourier coefficients as

$$h_s(\tau t_f) = \sum_{m=1}^{\infty} (g_m)^{1/2} \left[s_{1,m} \cos(\pi m \tau) - s_{2,m} \sin(\pi m \tau) \right], \tag{B.31}$$

which with $s_{1,m}, s_{2,m}$ being independent normal Gaussian variables gives the properties (B.20). Finally, this realization of the stochastic field is used to evaluate $V(t)$ from which the SSE (B.28) is solved. The result is then the solution averaged over the realizations. In the simulation, the Fourier coefficients are found using the fast Fourier transform.

Appendix C

Numerical results for bath observables

In this appendix, we show additional numerical results for the different energy flows involved in the system described by Eq. (2.1) from exact diagonalization and the SSE approach for a radially driven spin-1/2 coupled to a finite number of bosonic modes. These results were obtained for the work [33] and support the claims from Sec. 2.3:

1. In the regime of an efficient quantum dynamo effect, the dynamo efficiency improves for longer operation time.

2. For strong coupling, the energy of fluctuations defined from Eq. (2.65) will after some time dominate over the dynamo energy and the effect will thus break down.

In particular, we compare the work W_{dr} defined in Eq. (2.61), ΔE_{spin} defined from the integral of Eq. (2.60a), ΔE_{dyn} defined in Eq. (2.64) and $\Delta E_{\mathrm{fluct}}$ defined in Eq. (2.65). From the latter, we can identify different contributions to the energy of fluctuations by

$$\begin{aligned} E_{\mathrm{fluct}}(t) &= \sum_k \omega_k \left(\left\langle \left(b_k(t)^\dagger + \frac{g_k}{\omega_k} S(t) \right) \left(b_k(t) + \frac{g_k}{\omega_k} S(t) \right) \right\rangle - \left| \langle b_k(t) \rangle + \frac{g_k}{\omega_k} \langle S(t) \rangle \right|^2 \right), \\ &= \sum_k \omega_k \left[\left(\left\langle b_k^\dagger b_k \right\rangle - \left\langle b_k(t)^\dagger \right\rangle \langle b_k(t) \rangle \right) + \frac{g_k}{\omega_k} \left(\left\langle S(t)(b_k^\dagger + b_k) \right\rangle - \langle S(t) \rangle \left\langle b_k^\dagger + b_k \right\rangle \right) \right. \\ &\quad \left. + \frac{g_k^2}{\omega_k^2} \left(\left\langle S(t)^2 \right\rangle - \langle S(t) \rangle^2 \right) \right], \\ &= \sum_k E_{\mathrm{fluct,k}}^{\mathrm{bath}} + E_{\mathrm{fluct,k}}^{\mathrm{int}} + E_{\mathrm{fluct,k}}^{\mathrm{spin}}. \end{aligned} \tag{C.1}$$

For the model considered in Secs. 2.2 and 2.3, and for this appendix, we set $S(t) = \frac{\sigma^z(t)}{2}$.

The advantage of ED is that it allows a direct readout of all the energies, decomposed over the different bath modes. In contrast, when using the SSE approach (see App. B.2), we need to infer about the bath observables indirectly, from the result for the spin observables

together with analytical relations from the complete system dynamics, as demonstrated for the change in dynamo energy in Eq. (2.64). We first present results from ED for coupling to a single resonant mode, consequently generalize for coupling to several modes, and finally show results also from the SSE approach.

C.1 One resonant mode from ED

In the regime of an efficient dynamo (i.e., $\eta_{\mathrm{dyn}} \to 1$), the fluctuation energy is small compared to the dynamo energy, as expected from the energy balance in Eq. (2.36). This can be confirmed with ED, which is shown in Fig. C.1a). It is then interesting to study the individual contributions to the fluctuations according to Eq. (C.1) (see Fig. C.1b), which are in this case dominated by the spin fluctuations. This underlines that the effect of the mode on the spin is not that of a fluctuating force, but rather one could interprete this limit as the opposite. If we now choose a different regime of stronger coupling (see Fig. C.1c) and d)), we see that an initially efficient dynamo breaks down after a few rotations, which is signalled by the energy of fluctuations becoming larger than the dynamo energy. In this case, the energy fluctuation of the bath mode is growing rapidly. Lastly, for coupling so large that the spin gets frozen, the dynamo effect does not occur and the work done to the spin leads merely to a change of energy of the spin and the total fluctuations dominate the dynamo energy mainly due to spin fluctuations (see Fig. C.1e) and f)).

C.2 Results for several modes from ED

To depart from the one mode dynamo, we simulate a spin coupled to a (small) finite number of bosonic modes using ED, as described in Sec. 2.3.3 and App. B.1. In this case, one has access not only to the repartition of energy contributions between the dynamo energy and the corresponding fluctuations, but also to the contributions to each of these energy changes due to each mode. Results in the regime of an efficient dynamo are shown in Fig. C.2. At the poles, the dynamo energy dominates the fluctuation energy and running the dynamo for some time, it will also start to dominate for all times. We see that the main contribution to the dynamo energy comes from the resonant mode, as expected. While the total fluctuation energy is oscillating with an amplitude below the dynamo energy, its individual components can take large values which cancel each other. Note that at the poles, all components vanish. The numerical analysis is limited by the fact that the resonant mode reaches large occupations, which require a larger Hilbert space, making ED simulations difficult (cf. also App. B.1). Therefore, for stronger coupling, we resort to the stochastic approach in the following.

C.3 Results from SSE

Using the results from the stochastic approach, we obtain the spin dynamics and can infer on W_{dr}, ΔE_{S} and ΔE_{dyn}. The fluctuation energy $\Delta E_{\mathrm{fluct}}$ can then be calculated from the energy balance in Eq. (2.36). Numerical results for driving during half a period for different values of α are shown in Fig. C.3, with a comparison to the corresponding spin expectation values. We see that in the regime of an efficient dynamo and when $C_{\mathrm{dyn}} \approx 1$ (left column), the change in dynamo energy dominates the fluctuation energy. Consequently, when C_{dyn} starts to decrease (middle column), the efficiency of the dynamo decreases (i.e. $\Delta E_{\mathrm{dyn}} < W_{\mathrm{dr}}$), until at even stronger coupling (right column) the fluctuations dominate over the change in dynamo energy.

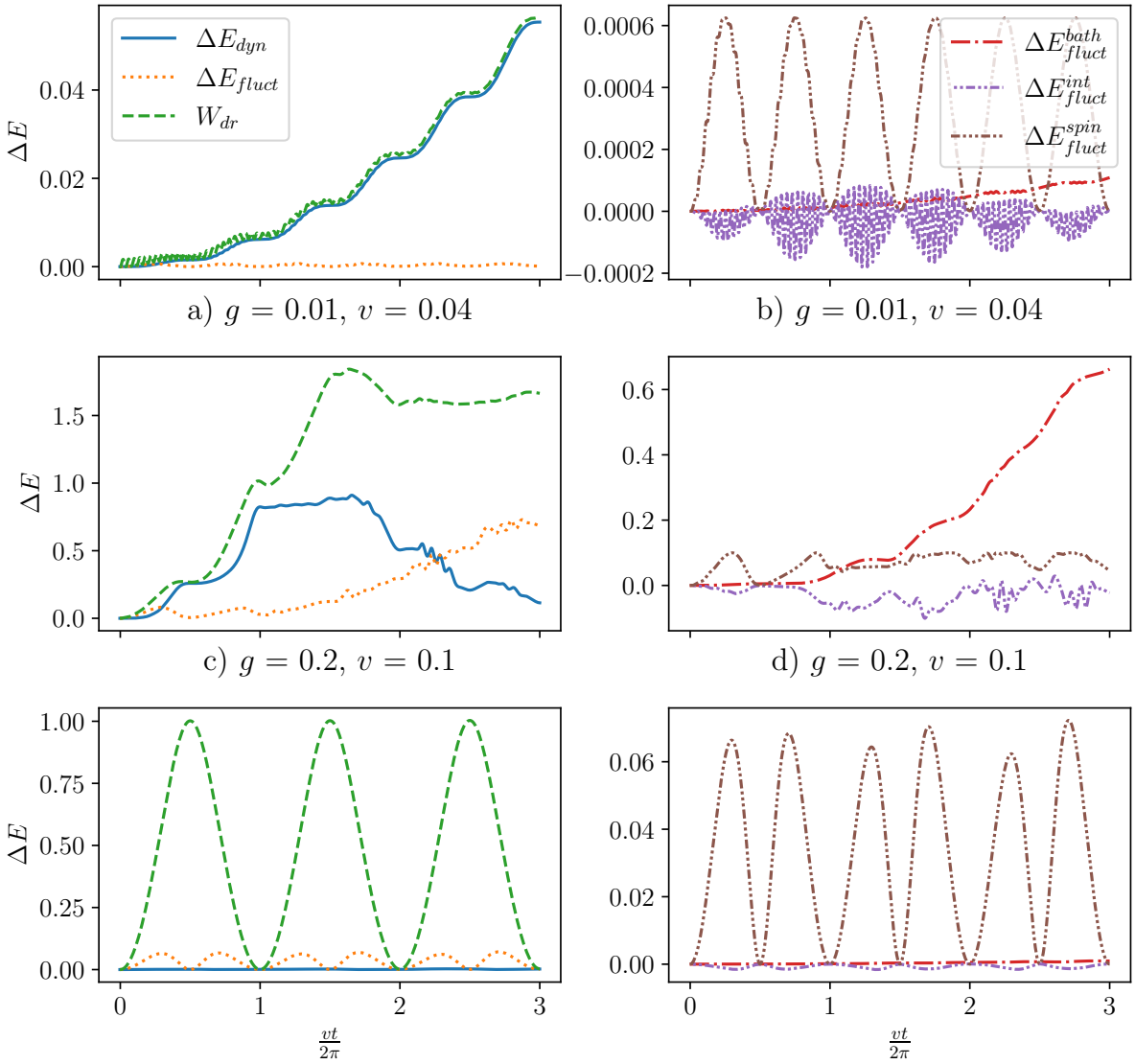

Figure C.1: Numerical results from ED for a spin coupled to one resonant mode for different value of the coupling strength g and the velocity v. On the left, we show results for the changes in the energies ΔE_{dyn}, ΔE_{fluct} and the work W_{dr}, while on the right we show the different components of ΔE_{fluct}. In these simulations, we set $H = 1.0$ and we truncate the Hilbert space of the bosonic degree of freedom at a value which we verify to be well above the maximally reached occupation.

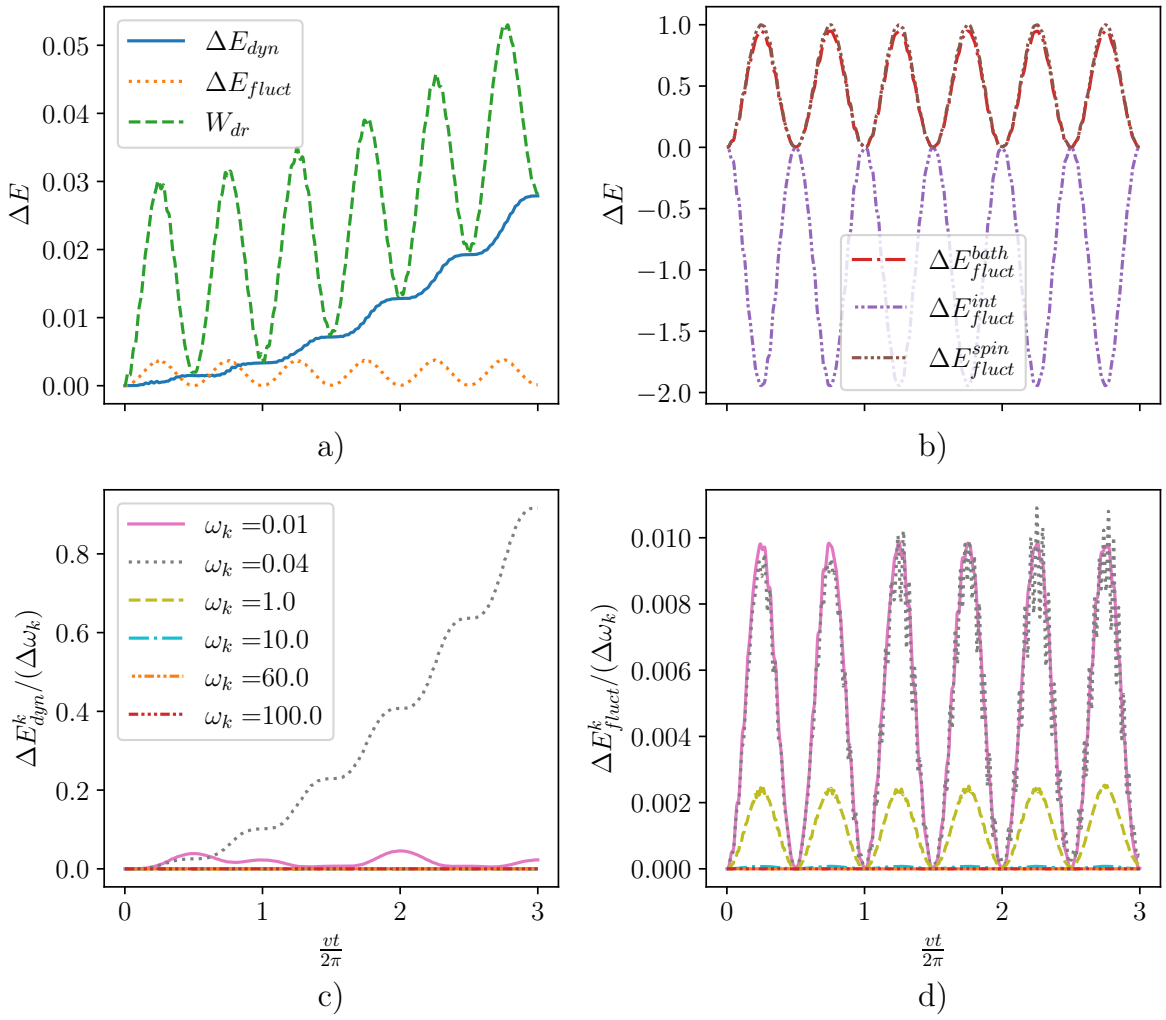

Figure C.2: a) Energy contributions for the total work and the change in dynamo and fluctuation energy, summed over all modes. b) Different contributions to the fluctuation energy. c) Individual contributions to the dynamo energy and d) to the fluctuations coming from some of the simulated modes (only the results for 6 out of 8 modes are plotted), normalized by the width of the part of the spectrum discretized by this mode. Here, we set $\alpha = 0.02$, used an Ohmic spectral density with a hard cut-off at $\omega_c = 100.0$, discretized it by $N = 8$ modes and checked that their occupations remain well below the value at which they are truncated. Furthermore, we set $H = 1.0$.

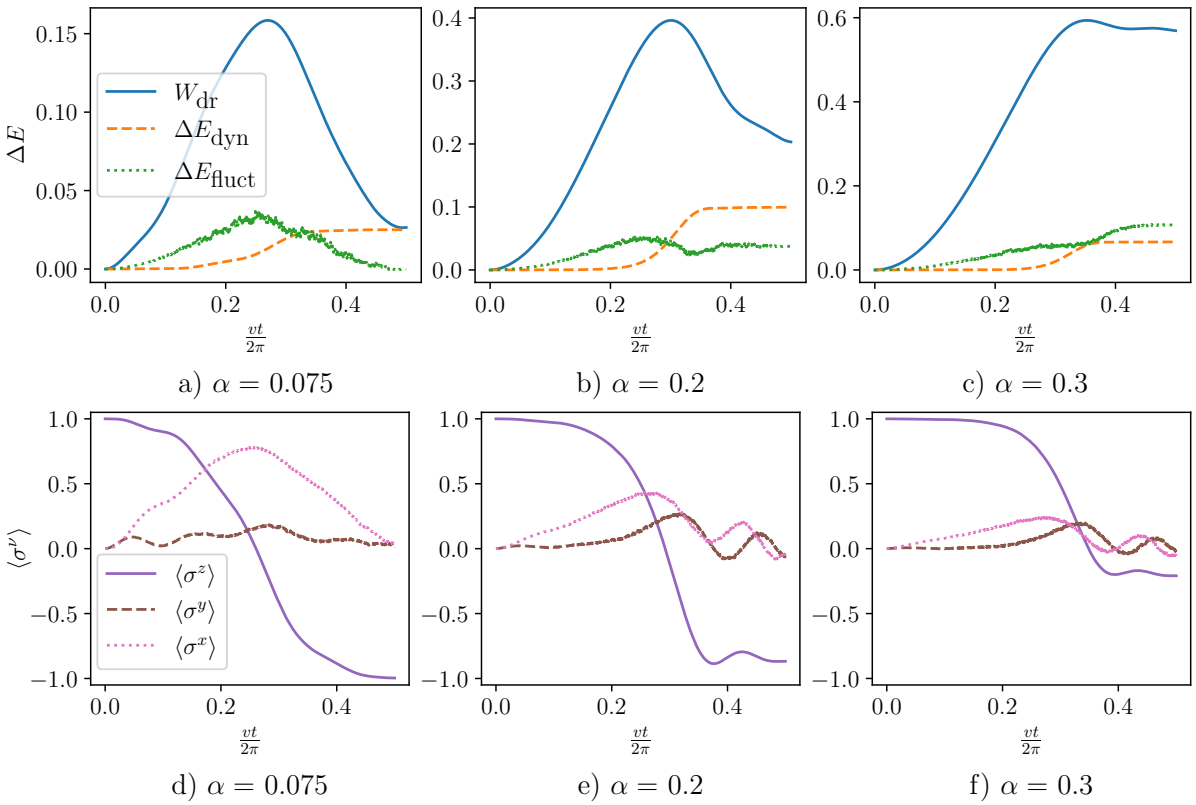

Figure C.3: Results from SSE with an Ohmic spectral density with exponential cut-off and $\omega_c = 100.0$, while $H = 1.0$. a)-c) show results for the changes in the relevant energies for three different values of α, while d)-f) show the corresponding spin expectation values for the corresponding values of α.

Appendix D

Calculations for open quantum dynamics

D.1 Adiabatic renormalization

In this section, we show how to understand the quantum phase transition in the spin-boson model without driving at coupling strength $\alpha = 1$ in terms of an adiabatic renormalization procedure for the tunneling amplitude, as described in Sec. 1.2.2 following [79]. Considering the model

$$\mathcal{H} = -\frac{\Delta}{2}\sigma^x + \frac{\sigma^z}{2}\sum_k g_k(b_k^\dagger + b_k) + \sum_k \omega_k b_k^\dagger b_k, \tag{D.1}$$

with an Ohmic spectral density with exponential cut-off, as in Eq. (1.50), we write the lowest lying eigenstates as

$$\begin{aligned} |\Sigma_\pm\rangle &= \frac{1}{\sqrt{2}}\left(|+\rangle_z \otimes |\psi_+\rangle \pm |-\rangle_z \otimes |\psi_-\rangle\right), \\ \text{with} \quad |\psi_\pm\rangle &= \prod_{k<l} |\psi_{\pm,k}\rangle\,, \\ \text{and} \quad |\psi_{\pm,k}\rangle &= \exp\left(\mp\frac{1}{2}\frac{g_k}{\omega_k}(b_k^\dagger - b_k)\right)|0\rangle\,. \end{aligned} \tag{D.2}$$

Here $\omega_l = p\Delta$ with $p \gg 1$, so that only frequencies larger than this cut-off are included and modes with lower frequencies are being ignored [79]. The overlap between the two states defines the renormalized tunneling element, i.e.,

$$\Delta'(\omega_l) = \Delta \prod_{k>l} \langle\psi_{\pm,k}|\psi_{\pm,k}\rangle = \Delta \exp\left(-\frac{1}{2\pi}\int_{\omega_l}^\infty d\omega \frac{J(\omega)}{\omega^2}\right). \tag{D.3}$$

The tunneling element decreases in this procedure and iterating the prescription, one can include lower lying modes, since now $\omega_l = p\Delta'$ (and p is fixed). This iteration will converge to a finite value if for a certain finite frequency ω_t, all lower lying frequencies

$\omega < \omega_t$ satisfy $\frac{\mathrm{d}\ln\Delta'(\omega)}{\mathrm{d}\ln\omega} < 1$, which from the structure of Eq. (D.3) is equivalent to [79]

$$\frac{J(\omega)}{2\pi\omega} < 1. \tag{D.4}$$

For our choice of an Ohmic spectral density, this translates to the condition that for frequencies below a certain threshold, we satisfy $\alpha e^{-\omega/\omega_c} < 1$. For $\alpha > 1$, this cannot hold true, therefore all tunneling is suppressed, i.e., the tunneling element Δ is renormalized to zero and the spin becomes completely localized. For $\alpha < 1$, the above inequality holds true, the tunneling element gets renormalized in this regime. This can be done by a self-consistent approach from Eq. (D.3)

$$\Delta_r = \Delta \exp\left(-\int_{p\Delta_r}^{\infty} d\omega \frac{\alpha e^{-\omega/\omega_c}}{\omega}\right), \tag{D.5}$$

giving [64, 79]

$$\Delta_r = \Delta\left(\frac{p\Delta}{\omega_c}\right)^{\frac{\alpha}{1-\alpha}} \sim \Delta\left(\frac{\Delta}{\omega_c}\right)^{\frac{\alpha}{1-\alpha}}. \tag{D.6}$$

In the last step, we neglected the constant p, which was essentially arbitrary. A careful analysis, discussed in [79], shows that this is justified with an Ohmic spectral function technically only for small α. Eq. (D.6) gives the expression for the energy scale Δ_r governing the dynamics in the regime $\alpha < 1$ used in the main text in Eq. (1.57) (which is valid strictly speaking only for small α).

D.2 Polaronic transformation

The Hamiltonian in Eq. (D.1), using a similar principle as above, can also be directly transformed using the so-called polaronic transformation, which displaces the bosonic modes at the level of the full Hamiltonian, so that the coupling is absorbed into the spin part of the Hamiltonian. The transformation reads [79]

$$U = \exp\left(-i\frac{\sigma^z}{2}\Omega\right) \text{ with } \Omega = i\sum_k \frac{g_k}{\omega_k}(b_k^\dagger - b_k), \tag{D.7}$$

transforming the Hamiltonian into

$$\tilde{\mathcal{H}} = -\frac{\Delta}{2}e^{-i\Omega}\sigma^+ - \frac{\Delta}{2}e^{i\Omega}\sigma^- + \sum_k \omega_k b_k^\dagger b_k. \tag{D.8}$$

Considering a situation of weak coupling, we can trace over the bath degrees of freedom by using the Gaussian property of the fluctuations of the bath modes and calculate [263]

$$\left\langle e^{\pm i\Omega} \right\rangle = e^{-\frac{1}{2}\left\langle \Omega^2 \right\rangle} = \exp\left(-\sum_k \frac{g_k^2}{2\omega_k^2} \right), \tag{D.9}$$

and from here one can again use the adiabatic renormalization procedure to obtain the renormalized tunneling element in the same form as in Eq. (D.3). The Hamiltonian for the spin then reads

$$\tilde{\mathcal{H}}_{\text{spin}} = -\frac{\Delta_r}{2}\sigma^x. \tag{D.10}$$

Appendix E

Bosonization of the XXZ chain

In this appendix, we show how to go from Eq. (4.26) to Eq. (4.28) from the analysis in [216]. In fermionic language, we had written the Hamiltonian as

$$\mathcal{H}_a = -2J_{xy}\sum_i c_i^\dagger c_{i+1} + \text{h.c.} + J_z\sum_i (2n_i - 1)(2n_{i+1} - 1) + \frac{U_{af}}{2}\sum_i \tau_i^z(2n_i - 1). \quad \text{(E.1)}$$

The Jordan-Wigner transformation (see Eq. (3.31)) maps between spin operators and fermionic operators on a chain. We can identify the spin raising and lowering operators with creation and annihilation fermion operators

$$c_i^\dagger = s_i^\dagger \mathrm{e}^{i\pi\sum_{j<i} n_j}. \quad \text{(E.2)}$$

We can decompose the bosonic operator into a density and a phase [203, 264]:

$$s_i^\dagger = \sqrt{\rho_i}\mathrm{e}^{i\tilde{\theta}_i}. \quad \text{(E.3)}$$

If we only consider low energy excitations, we can linearize the spectrum around the Fermi momenta and define left- and right-moving fermions according to the side of the spectrum at which they arise [232]. This corresponds to the description of the free fermion model as a Luttinger liquid [232, 265]. Passing to the continuum limit and using the relations (E.2) and (E.3), while changing the sum to an integral over an infinite chain, we can write for the left- and right-moving fermions upon linearizing the spectrum [203, 231]:

$$c_{R/L}^\dagger(x) = \frac{c_{j,R/L}^\dagger}{\sqrt{a}} \approx \frac{1}{\sqrt{a}}\mathrm{e}^{i\tilde{\theta}(x)}\mathrm{e}^{\pm i\pi\int_{-\infty}^{x}\rho(x)dx}. \quad \text{(E.4)}$$

We then decompose the continuous density operator into a mean and fluctuations $\rho(x) = (\rho_0 + \tilde{\rho})$ with $\rho_0 = ak_F/\pi$, and $\tilde{\rho}$ obeys the commutation relation $[\tilde{\theta}(x), \tilde{\rho}(y)] = i\delta(x - y)$

between the density and the phase [203]. We can write

$$\rho(x) = \rho_0 + \frac{\partial_x \tilde{\phi}(x)}{\pi}, \tag{E.5}$$

where we introduced the field $\phi(x)$ by $\tilde{\rho} = \partial_x \tilde{\phi}(x)/\pi$. Then the above commutation relation is achieved for $[\tilde{\theta}(x), \tilde{\phi}(y)] = i\frac{\pi}{2}\mathrm{sgn}(x-y)$. Plugging the form of $\tilde{\rho}$ into Eqs. (E.4) gives, upon accounting for the normalization imposed by Eq. (E.5),

$$c_R^\dagger(x) = \frac{1}{\sqrt{2\pi a}} \mathrm{e}^{i\tilde{\theta}(x)} \mathrm{e}^{ik_F x} \mathrm{e}^{i\tilde{\phi}}, \tag{E.6a}$$

$$c_L^\dagger(x) = \frac{1}{\sqrt{2\pi a}} \mathrm{e}^{i\tilde{\theta}(x)} \mathrm{e}^{-ik_F x} \mathrm{e}^{-i\tilde{\phi}}. \tag{E.6b}$$

Multiplying the right-hand sides of the equations (E.6) by the respective Klein factors $U_{R/L}$ where $U_R U_L = i$ gives Eqs. (4.27) [231]. The total density is then given by

$$\rho(x) = \rho_0 + \frac{\partial_x \tilde{\phi}}{\pi} = c_R^\dagger c_R + c_L^\dagger c_L + \mathrm{e}^{i2k_F x} c_R^\dagger c_L + \mathrm{e}^{-i2k_F x} c_L^\dagger c_R, \tag{E.7}$$

and we can write the density fluctuations as

$$\frac{\partial_x \tilde{\phi}}{\pi} = \lim_{a\to 0} c_R^\dagger(x+a) c_R(x) + c_L^\dagger(x-a) c_L(x).$$

For the hopping part of the initial Hamiltonian (E.1), we find in the continuum limit

$$\mathcal{H} = -2J_{xy} \int dx c^\dagger(x) c(x+a) + \mathrm{h.c.}. \tag{E.8}$$

Splitting into the right- and left-moving branches and taking the limit of $a \to 0$, we obtain after an integration by parts the Hamiltonian in the Dirac-form,

$$\mathcal{H} = iv_0 \int dx (c_R^\dagger(x) \nabla c_R(x) - c_L^\dagger(x) \nabla c_L(x)), \tag{E.9}$$

with $v_0 = 4aJ_{xy}$. The Hamiltonian in terms of the fields $\tilde{\phi}$ and $\tilde{\theta}$ reads

$$\mathcal{H} = \frac{v_0}{2\pi} \int dx ((\partial_x \tilde{\theta})^2 + (\partial_x \tilde{\phi})^2). \tag{E.10}$$

The interaction term in Eq. (E.1) takes the form $4J_z \sum_i \left(n_i - \frac{1}{2}\right)\left(n_{i+1} - \frac{1}{2}\right)$. As we consider the system at half-filling, we can replace terms like $n_i - \frac{1}{2}$ directly by the density fluctuations and then write the interaction term in the continuum limit and omitting the rapidly oscillating parts as

$$\frac{a 8 J_z/\pi}{2\pi} \int dx \left(\partial_x \tilde{\phi}\right)^2,$$

so that the interacting Hamiltonian can be written upon introducing the Luttinger parameter K and renormalizing the velocity v as

$$\mathcal{H}_a = \frac{v}{2\pi}\int dx \frac{1}{K}(\partial_x\tilde{\phi})^2 + K(\partial_x\tilde{\theta})^2, \tag{E.11}$$

with $v/a = \sqrt{(4J_{xy})^2 + 32J_zJ_{xy}/\pi}$ and $K = \sqrt{4J_{xy}/(4J_{xy} + 8J_z/\pi)}$.

Now, we study the disorder term $\frac{U_{af}}{2}\sum_j \sigma_j^z\tau_j^z$ with a staggered configuration $\tau_j^z = (-1)^j$. In the fermionic language this reads

$$\frac{U_{af}}{2}\sum_j (-1)^j 2n_j,$$

where we neglected a constant. In the continuum limit, we write $(-1)^j \to \mathrm{e}^{i\pi x/a}$ with $x = aj$ and thus obtain

$$\frac{U_{af}}{2a}\int dx \mathrm{e}^{i\pi\frac{x}{a}}(c_L^\dagger c_L + c_R^\dagger c_R) + \frac{U_{af}}{2\pi a}\int dx\, \mathrm{e}^{i\pi\frac{x}{a}} i\mathrm{e}^{i2k_Fx}\mathrm{e}^{i2\tilde{\phi}} + \text{h.c.}$$

The first integral can be neglected as it is oscillating rapidly. Since $k_F = \frac{\pi}{2a}$ and $x = aj$,

$$\mathrm{e}^{i\pi\frac{x}{a}}\mathrm{e}^{i2k_Fx} = (-1)^2 = 1$$

and we can write the second integral as

$$-\frac{U_{af}}{\pi a}\int dx \sin\big(2\tilde{\phi}\big).$$

Then the full Hamiltonian reads

$$\mathcal{H}_a = \frac{v}{2\pi}\int dx \left(\frac{1}{K}(\partial_x\tilde{\phi})^2 + K(\partial_x\tilde{\theta})^2\right) - \frac{1}{\pi}\int dx \frac{U_{af}}{a}\sin\big(2\tilde{\phi}\big). \tag{E.12}$$

This corresponds to Eq. (4.28) in Chap. 4.

ECOLE
DOCTORALE

Titre : Topologie et effets de désordre dans les systèmes de spin quantique ouverts et en interaction et leurs analogues

Mots clés : spin, phases topologiques, localisation, interactions, désordre, quantum

Résumé : Cette thèse de doctorat porte sur l'étude du désordre, de la localisation, de l'interaction avec un environnement et de la topologie dans des systèmes quantiques à plusieurs corps, en particulier dans les systèmes de spin. La topologie d'un spin-$1/2$ peut être mesurée en utilisant un protocole dynamique pilotant le champ magnétique au cours du temps. Pour cette configuration, la thèse étudie un 'effet de dynamo quantique' se produisant comme conséquence de la dynamique dissipative entraînée lors du couplage à un environnement. Cet effet présente un lien intriguant avec la 'topologie accédée dynamiquement' du spin. Dans les systèmes en interaction composés de plusieurs spins, la topologie de chaque spin peut être étudiée et il a été montré précédemment qu'elle donne des valeurs fractionnaires en fonction de la symétrie du modèle. Cette thèse met l'accent sur le comportement de cette phase topologique fractionnaire lors de l'introduction du désordre et montre que ce dernier peut conduire à son extension. Une interprétation de ces effets en termes de fermions de Majorana est discutée et permet d'envisager des applications en information quantique.
Les effets du désordre et de la physique de la localisation sont examinés en profondeur pour un modèle qui peut être réalisé à partir d'atomes froids et qui, dans une certaine limite, peut également être représenté par un modèle de spin. Une étude numérique utilisant la diagonalisation exacte démontre la présence d'une phase localisée à N-corps dans ce modèle. Elle est identifiée à partir du comportement de l'entropie d'intrication et attestée par les fluctuations bipartites et un courant local.
La thèse ouvre des perspectives pour une compréhension fondamentale de l'interaction de la topologie, de la dynamique des systèmes ouverts et des effets de désordre dans les systèmes quantiques et fait le lien avec les réalisations expérimentales et les applications.

Title : Topology and disorder effects in interacting and open quantum spin systems and analogues

Keywords : spin, topologial phases, localisation, interactions, disorder, quantum

Abstract : This PhD thesis is concerned with the interplay of effects of disorder, localization, interaction with the environment and topology in quantum many-body systems, in particular in spin systems. The topology of a spin-$1/2$ in a radial field can be probed from a dynamic protocol driving the magnetic field in time. In this setup, the thesis investigates a 'quantum dynamo effect' occurring as a consequence of the driven dissipative dynamics when coupling to an environment. This effect bears an intriguing connection with the 'dynamically accessed topology' of the spin. This thesis defines and investigates thermodynamic properties of this effect corresponding to a work-to-work conversion coherently displacing certain modes of the environment. It opens perspectives for energy transfers on the quantum scale through an environment when coupling several systems to a common bath. In interacting systems composed of several spins, the topology of each spin can be studied and has previously been shown to yield fractional values depending on the symmetry of the model. This thesis emphasizes the behavior of this fractional topological phase when disorder is introduced and shows that the latter can lead to its extension. An interpretation of these effects in terms of Majorana fermions is discussed, enabbling considerations for applications in quantum information.
The effects of disorder and localization physics are discussed in depth for a model which can be realized using cold atoms and can in a certain limit be mapped to a spin model as well. A numerical study using exact diagonalisation demonstrates the presence of a many-body localized phase in this model. This phase is identified from the scaling of the entanglement entropy and witnessed by the bipartite fluctuations and the local current. The thesis offers perspectives for a fundamental understanding of the interplay of topology, open system dynamics and disorder effects in quantum systems and bridges with experimental realizations and applications.

Institut Polytechnique de Paris
91120 Palaiseau, France